

**Fundamental properties of  
excitons and phonons in ZnO:**  
**A spectroscopic study of the dynamics,  
polarity, and effects of external fields**

vorgelegt von  
Diplom-Physiker  
Markus Raphael Wagner  
Berlin

Institut für Festkörperphysik  
Fakultät II - Mathematik und Naturwissenschaften  
Technische Universität Berlin

zur Erlangung des akademischen Grades  
Doktor der Naturwissenschaften  
Dr. rer. nat.

genehmigte Dissertation

Promotionsausschuss:

Vorsitzender: Prof. Dr. Michael Lehmann  
Berichter/Gutachter: Prof. Dr. Axel Hoffmann  
Berichter/Gutachter: Prof. Dr. Bruno K. Meyer  
Berichter/Gutachter: Prof. Dr. Christian Thomsen

Tag der wissenschaftlichen Aussprache  
09. Dezember 2010

Berlin 2010

D83

## Zusammenfassung

Die vorliegende Arbeit präsentiert spektroskopische Untersuchungen der optischen Übergänge und Gitterdynamik von ZnO unter dem Einfluss von externen Feldern. Eine vergleichende Studie von verschiedenen ZnO-Einkristallen und homoepitaktisch gewachsenen ZnO-Filmen zeigt deutliche Unterschiede in der Lumineszenz freier und gebundener Exzitonen, die auf Verunreinigungen und Verzerrungen zurückgeführt werden können. Der Ladungszustand und Donator- oder Akzeptor-Charakter aller flachen Exzitonen-Bindungscentren wird durch Photolumineszenz-Spektroskopie (PL) in externen Magnetfeldern identifiziert. Eine Korrelation zwischen den Lokalisierungsenergien der Exzitonen, die an Fremdatomen des gleichen chemischen Elementes in unterschiedlichen Ladungszuständen gebunden sind, wird dargelegt. Des Weiteren werden die angeregten Zustände der gebundenen Exzitonen untersucht und durch Anregungsspektroskopie und temperaturabhängige PL identifiziert.

Die Eigenschaften flach gebundener Exzitonen an Fremdatomen werden mit denen tief gebundener Exzitonen an Defekten verglichen. Durch die Kombination verschiedener experimenteller Techniken kann eine Vielzahl neuer Erkenntnisse abgeleitet werden. Diese umfassen die Defektart und den Ladungszustand der Bindungscentren, die Temperaturabhängigkeit der Lokalisierungsenergien, die Stärke der Exziton-Phonon-Kopplung der tief gebundenen Exzitonen, die Rekombinationsdynamik flach und tief gebundener Exzitonen, den Einfluss von uniaxialem Druck auf die elektronischen Energieniveaus sowie die räumliche Verteilung der Lumineszenz-Zentren. Basierend auf diesen Daten wird ein Defektmodell für tief gebundene Exzitonen in ZnO entwickelt, das alle experimentellen Ergebnisse erklärt und eine theoretische Abschätzung der Ausdehnung der Defektkomplexe ermöglicht.

Ein weiterer Teil dieser Arbeit ist der Untersuchung der Valenzbandordnung in ZnO gewidmet, die seit fast einem halben Jahrhundert kontrovers diskutiert wird. Die hier vorgestellten hochaufgelösten Magneto-PL-Messungen gebundener Exzitonen ermöglichen eine eindeutige Identifizierung der Valenzbandordnung und tragen somit zur Beendigung dieser Debatte bei. Durch die Auflösung einer bisher unerkannten Feinaufspaltung der Lochzustände in Kombination mit polarisations- und winkelaufgelösten Messungen werden schlüssige Beweise für eine umgekehrte Valenzbandordnung in ZnO im Vergleich zu anderen Wurtzit II-VI und III-V Verbindungshalbleitern präsentiert.

Die Gitterdynamik von ZnO-Kristallen unter dem Einfluss von äußerem Druck wird mittels der Raman-Spektroskopie untersucht. Eine Vielzahl wichtiger Materialparameter einschließlich präziser Werte der hydrostatischen Druck-Koeffizienten und Grüneisen Parametern aller Raman-aktiven Moden wird bestimmt. Für die transversale effektive Ladung nach Born wird eine fehlerhafte Druckabhängigkeit in der Literatur aufgezeigt und korrigiert. Außerdem werden zum ersten Mal Raman-Messungen an ZnO-Einkristallen unter uniaxialem Druck durchgeführt. In Kombination mit hydrostatischen Druckmessungen an denselben Proben wird erstmalig eine experimentelle Bestimmung der Phonon-Deformationspotentiale aller Raman-aktiven Moden in ZnO erreicht.

Darüber hinaus wird die resonante Raman-Streuung an gebundenen Exzitonen in ZnO untersucht. Der Einfluss der Anregungsenergie und der Temperatur auf die Dynamik der Phonon-Repliken und Raman-Moden wird analysiert. Die Dissoziation der Exzitonen bei erhöhten Temperaturen beeinflusst die Lebensdauer der LO-Phononen unter resonanter Anregung, die durch zeitaufgelöste Messungen im Pikosekundenbereich bestimmt werden.

## Abstract

The work in hand presents a spectroscopic study of optical transitions and lattice dynamics of ZnO under the influence of external fields. A comparative study of different ZnO single crystals and homoepitaxial ZnO films reveals pronounced differences in the free and bound exciton luminescence which can be related to different impurity centers and strain levels. The charge state and donor or acceptor character of all observed shallow bound exciton centers is identified by photoluminescence spectroscopy in external magnetic fields. A correlation between the localization energies of excitons bound to the same chemical element in the neutral and ionized charge state is reported. Furthermore, different excited states of the free and bound excitons are investigated and identified by photoluminescence excitation spectroscopy and temperature dependent photoluminescence spectroscopy.

The properties of the shallow impurity bound excitons are compared to defect related deeply bound excitons. Not much was known about the defect centers of these deeply bound excitons. By the combination of different experimental techniques, a multitude of new information is obtained including the defect type and charge state of the binding centers, the temperature dependence of the localization energies, the strength of the exciton-phonon coupling of the deeply bound excitons, the recombination dynamics of shallow and deeply bound excitons, the influence of uniaxial pressure on the electronic energy levels, and the spatial distribution of the luminescence centers. Based on these data, a defect model for deeply bound excitons in ZnO is developed which is capable of explaining all experimental results and provides a theoretical estimation of the extend of the defect complexes.

Another part of this work is dedicated to the study of the valence band ordering in ZnO which has been debated controversially for almost half a century. High resolution magneto-PL measurements of bound excitons are presented which allow to resolve this long lasting disagreement in the literature. A previously undetected hole fine splitting could be resolved which provides, in combination with polarization and angular resolved measurements, conclusive evidence for a reversed valence band ordering in ZnO compared to other wurtzite II-VI and III-V compound semiconductors.

The lattice dynamics of ZnO crystals are studied by Raman spectroscopy under the influence of external pressure. A variety of important material parameters is derived including high precision values of the hydrostatic pressure coefficients and Grüneisen parameters of all Raman active modes. The accuracy of the here reported values exceeds those of previously published values in the literature. For Born's transverse effective charge, an incorrect pressure dependence in the literature is discovered and revised. Raman measurements of ZnO single crystals under uniaxial pressure are reported for the first time. In combination with the hydrostatic pressure measurements on the same samples, the first experimental determination of the phonon deformation potentials of all Raman active modes in ZnO is achieved.

Furthermore, a study of the resonant Raman scattering at bound exciton states is presented. The influence of the excitation energy and temperature on the decay dynamics of phonon replicas and Raman modes is investigated. The dissociation of the bound excitons at elevated temperatures is found to alter the lifetimes of the LO modes under resonant excitation which are directly determined by time resolved measurements on the picosecond time scale.

# Contents

<b>1</b>	<b>Introduction</b>	<b>7</b>
1.1	Objective and thesis structure . . . . .	9
<b>2</b>	<b>Experimental techniques</b>	<b>12</b>
<b>3</b>	<b>Optical transitions near the band edge of ZnO</b>	<b>17</b>
3.1	Photoluminescence of ZnO . . . . .	17
3.2	Comparison of ZnO substrates from different manufacturers . . . . .	22
3.3	Exciton-polaritons . . . . .	23
3.4	Bound excitons . . . . .	26
3.4.1	Neutral and ionized donors . . . . .	29
3.4.2	Excited states of bound excitons . . . . .	33
3.5	Summary . . . . .	40
<b>4</b>	<b>Effects of external magnetic fields</b>	<b>41</b>
4.1	Excitons in magnetic fields . . . . .	41
4.2	The Zeeman effect . . . . .	42
4.3	Selection rules of exciton states in magnetic fields . . . . .	43
4.4	Zeeman splitting of excitonic states . . . . .	44
4.4.1	Neutral bound excitons . . . . .	44
4.4.2	Donor and acceptor bound excitons . . . . .	49
4.4.3	Free and ionized bound excitons . . . . .	52
4.5	Summary . . . . .	58
<b>5</b>	<b>The band structure of ZnO</b>	<b>60</b>
5.1	The band structure . . . . .	60
5.2	The valence band ordering . . . . .	62
5.2.1	The controversy about the valence band ordering in ZnO . . . . .	64
5.2.2	Symmetry states of bound excitons in magnetic fields . . . . .	66
5.2.3	Angular resolved magneto-PL . . . . .	70
5.2.4	Polarization dependent hole fine splitting . . . . .	71
5.2.5	Additional contribution to the VB ordering . . . . .	72
5.3	Summary . . . . .	74

---

<b>6</b>	<b>Structural defect bound excitons</b>	<b>75</b>
6.1	Deeply bound excitons in ZnO - An overview . . . . .	75
6.2	Defect type and charge state . . . . .	78
6.3	Temperature dependence of free-, shallow-, and deeply bound excitons	85
6.4	Phonon replica and two electron satellites . . . . .	88
6.5	Absorption in magnetic fields . . . . .	91
6.6	Excited states . . . . .	94
6.7	Recombination dynamics . . . . .	96
6.8	Uniaxial pressure coefficients . . . . .	100
6.9	Spatial distribution of defect centers . . . . .	102
6.10	Defect bound excitons in other compound semiconductors . . . . .	104
6.11	Discussion of possible defect models . . . . .	104
6.12	Summary . . . . .	109
<b>7</b>	<b>Raman scattering under uniaxial and hydrostatic pressure</b>	<b>110</b>
7.1	Elastic properties of wurtzite materials . . . . .	110
7.2	Hydrostatic pressure . . . . .	112
7.3	Raman effect . . . . .	115
7.4	Lattice dynamics and phonon dispersion of ZnO . . . . .	116
7.5	Raman scattering without external pressure . . . . .	118
7.6	Raman scattering under hydrostatic pressure . . . . .	121
7.6.1	Grüneisen parameters . . . . .	121
7.6.2	Born's transverse effective charge . . . . .	124
7.6.3	Line-shape asymmetry of the $E_2(\text{high})$ . . . . .	128
7.7	Phonon deformation potentials . . . . .	130
7.8	Summary . . . . .	134
<b>8</b>	<b>Exciton and phonon dynamics under resonant excitation</b>	<b>136</b>
8.1	Resonant Raman scattering at excitonic states . . . . .	136
8.2	Time resolved exciton and phonon dynamics . . . . .	142
8.2.1	Dynamics as function of the excitation energy . . . . .	142
8.2.2	Dynamics as function of the temperature . . . . .	147
8.3	Summary . . . . .	150
<b>9</b>	<b>Influence of substrate polarity on homoepitaxial ZnO epilayers</b>	<b>151</b>
9.1	The polar faces of wurtzite ZnO . . . . .	151
9.2	Analysis of the polar faces by HRTEM . . . . .	152
9.3	Depth resolved strain distribution . . . . .	155
9.4	Optical properties of the homoepitaxial layers . . . . .	158
9.5	Summary . . . . .	163

<b>10 Summary</b>	<b>165</b>
<b>11 Publications</b>	<b>169</b>
<b>12 Conference contributions</b>	<b>174</b>
<b>Bibliography</b>	<b>177</b>
<b>Acknowledgment</b>	<b>200</b>

# 1 Introduction

The II-VI semiconductor zinc oxide (ZnO) has a long research history which dates back to the first half of the 20th century. In the last 5 to 10 years, ZnO returned into the focus of research activities driven by the prospect of potential applications in optoelectronics, transparent electronics, and spintronics. The pronounced interest in this material system is governed by the combination of several advantages in comparison to the main competitor GaN. Among those are the large exciton binding energy of 60 meV which might pave the way for efficient micro-cavity based polariton lasers [1], its non-toxicity and bio-compatibility with organic systems making it a promising candidate for hybrid devices [2, 3], and the availability of bulk single crystals with low production costs. As a wide gap semiconductor, ZnO is an ideal candidate for optoelectronic devices such as blue to UV light emitting diodes (LEDs), laser diodes (LDs), and white light emitters with applications in high density data storage systems and solid-state lighting [4–7]. The transparency to visible light provides the opportunity to fabricate transparent electronics, UV opto-electronics, and integrated sensors from the same material system and makes ZnO an excellent choice for transparent front electrodes in solar cells and displays. Transparent thin film field effect transistors could exhibit enormous potential on the high power and high frequency electronics market [8–10]. The strong resistance to radiation also makes ZnO particularly promising for electronic devices in strong radiation environments, such as satellites and space probes [11–13].

The main obstacle for the commercialization of many ZnO based devices is a stable and reproducible p-type doping with high hole concentrations and mobilities. ZnO has an asymmetric doping limitation, it can be easily doped n-type by Al, Ga, or In on Zn lattice site [14–17], but is difficult to be doped p-type. This is related to the very low energy of the valence band relative to the vacuum level which results in the efficient compensation of acceptors [18]. On the one hand, several acceptors introduced by Li [19], Cu [20], and Ag [21] are known, but form deep energy levels which do not noticeably contribute to hole conduction. On the other hand, group V elements like N, P, and As may act as shallow acceptors but efficient acceptor compensation mechanisms, high acceptor ionization energies, and low solubility usually result in hole concentrations which are not sufficient for optoelectronic devices. Another problem concerns the experimental proof of p-type conductivity based on

integral electric measurements such as Hall effect or van der Pauw measurements. Point and extended structural defects can lead to an inhomogeneously distributed conductivity resulting in an erroneous identification of p-conductivity [22,23]. Consequently, the realization, improvement, and determination of p-type ZnO strongly depends on the successful control of dopants and defects.

Since defects and impurities which are relevant for the electron or hole conductivity form shallow donor or acceptor states, their incorporation into the lattice greatly affects the optical spectrum near the fundamental band gap. In as grown n-type ZnO, the prevalence of several shallow donor impurities gives rise to narrow emission lines in the luminescence spectra which originate from the radiative recombination of excitons bound to the shallow impurity states. These transitions can provide a multitude of information about the charge state, chemical identity, and dopant type (donor or acceptor) of the impurities. Despite the long lasting research on ZnO, these properties are by far not known for all observable bound exciton emission lines. A strong motivation for a comprehensive understanding of the radiative transitions near the fundamental band edge is additionally given by the recent progress [24,25] and future prospects of p-doping with shallow acceptor states, since these levels should best be monitored by the respective changes in the near band edge luminescence. However, the identification of these potential changes requires a precise and extensive understanding of the bound exciton emission lines. Therefore, a comparative study of various ZnO crystals is presented in this work which provides new insights on the excitonic features of ZnO. Another important requirement towards successful p-conductivity is the reduction of defect states which can introduce shallow donors or deep centers and thus promotes n-type or semi-insulating materials. The presence of structural defects such as interstitials, vacancies, dislocations, and stacking faults may create undesired radiative and non-radiative recombination channels and leads to the appearance of additional emission lines. The knowledge about the properties of these centers is still rather limited, thus providing a substantial inducement for a detailed analysis of the corresponding optical transitions. Furthermore, reports on a multitude of intrinsic properties of ZnO are controversial, questionable, or still missing in the literature. A selection of these open questions is addressed in this work including the ordering of the valence bands, the values of the Grüneisen parameters and phonon deformation potentials, the pressure dependence of Born's effective charge, the lifetimes of resonantly excited phonons, and the influence of the substrate polarity on the properties of homoepitaxial layers. The following section outlines the objective and structure of this work in detail.

## 1.1 Objective and thesis structure

The present work comprises a detailed study of impurities, defects and lattice dynamics in ZnO. It is the general aim of this work to extend and deepen the knowledge about the electronic states and optical transitions related to impurities and defects as well as to address several key issues in current ZnO research which are unknown or controversial. Thereto, different experimental methods and techniques are combined. The investigation is focused – but not limited – to the properties of excitons and phonons in external magnetic and stress fields. The application of external fields thereby provides a powerful technique to obtain additional information which might be otherwise inaccessible.

Following the general introduction in this chapter, the different experimental techniques used in this work are described in chapter 2. The fundamentals of these techniques are considered common knowledge, therefore only the specific parameters and individual setups are outlined. Because of the same reasoning and in order to limit the extend of this work, the physical basics of excitons and phonons and the fundamental properties of ZnO are not explained in a separate theoretical chapter. For an overview of these topics, the gentle reader may be referred to the books and reviews in Refs. [18, 26–30]. In general, a rather inductive approach is chosen in this work. Nevertheless, the more specific theoretical concepts involving the effects of magnetic and stress fields are introduced in the beginning of the corresponding chapters.

The experimental results derived within this work are presented in chapters 3 to 9. First, a comparative study of free and bound excitons in different ZnO bulk single crystals is performed in chapter 3. High sensitivity PL measurements are able to resolve the recombination lines of the exciton-polaritons involving holes from all three upper valence bands. These measurements reveal variations in the band- and LT-splittings depending on the growth method and structural quality of the crystals. In the spectral range of the bound excitons, up to 20 separate emission lines are identified. A correlation between the different transitions is investigated which originate from impurities in different charge states. The relation between donor binding energy and localization energy is studied for neutral and ionized bound excitons. Excited state transitions of free and bound excitons are investigated by photoluminescence excitation spectroscopy (PLE) and temperature dependent PL. In addition to the discussion of new results concerning the correlation of different bound exciton lines and their excited states, this chapter also serves as an introduction to the following chapters which study several outlined aspects in greater detail under the influence of external fields.

In order to identify the properties of the different impurities responsible for the

bound exciton lines, the luminescence is analyzed in an external magnetic field. The results of these measurements are discussed in chapter 4. Based on the Zeeman splitting in different orientations of the magnetic field, excitons bound to neutral and ionized impurities can be distinguished. The obtained data represent the first indisputable proof for the ionized charge state of bound exciton complexes with small localization energies. Furthermore, the thermalization of the Zeeman components of the bound excitons provides clear evidence as to the donor or acceptor nature of the related impurities. The experimental results are complemented by group theoretical considerations concerning the symmetry of exciton states and admixture of oscillator strength. From the theoretical description of the energy splitting in different orientations of the magnetic field, the electron and anisotropic hole g-factor are derived for all bound excitons.

Even more information about the symmetry of the electronic states can be derived by the combination of theoretical descriptions and high resolution magneto-PL measurements of bound excitons with exceptionally small line widths in high quality ZnO single crystals. This is demonstrated by the study of the valence band ordering in chapter 5, which was controversially discussed for almost half a century. A fine splitting of bound exciton transitions in high magnetic fields is reported for the first time. The consequences of this splitting on the symmetry ordering of the valence bands are analyzed in detail. Polarization and angular dependent measurements were performed and compared to theoretical predictions for the energy splittings of the bound exciton Zeeman components. Additionally, the influence of axial strain on the valence band energies is taken into account. The presented results provide clear evidence for a reversed valence band ordering compared to other wurtzite II-VI and III-V semiconductors and should thereby conclude the long lasting debate about the symmetry ordering of the valence bands in ZnO.

After the investigation of the free exciton-polaritons and impurity related shallow bound excitons, chapter 6 deals with the properties of deeply bound excitons and their binding centers. Based on a combination of various experimental techniques including PL, PLE, time resolved PL, CL, magneto-PL, magneto-transmission, and luminescence measurements as function of temperature and uniaxial pressure, it can be shown that the deeply bound excitons are not bound to impurities but rather to extended structural defects. Despite the great significance of structural defects for device operations, the knowledge about these exciton binding centers is still rather limited. The here presented results provide a multitude of new information which clearly demonstrate that the defect centers cannot be described by the effective mass approach for shallow donors. Instead, a possible defect model is developed which is capable of explaining all experimental results and delivers a prediction for the spatial extend of the defect.

In chapter 7, the lattice dynamics of ZnO is investigated by Raman spectroscopy as function of external pressure. Important material parameters such as the Grüneisen parameters are determined for all Raman active modes with high precision. For the pressure dependence of the effective charge, an erroneous relation in the literature is identified and corrected. Furthermore, the asymmetry of the line shape of the  $E_2^{high}$  is studied as function of hydrostatic pressure. A line width narrowing down to a symmetric line shape at pressures above 3 GPa is observed and explained considering the pressure dependence of the possible decay channels into acoustical modes. In addition, the frequency shift of the Raman modes in ZnO is investigated for the first time as function of uniaxial pressure. From the combination of the hydrostatic and uniaxial pressure measurements, the phonon deformation potentials are determined. These values were not available in the literature up to this work. The uniaxial and hydrostatic pressure coefficients and splittings of the polar modes are also compared to other II-VI and III-V semiconductors and correlations to the bond ionicity and Kleinman's internal strain parameter are discussed.

The influence of resonant and non-resonant excitation on phonons and excitons is studied in chapter 8. The enhancement of the Raman cross section under resonant excitation at bound exciton intermediate states is investigated. Different enhancements of the first and second order LO modes are discussed considering the wave vector dependence of the Fröhlich interaction. Time resolved measurements are used to study the influence of the resonance on the lifetimes of phonon replicas and Raman modes. These measurements are complemented by time resolved measurements as function of the temperature under resonant excitation which reveal a significant influence of the thermal dissociation of bound excitons on the resonant phonon lifetimes. Two different decay constants are determined and discussed in terms of a long non-coherent luminescence process and a fast coherent Raman process.

Finally, chapter 9 discusses the influence of the polarity of  $c$ -plane ZnO substrates on the optical and structural properties of simultaneously grown homoepitaxial layers. High resolution transmission electron microscopy can proof that the polarity of the substrate is maintained in the epilayers. A superior structural quality of the epilayers compared to the substrates is confirmed by XRD and depth-resolved micro Raman spectroscopy. Significant differences can be observed in the bound exciton luminescence of the epilayers with different polarities including the appearance of new lines in the O-face samples. These lines are studied by magneto-PL and time resolved photoluminescence. A possible correlation of these lines to a higher impurity concentration in the O-face samples as derived from secondary ion mass spectroscopy is discussed.

The findings and conclusions derived from the experimental and theoretical investigations are recapitulated in the summary in chapter 10.

## 2 Experimental techniques

The purpose of this chapter is to provide an overview of the experimental techniques which were applied to obtain the results discussed in this work. The experimental setup and specific settings for each method are briefly described. The hydrostatic Raman experiments were performed during a research visit at the University of Barcelona in the group of Prof. A. Goñi in cooperation with Dr. J. S. Reparaz. Growth of the homoepitaxial ZnO layers and SIMS characterization was carried out at the Justus-Liebig University Giessen in the group of Prof. B. K. Meyer. HRTEM measurements were conducted by T. P. Bartel at the Lawrence Berkeley National Labs. All other measurements were performed at the Technische Universität Berlin in the laboratories of Prof. A. Hoffmann and Prof. C. Thomsen.

### Photoluminescence (PL)

Standard photoluminescence spectroscopy was performed using the 325.0 nm continuous wave laser line of a HeCd laser with an output power of up to 40 mW for optical excitation. This wavelength (3.815 eV) is well above the band edge of ZnO at 2 K (3.437 eV) and also sufficient to excite excitons with hole states from deeper valence bands as well as their excited states. The 441.6 nm laser line and additional plasma lines of the HeCd laser were suppressed by appropriate interference and band pass filters. The samples were mounted either in a self-built helium bath cryostat or in a temperature controlled CryoVac flow cryostat. In addition, temperature dependent micro-PL measurements were performed using an Oxford micro-cryostat. The emitted light was collected and focused into a Spex-1404 double monochromator with a focal length of 1 m per single monochromator, gratings of 1200 lines/mm and a blaze wavelength of 500 nm. An aperture transformation from the cryostat to the monochromator ensured maximum resolution and signal intensity using appropriate UV lenses. Near band edge measurements were performed in second order with a spectral resolution of about 50  $\mu\text{eV}$ . The light was detected by an EMI 9789QB bi-alkali photo detector. The signal of the detector was amplified by a Keithley 417 picoampere meter and recorded using National Instruments A-D converters and suitable LabView software. High precision calibration was achieved by measuring an atomic spectral line of Ne or Hg together with each luminescence spectrum. The recorded wavelength was corrected for the vacuum wavelength and converted into electron volts using the relation:  $1 \text{ eV} = 1239.841856 \text{ nm}$ .

---

## Magneto-photoluminescence/-transmission

Magneto-photoluminescence and -transmission spectra were measured in an Oxford magnetic field cryostat with liquid helium cooled superconducting niobium coils which are able to produce a magnetic field strength of up to 6 Tesla. The samples were mounted on a turnable sample holder, thus allowing angular resolved measurements by variation of the direction of the crystal's  $c$ -axis with respect to the orientation of the magnetic field. For measurements in back-reflection geometry ( $\mathbf{k}||c$ ), a small mirror with a diameter of 6 mm was placed in between the collecting and focusing lenses (diameter 40 mm), thus shadowing less than 3 % of the emitted light. The orientation of the  $c$ -axis in this geometry was precisely controlled by the back-reflected laser pulse which is crucial for the interpretation of the magneto-PL spectra in chapter 5. The excitation was comparable to the description in the standard PL section. High resolution spectra in the excitonic range of ZnO were recorded in forth order using a SPEX 1402, 0.85 m double monochromator with gratings of 600 lines/mm and a blaze wavelength of 1600 nm. Circular polarized spectra were recorded using a  $\lambda/4$  plate in combination with a linear crystal polarizer as analyzer. For magneto-absorption measurements the light of a water cooled 450 W XBO lamp was focused on the samples in transmission geometry. Reference spectra were recorded to correct for the spectral system response.

## Micro-Raman spectroscopy

Micro-Raman spectra were recorded by using the 514.5 nm line of an Ar<sup>+</sup> laser which was focused by micro optics to a radial symmetric spot of about 500 nm in diameter. The Raman signal was recorded using a DILOR XY 800 triple-grating Raman spectrometer with 1800 lines/mm and a liquid nitrogen cooled CCD camera as detector. The scattered light was detected in backscattering geometry. The polarization of the incident and scattered light was selected using linear polarizers. A proper calibration of the spectra was achieved by recording atomic spectral lines from a Ne lamp.

## Raman spectroscopy under hydrostatic pressure

Raman spectra as function of hydrostatic pressure were collected at room temperature with a LabRam HR 800 system in backscattering geometry. The 514.5 nm line of an Ar<sup>+</sup> laser was used for excitation, focused onto the sample using a long distance 20x Olympus objective. Measurements under hydrostatic pressure were carried out using the diamond anvil cell (DAC) technique as described in detail in two review articles by Jayaraman [31, 32]. Thereto, a gasket made of a specific nickel alloy (Inconel X-750) with a small hole in the middle was placed in between two diamonds

which were pressed against each other using the Syassen-Holzappel method. The samples, which were thinned to about 30  $\mu\text{m}$  by mechanical polishing, were placed in the hole of the gasket together with a small ruby crystal and a pressure transmitting medium consisting of a 4:1 mixture of methanol and ethanol. Under pressure, the gasket was plastically deformed, thus enabling the hydrostatic compression of the samples in between the diamonds. The ruby was used to determine the pressure by measuring the shift of the  $R_1$  line of ruby which originates from a  $d-d$  transition of the  $\text{Cr}^{3+}$  ions and provides a precise pressure reference [33]. Depending on the size and precision of the hole in the gasket, hydrostatic pressures well beyond the phase transition in ZnO at about 9 GPa could be achieved (chapter 7.2).

### PL and Raman measurements under uniaxial pressure

Uniaxial pressure measurements were performed in a self-built pressure apparatus which was inserted into a bath-cryostat or temperature controlled CryoVac cryostat by replacing the usual sample holder. The pressure on the samples was applied by a stainless steel piston using a pneumatic construction. In order to apply the desired uniaxial pressure, a two stage pressure regulator attached to a helium gas bottle was used to fine tune the primary gas pressure in a pressure transmitting chamber on top of the piston. The pressure was thereby determined with an accuracy of about 2 mBar. The increase of the pressure in this chamber pushed the piston downwards against a hardened steel hemisphere in between which the samples were placed. The surface ratio between the pressure transmitting chamber and the surface area of the samples determined the pressure transmission ratio with typical values between 500 and 1000 for samples with surface areas between 2 to 4  $\text{mm}^2$ . Owned to the vertical construction of the pressure apparatus, the direction of the uniaxial stress was always perpendicular to the  $\mathbf{k}$ -vector of the incident and emitted or scattered light ( $\mathbf{P} \perp \mathbf{k}$ ) in the PL and Raman studies, respectively. However, depending on the surface cut of the ZnO samples, pressure could be applied parallel ( $c$ -plane) or perpendicular ( $a$ -plane) to the crystal's  $c$ -axis. PL and Raman measurements as function of uniaxial pressure were performed in backscattering geometry from the edge of the samples. The same excitation and detection systems as described in the respective sections were used, except for the fact that the distance between the samples and the outer window of the pressure setup required all measurements to be conducted in a macro- instead of a micro-setup.

### Time resolved PL and Raman spectroscopy

Time-resolved PL measurements (TRPL) were performed using a pulsed titan-sapphire laser (Spectra Physics Tsunami) which was pumped by the 514.5 nm con-

---

tinuous wave laser line of an argon ion laser (Spectra Physics Millennia Xs) with a typical output power of 7.5 W. Pulsed operation was ensured by active mode locking with an acousto-optic modulator (AOM) resulting in a pulse width of about 2 ps in the picosecond operation mode. For the used mirror set, the wavelength could be tuned between 706 and 800 nm. Second harmonic generation was achieved by extra-cavity up-conversion using an LBO crystal with an appropriate compensator to adjust for the lateral offset. For above band edge excitation of ZnO, the primary wavelength was set between 706 and 720 nm resulting in an excitation energy of 3.512 eV to 3.444 eV after frequency doubling. For the resonant time resolved photoluminescence and Raman spectroscopy, the excitation wavelength could be tuned over the full range of the free and bound exciton transitions down to about 3.1 eV, thus enabling the study of resonance effects with excitonic states (chapter 8). The typical quasi-cw power of the frequency doubled laser was between 10 and 150 mW depending on the primary output power and wavelength. The repetition rate of this laser system was fixed to 80 Mhz, thus limiting the accessible time window for measurements between two pulses to 12.5 ns. Alternatively, a second laser system was used for time resolved measurements consisting of an actively mode locked Nd:YAG laser (Coherent Antares 76-s) which produces 100 ps pulses with a frequency of 76 Mhz at 1064 nm. The second harmonic – which was generated in a LBO crystal by non-critical phase matching – was used to synchronously pump a dye laser (Coherent 701) with Rodamine 6G or Pyridine 1 as laser active dyes. The emission wavelength could be tuned between 570-620 nm in case of Rodamine 6G and 670-720 nm using Pyridine 1 with a typical pulse width of 4-8 ps. Extra-cavity frequency doubling of the dye laser was implemented using a nonlinear BBO crystal delivering a quasi-cw output power of up to 10 mW. By means of an intra-cavity pulse dumper, the pulse repetition rate could be adjusted between 76 Mhz and 150 kHz, thus allowing the extension of the time between two pulses from 13.1 ns to 6.6  $\mu$ s.

Time resolved data were recorded using the single-photon counting technique. Therefore, a fraction of the primary laser intensity was focused on a fast photo diode (Becker & Hickl PHD-400-N) which provides a reference time (start pulse) whereas the stop pulse was created when an emitted photon from the samples was registered by a micro channel plate serving as fast photo detector. Depending on the wavelength of the emitted light, either a Hamamatsu R3809U-52 (S-20) or R2809U-11 (S-20 extended) detector was used. The delay between these two events was converted into a voltage by a time-to-amplitude converter (TAC). This voltage is proportional to the time between the start and stop pulses and assigned to a discrete channel which counter is subsequently increased by one. The integration over many of such events results in the formation of a histogram which is referred to as a transient. In order to compensate for the time-off-arrival differences in single and

additive double spectrometers, only double spectrometers with a subtractive grating configuration were used. These were a 35 cm McPherson spectrometer in combination with the titan-sapphire laser system and a 1 m Jarrell Ash spectrometer in combination with the dye laser system. Another advantage of these spectrometers is the efficient suppression of scattered light which was specifically required for the time resolved resonant Raman measurements. The time resolution of the described setups was about 30-40 ps which allowed the determination of lifetimes down to 15 ps by deconvolution of the measured transients with the instrumental response functions.

### **Photoluminescence excitation spectroscopy (PLE)**

For photoluminescence excitation spectroscopy (PLE), a dye laser (Lambda Physik FL 3002) containing 2-methyl-5-*t*-butyl-*p*-quaterphenyl (DMQ) was used. The dye laser was pumped by the 308 nm line of a Coherent Complex Pro 110 XeCl excimer laser. The emission wavelength of this dye was tunable between 345 and 375 nm. The laser system was operated in pulsed mode with a pulse length of 20 ns, a repetition rate of 100 Hz, and a typical quasi-cw power of 10 mW. The emission wavelength could be tuned with a spectral precision of about 0.1 Å. The samples were mounted in a liquid helium bath cryostat and excited either in back-reflection or 45° geometry. A SPEX 1404 1 m double monochromator was used to select the detection wavelength combining the advantages of scattered light suppression and high spectral resolution ( $\approx 0.05$  Å). The light was detected as described for the standard PL setup. The excitation spectra were acquired by turning the intra-cavity grating of the dye laser, thus continuously changing the excitation wavelength while the intensity at the fixed detection wavelength was recorded.

## 3 Optical transitions near the band edge of ZnO

In this chapter, the low temperature photoluminescence of ZnO is studied. Following an introductory overview of the different emission regions, the discussion will focus on radiative exciton recombinations. Based on the emission lines in ZnO crystals from different manufacturers, common spectral features are identified. The exciton-polariton luminescence is compared in different samples which reveal variations in the LT splittings of the A, B, and C excitons. For the bound excitons, a correlation between the localization energies of neutral and ionized bound excitons is discussed. In addition, excited states of the free and bound excitons are observed and investigated by photoluminescence excitation spectroscopy. Apart from the study of zero-field emission lines of free and bound excitons, this chapter partly serves as introduction to the subsequent chapters in which many aspects of the electronic centers related to the here identified transitions are investigated in greater detail under the influence of external magnetic fields (chapters 4 and 5) as well as exciton resonance effects (chapter 8). A strong motivation for a comprehensive understanding of the radiative transitions is also given by the recent progress and future prospects of p-doping with shallow acceptor states since these levels can best be monitored by the respective changes in the near band edge luminescence.

### 3.1 Photoluminescence of ZnO

ZnO exhibits a large variety of different luminescence lines covering almost the whole visible and near UV spectral range from 2.0 eV to 3.45 eV. The strongest luminescence is typically found near the fundamental band edge with particularly diverse emission lines at low temperatures which originate from the radiative recombination of free and bound excitons. The first comprehensive studies of these transitions by luminescence, absorption, and reflectivity measurements date back to the 1960s [34–39]. Since then, a multitude of luminescence studies on ZnO single crystals, thin films, heterostructures, and nanostructures has been published (for an overview see e.g. the reviews and books [18,26,29,30,40] and references therein). Despite the long period of research and large quantity of relevant publications, several aspects still remain controversial or unclear. Among those are the attributions

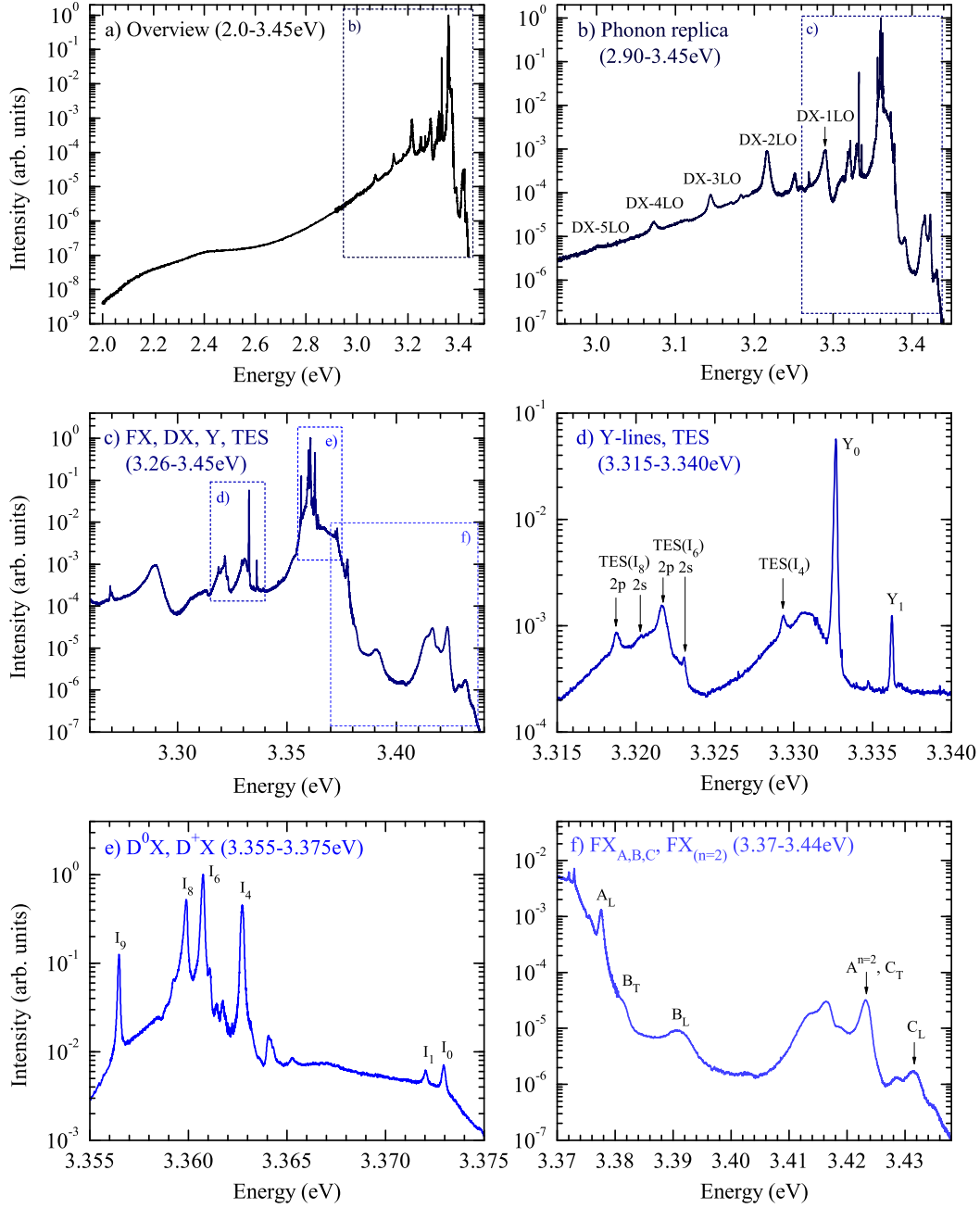


Figure 3.1: Photoluminescence spectra of a ZnO substrate provided by CermetInc at  $T = 2$  K. The dashed areas are magnified in the specified graphs. (a) overview spectrum (2.0-3.45 eV), (b) excitons and their phonon replica (2.90-3.45 eV), (c) near band-edge luminescence including free exciton-polaritons ( $FX$ ), donor ( $DX$ ) and defect bound excitons ( $Y$ ), two electron satellites ( $TES$ ), and the first phonon sideband (1LO) of the  $DX$  (3.26-3.45 eV), (d)  $TES$  and  $Y$  lines (3.315-3.340 eV), (e) neutral ( $D^0X$ ) and ionized donor bound excitons ( $D^+X$ ) (3.355-3.375 eV), (f) free exciton-polaritons including holes from the A, B, and C valence bands in the  $n = 1$  ground state and  $n \geq 2$  excited states (3.37-3.44 eV).

of particular exciton emission lines to donor or acceptor impurities, the chemical identity and charge state of these elements, the energy levels and properties of exciton excited states, and the size of the longitudinal-transversal splitting of free exciton-polaritons, to name but a few. For reasons of clarity and comprehensibility, the discussion in this chapter starts with an overview of the different luminescence regions of a typical ZnO bulk crystal before addressing the mentioned aspects by comparative luminescence studies of different ZnO substrates.

Fig. 3.1 shows the photoluminescence spectrum of a ZnO single crystal from CermetInc at a temperature of 2 K. The wide energy range of optical emission features on the one hand and the partly very narrow line width of down to 100  $\mu\text{eV}$  on the other hand requires a separate illustration of the relevant spectral regions which are shown in the graph (a)-(f) of Fig. 3.1. An overview of the total spectral range is displayed in graph (a). In the low energy range between 2.0 eV and 2.8 eV, a green luminescence band is commonly observed in ZnO with a maximum intensity at about 2.45 eV (see also Fig. 3.3). This luminescence was first reported by Ewles in 1938 [41]. The origin of the green band was controversial for decades since several defects can contribute to the luminescence in this spectral region. At least two different mechanisms should be distinguished - (i) the deep copper acceptor and (ii) intrinsic point defects such as Zn and O vacancies. The copper related luminescence arises from the radiative recombination of excitons intermediately bound to copper impurities ( $\text{Cu}^+(d^9+e),h$ ) [42–44]. Thereby, three internal transitions  $\alpha$ ,  $\beta$ , and  $\gamma$  at 2.8594, 2.8680, and 2.8733 eV occur between the upper  $\text{Cu}^{2+}(^2T_2)$  and lower ( $\text{Cu}^+,h$ ) charge states, respectively [45–47]. The chemical nature of the copper zero-phonon lines could be established by the study of different Cu isotopes [42–44, 48]. The strong coupling of the deep Cu center to the lattice phonons – which is expressed by a Huang-Rhys factor of  $S = 6.5$  – leads to a broad structured luminescence band consisting of more than ten phonon replicas with an intensity maximum at 2.41 eV [49].

Apart from the copper related luminescence, a structureless green emission band is frequently observed in ZnO and attributed to different transitions involving native point defects. Depending on the growth conditions and prevailing defect centers, the luminescence band may strongly vary in intensity and show one or two peak maxima at different energies in this spectral range. The proposed point defects responsible for the green luminescence include oxygen vacancies  $V_O$  [50–54], zinc vacancies  $V_{Zn}$  [55–59], zinc interstitials  $Zn_i$  [60], and antisites  $O_{Zn}$  [61] resulting in band-acceptor (e,A), donor-band (D,h), donor-acceptor pair (DAP), and intracenter  $V_O$  transitions. The variety of suggested defects and models impressively illustrates the dissension about the origin of this luminescence band. Nevertheless, recent first principle calculations by Janotti and Van de Walle identify the zinc vacancy as

most likely candidate for the green luminescence as it forms a deep acceptor with low formation energy [62]. With a  $-1/-2$  charge transfer level 0.87 eV above the valence band, the  $V_{Zn}$  acceptor could give rise to a band-acceptor (e,A) or DAP transition with an energy of 2.5 eV. The strong passivation of the green luminescence by hydrogen plasma treating [63] supports a relation to the zinc vacancy which acts as acceptor and can be passivated by hydrogen [64,65].

In the energy range between 2.9 eV and 3.3 eV (Fig. 3.1b), the luminescence spectrum of ZnO consists of a multitude of longitudinal optical phonon replica of the bound excitons with an energy spacing of 72 meV. In the displayed spectrum, up to five LO replicas are visible. In addition, donor-acceptor pair (DAP) transitions may appear in this region if a sufficient amount of shallow acceptor states is present. For example, a nitrogen related DAP band occurs around 3.235 eV with an acceptor binding energy of about  $E_A = 165$  meV [66]. In addition to the DAP and LO replica emission, luminescence feature between 3.315 and 3.340 eV are commonly observed in ZnO samples. This area is magnified in graph (d). Two narrow emission lines at 3.3328 eV ( $Y_0$ ) and 3.3363 eV ( $Y_1$ ) are visible. These lines can be attributed to the recombination of excitons bound to extended structural defects [40,67]. Their properties are studied in great detail in chapter 6. The remaining luminescence features in this region are related to two electron satellite transitions of the dominant bound excitons  $I_4$ ,  $I_6$ , and  $I_8$  [40]. These lines appear if the bound exciton recombination leaves the donor in an excited ( $2s$ ,  $2p$ ) state instead of the  $1s$  ground state. From the energy spacing between the TES and DX lines, the donor binding energy  $E_D$  can be derived in a hydrogen-like effective-mass-approach including corrections for the chemical potential of different impurities, polaron interactions, and the hexagonal anisotropy [40].

The strongest luminescence with several sharp emission lines is observed between 3.355 eV and 3.375 eV (e). These lines originate from the radiative recombinations of excitons bound to impurities. The impurity centers can exist in the neutral and ionized charge state. For ZnO, the ionized impurity bound excitons are found at higher energies (smaller localization energies  $E_{loc}$ ) than the neutrally charged ones. This relation depends on the electron and hole masses and can be inversed in other semiconductors as found e.g. in ZnSe [68]. The photon energy of a radiative bound exciton recombination is given by  $\hbar\omega = E_g + E_{kin} - E_b - E_{loc}$  with  $E_{loc}$  being the location energy of the bound exciton by which the emission energy is reduced as compared to the energy of the free transversal A exciton due to the binding of the exciton at the impurity. The other terms determine the energy of the free exciton given by the band gap energy  $E_g$ , the center of mass motion of the free exciton  $E_{kin}$ , and its binding energy  $E_b$ .

So far, up to 20 different bound exciton transitions were reported. As their at-

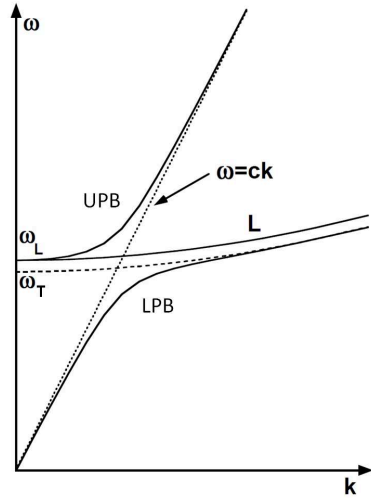


Figure 3.2: Schematic drawing of the dispersion relation of excitons and photons showing an anticrossing as a result of strong coupling. The curves can be divided into exciton-like parts with small slope and photon-like parts with steep slopes and small  $k$ -values. The resulting upper (UPB) and lower polariton branches (LPB) are displayed by solid lines. In addition, an exclusive exciton-like branch may exist. The dashed lines show the uncoupled dispersion of phonons and excitons. Taken from [71].

tribution to specific chemical impurities is not straightforward, Reynolds et al. [69] introduced a labeling for the emission lines of bound excitons from  $I_1$  to  $I_{10}$  whereby smaller indices also indicate smaller localization energies. Over the years, additional lines were observed which required an extension of this system by the introduction of additional letters, e.g.  $I_6$  and  $I_{6a}$ . However, this labeling system is not without flaws as it does not account for the origin of the transition lines, e.g. excitons bound the same chemical impurity in different charge states (section 3.4.1). The identification of specific bound exciton lines is complicated by several effects which are discussed in the following sections and chapters. For one thing, exciton excited states may occur at or close to the energies of other bound excitons in the ground state and mistakenly be identified as such (section 3.4.2). Another difficulty concerns the distinction between donor and predicted acceptor bound excitons since the range of their localization energies could overlap between 16 and 25 meV [70]. Thus, temperature dependent magneto-optical studies are required to identify the origin of transition lines in this energy range (chapters 4 and 6). Finally, different strain levels in ZnO samples lead to a shift of the absolute position of the emission or absorption lines, hence impeding the comparability of the exciton emission in different samples (see below).

Above the energies of the bound excitons, the free exciton luminescence is observable between 3.375 eV and 3.440 eV (Fig. 3.1f). The coupling of excitons with the electromagnetic field of the excitation results in the formation of exciton-polaritons which alters the dispersion relation of the excitons and leads to a splitting into an upper polariton branch (UPB) and a lower polariton branch (LPB). The energy gap between the UPB and the excitonic part of the LPB at  $k = 0$  determines the LT-splitting. Thereby, the size of the splitting, which occurs at the crossover point of the undisturbed exciton and photon dispersion curves, is proportional to the cou-

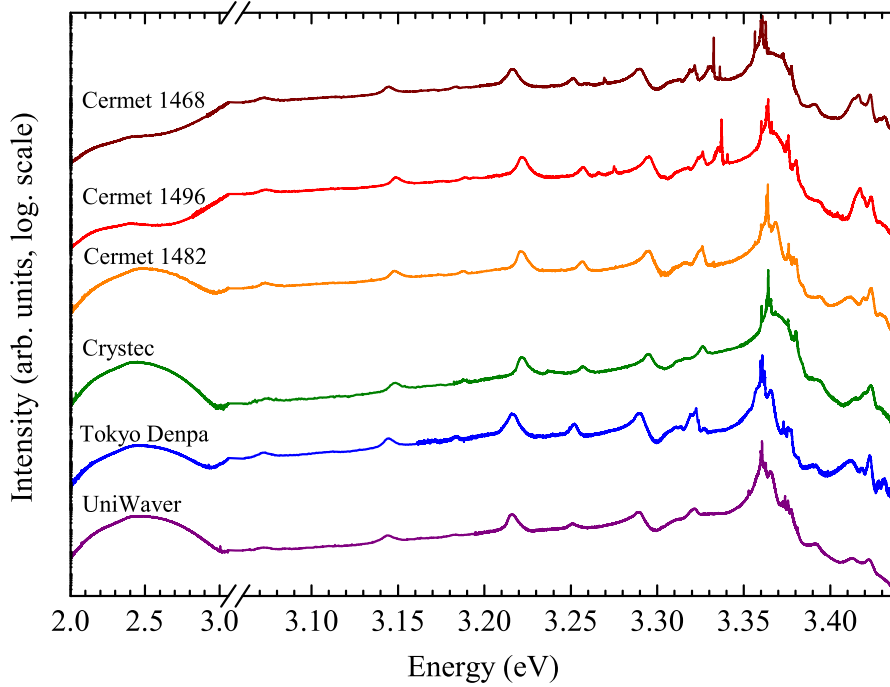


Figure 3.3: Photoluminescence spectra of different ZnO substrates between 2.0 eV and 3.44 eV at  $T = 2$  K. Note the different scaling of the x-axis below and above 3.0 eV.

pling strength between the two quasi particles. For small  $\mathbf{k}$ -vectors, the LPB has a linear (photon-like) dispersion which becomes exciton-like after the bottleneck region (Fig. 3.2). The UPB coincides with the longitudinal exciton branch at  $\mathbf{k} = 0$  and becomes photon-like. Detailed discussions about exciton-polaritons in ZnO can be found e.g. in Refs. [18, 36, 72, 73].

As can be seen from graph (f) in Fig. 3.1 not only excitons with holes from the A valence band, but also B and C exciton-polaritons are visible in high sensitivity PL studies. The luminescence of these features is up to six orders of magnitude weaker than the donor bound exciton emission thus requiring sufficiently sensitive and low-noise detection electronics. In addition to the ground state excitons ( $n = 1$ ), the  $n \geq 2$  excited states of the A and B excitons are observed and discussed in section 3.3.

### 3.2 Comparison of ZnO substrates from different manufacturers

Following the overview of the different energy regions in the PL spectrum of ZnO, a comparative study of the luminescence features in several ZnO crystals is conducted. Fig. 3.3 displays the PL spectra of six different ZnO substrates which are vertically

shifted to allow easy comparison. Although the main luminescence features such as free and bound exciton transitions and phonon replica are present in all samples, a closer look reveals significant differences in the optical spectra of the different crystals. These are most pronounced in the range of the bound excitons and the green luminescence band. While the former strongly depends on the existing impurities and their concentration in the samples the intensity of the green luminescence is mainly determined by native point defects which presence depends on the growth technique and conditions. The three ZnO samples by CermetInc were produced by the melt growth technique, whereas the other three samples (Crystec, Tokyo Denpa, UniWaver) were grown using the hydrothermal growth method. Among the three Cermet samples, Cermet 1482 is highly n-doped. Within the six different ZnO substrates, the intensity of the green luminescence band varies by more than three orders of magnitude compared to the intensity of the dominant bound exciton emission. The weakest green luminescence is found in the upper two graphs which represent the nominally undoped Cermet samples. Interestingly, these samples are the only ones showing sharp emission lines around 3.333 eV (*Y*-lines). Since the green luminescence in the absence of copper is mainly caused by transitions involving highly mobile native point defects, it is conceivable that these point defects move towards extended structural defects such as dislocation loops and stacking faults thus reducing local strain fields. A possible correlation between the absence of the green luminescence and the occurrence of the structural defect bound exciton lines is discussed in chapter 6.

### 3.3 Exciton-polaritons

The photoluminescence of the different ZnO substrates in the range of the free exciton-polaritons is shown in Fig. 3.4. Several common features in the different samples can be identified. The strongest emission originates from the transversal and longitudinal A exciton-polaritons with  $\Gamma_5$  symmetry. These transitions are dipole allowed without involving a spin-flip process (for details on the symmetry and selection rules of free excitons see the discussion in chapter 4). Furthermore, the dipole allowed luminescence lines of the free exciton-polaritons with holes from deeper valence bands (B and C) can be observed at higher energies. In particular, these are the  $B_T(\Gamma_5)$ ,  $B_L(\Gamma_5)$ , and  $C_T(\Gamma_1)$ ,  $C_L(\Gamma_1)$  transitions as indicated by the vertical drop lines in Fig. 3.4. Except for these  $n = 1$  ground state transitions,  $n \geq 2$  excited states of the A and B exciton-polaritons can be observed in some of the samples. Thereby, the  $A_L^{n=2}(\Gamma_5)$  emission overlaps with the  $C_T(\Gamma_1)$  ground state peak which prevents an unambiguous distinction between these transitions. The energy positions of the emission lines in the different samples listed in Table 3.1

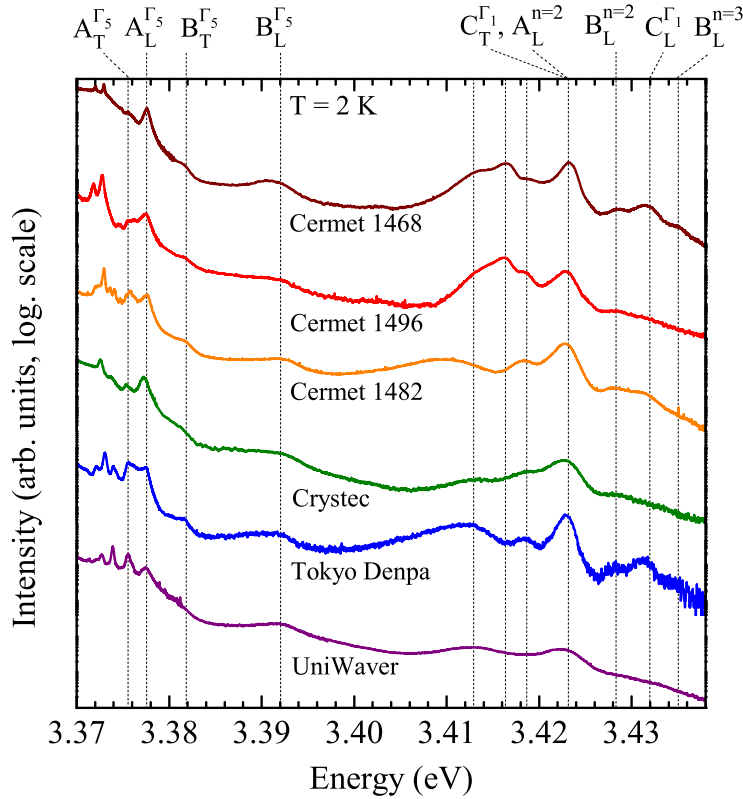


Figure 3.4: Photoluminescence spectra of different ZnO substrates in the region of the free exciton-polaritons at  $T=2$  K.

are in good agreement with published values of the free exciton ground and excited states [34, 39, 74–77]. Apart from the discussed transitions, three additional lines between 3.41 and 3.42 eV are observed in some of the samples (Cermet, Tokyo Denpa) which vary in intensity and spectral positions. These peaks are usually not observed and their origin is not self-evident to the moment. The only other report about a luminescence band in this spectral region was recently published by Chichibu et al. [78], who assigned a similar luminescence band to excited states of impurity bound excitons. However, no further discussion was conducted within that work. Based on experimental and theoretical studies of the excited states of donor bound excitons in section 3.4.2, no evidence is found to support this assignment, especially since the excited states of the donor bound excitons are not expected to be stable above the energy of the free exciton [79].

Table 3.1: Exciton-polariton energies in the  $n=1, 2, 3$  ground and excited states.

	$A_T^{\Gamma_5}$			$B_T^{\Gamma_5}$			$C_T^{\Gamma_1}$		
	$n=1$	$n=2$	$n=3$	$n=1$	$n=2$	$n=3$	$n=1$	$n=2$	$n=3$
C1468	3.3755	3.4232		3.3812	3.4285	3.4348	3.4232		
C1496	3.3755	3.4228		3.3812	3.4278		3.4228		
C1482	3.3758	3.4227		3.3815	3.4280		3.4227		
CT	3.3754	3.4227		3.3809	3.4277		3.4227		
TD	3.3755	3.4228		3.3815	3.4282		3.4228		
UW	3.3756	3.4229		3.3820			3.4229		
Ref. [34]	3.3768	3.4225		3.3830	3.4275				
Ref. [39]	3.3781	3.4282	3.4375	3.3856	3.4324	3.4412	3.4264	3.4722	3.4808
Ref. [74]	3.3768	3.4227	3.4309	3.3834	3.4276	3.4359	3.4223	3.4664	3.4747
Ref. [75]	3.3768	3.4231		3.3830	3.4290		3.4214	3.4679	
Ref. [76]	3.3783	3.4229		3.3858	3.4283		3.4245	3.4667	
Ref. [77]	3.3778	3.4214		3.3834	3.4276		3.4224	3.4630	

Table 3.2: Energy splitting between longitudinal and transversal excitons.

Sample / Ref	$\Delta A_{LT}^{\Gamma_5}$	$\Delta B_{LT}^{\Gamma_5}$	$\Delta C_{LT}^{\Gamma_1}$	$\Delta A_L^{\Gamma_5} - B_L^{\Gamma_5}$	$\Delta A_T^{\Gamma_5} - B_T^{\Gamma_5}$	$A_T^{\Gamma_5} - C_T^{\Gamma_1}$
Cermet 1468	2.03	9.37	8.33	13.01	5.67	47.64
Cermet 1496	1.96	10.20		13.94	5.70	47.32
Cermet 1482	1.82	10.28	8.35	14.23	5.77	46.97
CrysTec	1.85	8.62		12.27	5.50	47.35
Tokyo Denpa	1.96	8.36	8.37	12.33	5.93	47.32
UniWaver	1.84	9.14		13.57	6.27	46.60
Ref. [80]	1.80	10.20	11.90	13.60	5.20	44.00
Ref. [81]	1.90	11.30	11.80	15.10	5.70	45.00
Ref. [82]	1.42	9.97	11.02	15.12	6.57	45.63
Ref. [75]	1.50	11.10	13.90	15.80	6.20	44.60
Ref. [77]	2.70	10.60	12.10	13.50	5.60	44.60

A detailed comparison between the PL spectra of the ZnO samples reveals not only differences in the peak intensities of the free exciton-polaritons, but also slight shifts in the absolute energies of the emission lines. Of particular significance in this context are the energy spacings between the valence bands and the size of the longitudinal-transversal (LT) splittings as these properties are related to the strain and polariton coupling strength in the samples. The energies of the transition lines and splittings for the here studied samples are listed in Tables 3.1 and 3.2 and compared to reported values obtained by different experimental techniques. Usually, the free exciton-polariton energies are determined by absorption and reflection spec-

troscopy or ellipsometry [77] since the deeper valence band exciton-polaritons and excited states are difficult to detect in luminescence. The here presented measurements demonstrate, however, that high resolution high sensitivity PL measurements are well suited to obtain these values in good agreement with other experimental techniques. Apparently, the derived energy splittings for the different ZnO substrates exhibit some variations (e.g. in the case of the  $B_T(\Gamma_5) - A_T(\Gamma_5)$  splitting between 5.5 and 6.3 meV), which are also found in the published values by other authors [75, 77, 80–82]. While the presence of different strain levels can have a major influence on the exciton emission lines, it should also be considered that the attributions of emission lines to different transitions in the literature – in particular due to the assumption of a reversed valence band ordering or the negligence of polariton effects – may result in variations in the reported splitting values. In addition, different experimental techniques such as ellipsometry, reflection spectroscopy, or multi-photon luminescence access different intrinsic properties, which are not necessarily directly comparable. Consequently, caution is advised when comparing the values in Table 3.1.

### 3.4 Bound excitons

The presence of different impurities in varying concentrations greatly affects the near band-edge luminescence as they introduce shallow states which bind the free excitons at low temperature. This is visualized in Fig. 3.5 showing only the luminescence of the ZnO substrates in the spectral region of the bound excitons. Several narrow emission lines are visible between 3.350 eV and 3.375 eV which originate from the radiative recombination of excitons bound to different impurity atoms (Table 3.3). Without discussing each single transition, a few characteristics are worth mentioning: (i) The bound exciton with the strongest intensity in all substrates is the  $I_6$  at an energy of 3.3608 eV. This line is related to aluminum as demonstrated by implantation studies of Schilling et al. [83] which represents an omnipresent impurity in ZnO. (ii) The equally common gallium impurity gives rise to a second bound exciton transition line at 3.3598 eV ( $I_8$ ) with comparable intensity to  $I_6$  in most of the samples. The chemical identity of this transition was confirmed in ZnO implanted with the radioactive  $^{73}\text{Ga}$  isotope resulting in a decrease of the  $I_8$  intensity with a half life of  $^{73}\text{Ga}$  of 4.8 h [84]. This attribution is in agreement with earlier studies about Ga doping and diffusion by Ko et al. [85] and Meyer et al. [40]. (iii) The transition at 3.3567 eV ( $I_9$ ) originates from a bound exciton to the next heavier group III element indium. This correlation was established by diffusion experiments [40] and decay studies of the  $I_9$  in ZnO single crystals doped with radiative  $^{111}\text{In}$ . Although the  $I_9$  line is absent in the hydrothermally grown samples from Tokyo Denpa and UniWa-

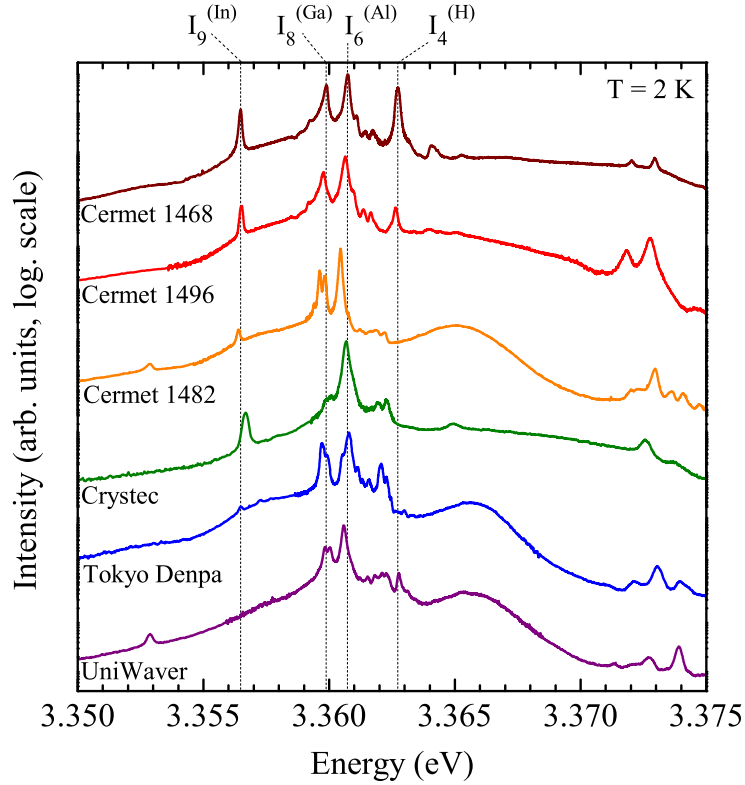


Figure 3.5: Photoluminescence spectra of different ZnO substrates in the region of the bound excitons at  $T=2$  K.

ver, it does not only appear in the melt grown samples from Cermet but also in the hydrothermally grown Crystec sample, thus the presence of indium is not limited to a certain growth method. (iv) On the high energy side of these group III donor bound excitons, a transition line at 3.3328 eV ( $I_4$ ) is visible in some of the samples. This transition arises from an exciton bound to a hydrogen atom. Hydrogen is a known contaminant in many semiconductors [86] and plays a substantial role in as-grown ZnO [64, 65, 87–89]. While molecular hydrogen ( $H_2$ ) has virtually no effect on the optical and electrical properties of the crystal, hydrogen in its atomic form can compensate shallow and deep defects, induce complexes, and shift positions of energy levels [90]. In addition, hydrogen can also passivate acceptors [64, 91] and thus could prove to be helpful in achieving higher p-type carrier densities, since acceptor passivation would prevent self compensation during growth and subsequent annealing would remove the H from the lattice at a temperature above 600°C [92], thus activating the acceptors.

Except for the four common donor bound exciton lines  $I_4$ ,  $I_6$ ,  $I_8$ , and  $I_9$ , several weaker transitions can be observed in the different samples which are listed in

Table 3.3: Exciton recombination energies and related properties in ZnO.  $E_{loc}$  is the localization energy, TES spacing marks the energy difference between the  $1S$  ground state and the  $2P_{x,y}$  excited state of the donor,  $E_D$  is the donor binding energy according to Haynes rule, and  $E_{loc}/E_D$  the ratio of localization and donor binding energy. Based on data in Ref. [40] and results in this work.

line	$\lambda$ [nm]	$E$ (eV)	$E_{loc}$ (meV)	TES spacing (meV)	$E_D$ (meV)	$E_{loc}/E_D$	exciton complex	chemical identity
$I_{0a}$	367.42	3.3745	1.4		49.0	0.029	$D^+X$	
$I_{0b}$	367.46	3.3741	1.8		50.0	0.036	$D^+X$	
$I_0$	367.61	3.3727	3.4		53.0	0.064	$D^+X$	Al
$I_1$	367.71	3.3718	4.1		54.6	0.075	$D^+X$	Ga
$I_{1a}$	368.13	3.3679	8.0		62.3	0.128	$D^+X$	
$I_2$	368.19	3.3674	8.5		63.2	0.134	$D^+X$	In
$I_3^*$	368.29	3.3665	9.4		63.2	0.134	$D^+X$	In
$I_{3a}$	368.34	3.3660	9.9		38.0	0.261	$D^0X$	Zn <sub>i</sub> ?
$I_4$	368.69	3.3628	13.1	34.1	46.1	0.284	$D^0X$	H
$I_{4a}$	368.69	3.3621	13.8		48.1	0.287	$D^0X$	
$I_{5a}$	368.80	3.3618	14.1		49.0	0.288	$D^0X$	
$I_5$	368.84	3.3615	14.4		50.0	0.288	$D^0X$	
$I_6$	368.92	3.3608	15.1	38.8	51.6	0.292	$D^0X$	Al
$I_{6a}$	368.96	3.3604	15.5	40.4	53.0	0.292	$D^0X$	
$I_7$	369.01	3.3600	15.9		54.1	0.294	$D^0X$	
$I_8$	369.03	3.3598	16.1	42.1	54.6	0.294	$D^0X$	Ga
$I_{8a}$	369.08	3.3593	16.6		55.9	0.297	$D^0X$	
$I_9$	369.37	3.3567	19.2	50.6	63.2	0.303	$D^0X$	In
$I_{10}$	369.76	3.3531	22.8	60.2	72.6	0.314	$D^0X$	
$I_{11}$	370.28	3.3484	27.5					

\* $I_3$  is the low energy  $\Gamma_{1,2}$  transition of the ionized bound excitons  $I_2$  which becomes allowed due to the spin-spin exchange interaction in magnetic fields (see chapter 4.4.3).

Table 3.3. Among the neutral donor bound excitons, these are in particular the transition lines  $I_5$  and  $I_7$  which are frequently observed, too. However, an unambiguous identification of the chemical identity of other donor related exciton transitions is not possible at present. In general, group III elements on Zn lattice site and group VII elements on O lattice site are expected to form shallow donors. In addition, it has been shown that hydrogen occupies an interstitial lattice site, thus acting as a shallow donor in ZnO [87, 88]. Among the group III elements, most of the donors could be identified which leaves only boron as a potential candidate. Since it is the lightest of the group III elements, an exciton localization energy below that of  $I_6$  would be expected. Although boron is not a typical impurity in bulk crystal and epitaxial films, a correlation to one of the rarely and weakly occurring donor bound

excitons  $I_5$ ,  $I_{5a}$ ,  $I_{4a}$  (see Table 3.3) cannot be completely ruled out. The more likely candidates for the stronger bound excitons lines are the group VII elements F, Cl, Br, and I. As confirmed by secondary ion mass spectroscopy, these halogens are frequently present in ZnO homoepitaxial films grown by CVD [93]. Furthermore, Cl could be identified as shallow donor by EPR [94]. In analogy to the group III donor bound excitons it would be conceivable that the  $I_5$  transition might be related to chlorine, the  $I_7$  to bromine, and iodine possibly giving rise to a donor in the range of the  $I_{10}$  bound exciton. However, it should be noted that no conclusive evidence of this attribution is available so far. Alternative candidates for the  $I_{10}$  such as shallow Li and Na donors could not be confirmed in doping experiments by Meyer et al. [40].

In addition to the discussed neutral bound excitons, several transitions can be observed which are of different origin. The emission lines between 3.370 eV and 3.375 eV in Fig. 3.5 are related to excitons bound to donors in the ionized charge state ( $D^+X$ ). Their correlation to the neutral donor bound excitons is substantiated in the following section. Furthermore, weak emission lines on the high energy side of the dominant bound exciton transitions can arise from excited states or bound excitons involving holes from the B instead of the A valence band which gain in intensity at slightly elevated temperatures. The properties of these excited states are studied in section 3.4.2. Finally, three samples in Fig. 3.5 show a broad band centered around 3.366 eV which origin is controversial in the literature. The most convincing attribution was published by Sann et al. [95] in ZnO powders by a combination of EPR and temperature dependent PL results. Based on this study, the band is related to zinc interstitials ( $Zn_i$ ) which form a shallow donor state with a donor binding energy of about 37 meV. Other works assign this band to the radiative recombination of excitons bound to surface states [96].

### 3.4.1 Neutral and ionized donors

Based on the previous overview of excitonic transitions in different ZnO samples, a correlation between several bound exciton line pairs can be identified. This is illustrated in Fig. 3.6 for a ZnO bulk crystal which exhibits a typical PL spectrum in the range of the neutral and ionized bound excitons. The dominant donor bound excitons  $I_6$  (Al donor),  $I_8$  (Ga donor), and  $I_9$  (In donor) are accompanied by transitions on their high energy side which have comparable intensity ratios. This is particularly apparent in the case of  $I_6$  and  $I_8$  and their counterparts  $I_0$  and  $I_1$ . A similar relation exists between  $I_9$  and  $I_2$ . The correlated occurrence of these three bound exciton pairs in different samples suggests a common chemical origin of the transitions. Thus, the lines  $I_0$ ,  $I_1$ , and  $I_2$  are attributed to Al, Ga, and In donors, respectively. The higher energy of these transitions originates from a smaller exciton binding energy which is expected for ionized donor centers. In chapter 4, it is

shown that the ionized charge states of these impurities can indeed be confirmed by magneto-optical measurements.

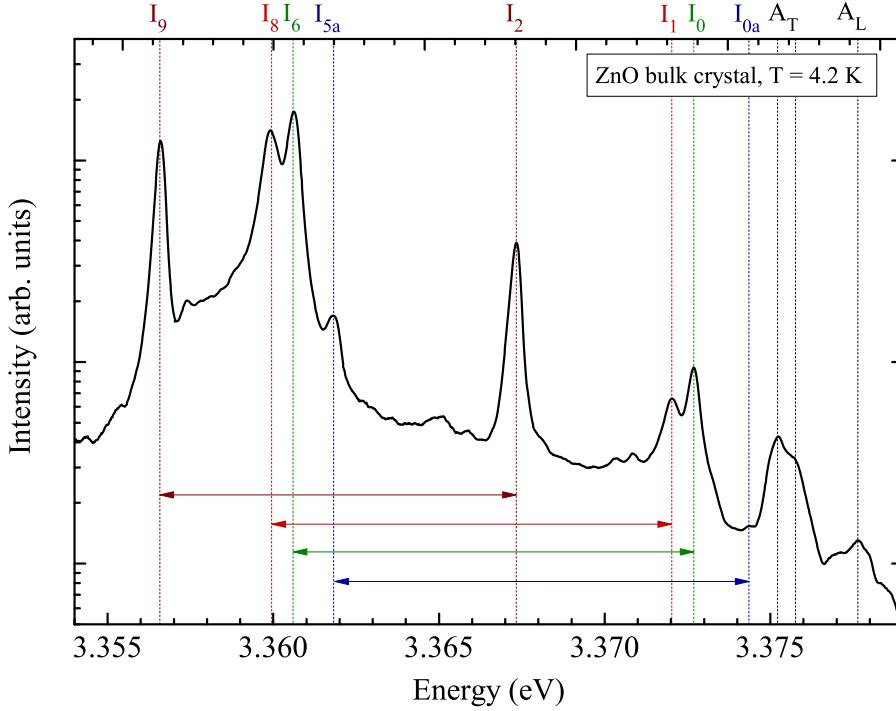


Figure 3.6: Photoluminescence spectrum of a ZnO bulk crystal in the range of the neutral and ionized bound excitons. Vertical drop lines of the same color indicate excitons bound to neutral and ionized donors of the same chemical identity.

The attributions of these exciton pairs to the same chemical impurity is supported by their combined presence in different samples: ZnO grown on  $\text{Al}_2\text{O}_3$  usually exhibits strong  $I_6$  and  $I_0$  transitions due to diffusion of aluminum from the substrate into the layer. For ZnO doped with radiative  $^{73}\text{Ga}$ , Johnston et al. [84] observed a comparable intensity decrease of the  $I_8$  and  $I_1$  in agreement with the half life of the gallium isotope. The exclusive presence of the  $I_2$  in samples with strong  $I_9$  emission is another indicator for this correlation. In addition to these line pairs, a comparison of the energy spacing between different bound excitons suggests the existence of additional pairs of excitons bound to chemically identical donors in the neutral and ionized charge state. Such a correlated pair is proposed in this work for the  $I_{5a}$  at 3.3618 eV and the weak line labeled  $I_{0a}$  at 3.3745 eV as indicated in Fig. 3.6.

Fig. 3.7 shows the PL spectra of four different ZnO substrates in the range of the neutral bound excitons (Fig. 3.7a) and the ionized bound excitons (Fig. 3.7b). The direct comparison between the samples reveals small energy shifts of the bound exciton lines associated with the same dopant. Several different reasons are conceivable.

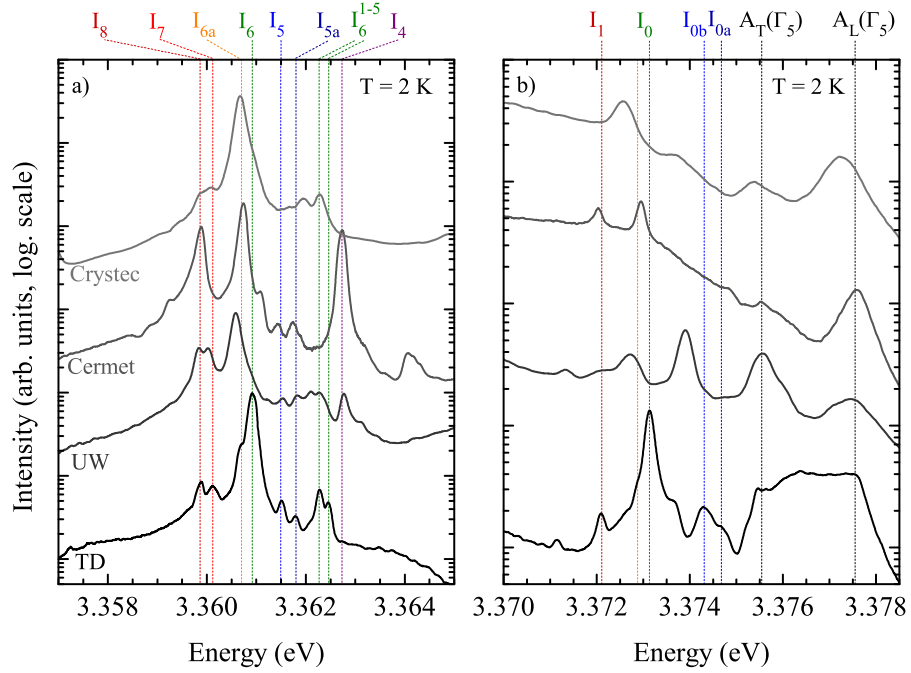


Figure 3.7: Photoluminescence of four different ZnO bulk crystals in the range of the neutral bound excitons (a) and ionized bound excitons (b). Spectra were recorded at a sample temperature of  $T=2$  K. Vertical drop lines of the same color indicate excitons bound to neutral and ionized donors of the same chemical identity.

Despite the fact that all spectra are recorded from bulk crystals (substrates), a minor spectral shift of typically not more than 0.5 meV can be induced by local strain fields due to different defect and impurity concentrations. This can result in slight variations of the bond length caused by the different ionic radii of the impurity atoms. In the case of the surface sensitive photoluminescence technique, another contribution to the energy shift could be caused by surface polishing, altering the local strain distribution due to near-surface structural defects. Additionally, high dopant levels may introduce free carrier concentrations close to the Mott transition, hence resulting in a red shift of the emission energies due to electron-electron interaction. Since the strain induced shift of the transition energies affects not only the bound excitons but the free exciton energies, too, the localization energy is more reliable indicator for the identification of the bound excitons lines rather than the absolute transition energy.

The vertical drop lines in Fig. 3.7 mark the transition lines in the TD sample which exhibits the most diverse fine structure in the range of the ionized bound exciton lines. A comparison between the energy spacing and intensities of neutral and ionized bound exciton transitions confirms the earlier discussed correlation between several

pairs of these lines. Although the emission lines in the other samples are slightly shifted compared to the indicated energy positions, it is apparent that the same correlation also applies for the exciton lines in the other samples. In agreement with observations in Fig. 3.6, two additional transitions in the Tokyo Denpa (TD) sample at 3.3745 eV ( $I_{0a}$ ) and 3.3741 eV ( $I_{0b}$ ) are assigned to ionized bound excitons which form correlated pairs with the neutral bound exciton transitions  $I_{5a}$  at 3.3618 eV and  $I_5$  at 3.3615 eV (blue vertical lines), respectively. This affiliation is based on the intensity ratio and energy spacing of these lines. Two additional lines at 3.3622 and 3.3624 eV in the TD samples are not correlated with ionized bound excitons. In the following chapter 3.4.2, it is shown that these lines do not originate from ground state excitons but vibrational-rotational excited states of the  $I_6$  as indicated by the green lines in Fig. 3.7a.

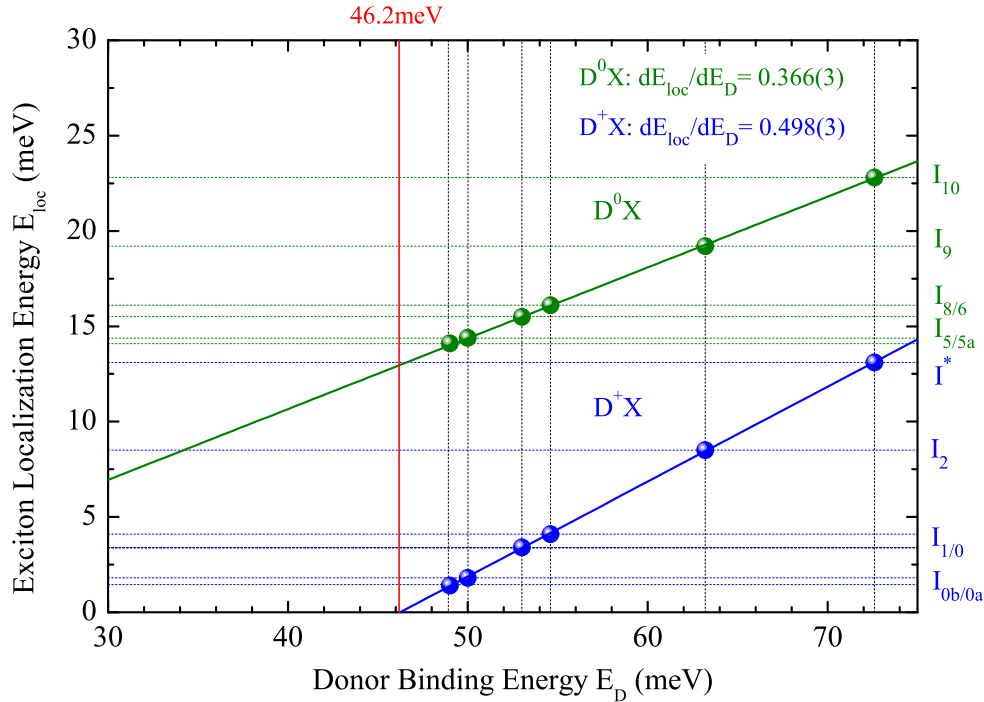


Figure 3.8: Exciton localization energy ( $E_{loc}$ ) as function of the donor binding energy  $E_D$  for neutral and ionized donor bound excitons in ZnO. The vertical red line indicates the minimum donor binding energy for the existence of ionized donor bound excitons.

Another interesting fact is the absence of an ionized bound exciton transition for the hydrogen related  $I_4$  transition (purple line) which can be clearly observed e.g. in the Cermet sample. In order to explain this characteristic, the localization energies of neutral and ionized bound excitons are plotted as function of the donor binding energy in Fig. 3.8. Apparently, neutral and ionized bound excitons show a linear

dependence with different slopes of the localization energy  $E_{loc}$  on the donor binding energy  $E_D$  [70]. These donor binding energies can be derived from the energy spacing of the bound excitons to their two electron satellite transitions [18, 40] and are listed in Table 3.3. From a linear fit of the ionized bound excitons energies, a minimum donor binding energy of  $E_D = 46.2$  eV is derived. Below this value, excitons do not bind to ionized donor centers as their energy would exceed the energy of the free exciton  $A_T$ . Since the  $I_4$  donor bound exciton corresponds to a binding energy of 46.1 meV which is below the threshold for ionized donors, no exciton transitions bound to ionized hydrogen donors occur. The different slopes in Fig. 3.8 are a consequence of the different influence of central cell effects on neutral and ionized donors [68]. In an effective mass approach (EMA), a donor binding energy  $E_D = 51$  meV is calculated for the effective mass like donor state without taking central cell effects into consideration [97]. The large deviation of the experimentally derived donor binding energy between 46.1 meV ( $I_4$ ) and 72.6 meV ( $I_{10}$ ) from the effective mass donor is caused by the central cell shift which demonstrates the impact of the impurity core on the binding energy. Since neutral donor bound excitons are less sensitive to central cell effects than ionized ones [68], a larger slope  $dE_{loc}/dE_D$  is observed for the ionized bound excitons. From the linear fits in Fig. 3.8, values of  $dE_{loc}/dE_D = 0.366(3)$  and  $0.498(3)$  are derived for the neutral and ionized donor bound excitons, respectively. The ratios of the localization energies and donor binding energies ( $E_{loc}/E_D$ ) for all observed exciton transitions are listed in Table 3.3 with values of 0.03 to 0.14 for the ionized donors and 0.26 to 0.31 for the neutral donor bound excitons. These values are in good agreement with theoretical calculations for neutral donors using effective mass ratios  $\sigma = m_e^*/m_h^*$  between 0.3 and 0.4 [98, 99] as recently discussed in a comprehensive study of neutral and ionized donors by Meyer et al. [70].

### 3.4.2 Excited states of bound excitons

In the first sections of this chapter, the optical transitions of different ZnO samples were studied with focus on the radiative recombination of neutral and ionized bound excitons. So far, only excitons in the ground state were considered which dominate the spectrum at very low temperatures. With increasing temperature additional lines can appear which are related to excited states of the bound exciton complexes. Fig. 3.9 shows the luminescence spectrum of a ZnO substrate by Cermet in the range of the neutral bound excitons at a temperature of  $T = 10$  K. Compared to the spectra in the previous section, new emission lines are visible which indicate that some of the transitions originate from ground states and others from excited states of the bound excitons.

The transitions marked by the solid lines in Fig. 3.9 labeled  $I_9$ ,  $I_7$ ,  $I_6$ ,  $I_{5a}$ ,  $I_{4a}$ , and

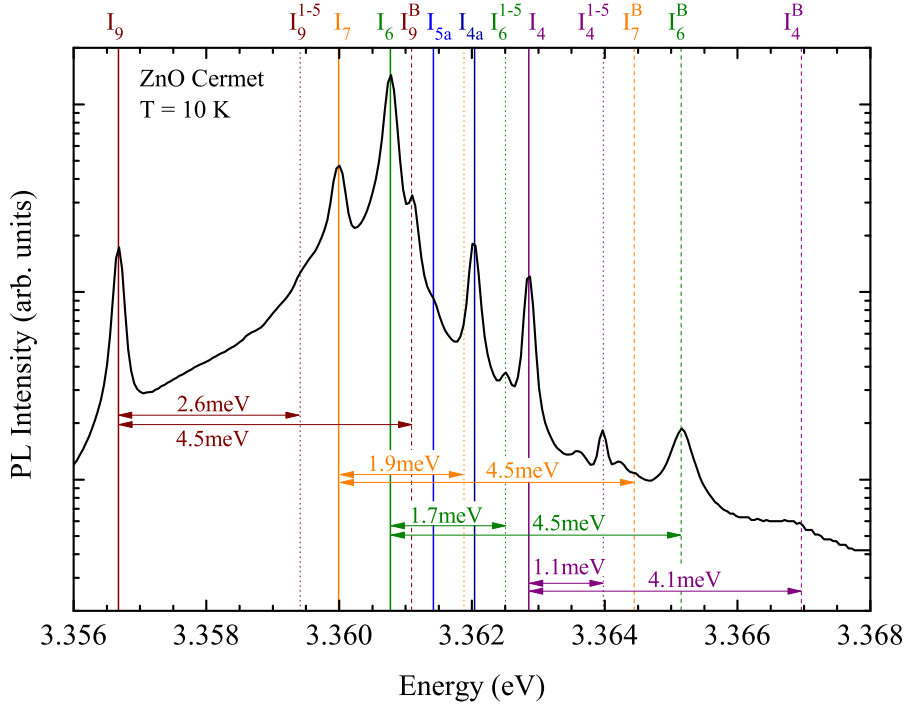


Figure 3.9: Photoluminescence spectrum of a ZnO single crystal recorded at  $T = 10$  K. Solid lines mark emission lines from neutral bound excitons in the ground state. Dotted and dashed lines of the same color indicate corresponding vibrational-rotational excited states and excitons with a hole from the B instead of the A valence band.

$I_4$  are related to bound exciton recombination lines in the ground state (Table 3.3). In addition, several weaker emission lines are observed in the  $T = 10$  K spectrum which arise from excited state transitions. Three different types of excited states of excitons bound to a neutral donor, which leave the donor in the ground state, can be distinguished. These are (i) excitons which involve a hole from the B instead of the A valence band, (ii) vibrational-rotational excited states of the excitons, and (iii) electronic excited states of the excitons. Recombination lines which belong to class (i) can be identified on the basis of their constant line separations from the corresponding  $D^0X_A$  transitions which should be in close agreement with the energetic distance between the A and B valence bands. As shown in Fig. 3.9,  $I_9$ ,  $I_7$ , and  $I_6$  have matching lines which are placed 4.5 meV higher in energy (dashed lines of the same color as the  $D^0X_A$  transitions). This distance is consistent with the energy spacing between the A and B valence bands of 4.7 meV [100]. For the  $I_4$  line, the distance is slightly smaller but the high energy line tentatively identified as  $I_4^B$  is significantly broader compared to  $I_6^B$  or  $I_7^B$ . The second class of transition lines which are related to vibrational-rotational excited states (ii) are

also observable in the spectrum in Fig. 3.9. These lines can be distinguished from excited states involving a hole from the B valence band by an increasing energy spacing between the ground state and excited state transitions as function of the localization energy. They are marked by dotted vertical lines in Fig 3.9. For the  $I_4$  to  $I_9$  bound excitons, the energy spacing increases from 1.1 meV to 2.6 meV. The third class of excited states – namely electronic excited states of the bound excitons (iii) – are not observed in the PL spectra but are well detectable by photoluminescence excitation spectroscopy (PLE) as is demonstrated below. These excited states are typically found at energies of 6 to 16 meV above the ground state.

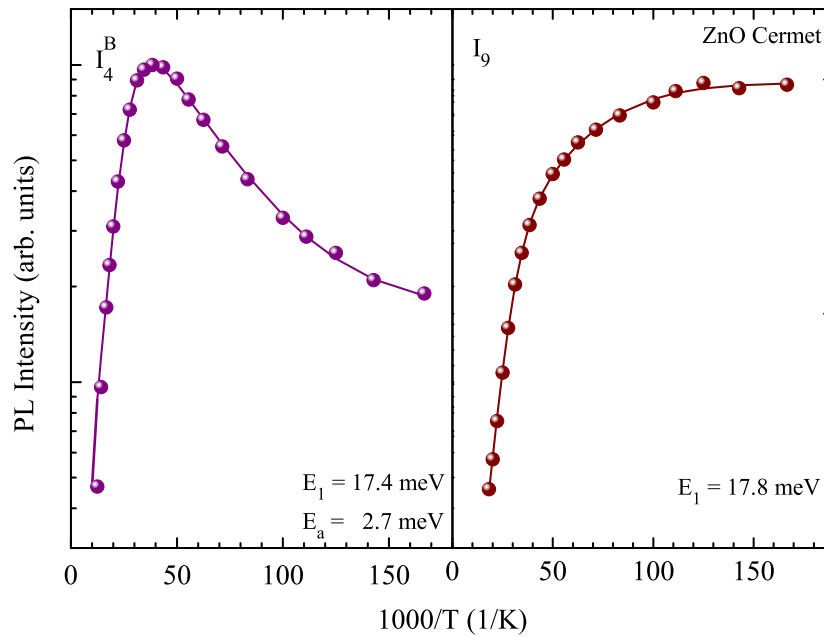


Figure 3.10: Arrhenius plots of the ground state recombination line  $I_9$  and the excited state recombination line  $I_4^B$  which involves a hole from the B valence band. Dots are experimental data, solid lines are fits to the data with the resulting activation energies. According to [101].

In the luminescence spectra, excited states can be distinguished from ground states by a different temperature dependence of the emission lines. This is demonstrated in Fig. 3.10 for the  $I_9$  and  $I_4^B$ . Apparently, the ground state exciton recombination line  $I_9$  rapidly loses intensity with increasing temperature whereas the intensity of the  $I_4^B$  first increases with increasing temperature before it decreases for temperatures higher than about 25 K. The experimental data are fitted by an Arrhenius model from which the activation energies of the different bound excitons can be derived. The thermally activated intensity decrease is expressed by the activation energies  $E_1$  which are related to the strength of the localization of the excitons at the impurities.

For the typical ground state emission lines  $I_4$  to  $I_9$ , activation energies between 15 and 20 meV are derived in accordance with the corresponding localization energies listed in Table 3.3. In the case of excited states – as exemplified here for  $I_4^B$  – a second activation energy  $E_a$  is derived which expresses the intensity increase due to the larger thermal occupation of the excited state energy level. The activation energies  $E_a$  between 2.5 and 4.0 meV obtained from the temperature dependent PL of different bound exciton states with B valence band holes are in fair agreement with the size of the A-B splitting.

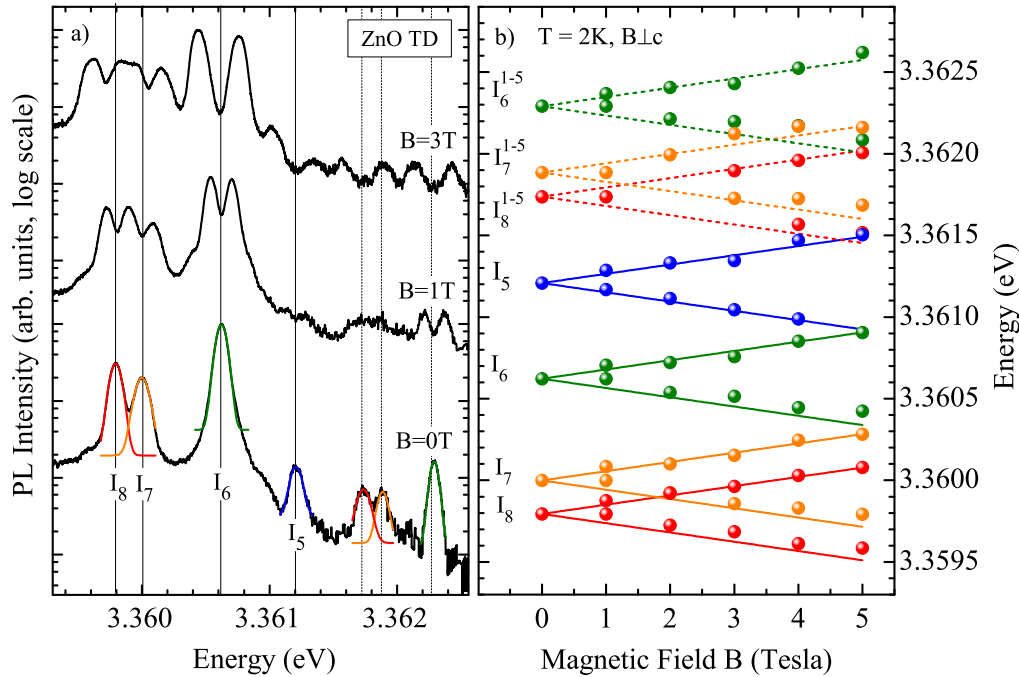


Figure 3.11: (a) Magneto-PL spectra of a homoepitaxial ZnO film recorded at 2 K at field strengths of 0 T, 1 T, and 3 T in the Voigt configuration ( $\mathbf{B} \perp \mathbf{c}$ ). Vibrational-rotational excited states are observed for the bound excitons  $I_8$ ,  $I_7$ , and  $I_6$ . (b) Peak energies of the Zeeman split transition lines for ground and excited states as function of the magnetic field strength between 0 T and 5 T.

Under the influence of an external magnetic field, the ground and excited states are split by the Zeeman effect according to their electron and hole g-factors (chapter 4). Fig. 3.11a shows the magneto-PL spectra of a homoepitaxial grown ZnO film in the Voigt configuration  $\mathbf{B} \perp \mathbf{c}$ . At zero field, not only the bound exciton ground state recombination lines  $I_6$ ,  $I_7$ , and  $I_8$  are observed, but also the corresponding vibrational-rotational excited states are visible for all three excitons. The narrow line-width of the bound excitons allows a spectral separation of the Zeeman components already at a field strength of 1 Tesla (see Fig. 3.11a). The peak energies

of the split ground and excited state lines are displayed as function of the magnetic field in Fig. 3.11b. From the size of the splitting, an electron g-value of  $g_e^\perp = 1.96$  is derived for the ground states of all three bound excitons in good agreement with previous magneto-PL studies of shallow bound excitons in ZnO [102–104]. Although an additional splitting of the exciton lines caused by a non vanishing hole g-factor  $g_h^\perp$  is clearly observed for magnetic fields greater than 3 T [104], this splitting is neglected in the fits of Fig. 3.11b for reasons of clarity and simplicity. A detailed discussion of this fine splitting and related valence band ordering is conducted in chapter 5.2.2. For the excited states of  $I_6$ ,  $I_7$ , and  $I_8$ , a comparable splitting into two Zeeman components is observed in the magneto-PL spectra. The analysis of the peak energies reveals that the splitting of the excited state transition line can be modeled by the same g-values as their respective ground state excitons. The comparable Zeeman splittings of ground state and excited state excitons support the assignment of these line to vibrational-rotational excited states since the same electron and hole states with equal g-factors as in the ground state are involved.

The experimentally determined energies of the vibrational-rotational excited states can be compared with theoretical calculations considering the analogy of these states to molecular vibrations. Using a Kratzer potential, the energy of different vibrational and rotational levels can be calculated. The results of these calculations for the excited states of different bound excitons are listed in Ref. [79]. A comparison of these values to the energy spacing in the PL spectra reveals an excellent agreement between theory and experiment. However, as the first five excited states are grouped into two main transitions which are separated by only 0.2 to 0.6 meV, it is experimentally not always possible to identify the particular vibrational and rotational states since they are very close in energy and partially overlap.

As mentioned earlier, the third class of excited states - electronic excited states of the exciton - can best be monitored in excitation spectra. In the PLE experiments, the intensity of a specific bound exciton transition is monitored while the excitation light is tuned to higher energies. The measured spectrum contains information about the different excitation channels due to charge and energy transfer processes. Fig. 3.12 shows the excitation spectrum of the neutral donor bound exciton  $I_6$ . Up to the energy of the free A exciton-polariton ( $A_T(\Gamma_5)$ ), several narrow lines are visible which originate from different excited states of the  $I_6$ . At higher energies, the ground and excited states of the free A, B, and C excitons appear in the excitation spectra of all bound excitons. These lines demonstrate the energy transfer from free to bound exciton states due to the capture of free excitons at impurities. The top axis of Fig. 3.12 denotes the energy spacing from the  $I_6$  up to the free excitons between 0 and 16 meV. The different excitation lines can be explained as follows: The lowest excited state of the  $I_6$  with an energy spacing of 1.4 meV is found for the

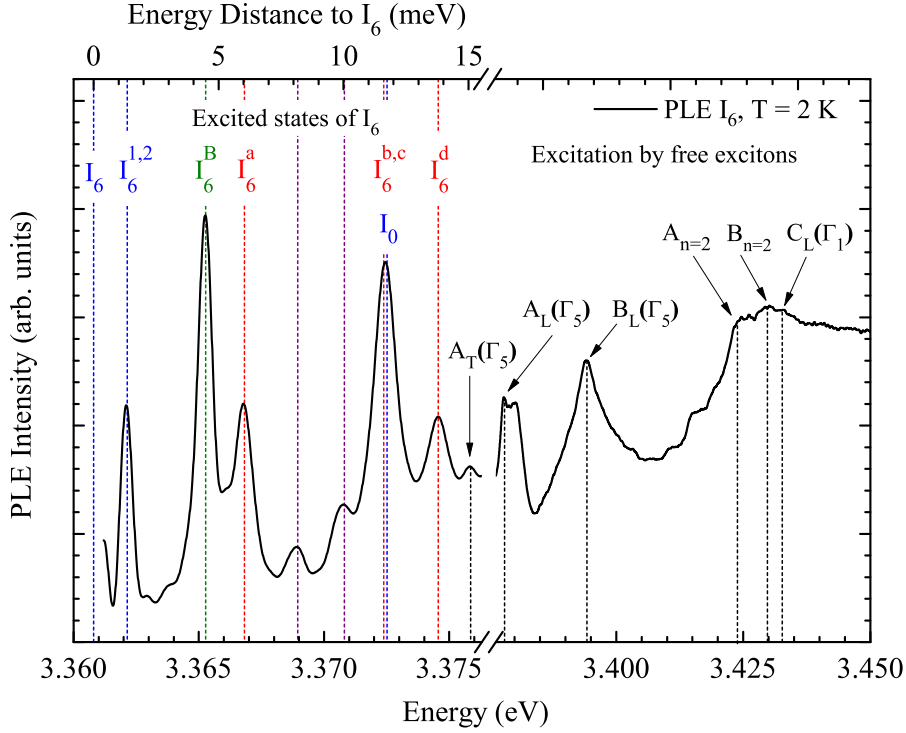


Figure 3.12: Luminescence excitation spectrum monitored at the  $I_6$  recombination line. Excitation channels exist via the free (A, B, C) exciton polaritons and their excited states ( $n = 2$ ) and for the neutral donor bound exciton excited states (note the change in the energy scale). The energy spacing of the excitation channels to the  $I_6$  line is displayed in the top x-axis.

vibrational-rotational levels in good agreement with the PL data and calculations. The strong excitation peak 4.5 meV above the  $I_6$  originates from an exciton with a hole from the B valence band. At higher energies, several peaks are observed which do not appear in the luminescence spectra and are labeled  $I_6^{a-d}$ . These lines represent the electronic excited states of the excitons bound to neutral donors.

From a theoretical point of view, the electronic excited states can be calculated by the formalism presented by Puls et al. [105] for donor-exciton complexes in CdS. Using appropriate values for the band gap energy, Bohr radii, and effective masses in ZnO, the electronic excited states of different donor bound excitons could be calculated [79]. Based on these calculations, four electronic excited states  $I_6^{a-d}$  marked by the red vertical lines in Fig. 3.12 can be identified. Thereby, the lowest energy excited state  $I_6^a$  has the same energy as the vibrational-rotational states of the  $I_6^B$  exciton ( $I_6^{B1,2}$ ). The calculations further predict rather similar values of the excited state energies for the different donor bound excitons with energies between 6 and 16 meV above the corresponding ground state [79]. In the case of bound

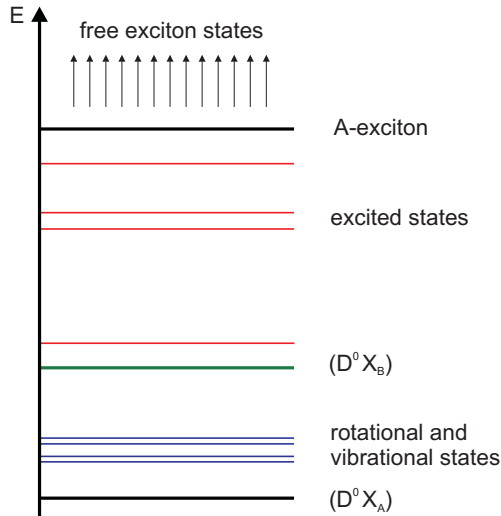


Figure 3.13: Schematic drawing of bound exciton ground and excited state energy levels in ZnO. From low to high energies are shown: bound exciton ground state (black), vibrational-rotational levels (blue), bound exciton with a hole from the B valence band (green), electronic excited states (red), and energy of the free A exciton (energies are not to scale).

excitons with small localization energies, e.g. for  $I_4$ , the higher excited states are therefore not observable as they would exceed the energy of the free A exciton and are consequently not stable. As seen in Fig. 3.12, there still remain two transitions (dashed purple lines with an energy of 8.1 meV and 10.0 meV above the  $I_6$ ) which cannot be explained by these attributions. Gutowski et al. [102] proposed that in the excitation spectrum of a specific exciton line (e.g.  $I_6$ ), transitions may show up which are related to the creation of more weakly bound excitons in the electronic ground state i.e.  $I_5$  and  $I_4$  and the ionized donor bound excitons  $I_3$  to  $I_0$ . However, the remaining lines do not exactly match the energies of known bound excitons in ZnO and no conclusive evidence for energy transfer processes from higher to lower energy excitons involving different impurity centers is found. However, charge transfer processes from ionized to neutral bound excitons bound to the same impurity can occur [106]. In the case of the  $I_6$ , the strong excitation peak at around 3.3725 eV might therefore consist of overlapping excitation channels involving the  $I_6^{b,c}$  electronic excited states and the corresponding ionized bound exciton  $I_0$  [106].

Based on the experimental observations and theoretical calculations of the various excited states of donor bound excitons, a simple schematic model can be constructed which describes the energy ordering of the different excited levels. This model is depicted in Fig. 3.13. The lowest excited states are the vibrational-rotational levels between 1.0 and 2.6 meV above the ground state. The different levels can basically be summarized into two energy transitions with an energy spacing of 0.2 to 0.6 meV. Their energy strongly depends on the localization energy of the ground state exciton and increases from  $I_4$  to  $I_9$ . At an energy of 4.5 meV above the ground state, the  $D^0 X_B$  transition appears which involves a hole from the B instead of the A valence band. Since the energy of this excited state only depends on the size of the AB splitting, no dependence on the localization energy occurs. At even higher

energies, the electronic excited states of the bound excitons are found (red lines in Fig. 3.13). These excited states are typically observed between 6 meV and 16 meV above the ground state. The energy of the excited states weakly increases as function of the localization energy. The first electronic excited state may coincide with the vibrational-rotational excited states of the B valence band exciton which however is expected to have significantly smaller oscillator strength. At an energy of 3.3759 eV, the free A exciton limits the stability of higher excited states as their energy would be sufficient to create free excitons.

### 3.5 Summary

In this chapter, the ground and excited states of free and bound excitons were intensively investigated. Following an introductory review of the different luminescence processes in ZnO including free exciton-polaritons, neutral and ionized bound exciton, two-electron-satellites, phonon sidebands and deep luminescence bands, the discussion concentrates on the near band edge luminescence of ZnO single crystals from different manufacturers. The influence of different growth techniques, impurity concentrations and build-in strain levels is expressed by shifted energy positions of the radiative recombinations of free and bound excitons. In the case of the free exciton-polaritons, the longitudinal and transversal excitons with holes from all three valence bands in the ground state and partly also in the  $n = 2$  excited state could be observed. From these measurements, the LT- and band splittings were derived and compared to reported values in the literature.

In the range of the bound excitons, the different transition lines were analyzed and discussed in detail. Several correlated pairs between neutral and ionized bound excitons could be identified. A linear increase of the localization energy as function of the donor binding energy is reported for all neutral and ionized donor bound excitons with different slopes, confirming the validity of Haynes rule. In addition, several different groups of excited states of donor bound excitons were identified by high resolution temperature dependent luminescence and luminescence excitation spectroscopy. These are vibrational-rotational excited states of the bound excitons, excitons which involve a hole from the B instead of the A valence band, and electronic excited states of the excitons. Magneto-PL measurements of the ground and vibrational-rotational excited states corroborate the identification of the excited states with comparable g-factors for all shallow donor bound excitons. In addition to the excited states, energy transfer processes via the ionized bound excitons and free exciton-polaritons were observed.

## 4 Effects of external magnetic fields

The description in the first part of this chapter is intended to establish the foundations of the influence of magnetic fields on the optical properties of free and bound excitons in ZnO. Group theoretical selection rules are introduced which are of great use to determine the behavior of exciton states in external magnetic fields. The previously introduced concepts are then applied to experimental measurements. Magneto-optical photoluminescence studies are presented which allow the attribution of individual bound excitons to donors or acceptors. In addition, the different bound exciton recombinations are identified as neutral and ionized impurity related, thus complementing and extending the discussion concerning the different bound exciton transitions in chapter 3. In the course of this thesis, the magneto-PL technique is applied again to determine the valence band ordering of ZnO in chapter 5 and to identify the binding centers of deeply bound excitons in chapter 6.

### 4.1 Excitons in magnetic fields

The investigation of optical transitions of free and bound excitons in magnetic fields enables the determination of binding energies, electron and hole g-factors, impurity types (donor or acceptor), and charge states of impurity and defect centers. In addition, the symmetry ordering of the valence bands can be derived from the splitting and polarization of excitons in magnetic fields as discussed in chapter 5. Exposed to a magnetic field  $B$ , electrons and holes perform a cyclotron motion which leads to a cyclotron energy

$$E_c = \hbar\omega_c = \hbar(eB/\mu), \quad (4.1)$$

where  $\omega_c$  is the cyclotron frequency and  $\mu$  is the reduced mass of the exciton. Depending on the binding energy of the free exciton and the strength of the magnetic field, two cases are distinguished. For cyclotron energies larger than the binding energy of the free exciton  $E_c \gg E_{ex}^b$ , the appearance of Landau levels can be observed. The formation of Landau levels results from the quantization of the carrier motion in the plane perpendicular to the direction of the magnetic field [74,107,108]. The required field strengths for ZnO are typically only available in pulsed magnetic fields. For static magnetic fields, the cyclotron energy is usually small compared to the binding energy of the free exciton with  $E_{ex}^b = 60$  meV [34]. Thus, the mag-

netic field can be treated as perturbation of the excitonic system. This low field approximation is valid until  $\gamma \leq 0.4$  with

$$\gamma = \frac{1}{2} \frac{e\hbar B}{\mu E_b^{ex}}. \quad (4.2)$$

For ZnO,  $\gamma = 0.4$  corresponds to a magnetic field of around 80 T [109]. In this regime, the exciton energy states are influenced by two major effects of the magnetic field - the diamagnetic shift  $\Delta E_{Dia}$  and the Zeeman splitting  $\Delta E_Z$ . The diamagnetic shift  $\Delta E_{Dia}$  is a quadratic effect that leads to a blue shift of the exciton energy level by

$$\Delta E_{Dia} = \frac{1}{2} c^2 a_B^2 B^2 / \mu, \quad (4.3)$$

where  $a_B$  is the exciton Bohr radius. For ground state excitons  $n = 1$  with a Bohr radius of  $a_B = 18 \text{ \AA}$  in ZnO, the diamagnetic shift is negligible compared to the energy shift by the linear Zeeman splitting. However, it should be noted that the diamagnetic shift greatly increases for excited states  $n \geq 2$  as the Bohr radius of the exciton increases approximately by a factor of 4 from the  $n = 1$  to  $n = 2$  state [109].

## 4.2 The Zeeman effect

The splitting of exciton lines in a magnetic field is caused by the interaction of the external magnetic field with unpaired electron and hole spins which contribute to a resulting magnetic moment. The size of the Zeeman splitting  $\Delta E_Z$  is determined by the effective g-factor of the exciton  $g_{exc}$  and depends linearly on the strength of the magnetic field

$$\Delta E_Z = g_{exc} \mu_B B, \quad (4.4)$$

where  $\mu_B$  is the Bohr magneton. The effective exciton g-factor depends on the electron and hole g-factors  $g_e$  and  $g_h$ . In a general expression  $g_{exc}$  is given by

$$g_{exc} = |g_e \pm g_h|. \quad (4.5)$$

The effective exciton g-value  $g_{exc}$  is not isotropic, which is mainly caused by the large anisotropy of the hole g-factor  $g_h$ . In addition, there is an angular dependence of the electron g-factor  $g_e$  with typical values for shallow donors of around 1.956 [88,110]. A detailed list of g-values for different centers is available in Ref. [40]. However, due to the small difference in the electron effective g-values ( $\Delta g_e = |g_e^\perp - g_e^\parallel| \cong 0.001$ ) which is usually not resolved in magneto-optical PL or absorption spectra but rather by EPR or ODMR, the electron anisotropy can be neglected in the following discussion of the Zeeman splitting.

For  $g_h$ , the absolute value of the hole anisotropic g factor is given by

$$g_h = \sqrt{|g_h^\parallel|^2 \cos^2 \theta + |g_h^\perp|^2 \sin^2 \theta}, \quad (4.6)$$

where  $\theta$  is the angle between the  $\mathbf{c}$ -axis and the direction of the magnetic field  $\mathbf{B}$  [111]. Apparently, Eq. 4.6 delivers  $g_h^\perp$  for  $\mathbf{B} \perp \mathbf{c}$  and  $g_h^\parallel$  for  $\mathbf{B} \parallel \mathbf{c}$ . The magnetic anisotropy of the hole g-factor can be explained in the quasi-cubic approximation considering the expectation values of the orbital angular momentum  $L_x$ ,  $L_y$ , and  $L_z$ . For a  $\Gamma_7$  valence state having  $p_x, p_y$  like character,  $L_z$  and  $L_{x,y}$  are nonzero, so that  $g_h \neq 0$  for any angle  $\theta$  between  $\mathbf{B}$  and  $\mathbf{c}$ . In the case of a  $\Gamma_9$  valence band,  $L_x$  and  $L_y$  are zero and  $L_z \neq 0$ . Hence, Eq. 4.6 can be simplified for a  $\Gamma_9$  hole state with  $g_h^\perp = 0$ . The effective hole g-value  $g_h$  for a valence state with  $\Gamma_9$  symmetry is then given by:

$$g_h = g_h^\parallel \cos\theta. \quad (4.7)$$

Consequently, the Zeeman splitting of a  $\Gamma_9$  hole state is only determined by  $g_h^\parallel$  and no splitting of the hole state occurs for  $\mathbf{B} \perp \mathbf{c}$ .

### 4.3 Selection rules of exciton states in magnetic fields

In order to determine whether a certain energy state in a crystal splits in an applied magnetic field, group theory considerations are beneficial. Thereto, the Kronecker product of the group representation of the magnetic field ( $\Gamma_B$ ) and the respective state ( $\Gamma_i$ ) must be calculated. A magnetic field leads to a splitting of a particular state, if the group representation of the state or the magnetic field is contained in the Kronecker product of the two:

$$g_{exc} \neq 0 \iff \Gamma_B \vee \Gamma_i \in \Gamma_i \otimes \Gamma_B. \quad (4.8)$$

The group representation of a magnetic field perpendicular to the  $\mathbf{c}$ -axis ( $\Gamma_{B\perp}$ ) is  $\Gamma_5$ , a magnetic field parallel to the  $\mathbf{c}$ -axis ( $\Gamma_{B\parallel}$ ) transforms like  $\Gamma_2$ . Thus, certain symmetries lead to zero or non-zero g-values in dependence of the directions of the magnetic field and consequently result in the presence or absence of a Zeeman splitting. Table 4.1 lists the Kronecker products of all symmetry states under the influence of parallel and perpendicular magnetic fields in crystals with the point group  $C_{6v}$  according to Koster et al. [112].

Table 4.1: Multiplication table for the point group  $C_{6v}$  for symmetry states in perpendicular ( $\Gamma_5$ ) and parallel ( $\Gamma_2$ ) magnetic fields.

$\Gamma_i$	$\Gamma_1$	$\Gamma_2$	$\Gamma_3$	$\Gamma_4$	$\Gamma_5$	$\Gamma_6$	$\Gamma_7$	$\Gamma_8$	$\Gamma_9$
$\Gamma_i \otimes \Gamma_2$	$\Gamma_2$	$\Gamma_1$	$\Gamma_4$	$\Gamma_3$	$\Gamma_5$	$\Gamma_6$	$\Gamma_7$	$\Gamma_8$	$\Gamma_9$
$\Gamma_i \otimes \Gamma_5$	$\Gamma_5$	$\Gamma_5$	$\Gamma_6$	$\Gamma_6$	$\Gamma_1 + \Gamma_2 + \Gamma_6$	$\Gamma_3 + \Gamma_4 + \Gamma_5$	$\Gamma_7 + \Gamma_9$	$\Gamma_8 + \Gamma_9$	$\Gamma_7 + \Gamma_8$

From this table, the splitting of electron and hole states can be easily predicted

using Eq. 4.8. For the possible symmetries of the conduction and valence bands in ZnO, the following relations are derived:

$$\Gamma_7 \otimes \Gamma_5 = \Gamma_7 + \Gamma_9 \iff g^\perp \neq 0, \quad (4.9)$$

$$\Gamma_9 \otimes \Gamma_5 = \Gamma_7 + \Gamma_8 \iff g^\perp = 0, \quad (4.10)$$

$$\Gamma_7 \otimes \Gamma_2 = \Gamma_7 \iff g^\parallel \neq 0, \quad (4.11)$$

$$\Gamma_9 \otimes \Gamma_2 = \Gamma_9 \iff g^\parallel \neq 0. \quad (4.12)$$

Apparently, the electron states of the conduction band with  $\Gamma_7$  symmetry split in any direction of the magnetic field. Naturally, the same applies for holes from a valence band with  $\Gamma_7$  symmetry. In general, non-zero g-values  $g^\parallel$  for  $\mathbf{B} \parallel \mathbf{c}$  occur for  $\Gamma_1, \Gamma_2, \Gamma_5, \Gamma_6, \Gamma_7, \Gamma_8,$  and  $\Gamma_9$  states. By contrast, non-zero g-factors  $g^\perp$  for  $\mathbf{B} \perp \mathbf{c}$  only appear for  $\Gamma_1, \Gamma_2, \Gamma_7,$  and  $\Gamma_8$  states. This also confirms that the g-factor of a  $\Gamma_9$  hole state in a parallel magnetic field is zero ( $g^\parallel = 0$ ) as stated in Eq. 4.7.

## 4.4 Zeeman splitting of excitonic states

The Zeeman splitting of the exciton energy levels and hence the energy of optical transitions between the split excited and ground states depends on the type of excitons. Free excitons and excitons bound to ionized impurities can be distinguished from those bound to neutral impurities by a nonlinear splitting of energy levels in the magnetic field perpendicular to the  $\mathbf{c}$ -axis (section 4.4.3), whereas excitons bound to neutral impurities exhibit a linear splitting behavior for  $\mathbf{B} \perp \mathbf{c}$  (section 4.4.1). The different splitting mechanisms are discussed in the following sections and used to identify the observed bound exciton transitions in magneto-PL experiments.

### 4.4.1 Neutral bound excitons

A neutral donor or acceptor bound exciton consists of an electron hole pair bound to an impurity or defect center which provides either one electron (donor) or one hole (acceptor) to the bound exciton complex. The neutral impurities as well as the bound exciton complexes represent doublet states ( $S = 1/2$ ) since the two like particles form pairs with antiparallel spins. This fact leaves an unpaired electron in the case of an acceptor or an unpaired hole in the case of a donor bound exciton complex (Fig. 4.1).

The energy level schemes for neutral donor and acceptor bound excitons involving hole states with  $\Gamma_7$  or  $\Gamma_9$  symmetry are displayed in Fig. 4.1 for magnetic fields parallel and perpendicular to the crystal  $c$ -axis. Considering exciton ground states ( $n = 1$ ) without orbital angular momentum, the energy states of a neutral bound exciton in an external magnetic field will split according to the g-value of the unpaired

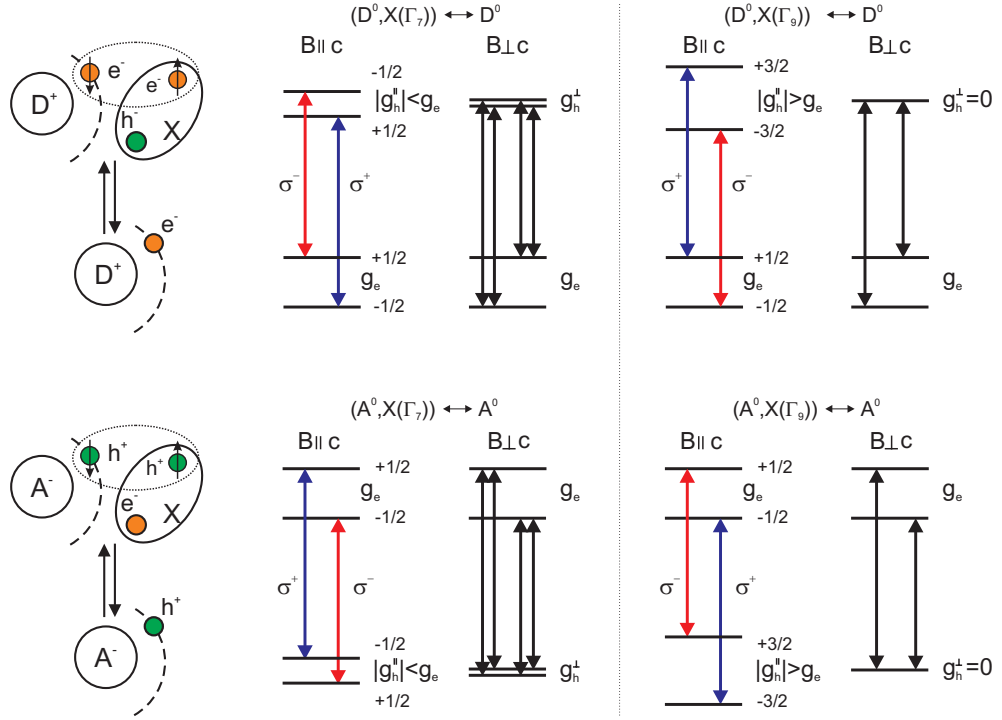


Figure 4.1: Zeeman splitting of neutral bound exciton complexes involving  $\Gamma_7$  electron states and  $\Gamma_7$  or  $\Gamma_9$  hole states in a constant external magnetic field with  $\mathbf{B} \parallel \mathbf{c}$  and  $\mathbf{B} \perp \mathbf{c}$ . The g-values in the ground and excited states depend on the spin of the unpaired particles. Circular polarized transitions are indicated by blue ( $\sigma^+$ ) and red ( $\sigma^-$ ) lines.

particle in the exciton complex. For a neutral donor bound exciton, the splitting of the ground state is determined by the almost isotropic electron g-factor  $g_e$  whereas the splitting of the excited state is governed by the anisotropic hole g-factor. The size of the effective hole g-factor depends on the direction of the magnetic field as given by Eq. 4.6. In the Faraday configuration ( $\mathbf{B} \parallel \mathbf{c}$ ), the parallel hole g-factor  $g_h^{\parallel}$  is smaller than  $g_e$  for a  $\Gamma_7$  hole and larger than  $g_e$  for a  $\Gamma_9$  hole state. The parallel magnetic field leads to a circular polarization of the emitted light whereby the high energy transition is always  $\sigma^+$  polarized and the low energy component is active in the  $\sigma^-$  polarization independent of the hole state symmetry (Fig. 4.1). In the Voigt geometry ( $\mathbf{B} \perp \mathbf{c}$ ) the perpendicular hole g-factor  $g_h^{\perp}$  is small for a  $\Gamma_7$  hole state and zero in the case of a  $\Gamma_9$  hole state as derived from group theory in the previous section. This fact is used for a detailed investigation of the valence band ordering of ZnO in chapter 5. For acceptor bound excitons, the energy level scheme in Fig. 4.1 is reversed, i.e. the splitting of the excited state is determined by the electron g-factor  $g_e$  whereas the splitting of the ground state is caused by the hole g-factor  $g_h$ . Apart from this difference, the selection rules for magnetic splittings

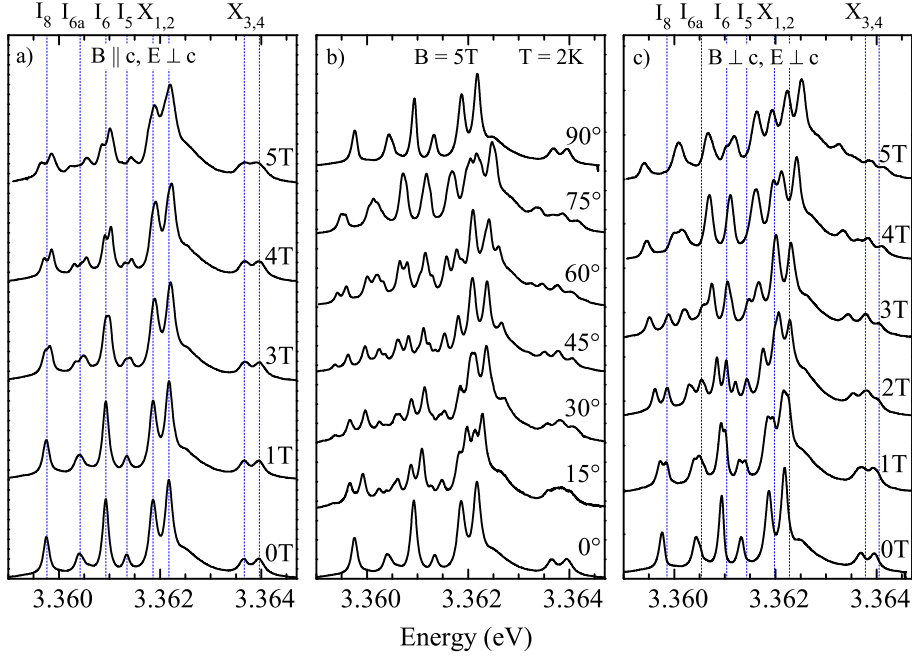


Figure 4.2: Magneto-PL spectra of neutral bound excitons  $I_8$  to  $I_5$  and  $X_1$  to  $X_4$  at 2 K. (a) Faraday configuration, (b) arbitrary angles  $\theta$  between  $\mathbf{B}$  and  $\mathbf{c}$  at  $B = 5$  T, (c) Voigt configuration. Vertical lines indicate the zero-field energy of the transition lines.

and optical transitions are equal for donor and acceptor bound excitons.

The energies of the Zeeman split transitions of neutral bound excitons can be calculated as a combination of the electron and hole g-factors displayed in Fig. 4.1. For arbitrary angles  $\theta$  between the magnetic field  $\mathbf{B}$  and the direction of the crystal  $\mathbf{c}$ -axis, four transition lines appear which energies are determined by

$$E^\pm = E \pm \frac{1}{2}\mu_B(g_e \pm g_h)B, \quad (4.13)$$

with  $g_h$  as given in Eq. 4.6. Using this relation, the electron and hole g-factors can be derived from the fit of the Zeeman splittings in different directions of the magnetic field.

The magneto-PL spectra of a homoepitaxial ZnO film grown on a O-face CysTec substrate are shown in Fig. 4.2. The spectra were recorded at  $T = 2$  K in the Faraday configuration (a), for varying angles between the  $c$ -axis and the direction of the magnetic field (b), and in the Voigt configuration (c). Apart from the commonly observed neutral donor bound excitons  $I_5$ ,  $I_6$ ,  $I_{6a}$ , and  $I_8$ , four additional transition lines are observed between 3.362 eV and 3.364 eV labeled  $X_1$  to  $X_4$ . These lines appear exclusively in homoepitaxial films grown on the O-polar face of ZnO substrates. The details of the influence of different substrate surface polarities are

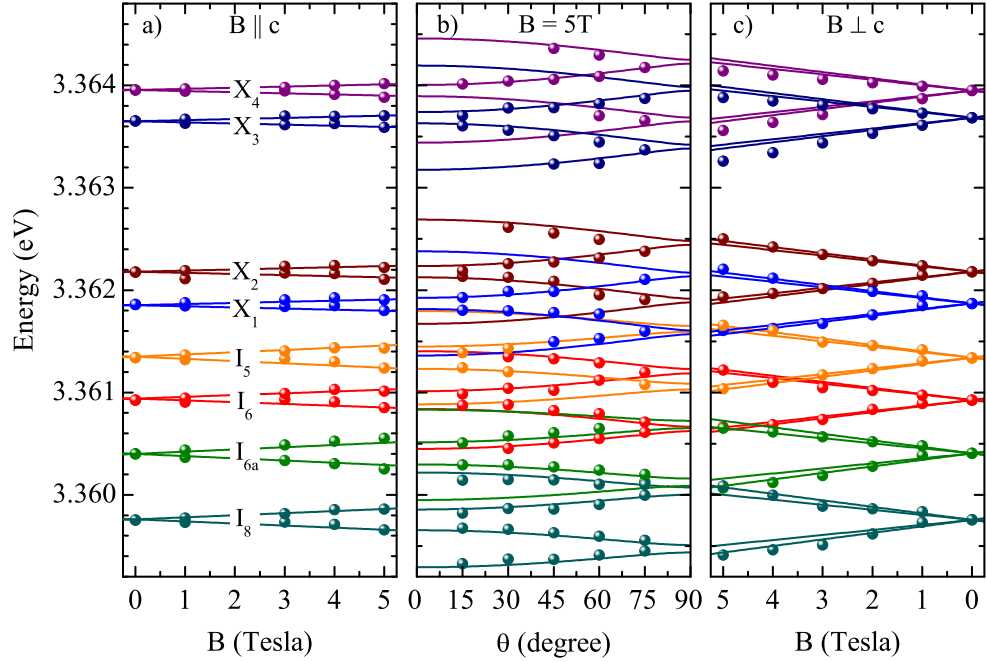


Figure 4.3: Zeeman splitting of neutral bound excitons  $I_8$  to  $I_5$  and  $X_1$  to  $X_4$  at 2 K. (a) Faraday configuration, (b) arbitrary angles  $\theta$  between  $\mathbf{B}$  and  $\mathbf{c}$  at  $B = 5$  T, (c) Voigt configuration. Dots indicate peak positions as derived from the magneto-PL spectra, lines represent fits to the experimental data.

discussed in chapter 9. Although the origin of the bound excitons  $I_6 / I_{6a}$  and  $I_8$  is firmly established in the literature (see chapter 3), the large quantity of narrow transition lines in this samples makes it an interesting candidate for magneto-PL studies.

In order to identify and distinguish the different lines at higher magnetic fields, the peak energies are determined by Gaussian fits and plotted in Fig. 4.3. The clearly observed linear splitting of all transitions in Fig. 4.3 proves the neutral charge state not only for the  $I_5$  to  $I_8$  related impurities, but also for the centers involved in the  $X_1$  to  $X_4$  lines. Using Eq. 4.13, excellent fits of the experimental data are obtained for the different angles  $\theta$  between the magnetic field and the  $c$ -axis as indicated by the solid lines. Although the hole fine splitting associated with the small hole g-factor  $g_h^\perp$  is not resolved in these spectra (see chapter 5), the fourfold splitting is clearly apparent for arbitrary angles  $\theta$ . The reduction of the angle  $\theta$  from  $\theta = 90^\circ$  towards  $\theta = 0^\circ$  at a constant magnetic field leads to an increased splitting of the outer Zeeman components and a decrease of the effective splitting of the inner transition lines (Fig. 4.3). This behavior is caused by the anisotropy of the hole effective g-value  $g_h(\theta)$ . For smaller angles  $\theta$ , the intensities of the outer Zeeman split transitions are reduced (Fig. 4.2). In the Faraday geometry ( $\theta = 0$ ), these lines are not observed

as the transitions are forbidden by selection rules in the  $\mathbf{E} \perp \mathbf{c}$  configuration, but active in  $\mathbf{E} \parallel \mathbf{c}$  geometry. The size of the effective Zeeman splitting in the Faraday configuration is significantly smaller compared to those in Voigt geometry which is caused by the negative hole  $g$ -factor  $g_h^{\parallel}$  (Eq. 4.5) in agreement with the model in Fig. 4.1.

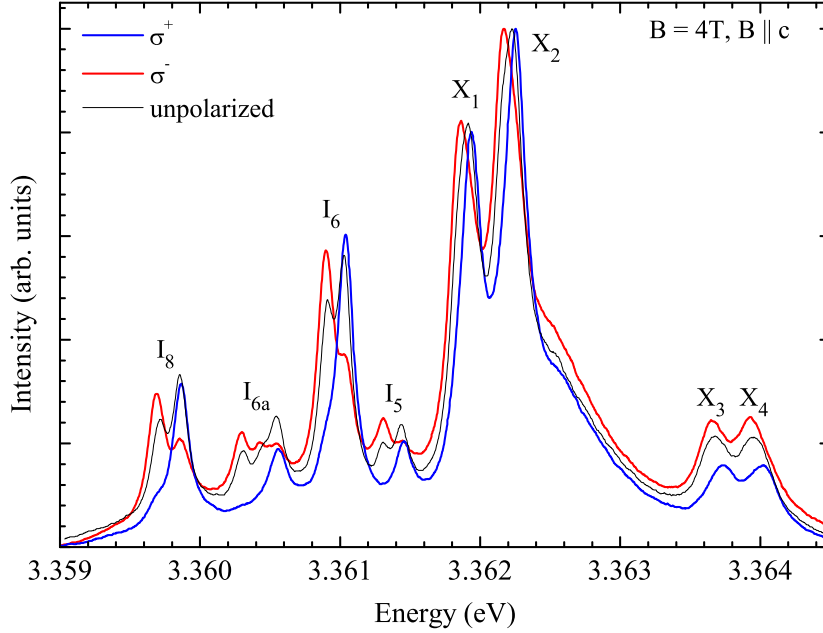


Figure 4.4: Circular polarized magneto-PL spectra of bound excitons in the Faraday configuration at  $B = 4$  T and  $T = 2$  K. Black line represents an unpolarized spectrum, red and blue graphs are  $\sigma^-$  and  $\sigma^+$  polarized, respectively.

As can be seen from the level scheme in Fig. 4.1, the emission lines in the Faraday configuration should be circular polarized. Consequently, polarization dependent measurements can be used to achieve a spectral separation of the Zeeman split recombination lines already at low magnetic fields since either the  $\sigma^+$  or  $\sigma^-$  polarized transitions can be suppressed. Fig. 4.4 displays the polarized spectra for a magnetic field strength of  $B = 4$  T. Apparently, the  $I_i$  lines and  $X_i$  lines exhibit the same polarization patterns. The high energy Zeeman component is  $\sigma^+$  polarized, while the low energy component is active in the  $\sigma^-$  orientation in agreement with the model in Fig. 4.1. The polarized spectra are used to determine the peak positions in Fig. 4.3 with increased precision which results in better fits of the experimental results.

From the fits in Fig. 4.3, the electron  $g$ -factor  $g_e$  and the hole  $g$ -factors  $g_h^{\perp}$  and  $g_h^{\parallel}$  of all observed transition lines can be derived. These values are listed in Table 4.2 together with relevant results from the literature. For the  $I_i$  lines, a good agreement

Table 4.2: Electron ( $g_e$ ) and hole ( $g_h^{\parallel}, g_h^{\perp}$ ) g-factors and zero-field exchange energies  $E_{ex}$  of free and bound excitons in ZnO.

Exciton	center	$g_e$	$g_h^{\parallel}$	$g_h^{\perp}$	$E_{ex}$ (meV)	Ref.
A( $\Gamma_{1,2}$ )	$FX_A$	1.95	-1.77	-	-	[113]
	$FX_A$	1.95	-1.75	-	-	[114]
	$FX_A$	1.95	-1.60	-	-	[115]
$I_0$	$D^+X$	1.95	-1.15	0.10	0.92	this study, [113]
$I_1$	$D^+X$	1.95	-1.15	0.10	0.96	this study, [113]
$I_{2,3}$	$D^+X$	1.95	-1.24	0.10	0.98	[103]
	$D^+X$	-1.94 <sup>a</sup>	-1.51	0	0.90	[69]
$X_i$	$D^0X$	1.95	-1.57	0.13	-	this work, [113]
$I_4$	$D^0X$	1.97	-1.21	0.10	-	[103]
$I_5$	$D^0X$	1.95	-1.20	0.20	-	this work, [113]
	$D^0X$	1.93	-1.45	0	-	[114]
$I_6$	$D^0X$	1.95	-1.35	0.20	-	this work, [113]
	$D^0X$	1.93	-1.41	0	-	[114]
	$D^0X$	1.92	-1.24	0.08	-	[103]
$I_{6a}$	$D^0X$	1.95	-1.20	0.25	-	this work, [113]
$I_8$	$D^0X$	1.92	-1.25	0.25	-	this work, [113]
	$D^0X$	1.93	-1.41	0	-	[114]
	$D^0X$	1.92	-1.24	0.08	-	[103]
	$D^0X$	1.87	-1.26	0.06	-	[116]
$I_9$	$D^0X$	1.86	-1.27	0.06	-	[103]
	-	-1.93 <sup>a</sup>	-1.24	0	-	[69]

<sup>a</sup> The inversed sign in the g-factors occurs since  $\Gamma_9$  symmetry was assumed for the hole state.

with previous studies is achieved. In the case of the  $X_i$  lines, no data has been published until now. It is remarkable that the absolute value of the parallel hole g-factor of the X-lines  $g_h^{\parallel} = -1.57$  is considerably greater than those of other neutral donor bound excitons with values of about  $-1.25$ . Although the origin of this deviation is not completely apparent, it could be correlated to a model which attributes the X-lines to one defect complex instead of four different impurity bound excitons. In this case, the four X-lines would possibly originate from transitions between two excited states and two ground states as suggested by Lautenschläger et al. [93]. This is elaborated in greater detail in chapter 9.

#### 4.4.2 Donor and acceptor bound excitons

Several publications report on the identification of donor and acceptor bound exciton complexes with partly contradicting attributions [40, 70, 102–104, 117–120]. While

the earlier works of Loose et al. [118] and Gutowski et al. [102] assign several bound excitons to acceptor impurities, the majority of recent publications attributes the shallow bound excitons to donor impurities [40, 70, 103, 120]. Rodina et al. [103] and Strassburg et al. [120] presented comprehensive temperature and magnetic field dependent thermalization studies of the  $I_{2/3}$ ,  $I_4$ , and  $I_9$  bound excitons which clearly establish the donor related character of these lines. This work is now complemented with the study of the bound excitons  $I_5$ ,  $I_6$ ,  $I_{6a}$ , and  $I_8$  as well as the lines  $X_1$  to  $X_4$  and their attribution to donor or acceptor bound excitons by their thermalization in a magnetic field.

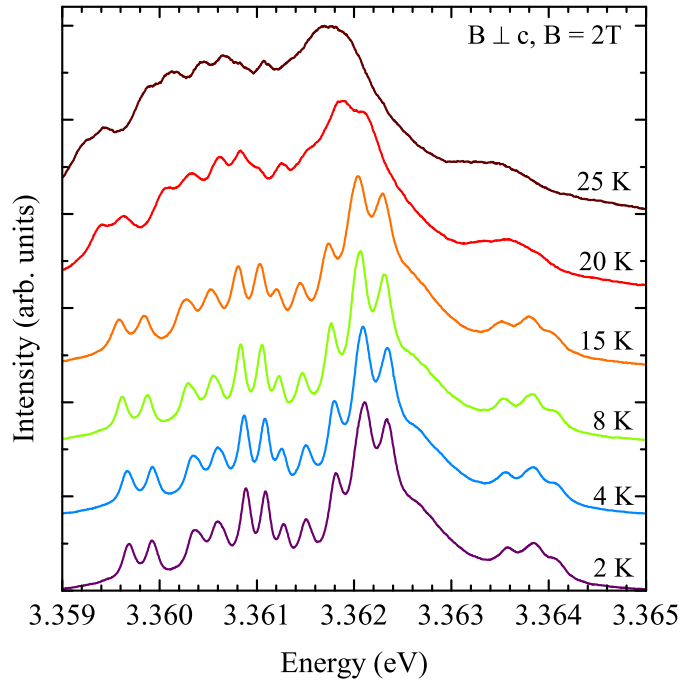


Figure 4.5: Temperature dependent magneto-PL spectra of bound excitons between 2 K and 25 K for a magnetic field of 2 T in the Voigt configuration ( $\mathbf{B} \perp \mathbf{c}$ ).

Fig. 4.5 displays the temperature dependent magneto-PL spectra of bound excitons in the  $\mathbf{B} \perp \mathbf{c}$  configuration for a magnetic field strength of  $B = 2$  T. The temperature is varied between 2 K and 25 K at which temperature the thermal energy leads to a significant broadening and intensity decrease of the emission lines due to the dissociation of the shallow bound excitons. The analysis of the peak intensities reveals a constant ratio between the two Zeeman components of each line as function of temperature. In order to explain this result, the thermalization effects for magneto-PL and -absorption are considered in the case of donor and acceptor bound excitons.

Based on the presented energy level scheme in Fig. 4.1, it is apparent that exci-

tons bound to neutral acceptors ( $A^0, X$ ) can be distinguished from neutral donor bound excitons ( $D^0, X$ ) by the thermalization of the Zeeman split luminescence and absorption lines in external magnetic fields. The thermalization behavior of the PL components depends on the splitting of the complex excited state ( $A^0, X$ ) or ( $D^0, X$ ) while the thermalization in absorption is caused by the splitting of the ground state ( $A^0$ ) or ( $D^0$ ) of the respective bound exciton complex. The determination of acceptor or donor bound exciton complexes is facilitated in the Voigt configuration since  $g_h^\perp$  is small for a  $\Gamma_7$  hole and zero for a  $\Gamma_9$  hole. Therefore, the thermalization only depends on the splitting caused by the electron g-factor  $g_e$ . According to Fig. 4.1, the splittings of the excited state of a donor bound exciton and the ground state of an acceptor bound exciton are given by  $g_h^\perp$ . Thus, equal intensities of the Zeeman split transition lines of donor bound excitons in luminescence and acceptor bound excitons in absorption are expected, which are independent of the temperature. These constant intensity ratios in luminescence are indeed observed for all emission lines in Fig. 4.5. Consequently, all lines originate from excitons bound to neutral donors.

By contrast, the splitting of the excited state for an acceptor bound exciton complex is given by the electron effective g-factor  $g_e$  (Fig. 4.1). As a consequence, the intensity of the high-energy component of the ( $A^0, X$ )  $\rightarrow$   $A^0$  transition at low temperatures should be smaller than the low energy component, but is expected to increase with rising temperature. This is explained by an increased occupation of the higher energy Zeeman level by thermal activation. In the case of donor bound excitons in absorption, the lower energy transition is weaker at low temperatures and increases for elevated temperatures. Similar considerations apply for the magnetic thermalization, where the increase of the magnetic field at a constant temperature results in a larger splitting of the ground or excited state. At low temperatures, the increased splitting results in a thermal depletion of the excited state and a stronger occupation of the lower energy Zeeman level. Therefore, an intensity comparison of the split Zeeman components in PL and absorption as function of the magnetic field strength can provide additional information for the determination of donor and acceptor bound excitons. In luminescence spectra with increasing magnetic field strength at low temperature, one would therefore expect a constant intensity ratio in the case of donor bound excitons and a decrease of the high energy transition with increasing magnetic field strength in the case of acceptor bound excitons. Although the determination of the peak intensities in Fig. 4.2c is complicated by the overlapping of adjacent emission lines, no decreasing intensity of any high energy Zeeman component can be identified. This is an additional confirmation that all observed transitions are donor related.

A remark should be made concerning the apparent misinterpretation of donor

bound excitons as acceptor related in earlier publications. Rodina et al. pointed out that self-absorption within the crystal can result in a misleading thermalization behavior in luminescence [103]. In that work, an increased intensity of the high energy PL line with increasing temperature was observed for the  $I_4$  and  $I_9$  bound exciton lines in  $\mathbf{B} \perp \mathbf{c}$  [103]. Following the previous discussion, such a behavior indicates an acceptor bound exciton, although the PL data in  $\mathbf{B} \parallel \mathbf{c}$  and absorption studies in the same work could prove that these lines originate from donor bound excitons in agreement with previous publications [67, 84, 121]. Consequently, magneto-absorption data are beneficial to confirm the thermalization results if no indisputable identification can be achieved by magneto-PL.

#### 4.4.3 Free and ionized bound excitons

Free excitons and excitons bound to ionized impurities exhibit a similar Zeeman splitting in an external magnetic field as the group representations of the energy states are the same [109]. For an ionized bound exciton, the ground state ( $\Gamma_1$  symmetry) consists of an impurity with no unpaired spin carrying particles and consequently does not split in an applied magnetic field. In the excited state of an ionized bound exciton, electron and hole spins of the exciton are unpaired. The same applies for free excitons where the ground state is the crystal ground state without excitons and the excited state is the free exciton with unpaired electron and hole spins. Hence, the Zeeman splitting of free and ionized bound excitons is solely determined by the splitting of the excited states. The symmetries of the free and ionized bound exciton states are determined by the Kronecker product of the symmetries of the electron and hole of the exciton together with an envelope function, which transforms like  $\Gamma_1$  for the exciton ground state ( $n = 1$ ). Since electrons and holes inherit the symmetry of their respective bands, the following symmetries are derived for excitons involving holes from the  $\Gamma_7$  and  $\Gamma_9$  valence bands:

$$\Gamma_7(2) \otimes \Gamma_7(2) \otimes \Gamma_1(1) = \Gamma_5(2) + \Gamma_2(1) + \Gamma_1(1), \quad (4.14)$$

$$\Gamma_7(2) \otimes \Gamma_9(2) \otimes \Gamma_1(1) = \Gamma_5(2) + \Gamma_6(2). \quad (4.15)$$

The values in brackets indicate the number of degenerated states.  $\Gamma_2$  and  $\Gamma_6$  are pure triplet states ( $S = 1$ ) which are forbidden for electric dipole (E1) transitions.  $\Gamma_5$  and  $\Gamma_1$  are mixed singlet-triplet states which are dipole allowed and are polarized in the  $\mathbf{E} \perp \mathbf{c}$  and  $\mathbf{E} \parallel \mathbf{c}$  direction, respectively.

The energy level schemes for free and ionized bound excitons with  $\Gamma_7$  and  $\Gamma_9$  hole states are displayed in Fig. 4.6 with and without an external magnetic field parallel and perpendicular to the crystal  $c$ -axis. According to Eq. 4.14, the exciton states have  $\Gamma_5$ ,  $\Gamma_2$ ,  $\Gamma_1$  symmetry for an exciton involving a hole from a  $\Gamma_7$  valence

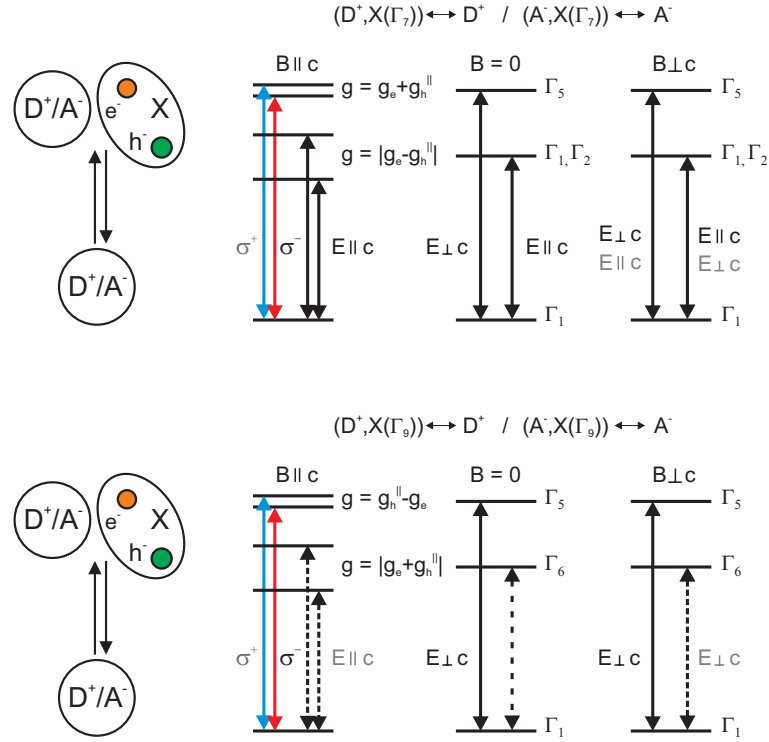


Figure 4.6: Exciton level scheme of ionized bound excitons in zero and constant magnetic field for hole states with  $\Gamma_7$  and  $\Gamma_9$  symmetry. Dash transitions are forbidden at 0 T but become allowed by admixture of oscillator strength (gray polarization).

band and  $\Gamma_5$  and  $\Gamma_6$  symmetry for a  $\Gamma_9$  valence state. In the absence of a magnetic field, only the  $\Gamma_5$  to  $\Gamma_1$  transitions are allowed in the  $\mathbf{E} \perp \mathbf{c}$  configuration. While the  $\Gamma_5$  exciton corresponds to a state with mainly antiparallel electron and hole spins, the  $\Gamma_1$  and  $\Gamma_2$  exciton states are constructed from products of the same band states but with the electron states interchanged. The dominant components of these states have parallel electron and hole spins. They are Kramers degenerate if the interaction with the crystal-field and spin-orbit split bands are neglected. From the level scheme in Fig. 4.6 it is apparent that the energies of the  $\Gamma_{1,2}$  and  $\Gamma_6$  states are smaller than the energy of the  $\Gamma_5$  exciton [69]. The splitting between these levels is caused by the spin-spin exchange interaction whereby the energy spacing is given by the zero field exchange energy [122]. An additional exchange splitting between the  $\Gamma_1$  and  $\Gamma_2$  exciton states is known to be small [100], thus only the degenerate  $\Gamma_{1,2}$  level is displayed in Fig. 4.6. In the  $\mathbf{E} \parallel \mathbf{c}$  polarization, the  $\Gamma_1$  exciton is dipole allowed for  $\mathbf{E} \parallel \mathbf{c}$  but has only small oscillator strength since a spin-flip process is involved in the transition. The  $\Gamma_2$  and  $\Gamma_6$  excitons also involve a spin-flip but are dipole forbidden resulting in a very weak oscillator strength.

In an external magnetic field  $\mathbf{B} \perp \mathbf{c}$ , the low energy transitions of the  $\Gamma_{1,2}$  and  $\Gamma_6$

exciton states become allowed due to the admixture of the  $\Gamma_5$  state by the magnetic field (Fig. 4.6). In general, two states  $\Gamma_i$  and  $\Gamma_j$  mix in a magnetic field with eigenstate  $\Gamma_B$  if the group representation of the one state  $\Gamma_i$  is contained in the Kronecker product of the other state  $\Gamma_j$  with  $\Gamma_B$  [114]:

$$\Gamma_i \text{ and } \Gamma_j \text{ mix} \iff \Gamma_i \in \Gamma_B \otimes \Gamma_j. \quad (4.16)$$

From this relation, the admixture of oscillator strength to the weak or forbidden  $\Gamma_1$ ,  $\Gamma_2$ , and  $\Gamma_6$  exciton states by magnetic fields  $\mathbf{B} \perp \mathbf{c}$  ( $\Gamma_5$ ) and  $\mathbf{B} \parallel \mathbf{c}$  ( $\Gamma_2$ ) can be determined using Table 4.1:

$$\mathbf{B} \perp \mathbf{c}: \Gamma_1 \otimes \Gamma_5 = \Gamma_5 \iff \Gamma_1 \text{ and } \Gamma_5 \text{ mix}, \quad (4.17)$$

$$\Gamma_2 \otimes \Gamma_5 = \Gamma_5 \iff \Gamma_2 \text{ and } \Gamma_5 \text{ mix}, \quad (4.18)$$

$$\Gamma_6 \otimes \Gamma_5 = \Gamma_3 + \Gamma_4 + \Gamma_5 \iff \Gamma_6 \text{ and } \Gamma_5 \text{ mix}, \quad (4.19)$$

$$\mathbf{B} \parallel \mathbf{c}: \Gamma_1 \otimes \Gamma_2 = \Gamma_2 \iff \Gamma_1 \text{ and } \Gamma_2 \text{ mix}, \quad (4.20)$$

$$\Gamma_2 \otimes \Gamma_2 = \Gamma_1 \iff \Gamma_2 \text{ and } \Gamma_1 \text{ mix}, \quad (4.21)$$

$$\Gamma_6 \otimes \Gamma_2 = \Gamma_6 \iff \Gamma_6 \text{ no admixture}. \quad (4.22)$$

$$(4.23)$$

In the case of a valence band with  $\Gamma_7$  symmetry, the presence of a magnetic field in the  $\mathbf{B} \perp \mathbf{c}$  orientation therefore mixes the exchange split  $\Gamma_5$  exciton states (allowed for  $\mathbf{E} \perp \mathbf{c}$ ) with the  $\Gamma_{1,2}$  states (weakly allowed for  $\mathbf{E} \parallel \mathbf{c}$ ). The resulting states become allowed for both polarization. The upper states have dominating  $\Gamma_5$  character with stronger  $\mathbf{E} \perp \mathbf{c}$  polarization but become allowed for  $\mathbf{E} \parallel \mathbf{c}$  with increasing magnetic field, too. The lower states have pronounced  $\Gamma_{1,2}$  symmetry and are stronger in  $\mathbf{E} \parallel \mathbf{c}$ , but become allowed for  $\mathbf{E} \perp \mathbf{c}$  with increasing magnetic field. In the case of a  $\Gamma_9$  valence band, the admixture of oscillator strength occurs between the  $\Gamma_5$  and  $\Gamma_6$  levels. In the first order,  $\Gamma_6$  is forbidden in zero field for any polarization. With increasing magnetic field the lower state gets admixture of  $\Gamma_5$  to  $\Gamma_6$  and becomes allowed in  $\mathbf{E} \perp \mathbf{c}$ . The additionally allowed polarizations due to the admixture of other states are indicated in Fig. 4.6 in gray.

The splittings between the different states in the Voigt configuration ( $\mathbf{B} \perp \mathbf{c}$ ) are mainly governed by the zero-field exchange energies. These exchange energies are labeled  $\Delta_{15}$ ,  $\Delta_{12}$ , and  $\Delta_{56}$  for the energy splittings between the respective exciton states considering  $\Gamma_7$  and  $\Gamma_9$  valence band symmetry. Since the splitting  $\Delta_{12}$  in ZnO is small, it is usually neglected [100, 103]. In addition to the splitting between these states, a small spectral shift occurs as function of the magnetic field strength which shifts the high energy  $\Gamma_5/\Gamma_{1,2}$  (or  $\Gamma_5/\Gamma_6$ ) transition to higher energies and the low energy  $\Gamma_{1,2}/\Gamma_5$  (or  $\Gamma_6/\Gamma_5$ ) transition to lower energies as the magnetic field strength

increases. The energies of these exciton states in the  $\mathbf{B} \perp \mathbf{c}$  configuration are given by:

$$E_{\Gamma_5/\Gamma_1}^\pm = E_{\Gamma_1} + \frac{\Delta_{15}}{2} \pm \frac{1}{2} \sqrt{\Delta_{15}^2 + (g_e^\perp + g_h^\perp)^2 (\mu_B B)^2}, \quad (4.24)$$

$$E_{\Gamma_5/\Gamma_2}^\pm = E_{\Gamma_2} + \frac{\Delta_{25}}{2} \pm \frac{1}{2} \sqrt{\Delta_{25}^2 + (g_e^\perp - g_h^\perp)^2 (\mu_B B)^2}, \quad (4.25)$$

$$E_{\Gamma_5/\Gamma_6}^\pm = E_{\Gamma_6} + \frac{\Delta_{56}}{2} \pm \frac{1}{2} \sqrt{\Delta_{56}^2 + (g_e^\perp)^2 (\mu_B B)^2}. \quad (4.26)$$

where  $\Delta_{25} = \Delta_{12} + \Delta_{15} \approx \Delta_{15}$ .

For a parallel magnetic field in the Faraday configuration ( $\mathbf{B} \parallel \mathbf{c}$ ), the energies of the Zeeman components of the  $\Gamma_{1,2}$  exciton and the  $\Gamma_5$  exciton involving  $\Gamma_7$  hole states ( $\Gamma_7^c \Leftrightarrow \Gamma_7^v$  transition) are determined by

$$E_{\Gamma_{1,2}}^\pm = E_{\Gamma_2} + \frac{\Delta_{12}}{2} \pm \frac{1}{2} \sqrt{\Delta_{12}^2 + (g_e^\parallel - g_h^\parallel)^2 (\mu_B B)^2}, \quad (4.27)$$

$$E_{\Gamma_5}^\pm = E_{\Gamma_5} \pm \frac{1}{2} \mu_B (g_e + g_h^\parallel) B, \quad (4.28)$$

whereas in the case of a  $\Gamma_7^c \Leftrightarrow \Gamma_9^v$  transition, the energies of the Zeeman components of the  $\Gamma_5$  and  $\Gamma_6$  exciton states in a magnetic field  $\mathbf{B} \parallel \mathbf{c}$  are given by

$$E_{\Gamma_6}^\pm = E_{\Gamma_6} \pm \frac{1}{2} \mu_B (g_h^\parallel + g_e^\parallel) B \quad (4.29)$$

$$E_{\Gamma_5}^\pm = E_{\Gamma_5} \pm \frac{1}{2} \mu_B (g_h^\parallel - g_e^\parallel) B. \quad (4.30)$$

For arbitrary angles  $\theta$  between the magnetic field vector  $\mathbf{B}$  and the direction of the  $\mathbf{c}$ -axis, the equations are more complicated. In the case of hole states with  $\Gamma_9$  symmetry, the energy of the four Zeeman components can be derived by

$$E_{\Gamma_5}^\pm = E_{\Gamma_6} + \frac{\Delta_{56}}{2} \pm \frac{1}{2} \mu_B B g_h^\parallel \cos\Theta + \frac{1}{2} \sqrt{(\Delta_{56} \mp \mu_B B g_e^\parallel \cos\Theta)^2 + (g_e^\perp)^2 (\mu_B B \sin\Theta)^2} \quad (4.31)$$

$$E_{\Gamma_6}^\pm = E_{\Gamma_6} + \frac{\Delta_{56}}{2} \pm \frac{1}{2} \mu_B B g_h^\parallel \cos\Theta - \frac{1}{2} \sqrt{(\Delta_{56} \mp \mu_B B g_e^\parallel \cos\Theta)^2 + (g_e^\perp)^2 (\mu_B B \sin\Theta)^2} \quad (4.32)$$

These formulas can be simplified if one neglects the small anisotropy of the electron  $g$ -factor with  $g_e^\parallel = g_e^\perp = g_e$ . In the case of hole states with  $\Gamma_7$  symmetry, additional simplifications have to be made in order to obtain manageable analytical expressions. For negligible values of the zero field exchange energy between the  $\Gamma_1$  and  $\Gamma_2$  states ( $\Delta_{12} \approx 0$ ) and the perpendicular hole  $g$ -factor ( $g_h^\perp \approx 0$ ), the equations look similar

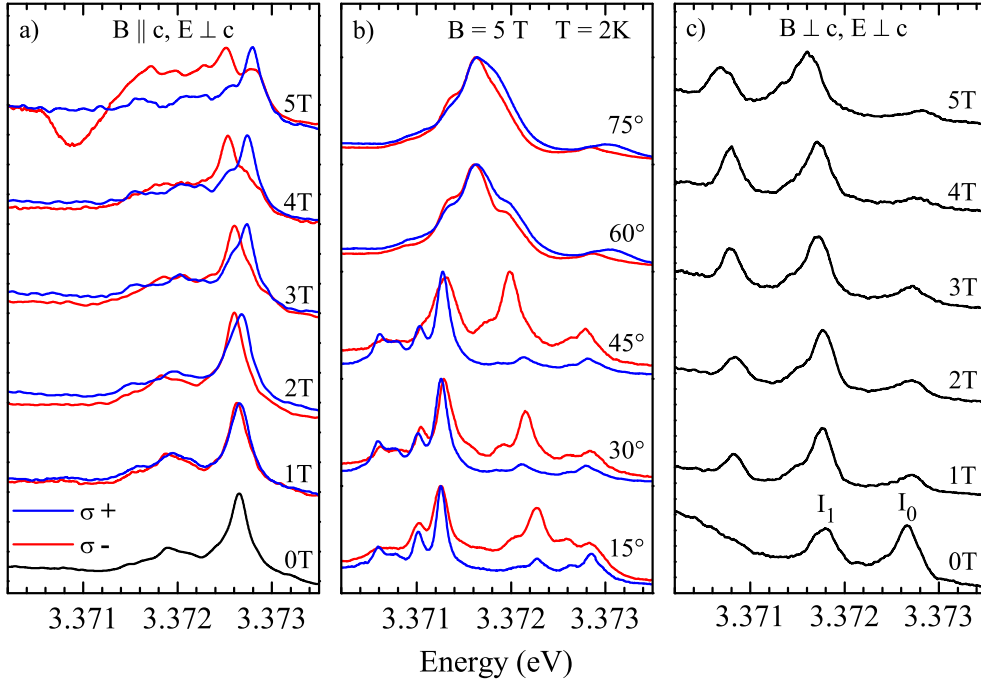


Figure 4.7: Magneto-PL spectra of the ionized bound exciton  $I_0$  and  $I_1$  at 2 K. (a) Faraday configuration, (b) arbitrary angles  $\theta$  at  $B = 5$  T, (c) Voigt configuration.

to those for  $\Gamma_9$  hole states (note the reversed ordering of  $\pm$  and  $\mp$ ):

$$E_{\Gamma_5}^{\pm} = E_{\Gamma_{1,2}} + \frac{\Delta_{15}}{2} \pm \frac{1}{2}\mu_B B g_h^{\parallel} \cos\Theta + \frac{1}{2}\sqrt{(\Delta_{15} \pm \mu_B B g_e^{\parallel} \cos\Theta)^2 + (g_e^{\perp})^2 (\mu_B B \sin\Theta)^2} \quad (4.33)$$

$$E_{\Gamma_{1,2}}^{\pm} = E_{\Gamma_1} + \frac{\Delta_{15}}{2} \pm \frac{1}{2}\mu_B B g_h^{\parallel} \cos\Theta - \frac{1}{2}\sqrt{(\Delta_{15} \pm \mu_B B g_e^{\parallel} \cos\Theta)^2 + (g_e^{\perp})^2 (\mu_B B \sin\Theta)^2}. \quad (4.34)$$

These equations can now be used to determine the electron and hole  $g$ -factors of free and ionized bound excitons.

Fig. 4.7 displays the magneto-PL spectra of the bound excitons  $I_0$  and  $I_1$  in the Faraday configuration (a), for arbitrary angles  $\theta$  between the direction of the magnetic field  $\mathbf{B}$  and the crystal  $\mathbf{c}$ -axis (b), and in the Voigt configuration (c). With increasing magnetic field strength  $\mathbf{B} \perp \mathbf{c}$ , the appearance of new emission lines at the low energy side of  $I_0$  and  $I_1$  is observed (Fig. 4.7c). In the case of the  $I_0$  exciton, the new line overlaps with the zero-field transition line of the  $I_1$  which results in an increased intensity of this peak. In addition, the intensity of the zero field  $I_0$  exciton ( $\Gamma_5$ ) is reduced. For the  $I_1$  the appearance of a new transition in the perpendicular magnetic field is clearly observed as the low energy transition does not coincide with another bound exciton line. With increasing magnetic field the

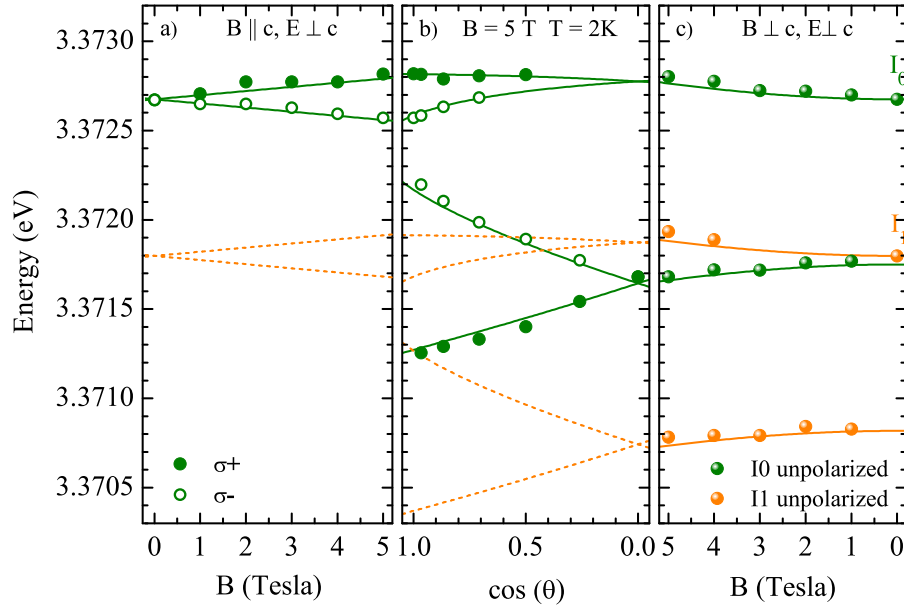


Figure 4.8: Zeeman splitting of the ionized bound exciton  $I_0$  and  $I_1$  at 2 K. (a) Faraday configuration, (b) arbitrary angles  $\theta$  at  $B = 5$  T, (c) Voigt configuration. Filled and open circles represent  $\sigma^+$  and  $\sigma^-$  polarized transitions, respectively. The transitions in the Voigt configuration are unpolarized. Solid and dashed lines are fits and predictions to the experimental data.

intensity of the low energy emission lines increases. Based on the previous discussion the newly occurring lines in a perpendicular magnetic field can be attributed to  $\Gamma_{1,2}$  exciton states which are separated from the  $\Gamma_5$  state by the zero-field exchange energy. The increasing intensity of the low energy  $\Gamma_{1,2}$  transitions of  $I_0$  and  $I_1$  is associated with the larger admixture of the dipole allowed  $\Gamma_5$  transition to the  $\Gamma_{1,2}$  state for increasing magnetic field strength. The appearance of a weak or forbidden transition at the low energy side of an exciton line (nonlinear zero field splitting) in the  $\mathbf{B} \perp \mathbf{c}$  configuration clearly differentiates the free and ionized bound excitons from the neutral bound excitons [111, 123]. Such an exchange interaction cannot occur in transition lines originating from excitons bound to neutral impurities, for the spins of the two like particles are antiparallel. Consequently, both exciton lines  $I_0$  and  $I_1$  have to originate from ionized bound excitons.

In the  $\mathbf{B} \parallel \mathbf{c}$  configuration, a linear splitting as function of the magnetic field strengths is observed between the high energy  $\sigma^+$  polarized Zeeman component and the low energy  $\sigma^-$  component of the  $I_0$  bound exciton line (Fig. 4.7). Although the same splitting occurs for the  $I_1$  transition, it is not well resolved in this geometry. The difference in the luminescence spectra might be caused by an inhomogeneous impurity distribution in the investigated epilayer leading to a weaker intensity of the

$I_1$  transition in the Faraday measurements than in the Voigt spectra. According to the model in Fig. 4.6, a parallel magnetic field splits each of the  $\Gamma_5$  and  $\Gamma_{1,2}$  states of free and ionized bound excitons into two levels. The energy splitting of these levels is determined by the combined electron g-factor and parallel hole g-factor. For excitons involving hole states with  $\Gamma_7$  symmetry, the total g-factors is given by  $g = g_h^{\parallel} + g_e$  ( $\Gamma_5$  state) and  $g = |g_e - g_h^{\parallel}|$  ( $\Gamma_{1,2}$  state). In the case of an exciton with a hole from the  $\Gamma_9$  valence band, the g-factor is determined by  $g = g_h^{\parallel} - g_e$  ( $\Gamma_5$  state) and  $g = |g_e + g_h^{\parallel}|$  ( $\Gamma_6$  state). In both cases, the high energy state of the  $\Gamma_5$  exciton is  $\sigma^+$  polarized and the low energy one is  $\sigma^-$  polarized. By contrast, the optical transitions of the two  $\Gamma_{1,2}$  or  $\Gamma_6$  exciton states are allowed for  $\mathbf{E} \parallel \mathbf{c}$  polarization.

In order to determine the electron and hole g-factors and the zero-field exchange energy, the transition lines in Fig. 4.7 are fitted by Gaussian peaks. The peak energies derived from these fits are plotted in Fig. 4.8, whereby filled and open circles represent  $\sigma^+$  and  $\sigma^-$  polarized transitions, respectively. The solid lines are fits to the experimental data points using the previously discussed equations Eq. 4.24 to Eq. 4.34 for the different orientations of the magnetic field with respect to the  $c$ -axis. Apparently, an excellent agreement with the experimental data is achieved. The dashed lines in the case of the  $I_1$  mark theoretical predictions for the peak energies in the Faraday configuration and for the angular dependence. The derived  $g$ -factors are listed in Table 4.2. From the extrapolation of  $\Gamma_{1,2}$  peak positions in the  $\mathbf{B} \perp \mathbf{c}$  configuration to  $B = 0$  T, the zero-field exchange energy can be determined to 0.92 meV for the  $I_0$  and 0.96 meV for the  $I_1$ . These values are in good agreement with the exchange energy derived for the ionized bound exciton  $I_{2/3}$  of 0.98 meV [103] (Table 4.2). As a marginal note, it should be minded that the labeling  $I_{2/3}$  in the original work of Reynolds et al. [69] is misleading and should be substituted by just  $I_2$ . The term  $I_{2/3}$  was originally introduced due to the appearance of a new low energy transition line (labeled  $I_3$ ) in a perpendicular magnetic field. However, as was correctly pointed out by Rodina et al. [103], the appearance of this zero-field forbidden transition reflects the spin-spin exchange interaction between  $\Gamma_5$  and  $\Gamma_{1/2}$  states which results in an admixture of oscillator strength to the forbidden  $\Gamma_{1/2}$  transitions. Consequently, the low energy component of  $I_2$  should not be labeled  $I_3$  as it is an inherent feature to every ionized bound exciton.

## 4.5 Summary

In this chapter, the effects of magnetic fields on free and bound excitons were discussed with particular focus on the Zeeman splitting of neutral and ionized bound excitons. Group theoretical concepts were introduced which are of great use to determine the splitting and mixing of exciton states in magnetic fields. The different

splitting mechanisms were explained in order to distinguish between ionized and neutral as well as donor and acceptor bound excitons in ZnO. The neutral charge state of the bound exciton lines  $I_5$ ,  $I_6$ ,  $I_{6a}$ ,  $I_8$  and of the transitions  $X_1$ ,  $X_2$ ,  $X_3$ ,  $X_4$  was proven by comprehensive magneto-PL measurements. Based on the thermalization of their Zeeman components in external magnetic fields, all of these transitions could be identified as donor bound exciton related. In addition, the high energy bound exciton transitions  $I_0$  and  $I_1$  were investigated. A non-linear zero-field exchange splitting in the Voigt configuration was observed, thus doubtlessly identifying these transitions as recombinations of ionized donor bound excitons. The energy splittings for exciton states in magnetic fields with arbitrary directions to the crystal  $c$ -axis were theoretically described considering the selection rules and possible symmetry states as derived by group theory. Based on this description, the electron and anisotropic hole  $g$ -factors for all bound excitons as well as the zero-field exchange energy for the ionized bound excitons were quantitatively determined.

## 5 The band structure of ZnO

This chapter deals with the electronic band structure of ZnO with particular emphasis on the symmetries of the valence bands and their energetic ordering. The band structure is presented based on experimental data and first principle calculations (chapter 5.1). The discussion subsequently focuses on the valence band ordering in ZnO which has been debated for almost half a century. The basic phenomena that lead to the valence band splitting and symmetry ordering are explained in chapter 5.2. The most important contributions along this controversial dispute are briefly reviewed (section 5.2.1). In particular, this includes the influence of the Zn ( $3d$ ) bands on the crystal-field, spin-orbit, and valence band splittings. Following this overview, high resolution magneto-optical luminescence measurements of neutral donor bound excitons are presented which – in combination with theoretical considerations – allow to resolve the long lasting disagreement about the symmetry ordering of the valence bands (section 5.2.2). In addition to the existing arguments in the literature, a newly observed hole fine splitting in combination with polarization and angular resolved measurements provides conclusive evidence for the  $\Gamma_7$  symmetry of the A valence band (sections 5.2.3 and 5.2.4). Possible arguments objecting to this attribution are extensively discussed and confuted (section 5.2.5).

A detailed discussion about the properties of the within this chapter studied bound excitons and their excited states is conducted in chapter 3. The fundamental effects of magnetic fields on the free and bound excitons states are explained in chapter 4. The magneto-PL measurements were performed as described in the experimental part in chapter 2.

### 5.1 The band structure

The optical properties of semiconductors such as the allowed and forbidden optical transitions, their energies, oscillator strengths, and polarization patterns are greatly influenced by the electronic band structure. Consequently, a precise model for the band structure is crucial. A variety of theoretical approaches were employed to compute the energy and dispersion of the electronic bands in ZnO [100, 124–128]. Laskowski et al. [126] published ab initio calculations solving the Bethe-Salpeter equation within the framework of the density functional theory (DFT) where the

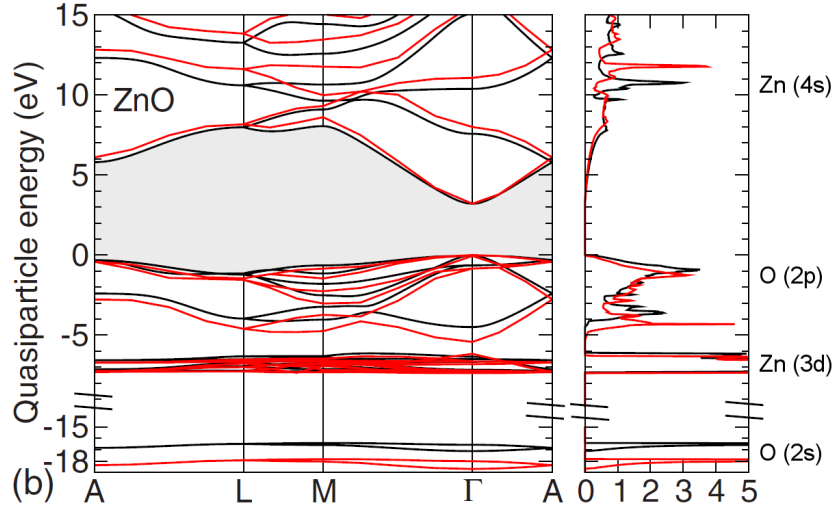


Figure 5.1: Quasiparticle band structures (left) and densities of states (right) of ZnO calculated within the GGA+U+ $\Delta$  approach (black lines) and the HSE03+GW approach (red lines). The valence band maximum is set to zero energy, the fundamental gap region is shaded gray. Taken from [132].

band gap energy between the lowest conduction band and the highest valence band at the  $\Gamma$ -point was corrected by means of a scissors operator. In order to correct for the overestimated energy position [129] and wrong spectral position of the density of states [100] of the Zn  $3d$  bands, the LDA+U [130, 131] method was applied which greatly improved the calculated optical spectra. In addition, the binding energies of the A, B, and C free excitons were derived with values of 67-68 meV in good agreement with experimental values (chapter 3.3).

Recently, Schleife et al. [132] reported ZnO band structure calculations by projecting the quasiparticle (QP) scheme onto the results of the generalized gradient approximation including Coulomb repulsion (GGA+U) [130, 133]. Thereto, the QP band structures and density of states were first calculated by the HSE03+GW [134] approach. The quasiparticle energies are then calculated by shifting the GGA+U eigenvalues of the conduction bands by a scissors operator. The band structure and the density of states derived from these calculations are displayed in Fig. 5.1.

From an experimental point of view, the electronic band structure can be measured by angular resolved photoemission spectroscopy (ARPES), x-ray absorption and emission spectroscopy (XAS and XES), and resonant inelastic x-ray scattering (RIXS). However, the determination of quantitative values such as the energetic position of the Zn ( $3d$ ) bands is not easy due to the usually limited energy resolution and overlapping of bands which leads to a half width of the spectral features of more than 200-300 meV. Nevertheless, these measurements can promote the improvement

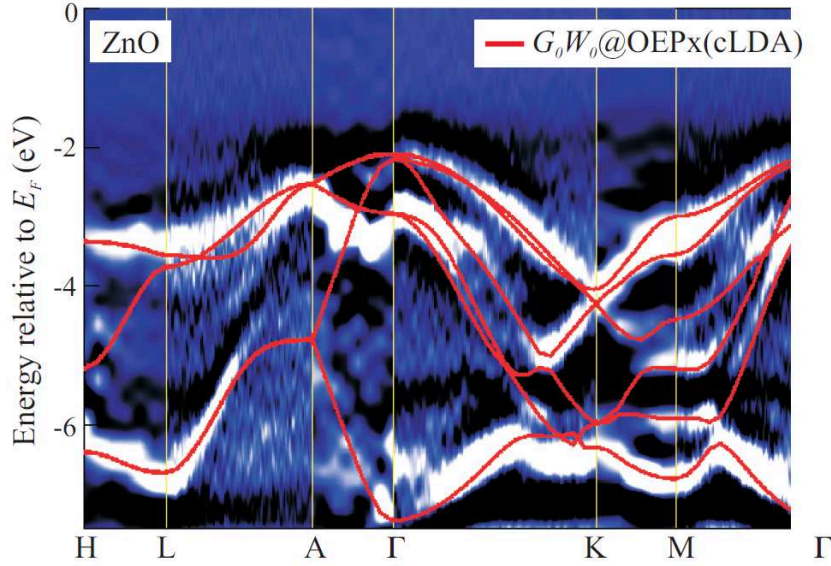


Figure 5.2: Angular resolved photoemission spectroscopy (ARPES) data [135] for the upper valence bands of ZnO superimposed with theoretical band structure calculations. Taken from [136].

of theoretical calculations and contribute to a more precise description of the electronic band structure. For ZnO, a few studies were recently published applying the ARPES [135, 137, 138], XAS and XES [139–141], and RIXS [142] techniques.

Figure 5.2 displays the angular-resolved photoemission spectroscopy (ARPES) data for the upper valence bands of ZnO based on the work of Kobayashi et al. [135]. The experimental graphs are superimposed by state-of-the-art band structure calculations by Yan et al. [136]. A very good agreement between experimental ARPES data and theoretical calculations was achieved for both the band energies as well as band curvatures. However, the experimental data also demonstrates that experimentally determined band structures are not yet accurate enough to derive band parameters such as effective masses or crystal-field splittings without first-principles calculations.

## 5.2 The valence band ordering

The crystal symmetry of hexagonal ZnO in the wurtzite structure is described by the point group  $C_{6v}$  (space group  $C_{6v}^4$ ) with the  $c$ -axis being the principal axis. The conduction band is formed from the  $4s$  electrons of Zn having  $s$ -like character, while the upper valence bands have  $p$ -like character and are generated by the  $2p$  electrons of the oxygen atoms (Fig. 5.1). The valence band at the  $\Gamma$ -point is split due to the crystal field  $\Delta_{cf}$  and spin-orbit interaction  $\Delta_{so}$  into three doubly degenerated

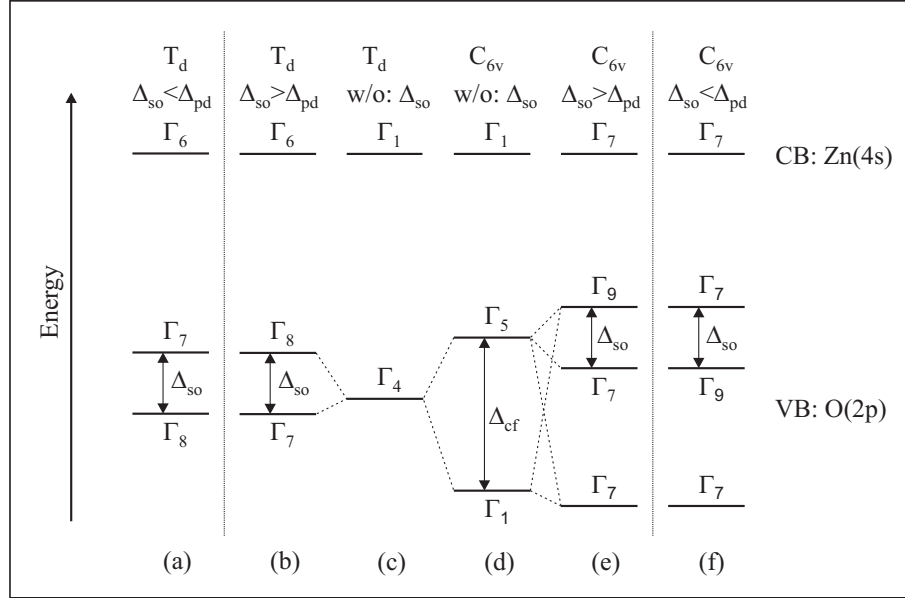


Figure 5.3: Energy level scheme of the valence band splitting in ZnO considering the effects of crystal-field splitting and spin-orbit coupling. (a) spin-orbit coupling without crystal field (zinc-blende structure) and strong  $p-d$  repulsion, (b) same as (a) but weak  $p-d$  repulsion, (c) without crystal field and spin-orbit coupling, (d) only crystal field splitting (wurtzite), (e) crystal field splitting and spin orbit coupling with weak  $p-d$  repulsion (common ordering), (f) same as (e) but strong  $p-d$  repulsion (inverted valence band ordering). According to [34, 35, 126, 143, 144].

sub-bands, which are labeled  $A$ ,  $B$ , and  $C$  from the highest to the lowest band. Without these interactions (e.g. in a cubic zinc-blende structure neglecting spin-orbit coupling), the symmetry at the center of the Brillouin zone for the conduction band is  $\Gamma_1$  and for the valence band is  $\Gamma_4$  (Fig. 5.3c). The crystal field in wurtzite ZnO leads to a discrimination of the  $p_z$ -like states from the  $p_x/p_y$ -like ones resulting in a splitting of the  $\Gamma_4$  state into an upper  $\Gamma_5$  ( $p_x, p_y$ ) doublet and a lower  $\Gamma_1$  ( $p_z$ ) singlet state (Fig. 5.3d).

The inclusion of the spin-orbit coupling in group theory is achieved by calculating the Kronecker product of the spatial wave function times a spin function which transforms as  $D_{1/2}$ . If more than one representation of the double group occurs in the decomposition of the direct product, a spin-orbit splitting of the level is indicated. Without a crystal field this results in

$$\Gamma_1 \otimes D_{1/2} = \Gamma_6, \quad (5.1)$$

$$\Gamma_4 \otimes D_{1/2} = \Gamma_7 + \Gamma_8 \quad (5.2)$$

for the conduction band and the valence band, respectively (see Fig. 5.3b) [145]. That means that for the valence band, the spin-orbit coupling leads to a splitting into

a twofold degenerate  $\Gamma_7$  state ( $J = 1/2$ ) and a fourfold degenerate  $\Gamma_8$  state ( $J = 3/2$ ). Usually, the energy of the  $\Gamma_7$  state is lower than the one of the  $\Gamma_8$  level (Fig. 5.3b) in zinc-blende semiconductors. However, the contribution of shallow Zn ( $3d$ ) levels in ZnO might reverse this ordering (Fig. 5.3a). Uniaxial stress measurements could be used to identify the ordering of the valence bands since the  $\Gamma_8$  band would split into a heavy hole and a light hole band as found e.g. in ZnSe and ZnTe. Unfortunately, cubic ZnO is not stabilized by bulk growth techniques.

Considering the spin-orbit coupling  $\Delta_{so}$  for the wurtzite configuration with a crystal field splitting  $\Delta_{cf} \gg \Delta_{so}$ , the following symmetries are deduced:

$$\Gamma_1 \otimes D_{1/2} = \Gamma_7, \quad (5.3)$$

$$\Gamma_5 \otimes D_{1/2} = \Gamma_7 + \Gamma_9. \quad (5.4)$$

Consequently, an additional splitting of the  $\Gamma_5$  state into a  $\Gamma_7$  state and a  $\Gamma_9$  state occurs (Fig. 5.3e,f). Fig. 5.3e shows the regular energy level ordering while Fig. 5.3f displays the inversed ordering due to the influence of Zn ( $3d$ ) levels. From a comparison with other II<sup>b</sup> – VI semiconductors it can be concluded that the value of  $\Delta_{so}$  mainly depends on the nuclear charge of the anion with  $\Delta_{so} = Z^{2.2}$  [18] which results in a spin orbit splitting of  $\Delta_{so} = 17$  meV. However, this value does not represent the splitting between the A and B valence band of about 5 meV as the influence of the  $3d$  levels is neglected. In a crystal field including the effects of spin-orbit coupling, the  $3d$  band splits into an upper  $\Gamma_7$  band and lower energy  $\Gamma_8$  and  $\Gamma_9$  bands. Since ZnO has the smallest energy distance between the  $3d$  and upper  $p$  bands in all Zn-VI materials [28], a particularly strong  $p - d$  repulsion occurs. Depending on strength of the interaction, the level repulsion between the highest  $\Gamma_7$   $d$  band and the upper  $\Gamma_7$   $p$  band can lead to a shift  $\Delta_{pd}$  of the upper  $\Gamma_7$  valence band below (Fig. 5.3e) or above (Fig. 5.3f) the energy of the  $\Gamma_9$  valence band. This ordering and thus the size of the effective spin-orbit coupling including  $p - d$  interaction is basically the quintessence of the almost 50 years enduring controversy.

### 5.2.1 The controversy about the valence band ordering in ZnO

The symmetry ordering of the valence bands in wurtzite ZnO has been subject to extensive discussions [34, 37, 39, 69, 100, 103, 146, 147] since the first investigations of the valence-band maximum fine structure by Thomas and Hopfield in 1960 [34, 35]. Numerous reports have emerged over the past 50 years postulating either  $\Gamma_7$  symmetry [34, 35, 38, 39, 74, 81, 100, 102, 103, 109, 115, 117, 118, 126, 146, 148–151] or  $\Gamma_9$  symmetry [37, 69, 75, 147, 152–156] for the uppermost A valence band. Based on polarization dependent reflection and absorption spectra, Thomas and Hopfield came to the conclusion that the symmetry of the A, B, and C valence bands is  $\Gamma_7$ ,  $\Gamma_9$ ,  $\Gamma_7$  rather than  $\Gamma_9$ ,  $\Gamma_7$ ,  $\Gamma_7$  and therefore anomalous compared to the usual ordering

in other wurtzite II-VI materials like ZnSe and CdS [34, 35]. This assignment was supported by Liang and Yoffe who reported an effective negative spin-orbit coupling based on polarized transmission spectroscopy [39]. In contradiction to these works, reflectivity and Zeeman measurements were published by Reynolds and Park rejecting the inversed valence band ordering and claiming  $\Gamma_9$  symmetry for the upper valence band [37, 69, 152]. In the following three decades between 1969 and 1999, most authors adopted the originally proposed inverse valence band ordering. Additional support for the  $\Gamma_7$  symmetry of the highest valence band was provided by Hümmer et al. [146] who observed a  $k$ -linear energy term in the Zeeman splitting of the A exciton emission, which should only occur for a  $\Gamma_7$  valence band.

In 1999, Reynolds et al. [147] revived the discussion by a study of reflection and magneto-photoluminescence measurements which led to the conclusion of  $\Gamma_9$  symmetry for the A valence band. In the following years this claim was supported by works of Gil et al. [153], Chichibu et al. [75, 154], and Adachi et al. [155, 156]. By contrast, Rodina et al. published evidence for  $\Gamma_7$  symmetry of the highest valence band based on the magneto-optical properties of bound excitons [103]. Theoretical calculations by Lambrecht et al. [100] and Laskowski et al. [126] within the framework of the local density approximation (LDA) [157] supported the original ordering proposed by Thomas and Hopfield. Lambrecht explained the reversed order of the top valence bands by an effective negative spin-orbit coupling which originates from the contribution of Zn ( $3d$ ) bands [100]. Such an effective negative splitting was first discussed in copper and silver halides by Cardona [158] and explained by the  $p-d$  interaction with  $d$ -bands by Shindo et al. [159].

Fig. 5.4 displays the crystal field splitting  $\Delta_{cf}$ , spin orbit splitting  $\Delta_{so}$ , and the valence band splittings  $E_A - E_B$  and  $E_B - E_C$  as function of the energy position of the Zn ( $3d$ ) bands according to the calculations of Lambrecht et al [100]. The horizontal green lines represent the A-B and B-C band splittings as derived from experiments [40]. These values coincide with the theoretical values for  $d$ -band positions of -6.6 eV in the case of the A-B splitting and -6.0 eV in the case of the B-C splitting as indicated by the vertical lines. Within this energy range of the Zn ( $3d$ ) bands, the spin-orbit coupling  $\Delta_{so}$  is found to be negative for all values of the  $3d$  bands as indicated by the shaded area. Only for a  $3d$  band position below -6.9 eV, a positive spin-orbit coupling is derived. Consequently, these theoretical calculations support  $\Gamma_7$  symmetry for the A valence band. Furthermore, previous experimental results by Reynolds et al. [147] assuming  $\Gamma_9$  symmetry could also be theoretically explained with  $\Gamma_7$  symmetry [100]. Nevertheless, a variety of new publications has emerged in recent years which assert  $\Gamma_9$  symmetry for the top valence band [154–156] or avoid a clear statement concerning the valence band ordering [160–163]. The still existing controversy about the ordering of the valence bands in ZnO provides a

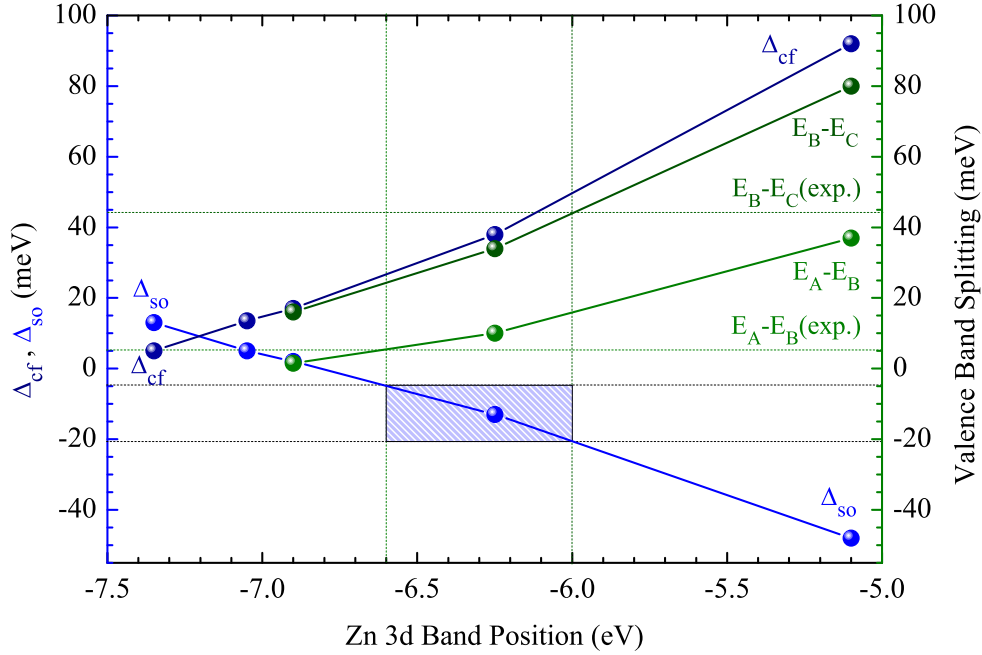


Figure 5.4: Crystal field splitting  $\Delta_{cf}$ , spin-orbit splitting  $\Delta_{so}$ , and valence band splittings  $E_A - E_B$ ,  $E_B - E_C$  as function of the energy of the Zn (3d) band at the  $\Gamma$  point. According to [100].

strong motivation to reinvestigate and resolve this issue. In the following sections, comprehensive magneto-optical measurements on bound excitons are presented and discussed which provide new and conclusive evidence for the originally proposed valence band ordering by Thomas and Hopfield with the A valence band having  $\Gamma_7$  symmetry in ZnO.

### 5.2.2 Symmetry states of bound excitons in magnetic fields

Fig. 5.5 displays the energy level scheme of donor bound excitons involving hole states from the  $\Gamma_7$  (Fig. 5.5a) and  $\Gamma_9$  (Fig. 5.5b) valence bands under the influence of an external magnetic field. The excited state in this level scheme is represented by an exciton bound to a neutral donor ( $D^0, X$ ), whereas the ground state is characterized by the donor level without the exciton ( $D^0$ ). In the case of a constant magnetic field, the Zeeman splitting of the ground state does not change as function of the orientation of the magnetic field  $\mathbf{B}$  relative to the  $\mathbf{c}$ -axis as determined by the (in first approximation) isotropic electron g-value  $g_e$ . In contrast, the hole g-value  $g_h$  – which determines the size of the Zeeman splitting in the excited state of a donor bound exciton complex – is anisotropic due to the discrimination of the expectation values of the orbital angular momenta for the  $p_x / p_y$  and  $p_z$  like states. For acceptor bound

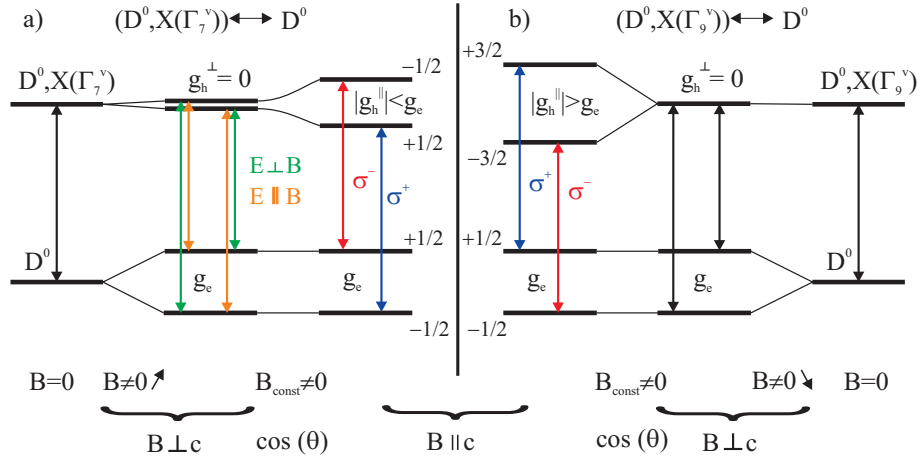


Figure 5.5: Level scheme and splitting of donor bound exciton states under the influence of external magnetic fields. Holes originating from valence bands with different symmetry representations lead to variations in the hole g-values as expressed by the size of the Zeeman splitting [104].

excitons, the ground states and excited states in Fig. 5.5 have to be reversed [103].

As a first step, the influence of the valence band symmetry on the Zeeman splitting of bound excitons needs to be considered. In the Voigt configuration ( $\mathbf{B} \perp \mathbf{c}$ ) the hole g-value is zero ( $g_h^\perp = 0$ ) in case of an exciton involving a  $\Gamma_9$  hole state and small but non-zero for a hole originating from a  $\Gamma_7$  valence band. Consequently, the magnetic field does not only lift the degeneracy of the ground state of the donor bound exciton complex in the case of  $\Gamma_7$  symmetry, but also results in a small splitting of the excited state (Fig. 5.5a). The additional splitting of the excited state engenders a fourfold splitting of the bound exciton recombination line due to the non-zero g-values of electron and hole in  $\mathbf{B} \perp \mathbf{c}$ . This is not the case if the exciton hole corresponds to a state with  $\Gamma_9$  symmetry (Fig. 5.5b) since no splitting of the excited state exists ( $g_h^\perp = 0$ ). Therefore, only a twofold splitting determined by the electron g-value  $g_e$  occurs.

In order to determine the symmetry of the hole states involved in the bound exciton complexes in ZnO, the photoluminescence is studied under the influence of an external magnetic field. Fig. 5.6 shows the magneto-PL spectra of the dominant lines  $I_{6a}$ ,  $I_7$ , and  $I_8$  in Faraday configuration ( $\mathbf{B} \parallel \mathbf{c}$ ) (a), for various angles  $\theta$  between the directions of  $\mathbf{B}$  and  $\mathbf{c}$  (b), and in the Voigt configuration ( $\mathbf{B} \perp \mathbf{c}$ ) (c). The zero-field PL spectrum shows very narrow bound exciton lines with a full width at half maximum (FWHM) of  $\Gamma \leq 80 \mu\text{eV}$ . Thus, the different Zeeman components of the transition lines can already be resolved at low magnetic fields of  $B = 1 \text{ T}$ . Similar exciton spectra with narrow half widths of the  $I_{6a}$  and  $I_8$  bound excitons were also

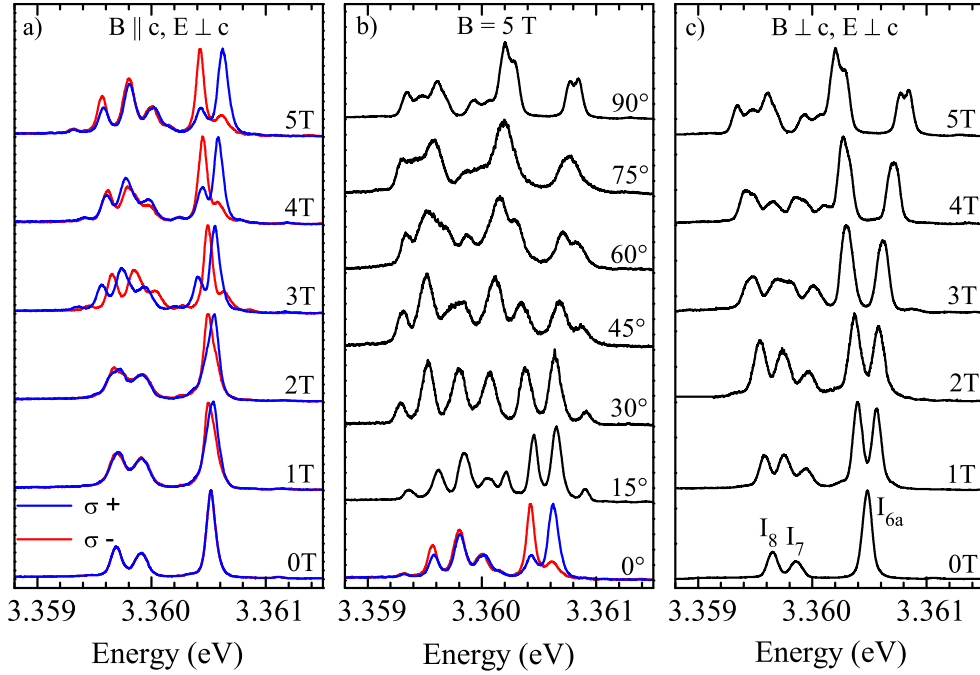


Figure 5.6: Photoluminescence spectra of the  $I_{6a}$ ,  $I_7$ , and  $I_8$  bound exciton lines at 2 K for different magnetic fields, orientations and angles. (a) Faraday configuration ( $\mathbf{B} \parallel \mathbf{c} \parallel \mathbf{k}$ ), (b) angles  $\theta = 0, 15, 30, 45, 60, 75, 90$  between  $\mathbf{B}$  and  $\mathbf{c}$  with  $B = 5$  T, (c) Voigt configuration ( $\mathbf{B} \perp \mathbf{c} \parallel \mathbf{k}$ ). The blue and red lines indicate the right  $\sigma^+$  and left  $\sigma^-$  polarized light, respectively. Black lines represent unpolarized measurements [104].

obtained from epilayers grown on Zn polar CrysTec substrates [93, 164].

First, the splitting behavior in the  $\mathbf{B} \perp \mathbf{c}$  configuration is investigated in order to determine the charge state of the impurities. All lines exhibit a linear splitting which is expected for neutral bound excitons (see chapter 4). Consequently, the bound exciton transitions  $I_4$ ,  $I_{6a}$ ,  $I_7$ , and  $I_8$  are attributed to neutral bound excitons in agreement with earlier publications [40, 69, 70, 102, 118]. By contrast, the splitting of ionized impurity bound excitons does not scale linearly with the magnetic field due to a zero-field exchange splitting which leads to a mixing of states and the appearance of previously forbidden transitions [111, 123]. Such behavior is observed for the bound excitons  $I_0$  and  $I_1$  [70, 165] (chapter 4) and was reported by Rodina et al. for the  $I_2/I_3$  [103].

Fig. 5.7 displays the energetic position of the bound exciton lines as function of the magnetic field  $B$  and angle  $\theta$ . Since the bound exciton transitions  $I_4$ ,  $I_{6a}$ ,  $I_7$  and  $I_8$  exhibit a comparable Zeeman splitting in all configurations, only the  $I_{6a}$  line is shown for clarity. In addition, the  $I_{6a}$  exhibits the highest intensity, smallest FWHM, and a sufficient spectral separation to the  $I_7$  and  $I_8$  bound exciton lines

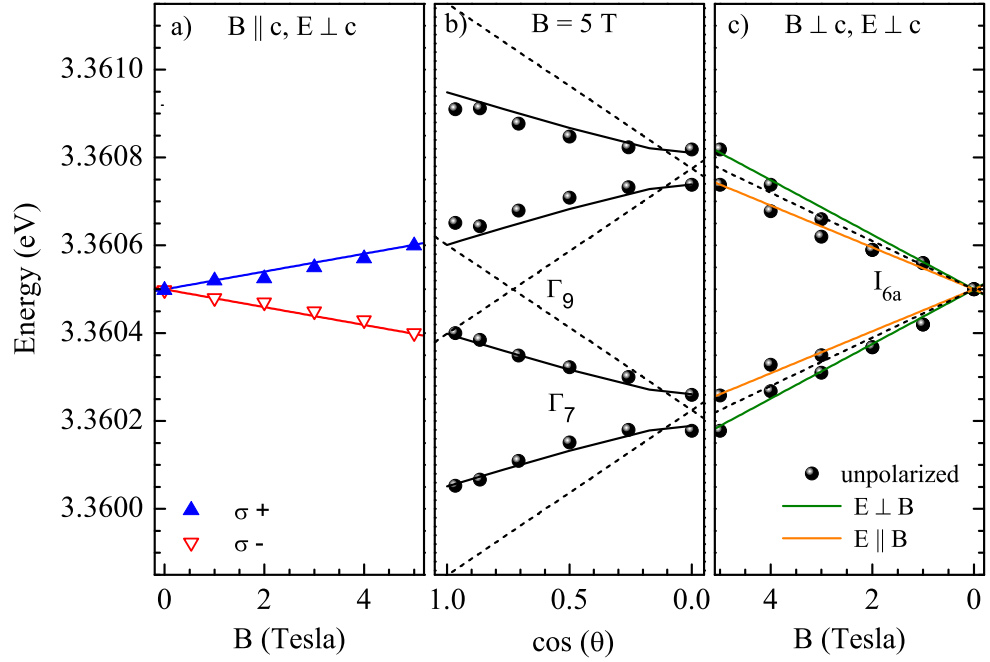


Figure 5.7: Zeeman splitting of the  $I_{6a}$  bound exciton line at 2 K. (a) Faraday configuration ( $B \parallel c \parallel \mathbf{k}$ ), (b) various angles  $\theta$  between  $B$  and  $c$  with  $B = 5$  T, (c) Voigt configuration ( $B \perp c \parallel \mathbf{k}$ ). Solid (blue) and open (red) triangles (a) indicate the peak position for  $\sigma^+$  and  $\sigma^-$  polarized light, respectively. Solid black dots show the peak energies in the unpolarized measurements. Green and orange lines (c) represent theoretical fits for  $E \perp B$  and  $E \parallel B$ , respectively [104].

so that the evaluation of its shifting and splitting behavior in a magnetic field is not affected by the overlapping of adjacent lines in close energetic proximity. With increasing magnetic field strength in  $B \perp c$ , a fourfold splitting of the  $I_{6a}$  bound exciton can be observed (Figs. 5.6c and 5.7c). This splitting can only be explained if not only the donor ground state splits in a magnetic field with the electron  $g$ -factor  $g_e$ , but also requires a splitting of the excited state (Fig. 5.5). Since the splitting of the excited state of a neutral donor bound exciton is determined by the hole  $g$ -value  $g_h^\perp$  in  $B \perp c$ , the experimental data requires a non-zero hole  $g$ -value  $g_h^\perp \neq 0$ . Applying group theoretical considerations as introduced in chapter 4, one can easily determine for which valence band symmetries zero or non-zero  $g$ -factor are expected. A magnetic field leads to a splitting of a certain state, if the group representation of the state ( $\Gamma_i$ ) or those of the magnetic field ( $\Gamma_B$ ) is contained in their Kronecker product:

$$g \neq 0 \iff (\Gamma_B \vee \Gamma_i) \in \Gamma_i \otimes \Gamma_B. \quad (5.5)$$

The group representation of a magnetic field perpendicular to the  $c$ -axis ( $\Gamma_{B\perp}$ ) is  $\Gamma_5$ , a magnetic field parallel to the  $c$ -axis ( $\Gamma_{B\parallel}$ ) transforms like  $\Gamma_2$ . For a perpendicular

magnetic field, the following Kronecker products for hole states with  $\Gamma_7$  and  $\Gamma_9$  symmetry are derived from Eq. 5.5 according to Koster et al. [112]:

$$\Gamma_7 \otimes \Gamma_5 = \Gamma_7 + \Gamma_9 \iff g_h^\perp(\Gamma_7) \neq 0, \quad (5.6)$$

$$\Gamma_9 \otimes \Gamma_5 = \Gamma_7 + \Gamma_8 \iff g_h^\perp(\Gamma_9) = 0. \quad (5.7)$$

Hence, the observed non-zero hole g-value  $g_h^\perp$  can only be explained for a hole originating from the  $\Gamma_7$  valence band. Consequently, the topmost valence band in the investigated samples must have  $\Gamma_7$  symmetry, which is in agreement with the originally proposed valence band ordering of  $\Gamma_7, \Gamma_9, \Gamma_7$  [34,35]. However, the observation of the  $g_h^\perp$  induced fine splitting may often be hindered by a larger FWHM of the excitonic emission lines or an insufficient spectral resolution at typical magnetic field strengths. In the case of GaN, magneto-reflection spectra up to 27 T revealed a four-fold splitting of the B and C exciton, whereas the A exciton only split into two Zeeman components [166]. Since the valence band ordering of the upper two bands in GaN ( $\Gamma_9, \Gamma_7, \Gamma_7$ ) is reversed compared to ZnO ( $\Gamma_7, \Gamma_9, \Gamma_7$ ), the observed four-fold splitting of the bound excitons in ZnO involving hole states from the A valence band is in perfect agreement with the splitting of the B and C excitons with  $\Gamma_7$  valence band symmetry in GaN.

### 5.2.3 Angular resolved magneto-PL

Additional evidence for the  $\Gamma_7, \Gamma_9, \Gamma_7$  valence band ordering in ZnO is given by the angular resolved spectra in Fig. 5.6b and their respective peak positions in Fig. 5.7b. The solid lines in Fig. 5.7 represent fits for  $\Gamma_7$  hole states, whereas the dashed lines are related to  $\Gamma_9$  states. Since the hole g-value for a  $\Gamma_9$  state in  $B||c$  would be larger than the electron g-value  $g_e$  [100,103], a crossing of the inner Zeeman components in Fig. 5.7b should occur for a  $\Gamma_9$  hole. This behavior has been observed for neutral bound excitons in other wurtzite semiconductors like e.g. CdS [111,167], where the A valence band has  $\Gamma_9$  symmetry. Evidently, this is not the case in the here presented data which is in agreement with previously obtained results for the bound excitons  $I_4$  and  $I_9$  by Rodina et al. [103]. From the fits in Fig. 5.7 the following values for the electron- and hole g-factors are derived:  $g_e = 1.9$ ,  $g_h^\parallel = -1.2$ , and  $g_h^\perp = 0.25$ . Previously, experimental values of  $g_h^\perp$  around 0.1 [103,151] as well as  $g_h^\perp = 0.3$  [149] were reported for the  $\Gamma_7$  hole in ZnO. Theoretical calculations within the quasi-cubic approximation [168] with the effective mass parameters of ZnO obtained from first principles calculations [100] predict the values  $g_h^\parallel = -1.23$  and  $g_h^\perp = 0.14$  for the upper  $\Gamma_7$  hole in bound excitons. These values are in good agreement with the here presented experimental results.

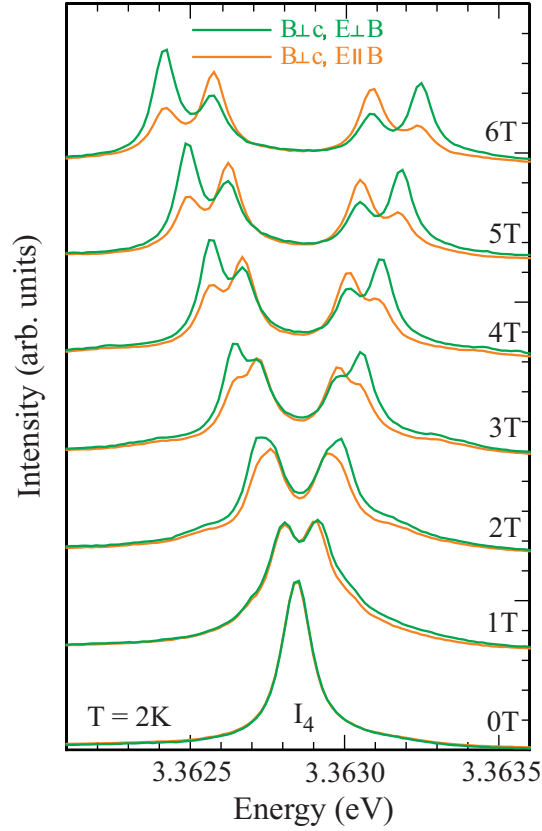


Figure 5.8: Photoluminescence spectra of the  $I_4$  bound exciton line at 2 K for magnetic fields of 0-6 T recorded in the Voigt configuration ( $\mathbf{B} \perp \mathbf{c}$ ). Green and orange lines represent linear polarized measurements in the  $\mathbf{E} \perp \mathbf{B}$  and  $\mathbf{E} \parallel \mathbf{B}$  orientation, respectively [104].

#### 5.2.4 Polarization dependent hole fine splitting

So far, the fourfold splitting in the  $\mathbf{B} \perp \mathbf{c}$  configuration was discussed without considering the polarization of these transitions. Apart from the circular polarized spectra in the  $\mathbf{B} \parallel \mathbf{c}$  orientation, the spectra and peak position in the Figs. 5.6b,c and 5.7b,c originate from unpolarized measurements. However, another important theoretical prediction in the framework of the quasi-cubical model can be established concerning the polarization of the Zeeman components in the Voigt configuration. Using the  $\Gamma_7$  basis functions and Zeeman terms described in Ref. [100, 168], one can predict a linear polarization of the inner transitions with  $\mathbf{E} \parallel \mathbf{B}$  and of the outer transitions with  $\mathbf{E} \perp \mathbf{B}$  in the geometry  $\mathbf{B} \perp \mathbf{k} \parallel \mathbf{c}$  as indicated by the orange and green lines in Fig. 5.7c. This theoretical prediction is experimentally observed for the  $I_4$  and  $I_8$  lines in nominally undoped ZnO substrates from EaglePicher. The linear polarized magneto-PL spectra in the Voigt configuration are shown in Fig. 5.8. For clarity,

only the energy regime of the  $I_4$  bound exciton is displayed. Apparently, the inner Zeeman components are linear polarized with  $\mathbf{E} \parallel \mathbf{B}$ , whereas the outer components show an increased oscillator strength in the  $\mathbf{E} \perp \mathbf{B}$  polarization. These experimental data are in excellent agreement with the theoretical considerations and provide an additional strong evidence for the  $\Gamma_7$  symmetry of the hole. It should be noted that for an opposite sign of  $g_h^\perp$ , the  $\mathbf{E} \parallel \mathbf{B}$  polarization would be observed for the outer Zeeman components instead of the inner ones.

### 5.2.5 Additional contribution to the VB ordering

Possible objections and counter-arguments (*italic letters*) which might contradict the interpretation of the A valence band possessing  $\Gamma_7$  symmetry shall now be discussed and excluded.

(i) *The observed bound exciton  $I_{6a}$  may result from a B valence band and therefore shows the behavior of a  $\Gamma_7$  hole state:* This explanation can be excluded since no  $I_{6a}$  related exciton transition is observed at lower energies with a typical A-B energy spacing of 4.7 meV (see also the discussion about excited state properties of donor bound excitons in section 3.4.2). Furthermore, the  $I_{6a}$  bound exciton is well established in the literature and is also the dominant excitonic recombination in this sample which should involve a hole from the topmost valence band.

(ii) *The valence band ordering in the investigated sample might be altered due to the presence of large strain fields:* It was pointed out by Gil et al. [169–171] and Shan et al. [172] that the valence band ordering in GaN and ZnO is rather sensitive to strain which can lead to a reversal of the usual symmetry ordering. However, this is not the case in the present study since no significant strain induced shift of the non-polar  $E_2(\text{high})$  Raman mode was observed from its relaxed value of  $437 \text{ cm}^{-1}$  [173]. The absence of a strain induced energy shift also applies for the energetic positions of the free and bound excitons in the PL spectra which deviate by less than 0.15 meV from the values provided by Meyer et al. [40]. In addition, ab initio calculations by Schleife et al. revealed that only the crystal field determined A-C splitting is strongly affected by biaxial strain which would – even in the case of a A-C valence band crossing for large strain fields – lead to a top valence band with  $\Gamma_7$  symmetry [174].

(iii) *The additional splitting in the Voigt configuration could appear in the case of a  $\Gamma_9$  hole state if an anisotropic in-plane stress perpendicular to the  $c$ -axis is present in the sample:* This stress would not change the ordering of the valence subbands but result in the admixture of the  $\Gamma_7$  character to the  $\Gamma_9$  hole. Therefore, a non-zero perpendicular hole  $g$ -factor could appear even for a  $\Gamma_9$  hole. For example, it was shown that the simultaneous application of strong in-plane stress and uniaxial stress along the  $c$ -axis may even lead to a nearly isotropic  $g$ -factor tensor of the  $\Gamma_9$  hole [175,

176]. However, the presence of uniaxial in-plane stress would lead to a reduction of the crystal lattice symmetry, which is described by the point group  $C_{6v}$  in the unstrained case and  $C_{2v}$  in the case of uniaxial stress perpendicular to the  $c$ -axis. Therefore, a splitting of the zero-field exciton lines should appear which was observed by Langer et al. [177, 178] and Wrzesinski et al. [82] under applied uniaxial pressure  $P \perp c$ . Without external pressure or magnetic fields, Reynolds et al. [179] observed a fourfold splitting for ZnO grown from the gas-phase using ZnSe as starting material, but no splitting when ZnS was used. They explained the splitting by the combined effect of spin-exchange and local strain due to the presence of residual selenium in the ZnO lattice, based on the theoretical description by Akimoto and Hasegawa [180]. The splitting was modified in a magnetic field applied perpendicular to the  $c$ -axis due to the additional Zeeman splitting of the electrons. The observed fourfold splitting was significantly different for two different donor centers which additionally indicated the influence of the local potential. By contrast, no indications of uniaxial in-plane stress such as line splittings or line-shape broadenings in zero-field are observed in the present study, although the spectral resolution was sufficient to resolve these effects. In addition, no residual Se contamination leading to large local strain fields is expected in the here investigated ZnO epilayers and substrates. Consequently, anisotropic uniaxial in-plane stress can be excluded as possible explanation for the non-zero hole  $g$ -value  $g_h^\perp \neq 0$ .

(iv) *The crystal  $c$ -axis might be improperly aligned to the direction of the  $B$ -field which would lead to a deviation from the Voigt geometry and allow the appearance of two additional lines due to the angular dependence of the hole  $g$ -value (Fig. 5.5):* Two possible reasons for such a misalignment are conceivable. First, the orientation of the turnable sample holder might deviate from the perpendicular setting with respect to the direction of the magnetic field and second, the sample might exhibit a tilting of the  $c$ -axis due to lattice imperfections and micro crystal formations. However, both possibilities can be excluded. The crystal orientation is calibrated by the back reflection of the HeCd laser spot. The error in the angular orientation at  $0^\circ$  and  $90^\circ$  is smaller than  $0.5^\circ$ . Hence, an additional splitting of the observed size could not occur. The second possible explanation involving a tilted  $c$ -axis also has to be discarded as demonstrated by high resolution X-ray diffraction. No signs of a tilted  $c$ -axis could be found and the (0002) reflection shows a perfectly symmetric shape with a full width at half maximum of  $17''$  in the  $\omega$  scan.

(v) *Finally, one could argue that the ordering of the valence bands might be different from the ordering of the corresponding excitons due to the mixing and interaction of states:* Concerning this objection, the extensive exciton fine structure calculations of Lambrecht et al. should be taken into account [100]. Within this work, it could be shown that the excitons closely maintain their principal valence band character

even when band mixing effects are considered. The same results confirming the  $\Gamma_7$  character of the upper valence band and of the upper *A* exciton were obtained later by ab initio calculations of excitons in ZnO [126].

### 5.3 Summary

In the first part of this chapter, the band structure of ZnO was discussed and the long lasting dispute about the valence band ordering was summarized. Subsequently, high resolution magneto-optical luminescence measurements on bound excitons in ZnO were presented which are able to resolve the controversy about the symmetry of the topmost valence band. In particular, a hole state related fine splitting in the Voigt configuration could be observed. Theoretical considerations clearly demonstrate that the splitting is caused by the  $\Gamma_7$  symmetry of the hole state. This assignment is doubtlessly confirmed by angular and polarization dependent measurements. The parallel and perpendicular hole *g*-values were obtained in good agreement with earlier first principle calculations. Possible counter-effects that might lead to alternative explanations of the observed data including the effects of strain, misalignments, and the involvement of B-valence band holes were extensively discussed and excluded. In conclusion of these arguments, the observed fine splitting provides definitive proof that the uppermost A valence band in ZnO has  $\Gamma_7$  symmetry.

## 6 Structural defect bound excitons

This chapter presents a detailed investigation of deeply bound excitons and their relation to structural defects in ZnO. A comparative analysis of the properties of deeply bound excitons and shallow donor bound excitons is performed. Thereto, a wide range of experimental techniques is applied including studies in external magnetic and stress fields. The direct comparison of the deeply bound excitons to the shallow donor bound excitons  $I_0$ - $I_{10}$  reveals striking differences which are discussed in detail. In the first part of this chapter (section 6.1), an overview of several publications is provided which report on the observation of deeply bound excitons in differently grown ZnO samples. In the following sections, a variety of different properties of these exciton lines are studied. In particular, these are the defect type and charge state of the binding centers (6.2), the temperature dependence of localization energies (6.3), the exciton-phonon coupling and two electron satellites (6.4), the absorption in magnetic fields (6.5), the excited states of deeply bound excitons and two electron satellites (6.6), the recombination dynamics of shallow and deeply bound excitons (6.7), the influence of uniaxial pressure (6.8), and the spatial distribution of the luminescence centers (6.9). Subsequently, similar results in other compound semiconductors are briefly discussed (6.10). Finally, the different experimental results are connected in order to develop a model of the defects and electronic states contributing to the optical transitions of deeply bound excitons in ZnO. This model and its impact on the deeply bound exciton properties are extensively discussed and a theoretical estimation of the defect extent is provided in section 6.11.

### 6.1 Deeply bound excitons in ZnO - An overview

ZnO single crystals, epilayers and nanostructures often exhibit a variety of narrow emission lines in the spectral range between 3.33 eV and 3.35 eV. The most prominent feature in this range is the commonly observed emission line at 3.333 eV ( $Y_0$ ). This line was reported in a multitude of different ZnO samples such as substrates [181–184], homoepitaxial- [185, 186] and heteroepitaxial films [187–190], micro- and nanocrystals [191–193], nanowires [194], and quantum wells [195]. In nanomaterials, the 3.333 eV line is only observed in structures with sufficiently large lateral dimensions. Stichtenoth et al. [194] observed the 3.333 eV emission in

ZnO nanowires with diameters greater than 100 nm, whereas it is not observed in nanowires with smaller diameters [194, 196, 197]. This is also confirmed by Robin et al. [190], who found the 3.333 eV transition in ZnO nanowires with diameters of about 300 nm on GaN substrates but not on sapphire, where the ZnO nanowires had a diameter of about 150 nm. In ZnO nanocrystals, similar observations were reported by Fallert et al. [192]. Untreated ZnO nanocrystals with diameters between 70 and 120 nm did not exhibit the 3.333 eV transition. However, after annealing larger polycrystalline clusters with diameters up to 1  $\mu\text{m}$  were formed and a pronounced 3.333 eV line could be observed.

Several controversial interpretations for the narrow emission lines around 3.333 eV are discussed in the literature including deep donor bound excitons (DX) [84, 182, 183], acceptor bound excitons ( $A^0X$ ) [187], nitrogen related electron-acceptor transitions ( $e, A_N$ ) [198], transitions related to intrinsic point defects ( $V_O, Zn_i$ ) [188, 199], extended structural defects [40, 67], and two electron satellites (TES) [78, 89, 121, 185, 191]. A few examples of these works shall be mentioned here. Schildknecht et al. [182] studied different ZnO substrates grown by chemical vapor transport (CVT) from EaglePicher and by hydrothermal growth technique. A strong emission line at 3.333 eV could be observed in the CVT grown samples before and after annealing whereas it was absent in the hydrothermally grown samples. This line was attributed to an unknown deep donor excitonic transition. Johnston et al. [84] observed that the same line appeared in ZnO hydrothermal crystals from Rubicon Technology after annealing and ion implantation with stable and radiative Zn and Ga isotopes. Frequently, the 3.333 eV line is also reported in heteroepitaxial layers. Kato et al. [187] observed the 3.333 eV line in MBE grown ZnO on  $\alpha\text{-Al}_2\text{O}_3$  substrates. Based on the spectral position they ascribed the emission to the recombination of excitons bound to neutral acceptors ( $A^0X$ ). Other publications attribute this emission in nominally undoped MBE grown samples to donor bound exciton transitions due to oxygen vacancies ( $V_O$ ) and/or interstitial zinc ( $Zn_i$ ) [188, 199, 200]. In addition, several works identify the 3.333 eV line or peaks in close spectral proximity as two electron satellite transitions of shallow bound excitons such as the  $I_4$  at 3.3628 eV. However, this identification is (in the absence of absorption measurements) not necessarily unambiguous, especially if alternative candidates for the TES transitions around 3.330 eV are present [185] or a deviating temperature dependence compared to the shallow bound excitons is observed [191]. This differentiation is further complicated by energetic shifts of the emission lines due to biaxial in-plane strain as often observed in epitaxial layers [164, 201].

Despite the large quantity of PL studies showing the 3.333 eV transition, only few publications investigate the properties of this transition in detail. So far, the most extensive studies were published by Alves et al. [67] and Meyer et al. [40]. In these

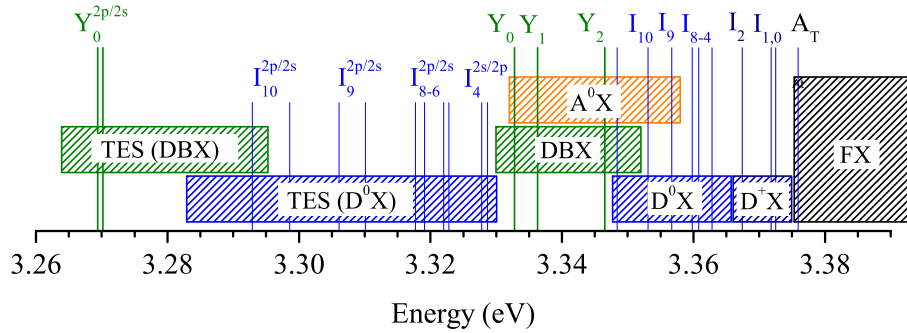


Figure 6.1: Schematic drawing of the energy ranges of various optical transitions at low temperature. Selected transitions are indicated by vertical lines. The different areas mark the energy range of free exciton-polariton (FX), ionized donor bound excitons ( $D^+X$ ), neutral donor bound excitons ( $D^0X$ ), acceptor bound excitons ( $A^0X$ ), deeply bound excitons (DBX), and two electron satellites of the donor and deeply bound excitons TES in the  $2s$  and  $2p$  states.

works, the 3.333 eV line was attributed to the recombination of an excitonic complex with an activation energy of around 10-11 meV. This assignment was founded on the temperature dependence of the luminescence and rather fast recombination times. Based on the spot-like and localized character of the luminescence band in CL images, the transition was ascribed to deeply bound excitons at structural defects. Following these works, several authors adopted this attribution for different ZnO samples [192, 195, 202–205]. However, a convergent picture concerning the defect identification and the electronic properties of the 3.333 eV line has not yet emerged as can be seen from the large variety of contradicting attribution in recent years. Even less is known about the often weaker lines between 3.33 eV and 3.35 eV which sporadically appear in combination with the 3.3328 eV transition. The large uncertainties as to the nature and properties of these deeply bound exciton transitions provide a strong motivation for the here presented comprehensive study.

The spectral position of these lines fall into a region where donor bound excitons ( $D^0X$ ), predicted acceptor bound excitons ( $A^0X$ ), structural defect bound excitons and two electron satellites of shallow donor bound excitons (TES  $D^0X$ ) could occur and may overlap. Hence, an identification of the involved impurity or defect centers which is solely based on the exciton recombination energy would be extremely questionable. The typical energy regions of the different optical transitions in the near band-edge luminescence of ZnO are displayed in a schematic drawing in Fig. 6.1. The vertical lines in the figure mark the energetic positions of common features in the luminescence spectra. Apparently, no conclusive identification of the transitions in this range is possible based on their spectral position. The DBX (deeply bound

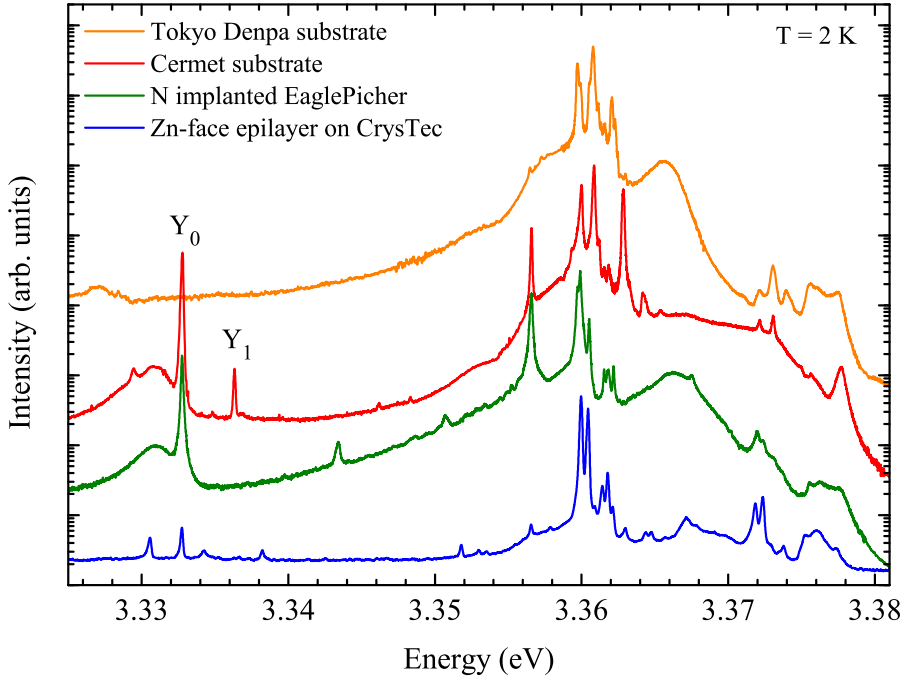


Figure 6.2: Photoluminescence spectra of different ZnO single crystals and epilayers at  $T=2$  K. In the spectral range between 3.33 eV and 3.35 eV, several narrow emission lines are visible. The strongest peaks are the  $Y_0$  (3.3328 eV) and the  $Y_1$  (3.3363 eV). The spectra are normalized to the strongest bound exciton line.

excitons) labeled area marks the range of the optical transitions which are studied in this chapter. It should be noted that the depicted area of the acceptor bound excitons is solely based on theoretical considerations [70] as a doubtless proof for acceptor bound exciton emissions is still missing.

For the experimental study of these lines, different ZnO substrates and epitaxial ZnO layers were investigated. The analysis in the following sections mainly focuses on three different samples with pronounced luminescence features. These are a commercially available ZnO substrate provided by CermetInc, a nitrogen implanted ZnO single crystal by EaglePicher, and a ZnO epilayer grown by CVD on a Zn polar ZnO substrate by CrysTec. As a reference, a ZnO substrate from Tokyo Denpa which does not exhibit any luminescence lines between 3.33 and 3.35 eV is analyzed. The different experimental techniques used in this study are described in chapter 2.

## 6.2 Defect type and charge state

First, the defect type and charge state of the deeply bound excitons is studied by magneto-PL spectroscopy. Fig. 6.2 displays the free and bound exciton photolumi-

nescence (PL) spectra of the different ZnO samples at a temperature of 2 K. From bottom to top, the PL spectra of the homoepitaxial ZnO layer on a Crystec substrate, the nitrogen implanted EaglePicher crystal, the Cermet substrate, and the substrate by Tokyo Denpa are shown. In the energy range between 3.38 eV and 3.35 eV, all samples exhibit a large quantity of emission lines which differ in their energetic position and intensity. The luminescence lines in this range are related to the radiative recombination of the free exciton-polaritons, ionized and neutral bound excitons and were studied in detail in chapter 3. Between 3.33 eV and 3.35 eV several additional luminescence features are observed. In particular, these are the emission lines at 3.3328 eV ( $Y_0$ ) and 3.3363 eV ( $Y_1$ ). The most pronounced feature in this region is the commonly observed narrow line  $Y_0$  at an energy of 3.3328 eV which is sometimes also labeled DBX [40], DD [84, 182, 183] or just 3.333 eV line. This line has the same energy and line shape in different samples despite the variations in the rest of the free and bound exciton luminescence. The presence of the  $Y_0$  line in the different types of samples makes its attribution to a specific dopant or growth technique unlikely. This statement is supported by the absence of any emission lines in this spectral range in the Tokyo Denpa sample, even though similar luminescence features compared to the other three samples are present in the free and bound exciton region. However, this fact does not exclude the possibility of structural defect bound excitons as they may appear under very different growth conditions and independent of the bound exciton luminescence structure. The occurrence of  $Y_0$  line is not restricted to hetero-epitaxial films which often form dislocations and structural defects due to the lattice mismatch between different layers. Instead, this line also appears in single crystals and homoepitaxial films. In particular, additional defects in single crystals can be introduced by cutting, polishing or etching processes, giving rise to new localized luminescence centers related to structural defects close to the surface [206]. Furthermore, ion implementation often leads not only to the usually intended incorporation of dopants but also the creation of new structural defects which may serve as radiative recombination centers for deeply bound excitons [84, 207]. Similar considerations also apply for the transitions at 3.3363 eV ( $Y_1$ ) and a third line at 3.3465 eV ( $I_{12}/Y_2$ ) which is newly introduced after the application of uniaxial pressure (see section 6.8). In a publication of Johnston et al. [84], a weak luminescence peak with an energy of 3.5 meV above the energy of the 3.333 eV transition was observed but not discussed. Although the absolute energies of the transitions line are slightly shifted possibly due to strain [164, 201], the energy spacing between these two lines matches precisely the distance between the here studied  $Y_0$  and  $Y_1$  features at 3.3328 eV and 3.3363 eV, respectively. Therefore, the small peak in this work is identified as  $Y_1$  line. Only recently, the  $Y_2$  ( $I_{12}$ ) emission was studied by Brandt et al. [106] and Ohno et al. [208] and could be identified as donor

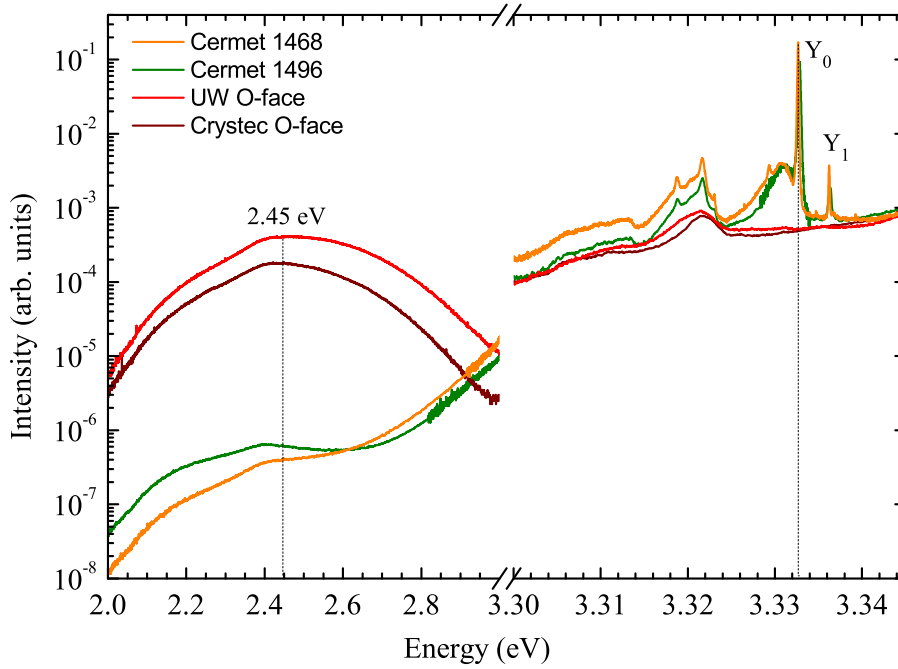


Figure 6.3: Photoluminescence spectra of different ZnO substrates in the range of the green luminescence band and 3.333 eV transitions at  $T = 2$  K. A strong  $Y_0$  line is observed in samples with weak green luminescence bands (Cermet), whereas substrates with strong emission bands around 2.45 eV do not show the 3.333 eV transition (CrysTec and UniWaver).

bound exciton, presumably requiring a distorted lattice structure.

Fig. 6.3 shows the luminescence spectra of four different ZnO substrates from Cermet, CrysTec, and UniWaver in the range of the green luminescence band at 2.45 eV and the  $Y_0$  at 3.333 eV. The Cermet samples exhibit pronounced  $Y_0$  and  $Y_1$  emission lines but very weak green luminescence, whereas the green defect band is by about three orders of magnitude stronger in the other samples and no  $Y$  transitions are observed. Based on these observations, a correlation of these two luminescence features is conceivable. As discussed in chapter 3.1, the green luminescence originates (in the absence of copper) from mobile point defects such as zinc or oxygen vacancies. Therefore, it is possible that the appearance of the 3.333 eV is accompanied by a reduction of the native point defect. In this case, it could be argued that mobile intrinsic point defects such as Zn and O vacancies are collected by dislocations which results in an reduction of the 2.45 eV band and an intensity increase of the luminescence lines of excitons bound to extended structural defects.

In order to gain information about the properties of the defects involved in these transitions, the photoluminescence is investigated under the influence of an external magnetic field up to 5 Tesla. Although the following discussion focuses primarily

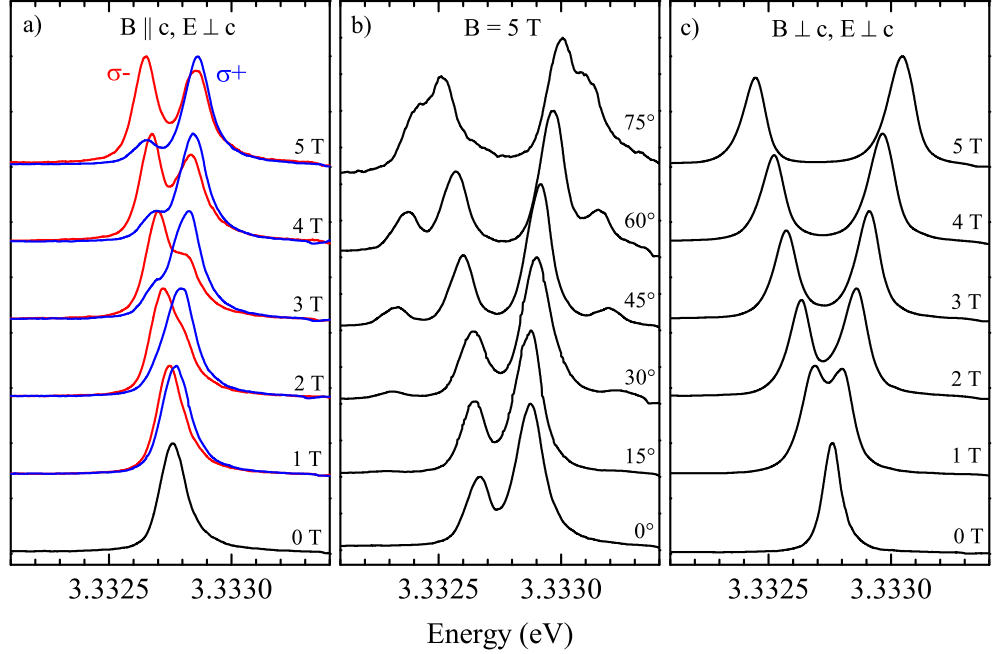


Figure 6.4: Photoluminescence spectra of the 3.3328 eV line at 1.6 K for different magnetic fields, orientations and angles. (a) Faraday configuration ( $\mathbf{B} \parallel \mathbf{c} \parallel \mathbf{k}$ ), (b) angles  $\theta = 0^\circ, 15^\circ, 30^\circ, 45^\circ, 60^\circ, 75^\circ$  between  $\mathbf{B}$  and  $\mathbf{c}$  with  $B = 5$  T, (c) Voigt configuration ( $\mathbf{B} \perp \mathbf{c} \parallel \mathbf{k}$ ). Blue (dark) and red (light) lines in Faraday configuration indicate the right  $\sigma^+$  and left  $\sigma^-$  polarized light, respectively.

on the  $Y_0$  line at 3.3328 eV, it is equally valid for the  $Y_1$  line at 3.3363 eV. Fig. 6.4 displays the low temperature magneto-PL spectra of the 3.3328 eV line in Faraday configuration  $\mathbf{B} \parallel \mathbf{c}$  (a), for various angles  $\theta$  between the directions of  $\mathbf{B}$  and  $\mathbf{c}$  (b), and in the Voigt configuration  $\mathbf{B} \perp \mathbf{c}$  (c). The zero field spectrum shows a narrow recombination line with a full width at half maximum (FWHM) of around  $120 \mu\text{eV}$ . With increasing magnetic field in the  $\mathbf{B} \perp \mathbf{c}$  configuration, the 3.3328 eV line exhibits a Zeeman splitting into two components as displayed in Fig. 6.4c. The additional fine splitting related to the  $\Gamma_7$  hole state as discussed in chapter 5.2.2 and Ref. [104] is not resolved in these spectra. This is most likely caused by the fact that the energy splitting determined by the perpendicular hole g-value  $g_h^\perp$  in a magnetic field  $B = 5$  T is exceeded by the spectral line width of the 3.333 eV transition. Consequently, it is not possible to observe the additional splitting of the transitions in  $\mathbf{B} \perp \mathbf{c}$ . In the Faraday configuration ( $\mathbf{B} \parallel \mathbf{c}$ ), the emitted light has a pronounced circular polarization as shown in Fig. 6.4a. The high energy Zeeman component has  $\sigma^+$  polarization (blue lines) whereas the lower energy transition is  $\sigma^-$  polarized (red lines). This is consistent with the theoretical considerations and experimental observation on shallow bound excitons discussed in chapter 4.4.1.

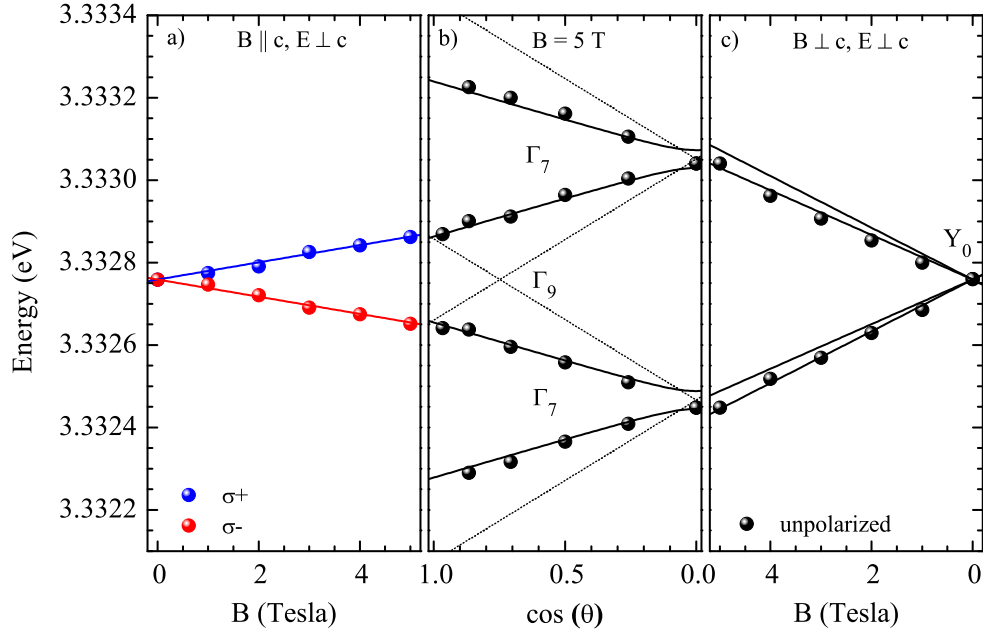


Figure 6.5: Zeeman splitting of the 3.3328 eV line at 1.6 K. (a) Faraday configuration ( $\mathbf{B} \parallel \mathbf{c} \parallel \mathbf{k}$ ), (b) various angles  $\theta$  between  $\mathbf{B}$  and  $\mathbf{c}$  with  $B = 5$  T, (c) Voigt configuration ( $\mathbf{B} \perp \mathbf{c} \parallel \mathbf{k}$ ). (a) Blue and red data points indicate the peak position for  $\sigma^+$  and  $\sigma^-$  polarized light, respectively. Black dots show the peak energies in the unpolarized measurements. Solid lines represent fits for hole states with  $\Gamma_7$  symmetry, dotted lines indicate predicted angular dependence for exciton hole states with  $\Gamma_9$  symmetry.

The peak positions of the Zeeman components as function of the magnetic field and angle between  $\mathbf{B}$  and  $\mathbf{c}$  are displayed in Fig. 6.5. The linear splitting with increasing magnetic field in the  $\mathbf{B} \perp \mathbf{c}$  orientation is characteristic for an exciton bound to a neutral defect center. In the case of an ionized complex, a nonlinear splitting due to the spin-exchange interaction is expected (section 4.4.3). This would lead to a zero field splitting as has been reported for dislocation bound excitons in CdS [209] and the impurity bound exciton lines  $I_0$ ,  $I_1$ , and  $I_{2/3}$  in ZnO [70,103,165]. Evidently, this is not the case for the 3.3328 eV line (Fig. 6.5c). From the fits of the peak positions in Fig. 6.5, the electron and hole g-factors of the  $Y_0$  exciton are derived with values of  $g_e = 2.02$ ,  $g_h^\perp = 0.15$ , and  $g_h^\parallel = -1.3$ . The electron  $g_e$  factor of 2.02 is considerable larger compared to those of shallow impurity related donor states with typical values between 1.955 and 1.958 [88,94,103,110]. Instead, it is in excellent agreement with reported values for defects such as e.g. the Zn vacancy center which were obtained by electron paramagnetic resonance (EPR) and optical detection magnetic resonance (ODMR) [210–213]. However, the Zn vacancy itself cannot be responsible for the excitonic emission at 3.333 eV as it forms a deep acceptor state in ZnO (section 3.1

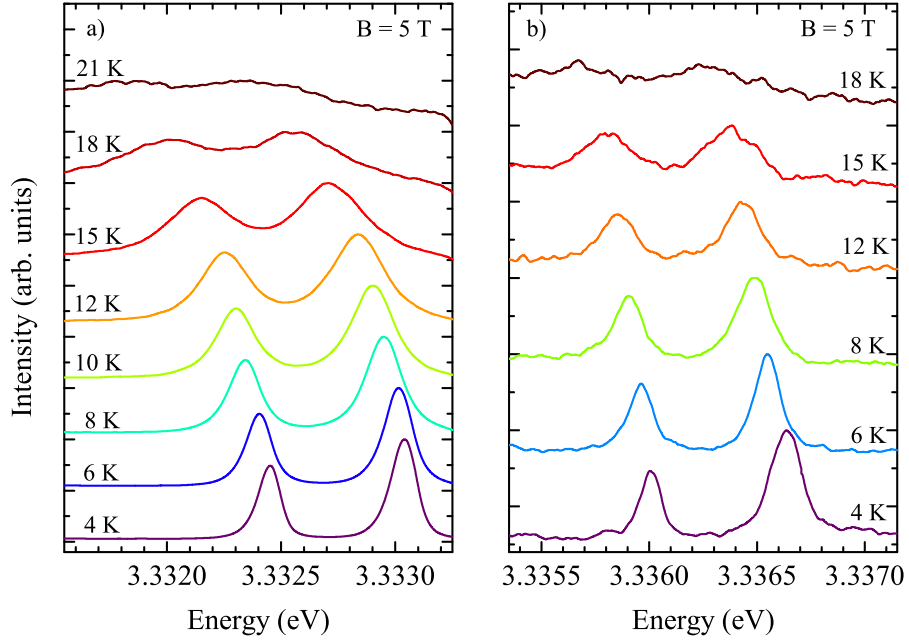


Figure 6.6: PL spectra of the 3.3328 eV (a) and 3.3363 eV (b) emission lines as a function of temperature between 4 K and 21 K. Spectra are recorded in a magnetic field of  $B = 5$  T with  $\mathbf{B} \perp \mathbf{c}$ .

and Refs. [52, 56, 214]).

Following the determination of charge state and  $g$ -values, it should be clarified if the  $Y_0$  and  $Y_1$  transitions at 3.3328 eV and 3.3363 eV involve hole states from the A or B valence band. Thereto, the angular dependent energy shift of the  $Y$  lines in a magnetic field is analyzed in Fig. 6.5b (not shown for the  $Y_1$  line). In agreement with the presented angular resolved magneto-optical studies of neutral bound excitons in section 5.2.3, the energetic shifts of the  $Y$  lines show no crossing of the inner two Zeeman components. Consequently, the bound excitons at 3.3328 eV and 3.3363 eV involve holes from a valence band with  $\Gamma_7$  symmetry, since  $\Gamma_9$  hole states would lead to an angular crossing at around  $40^\circ$  in Fig. 6.5b. In light of the conducted study of the valence band ordering in ZnO (chapter 5) which proves the originally proposed  $\Gamma_7$ ,  $\Gamma_9$ ,  $\Gamma_7$  symmetry ordering by Thomas and Hopfield [34], it is evident that both  $Y$  recombinations involve hole states from the topmost A valence band with  $\Gamma_7$  symmetry.

Fig. 6.6 displays the temperature dependent PL spectra of the  $Y_0$  and  $Y_1$  lines under the influence of a magnetic field of 5 T in the  $\mathbf{B} \perp \mathbf{c}$  configuration. Both lines show a rapid intensity decrease with increasing temperature between 4 K and 20 K. Based on the study of their thermalization behavior in an external magnetic field, the emission lines can be attributed to donor or acceptor bound excitons

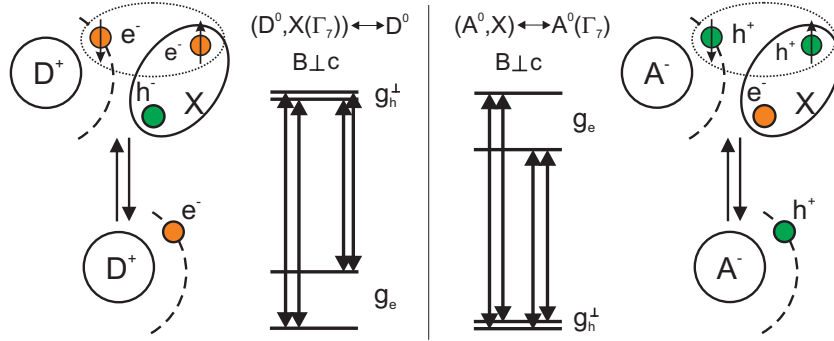


Figure 6.7: Zeeman splitting of neutral donor and acceptor bound exciton complexes involving  $\Gamma_7$  electron and hole states in a constant external magnetic field with  $B \perp c$ . The  $g$ -values in the ground and excited states depend on the spin of the unpaired particles. The depicted models also apply for any complex involving two electrons and one hole (donor complex) or one electron and two holes (acceptor complex), even if the core centers are different from  $D^+$  or  $A^-$ , respectively.

(section 4.4.2). Thereto, the different splittings for neutral donor and acceptor bound excitons with  $\Gamma_7$  hole state symmetry have to be analyzed. The corresponding energy level schemes in the Voigt configuration with  $B \perp c$  are displayed again in Fig. 6.7. In the case of a donor bound exciton, the splitting of the ground state is determined by the electron  $g$  value  $g_e$ , whereas the splitting of the excited state is given by the much smaller hole  $g$  value  $g_h^\perp$ . For an acceptor bound exciton this order is reversed (Fig. 6.7b). Apparently, the intensity ratio of the two Zeeman components shows no significant changes with rising temperature for both lines. Since the thermalization in luminescence depends exclusively on the splitting of the excited state, the constant PL intensities indicate that no sufficient splitting of the excited state is present to create a pronounced thermalization (increasing intensity of the high energy component). This is expected for a donor and confirms the attribution of these transition lines to donor bound exciton recombinations.

It should be noted that the observed linear splitting in the Voigt configuration will occur not only for isolated neutral impurities, but for any complex involving two paired and one single charge carrier. Thus, the magneto-PL and temperature dependent data for the  $Y_0$  and  $Y_1$  lines indicate that these lines should in fact be attributed to the exciton emission from complexes involving two electrons and one hole of  $\Gamma_7$  symmetry. If these complexes possess singly charged  $D^+$  cores, one would expect larger donor binding energies for these centers compared to the previously studied shallow donor bound exciton lines. Alternative models based on the experimental data are discussed in section 6.11.

### 6.3 Temperature dependence of free-, shallow-, and deeply bound excitons

Aside from the identification of excitons bound to donors or acceptors by temperature dependent PL in magnetic fields, the study of the energetic shift as function of temperature in zero field provides additional information about the origin of the optical transitions. The most significant contribution in the case of shallow defect states is usually given by the temperature dependence of the band edge. Several models which describe this energy shift are found in the literature [215–218]. Although the empirical Varshni equation [215] is often applied, it should be considered that the Varshni model involves certain deficiencies such as a systematic deviation in the cryogenic temperature region and a high instability of the Varshni parameter set [218]. In particular, the Varshni model is inadequate if the investigated temperature range is much lower than the Debye temperature of 920 K in ZnO [219]. Since the deeply bound exciton lines already disappear at temperatures above 25 K (Fig. 6.6), the Varshni model is not applicable here. Therefore, the temperature dependence is computed by the model suggested by Viña et al. [217, 220], which is based on a Bose-Einstein model and delivers a more reliable description in the low temperature range.

Fig. 6.8a displays the experimentally determined spectral shift of the  $A_T$ ,  $I_6$ , and  $Y_0$  lines as function of temperature. The solid lines indicate least-squares fits to the experimental data. Although the calculated parameters have large uncertainties due to the limited temperature range, it is evident that the free excitons, shallow bound excitons, and deeply bound excitons exhibit different energy shifts as function of temperature. Nevertheless, the temperature dependence of the longitudinal and transversal free excitons ( $A_T$ ,  $A_L$ ), the shallow bound excitons ( $I_i$ ), and the deeply bound excitons ( $Y_i$ ) is found to be equal within each group. The distinction between the temperature dependence of different free and bound exciton transitions is usually not reported and analyzed in other temperature dependent studies of the near band edge luminescence in ZnO. Typically, temperature dependent measurements cover the full range from liquid helium temperature up to room temperature and above [221–223]. As a practical tribute to the large temperature region, only a few temperature steps between 2 K and 30 K are measured. In addition, the spectral resolution at low temperatures might be considered circumstantial due to the dissociation of bound excitons and broadening of free excitons at elevated temperatures. Consequently, a precise analysis of the temperature dependence of the different exciton transitions in the low temperature range would not be possible. All these problems were avoided in this work by recording PL spectra of the free and bound excitons with temperature steps of 2 K and a spectral resolution better than

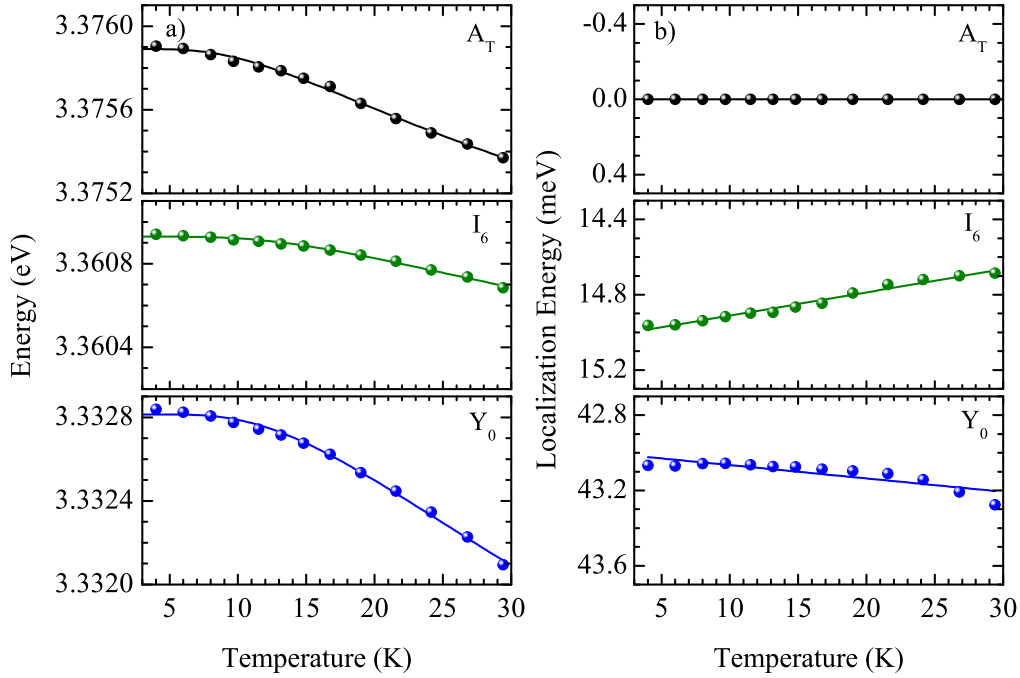


Figure 6.8: Energy of the  $A_T$ ,  $I_6$  and  $Y_0$  lines as function of temperature between 4 K and 30 K. The energy shift is displayed for absolute energies (a) and localization energies (b). Solid lines represent fits based on a Bose-Einstein model (a) and linear fits (b).

50  $\mu\text{eV}$ , thus enabling the distinction between all observed exciton lines.

The large discrepancy in the temperature shift between the  $Y_0$  and  $I_6$  contradicts an attribution of the  $Y$  lines to shallow bound excitons. This becomes even more evident if the temperature dependence of the localization energy is analyzed as plotted in Fig. 6.8b. The localization energy of  $A_T$  is trivially constant at  $E_{loc} = 0$ . For the shallow bound excitons (e.g.  $I_6$ ), a pronounced decrease of the localization energy is observed with increasing temperature. This relation is in contrast to the  $Y$  lines (e.g.  $Y_0$ ) which exhibit a stronger red shift compared to the other exciton lines resulting in an increase of the localization energy with increasing temperature. The observed temperature dependence of the  $Y$  lines provides a first indicator that the description of these centers requires a different model than for shallow bound excitons. This necessity is further emphasized by a study of the binding energies of these excitons which are determined in an Arrhenius plot by fitting the peak intensities as a function of the reciprocal temperature. Despite the large localization energies of  $E_{loc} = 43.1$  meV and 39.6 meV for the exciton lines at 3.3328 eV and 3.3363 eV, respectively, a thermal activation energy  $E_a \approx 12 \pm 2$  meV is derived for both centers. This energy is in agreement with reported values of 10-11 meV for the 3.333 eV

line [40, 67, 188]. By contrast, the activation energies of the shallow bound excitons approximately coincide with the localization energies. The small activation energies  $E_a < E_{loc}$  observed for the  $Y$  lines indicate that the respective defect centers, in contrast to the shallow donors, do not bind the exciton as a whole quasiparticle. As result, the lowest ionization potential of such a complex – the activation energy – does not correspond to the detachment of an exciton as a whole. Possible models of the binding centers for these three-particle complexes (two electrons and one hole) are discussed in section 6.11.

In addition, the high precision of the temperature dependent measurements allows the investigation of another interesting aspect of the near band-edge luminescence. For ZnO, as for a large variety of other materials, a negative thermal expansion coefficient was reported in the low temperature range [224–226]. This can be explained considering that the origin of thermal expansion is the anharmonicity of the phonon eigenmodes [227, 228]. The volume dependence of the vibration frequency  $\omega$  of each mode is given by the mode Grüneisen parameter  $\gamma$  as defined in Eq. 7.29 in chapter 7.6.1. The expansion coefficient in the different temperature regions is then determined by the Grüneisen parameters of those modes which are activated at the respective temperatures. Since the high energy optical modes are not excited at temperatures below about 100 K, the thermal expansion is governed mainly by the low-frequency transverse acoustical (TA) modes which exhibit negative Grüneisen parameters at the zone edge [229, 230], resulting in a negative expansion coefficient. Since a negative expansion, i.e. decreasing lattice constants, should correlate with an increase of the band gap energy due to stronger repulsion of overlapping electron wave functions, an increase of the exciton emission energies could be expected. However, despite the high spectral resolution, no shift of the exciton lines to higher energies is observed in the low temperature region. Consequently, a competing process to the negative thermal expansion governed by TA modes must exist which is attributed to Fröhlich and deformation potential interaction between excitons and longitudinal optical phonons with positive Grüneisen parameters (chapter 7). Since the LO phonons are optically excited, they can also couple to the excitons at temperatures well below their thermal activation energy. Consequently, no increase in the exciton emission energy is observed. This argumentation, however, does not account for the larger effect of the temperature on the localization energy of the  $Y$  lines, whose interaction with phonons is very weak as determined in the following section. Furthermore, a slight deviation from a linear shift of the  $Y_0$  lines is observed in Fig. 6.8b. These effects can possibly be explained by the temperature dependence of an extended defect complex as discussed in section 6.11.

## 6.4 Phonon replica and two electron satellites

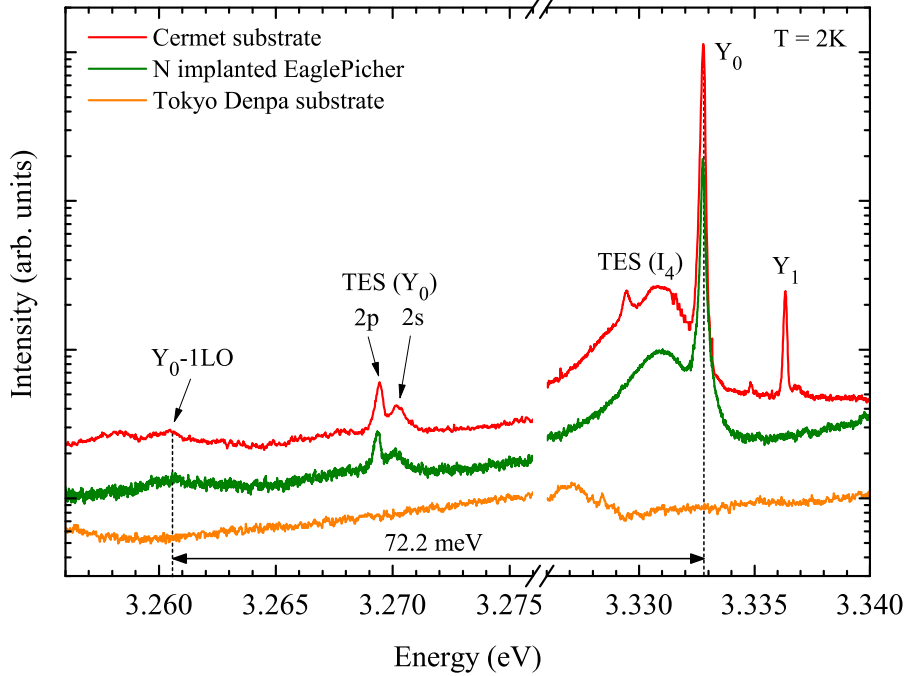


Figure 6.9: PL spectra of  $Y$  lines with the 1LO phonon replica and two electron satellites of the 3.3328 eV line. The LO and TES features are not observed in samples without pronounced  $Y_0$  line (Tokyo Denpa substrate).

Fig. 6.9 displays the low temperature PL spectra of the Cermet and EaglePicher samples in comparison to the substrate by Tokyo Denpa which does not exhibit any  $Y$  lines. At the low energy side of the 3.3328 eV line, a weak luminescence sideband with a maximum at 3.2606 eV is observed for the two samples with pronounced  $Y_0$  emission. The energy spacing to the 3.3328 eV line is 72.2 meV, matching precisely the energy of the LO phonons in ZnO [173]. The fact that this luminescence band is only present in samples with a strong  $Y_0$  line supports the attribution to a phonon replica. From the intensity ratio of the different LO-phonon replicas, the Huang-Rhys factor  $S$  [231] can be determined by the Poisson distribution [232, 233]

$$I_n = \exp(-S) \frac{S^n}{n!} \quad (6.1)$$

where  $n = 0$  corresponds to the zero-phonon line (ZPL) and  $n$  is the number of the phonon replica. The parameter  $S$  determines the mean number of created phonons and therefore describes the coupling strength of an electronic transition to the longitudinal optical polarization field. For the  $Y_0$  transition, a Huang-Rhys factor of  $S = 0.004 \pm 0.002$  is derived. This value is exceptionally small in relation to the spectral position of the  $Y_0$  line below the band gap.

Table 6.1: Energy of shallow and deeply bound excitons and their two electron satellite transitions.  $E_{loc}$  denotes the localization energy of the exciton,  $E_a$  the activation energy,  $E_D$  the donor binding energy, TES(2s) and TES(2p) the energies of the two electron satellites in the 2s and  $2p_{x,y}$  states,  $E_{1s-2p}$  and  $E_{2s-2p}$  the energy spacing between the exciton line and the specified TES transition.

exciton	energy $E$ (eV)	$E_{loc}$ (meV)	$E_a$ (meV)	$E_D$ (meV)	TES(2s) (eV)	TES(2p) (eV)	$E_{1s-2p}$ (meV)	$E_{2s-2p}$ (meV)
$I_4$	3.3628	13.1	13	46.1	3.3278	3.3287	34.1	-0.9
$I_6$	3.3608	15.1	15	51.5	3.3228	3.3220	38.8	0.8
$I_8$	3.3598	16.1	16	54.6	3.3191	3.3177	42.1	1.4
$I_9$	3.3567	19.2	19	63.2	3.3101	3.3061	50.6	4.0
$I_{10}$	3.3531	22.8	23	72.6	3.2986	3.2929	60.2	5.7
$Y_1$	3.3363	39.6	12	$-^a$	$-^b$	$-^b$	$-^b$	$-^b$
$Y_0$	3.3328	43.1	12	$-^a$	3.2702 $^c$	3.2694 $^c$	63.4 $^c$	0.8 $^c$

<sup>a</sup> These centers cannot be described by an effective mass approach.

<sup>b</sup> No TES states are observed due to the small intensities of the  $Y_1$  line.

<sup>c</sup> Electronic configuration of the excited states might be different for  $Y$  centers.

For free excitons, the value of the Huang-Rhys parameter is usually overestimated if based on the intensity of the zero-phonon line  $I_0$ . The reason is the large absorption in the range of the free exciton which results in an increased  $I_n/I_0$  ratio. In the case of strongly localized excitons, the opposite effect may occur as not all excitons contribute to phonon replicas [195, 234]. Particularly in confined structures such as quantum dots and quantum wells this effect can result in the determination of too small values of  $S$ . Consequently, only the intensities of the phonon replicas without the ZPL should be analyzed. Unfortunately, this is not possible for the  $Y_0$  line as no 2 LO phonon band is observed due to the extraordinary weak coupling. Since the energetic positions of the  $Y$  lines are far off the absorption edge of ZnO, an overestimation of the Huang-Rhys parameter due to absorption can be excluded. Concerning the latter effect, an influence of confinement cannot be completely ruled out due to the localization of the bound excitons. Consequently, the real Huang-Rhys parameter might be larger than the determined value, however certainly not more than one order of magnitude [234] which still represents a very weak coupling.

The small Huang-Rhys parameter for the  $Y_0$  transition seems to correlate with the small activation energy discussed in the previous section. Usually, the value of  $S$  is expected to increase as function of the localization energy [232, 235, 236]. In order to verify the validity of this relation for the deeply bound excitons, the Huang-Rhys factor of the  $Y_0$  line is compared with those of the three dominant bound exciton  $I_4$ ,  $I_6$ , and  $I_9$  in the Cermet sample. The presence of up to four

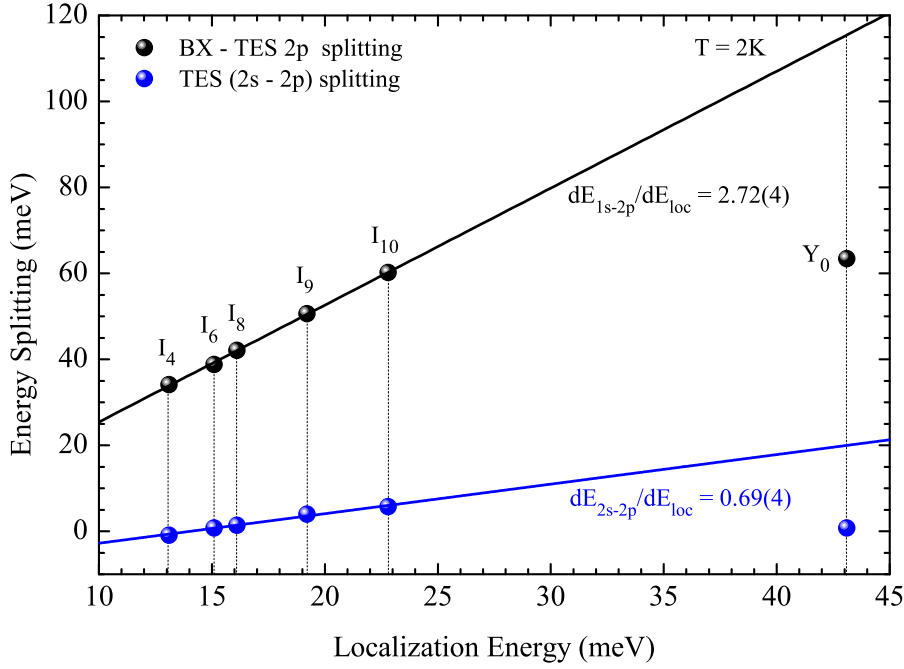


Figure 6.10: Energy splittings of bound excitons and TES states for shallow bound excitons [40] and the  $Y_0$  exciton line.

phonon replicas for these lines enables a reliable determination of their Huang-Rhys parameters. Using Eq. 6.1,  $S$  values of 0.052 ( $I_4$ ), 0.058 ( $I_6$ ), and 0.067 ( $I_9$ ) are derived by least squares fits which demonstrate the increasing phonon coupling with increasing localization energy. For the nitrogen related DAP emission at 3.235 eV in ZnO, an even stronger coupling with  $S = 0.85$  was reported [66]. Apparently, the exceptionally small Huang-Rhys factor of the  $Y_0$  center violates the discussed relation with its large localization energy. The weak coupling of the  $Y$  lines may be explained if they involve recombinations at extended defects, within which strong delocalization of the binding potential occurs as suggested by Dean for the  $Y$  and  $Z$  lines in ZnSe [237]. This property of the extended defect is discussed in section 6.11 where different models for the binding centers of the  $Y$  lines are considered.

Apart from the weak 1 LO sideband another luminescence structure on the low energy side of the  $Y_0$  line is apparent in Fig. 6.9. At 3.2702 eV and 3.2694 eV, two peaks are observed which are not present in samples without the 3.3328 eV line. Based on this exclusive appearance in combination with the  $Y_0$  line, a correlation between these peaks is evident. The transitions are identified as the  $2s$  and  $2p$  TES transitions of the  $Y_0$  exciton. The energy spacing of the bound exciton lines to the TES  $2p$  states as well as the size of the  $2s - 2p$  splitting are shown for the excitons  $I_4$  to  $I_{10}$  and the  $Y_0$  in Fig. 6.10. The  $1s - 2p$  and  $2s - 2p$  splitting increase linearly

as function of the localization energy for the shallow bound excitons  $I_4$  to  $I_{10}$  [40]. However, the TES spacing of the  $Y_0$  does not follow this relationship. Instead, significantly smaller values for the  $1s - 2p$  and  $2s - 2p$  splitting are obtained. The size of the  $1s - 2p$  splitting of the  $Y_0$  line indicates a small binding energy of the electron in the complex ground state. Thereby, the binding energy of the ground state electron seems to be of the order of the shallow donor binding energy  $I_{10}$  (see Table 6.1). At the same time, the  $2s - 2p$  splitting for the  $Y_0$  line is smaller than those for the  $I_{10}$  line. The fact that the TES splitting of the  $Y$  lines does not follow the relation for the  $I$  lines provides important information about the possible defect centers as discussed in detail in section 6.11.

Similar luminescence features were also observed by Wang et al. [202] in ZnO crystals grown by EaglePicher using the seeded chemical vapor transport method. These samples showed, apart from the 3.333 eV emission, weak emission lines at 3.26 eV and 3.27 eV. Both lines disappeared at temperature above 15 K in agreement with the discussed temperature dependence of the 3.333 eV line. Despite the mismatching LO phonon energy, the 3.27 eV emission was attributed to a phonon sideband of the 3.333 eV transition [202]. Instead, it is suggested in this work that the 3.26 eV line originates from the first LO phonon replica with an energy spacing of about 73 meV and that the 3.27 eV emission in the work of Wang et al. may originate from the not resolved  $2s/2p$  two electron satellite transitions of the 3.333 eV line.

## 6.5 Absorption in magnetic fields

The attribution of the 3.333 eV emission line to a deeply bound exciton is not unambiguous if solely based on luminescence studies. The difficulties in a doubtless identification arise mainly from the energetic proximity to the two electron satellites (TES) of the dominant shallow bound excitons. These features may also possess narrow transition lines in the same spectral range and exhibit a similar thermal dependency. Several authors reported an emission line in close proximity to the 3.333 eV transition which is attributed to a TES transition of a donor bound exciton at 3.363 eV possibly related to the hydrogen donor bound exciton  $I_4$  [89, 121]. In fact, pronounced TES lines around 3.330 eV are also observed in Fig. 6.2. In order to distinguish these transitions from the deeply bound exciton lines, absorption measurements are of great use. Due to the nature of the TES lines which occur when a donor is left in an excited state after the recombination of a bound exciton, these lines will not appear as absorption lines in transmission spectroscopy.

Fig. 6.11 shows the transmission spectrum of the nitrogen implanted ZnO single crystal from EaglePicher in the energetic range of the 3.333 eV transition. In

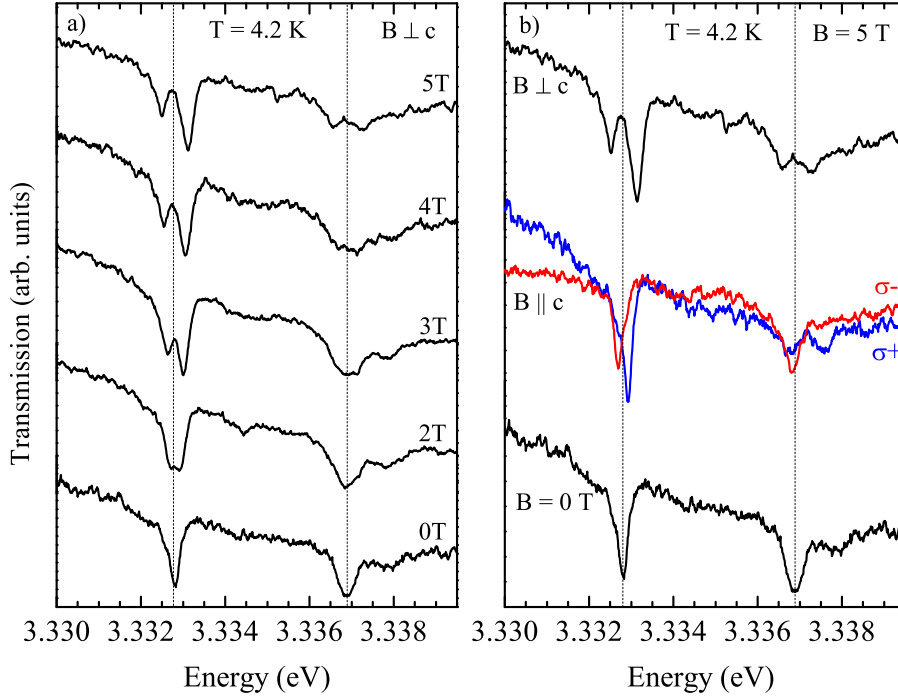


Figure 6.11: Magneto-optical transmission spectroscopy of deeply bound excitons in N implanted ZnO single crystals. Left (a): The spectra were recorded in Voigt configuration with field strengths between 0 T and 5 T. Right (b): Top:  $\mathbf{B} \perp c$  at 5 T, center:  $\mathbf{B} \parallel c$  at 5 T with polarization directions  $\sigma^+$  and  $\sigma^-$ , zero-field transmission. All spectra are recorded at a temperature of 4.2 K.

addition to the zero field spectrum, absorption spectra are displayed for variable external magnetic field strengths up to 5 T. In the zero-field spectrum, a strong absorption line appears at 3.3328 eV which precisely matches the transition energy in the PL spectra (Fig. 6.2). The presence of this line in the absorption and emission spectra excludes the possibility of a two electron satellite transition. For an applied magnetic field, the splitting of the  $Y_0$  line at 3.3328 eV into two Zeeman components is clearly visible. The size of the splitting for a given magnetic field strength is in excellent agreement with the observed splitting in the magneto-PL spectra in Fig. 6.4c. From the intensity ratio of the two Zeeman components in Fig. 6.11a, it is obvious that the lower energy peak decreases in intensity with increasing magnetic field compared to the higher energy absorption line. The observed thermalization can only be explained if the dominant splitting in Fig. 6.7 exists in the ground state and not in the excited state of the bound exciton complex (chapter 4.4.2). With increasing magnetic field, the ground state splitting increases leading to a lower occupation of the higher energy ground state level at low temperatures. This leads to the observed decrease in the intensity of the low energy absorption line. Con-

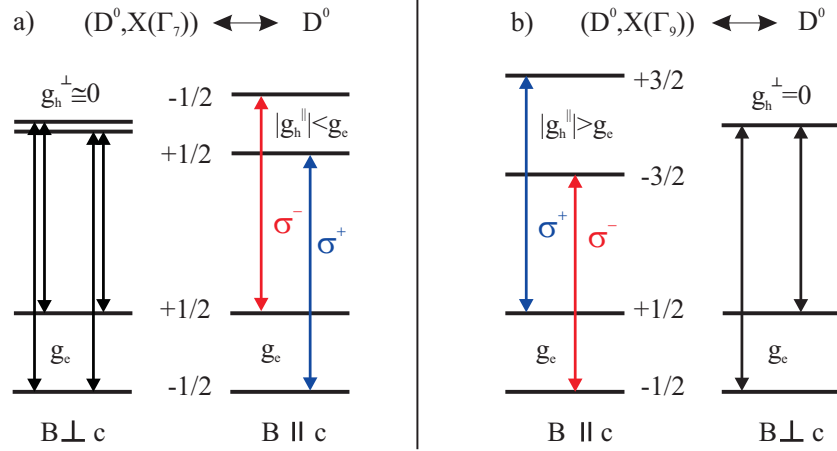


Figure 6.12: Level scheme of neutral donor bound exciton transitions involving hole states with  $\Gamma_7$  and  $\Gamma_9$  symmetry in a constant magnetic field. The selection rules for circular polarized optical transitions are indicated.

sequently, the magnetic thermalization in absorption provides additional evidence that the  $Y_0$  exciton is bound to a donor. The same argumentation also applies for the thermalization of the  $Y_1$  transition at 3.3363 eV.

In addition to the 3.3328 eV line, a second absorption line at 3.3369 eV is observed in Fig. 6.11 which is not present in the PL spectra in Fig. 6.2. Despite the close proximity to the  $Y_1$  transition at 3.3363 eV, the absorption line at 3.3369 eV is of different origin as will be demonstrated. The energy spacing of 4.1 meV is close to the reported energy distance of the A and B valence bands of 4.7 meV at the  $\Gamma$  point [70,100] and in good agreement with the in chapter 3.4.2 studied A-B spacing between the recombination lines of shallow donor bound excitons of 4.5 meV for the  $I_6$  to  $I_9$  and about 4.1 meV for the  $I_4$ . Thus, it is possible that the higher energy absorption line results from the same defect bound exciton involving a hole state from the B valence band. Since the B valence band has  $\Gamma_9$  symmetry (chapter 5), the 3.3369 eV transition should exhibit a crossing of the inner two Zeeman components in angular dependent measurements as described in section 5.2.3. Unfortunately, the intensities of the Zeeman split absorption lines of the 3.3369 eV transition are too small for a doubtless attribution at high magnetic fields so that no reliable angular dependent data are available. However, the absorption spectra in Faraday configuration (Fig. 6.11b) display an interesting difference between the two absorption lines. In agreement with the magneto-PL spectra in Fig. 6.4a and previous studies of donor bound exciton in ZnO [103,104,115], the low energy Zeeman component of the 3.3328 eV transition is seen for  $\sigma^-$  polarized light whereas the high energy Zeeman component is active for  $\sigma^+$  polarized light. A comparison of the intensity

of the Zeeman split lines reveals a stronger absorption for the  $\sigma^+$  transition. This is in agreement with the level scheme for a donor bound exciton with  $\Gamma_7$  hole symmetry in Fig. 6.12a, since the transition from the stronger populated ground state at low temperatures is  $\sigma^+$  polarized. By contrast, the opposite intensity ratio between the circular polarized absorption lines in a parallel magnetic field is expected for a donor bound exciton which involves a hole state with  $\Gamma_9$  symmetry. In this case, the lower energetic  $\sigma^-$  transition originates from the lowest most occupied energy level (Fig. 6.12b). This intensity distribution is indeed observed for the second absorption line at 3.3369 eV which exhibits strong absorption in the low energy  $\sigma^-$  component, but only weak absorption for the  $\sigma^+$  polarized high energy transition. Consequently, it is suggested that the exciton transition at 3.3369 eV belongs to the same defect center as the  $Y_0$  but involves a hole from the B valence band with  $\Gamma_9$  symmetry.

## 6.6 Excited states

For a detailed analysis of the excited states and energy transfer processes, the excitation channels of the different emission lines are studied by photoluminescence excitation (PLE) spectroscopy. Fig. 6.13a shows the PL spectrum of the ZnO Cermet substrate, excited by a pulsed tunable dye laser at an energy of 3.4440 eV. Solid vertical lines mark the peaks for which the PLE spectra are shown. The excitation channels of the  $Y_0$  line at 3.3328 eV (Fig. 6.13b) are compared with those of the two electron satellite transitions of the  $I_4$  (Fig. 6.13c) and  $I_6$  (Fig. 6.13d). The TES transitions exhibit a large quantity of narrow excitation channels in the range of the shallow donor bound excitons. The strong excitation peak with the lowest energy in each of the TES spectra represents the ground state of the related exciton transition. These excitation channels are observed at 3.3628 eV ( $I_4$ ) and 3.3608 eV ( $I_6$ ) in agreement with the energy of these excitons in the PL spectrum as indicated by the dashed lines. The excitation channels at the high energy side of these lines are equal to the excited states of the related bound excitons  $I_4$  and  $I_6$  as shown by the values in Table 6.2. The observed excitation resonances can be divided into groups according to the different excitation mechanisms as discussed in chapter 3.4.2. With the lowest energy spacing, the vibrational and rotational states of the excitons ( $D^0, X_A$ ) are observed (1-2 meV). Since the differences between these energy levels are not resolved, the vibrational-rotational states are summarized to one energy level which is labeled  $Y_i^*$  or  $I_i^*$  in Fig. 6.13 and Table 6.2. At an energy spacing between 4.1 and 4.5 meV, the excitation resonance originates from the formation of an exciton with a hole from the B valence band ( $D^0, X_B$ ). The third group of excitation channels consists of electronic excited states of the exciton with energies greater than 5 meV. Finally, energy transfer also occurs via the free exciton polaritons above 3.375 eV.

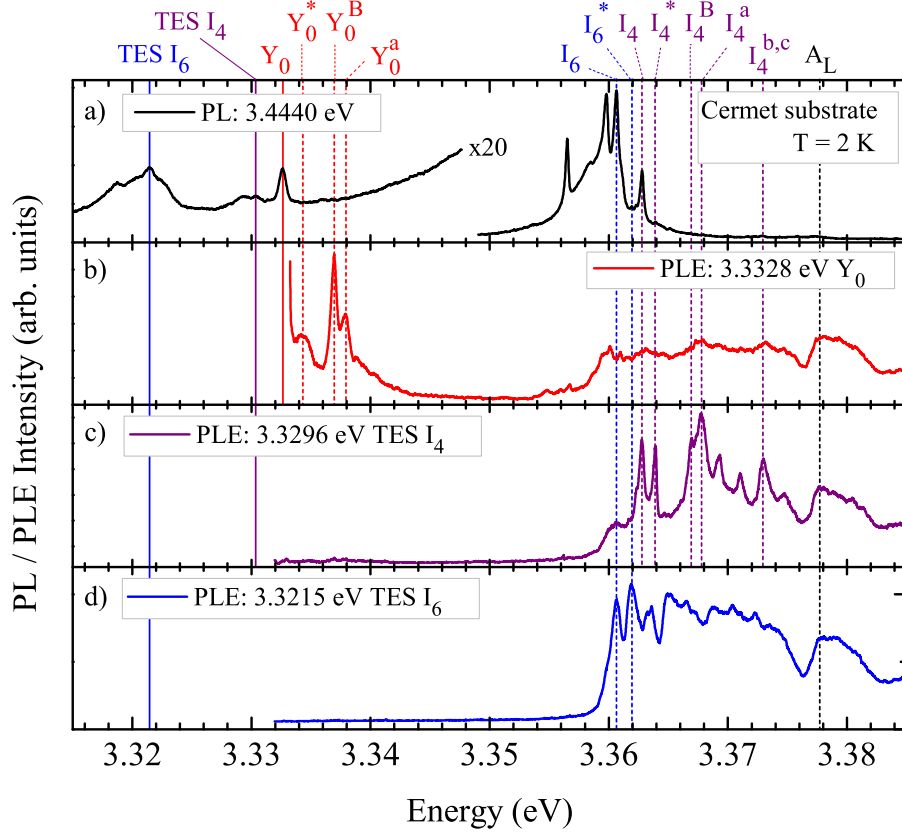


Figure 6.13: PL and PLE spectra of the ZnO Cermet substrate at  $T = 2$  K. (a) PL spectrum excited by a pulsed tunable dye laser at an energy of 3.4440 eV, (b-d) Excitation spectra of  $Y_0$  (3.3328 eV), TES  $I_4$  (3.3296 eV), and TES  $I_6$  (3.3215 eV).

Similar to the shallow bound excitons and their two electron satellites, the excitation band in the range of the A and B free exciton polaritons shows an efficient excitation of the  $Y_0$  line by the capture of free excitons. However, in the range of the shallow bound excitons, only a weak and broadly distributed excitation band is observed. In particular, no sharp excitation channels in this region are observed which could be attributed to a specific bound exciton. This demonstrates that the  $Y$  lines are not correlated to any other impurity bound excitons and clearly differentiates these transitions from the adjacent two electron satellites. The most striking features in the excitation spectrum of the  $Y_0$  line are the strong excitation resonances at energy spacings of 1.2, 4.1, and 5.1 meV. These lines are similar to the excitation channels of shallow bound excitons and are attributed to vibrational-rotational excited states ( $Y_0^*$ ), an exciton involving a hole from the B valence band ( $Y_0^B$ ), and the first electronic excited state  $Y_0^a(0, 1)$ . The values in brackets (see also Table 6.2) denote the orbital and angular momentum quantum numbers of the

Table 6.2: Excited states of the defect bound exciton  $Y_0$  and the donor bound excitons  $I_4$  and  $I_6$ . ( $D^0, X$ ) labels the donor bound exciton in the  $1s$  ground state and TES( $2p$ ) denotes the  $2p_{x,y}$  donor excited state (two electron satellite) [40]. The excited state energies are given in relation to the ( $D^0, X$ ) ground state energy. Experimental values are determined by the PLE spectra shown in Fig. 6.13. Theoretical values are provided as calculated in Ref. [79]. All values are given in meV.

	$Y_0$ ( $D^0, X$ )	$I_4$ TES( $2p$ )	$I_4$ ( $D^0, X$ )	$I_6$ TES( $2p$ )	$I_6$ ( $D^0, X$ )		
	3.3328 eV	3.3296 eV	3.3628 eV	3.3215 eV	3.3608 eV		
	(exp.)	(exp.)	(exp.)	(exp.)	(exp.)	(calc.)	(calc.)
$I_i^*$	1.2	1.1	1.1	1.3	1.4	1.06	1.32
$I_i^B$	4.1	4.1	4.1	4.5	4.5	-	-
$I_i^a(0, 1)$	5.1	5.1	5.2	5.9	5.9	5.8	5.9
$I_i^b(1, 1)$	-	10.2	10.3	11.6	11.5	11.9	12.1
$I_i^c(0, 2)$	-	10.2	10.3	11.6	11.7	12.0	12.4

exciton. Apparently, the (0, 1) excited state of the  $Y_0$  has the same energy (5.1 meV) as the (0, 1) excited state of the  $I_4$ , whereas greater values of the excited states are found for stronger localized excitons such as the  $I_6$ . Based on the energy of the (0, 1) excited state, higher electronic excited states of  $Y_0$  should be expected above 10 meV. However, no excitation channels are observed in this range. The absence of higher excited states correlates with the small activation energy of about 12 meV, since higher energies result in the detachment of a weakly bound hole as discussed in section 6.11. It should be noted, that the strongest excitation line occurs at an energy of 3.3369 eV ( $Y_0^B$ ), which coincides with the energy of the absorption line in the magneto-absorption spectra (Fig. 6.11) and confirms the attribution of this transition to a  $Y_0$  exciton involving a hole from the B valence band. The large intensity of this line indicates that the capture of a free hole at the defect complex constitutes an efficient alternative excitation channel apart from the energy transfer from free excitons. In accordance with these results, similar excitation channels for the  $Y_1$  and  $Y_2$  lines are observed although the oscillator strength is much smaller for these transitions.

## 6.7 Recombination dynamics

The question arises if the different excitation mechanism also affect the excitation and recombination dynamics of the shallow and deeply bound excitons. In order to address this issue, time resolved photoluminescence spectroscopy is performed. In general, time resolved spectroscopy can provide information about the dynamical processes in semiconductors including the excitation, recombination, relaxation, and

dephasing processes. The lifetimes of the excitonic transitions are commonly used as an indicator for the defect density of the samples [238]. Therefore, many works investigate the decay dynamics of the free exciton luminescence at room temperature. These lifetimes differ significantly in bulk samples, epilayers, and nanostructures. The longest reported lifetimes of the free exciton emission in ZnO are 3.8 ns for the non-radiative process in ZnO epilayers [78], a biexponential decay with lifetimes of  $\tau_1=1$  ns and  $\tau_2=14$  ns in single crystals [238], and a lifetime of up to 27.7 ns in ZnO tetrapods [239]. In order to compare the dynamics of the different bound exciton transitions, room temperature measurements are not applicable as the bound excitons in ZnO typically dissociate at temperatures below 80 K. Consequently, the recombination dynamics of the various bound exciton transitions are studied by time resolved photoluminescence (TRPL) at a temperature of  $T = 2$  K.

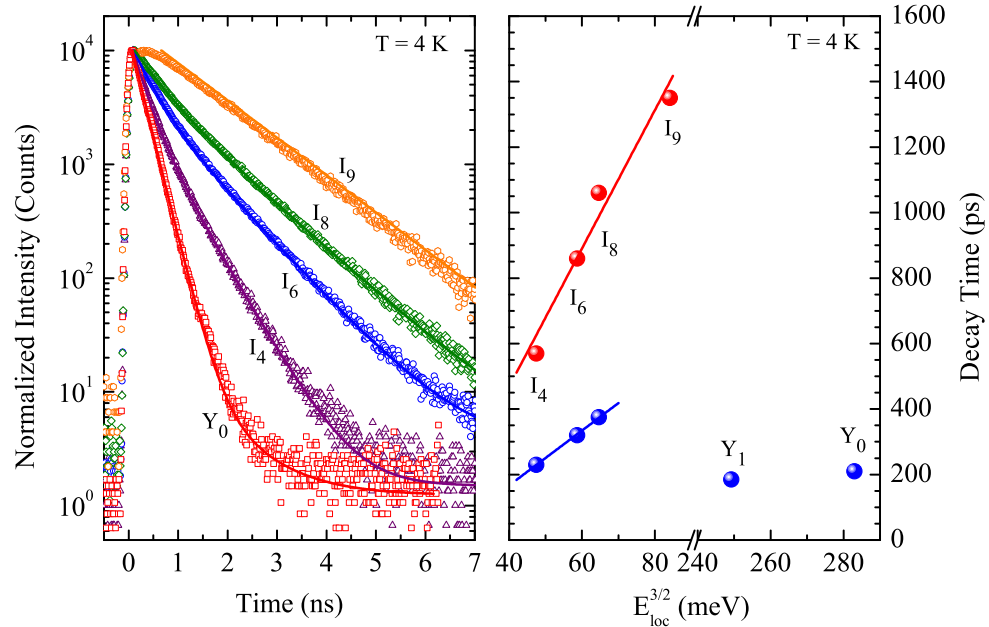


Figure 6.14: (a) Transients of the bound excitons  $I_4$ ,  $I_6$ ,  $I_8$ ,  $I_9$ , and  $Y_0$  at a temperature of 2 K. (b) Lifetimes as function of the localization energy: dots indicate measured values, solid lines represent fits based on the model by Rashba et al. [240].

Fig. 6.14a displays the transients of bound exciton lines  $I_4$  to  $I_9$  as well as the deeply bound exciton  $Y_0$  at 3.3328 eV together with their fits. The bound exciton lines  $I_4$ ,  $I_6$  and  $I_8$  are well described by the biexponential decay function  $A_1 \exp(-t/\tau_1) + A_2 \exp(-t/\tau_2)$  with a fast decay constant  $\tau_1$  between 230 ps and 375 ps and a slow decay constant  $\tau_2$  of 570 ps to 1060 ps. The lifetimes and their amplitude ratio  $A_2/A_1$  are listed in Table 6.3. This ratio increases towards longer lifetimes which expresses the increasing impact of the long time constant for excitons

Table 6.3: Lifetimes of shallow and deeply bound excitons at 2 K.  $E_{loc}$  denotes the localization energy of the exciton,  $\tau_r$  the raise time,  $\tau_1$  and  $\tau_2$  the decay times, and  $A_2/A_1$  the amplitude ratio of the decay processes.

exciton	energy (eV)	$E_{loc}$ (meV)	$E_a$ (meV)	$\tau_r$ (ps)	$\tau_1$ (ps)	$\tau_2$ (ps)	$A_2/A_1$
$I_4$	3.3628	13.1	13	-	230	570	0.33
$I_6$	3.3608	15.1	15	-	320	860	0.56
$I_8$	3.3598	16.1	16	-	375	1060	1.01
$I_9$	3.3567	19.2	19	200	-	1350	-
$Y_1$	3.3363	39.6	12	-	185	-	-
$Y_0$	3.3328	43.1	12	-	210	-	-

with larger localization energy. The biexponential decay indicates the presence of a second initial decay channel in addition to the exciton recombination which saturates after a certain time period [241, 242]. In the case of the shallow bound exciton, this channel might be the capture process of the excitons to deeper (nonradiative) centers [242]. Therewith, the initial decay time  $\tau_1$  corresponds to the combination of recombination and capture processes  $1/\tau_1 = 1/\tau_{rec} + 1/\tau_{cap}$ , whereas the second decay time constant  $\tau_2$  corresponds to the recombination time  $\tau_{rec}$ .

For the  $I_9$  bound exciton, only the long time constant  $\tau_2$  is observed with a monoexponential decay time of 1.35 ns. In addition, a raise time  $\tau_r$  of 200 ps occurs for the  $I_9$  bound exciton which corresponds to the nonradiative relaxation time of free excitons determined by capture and trapping processes at the impurities [241, 243]. The fact that no rise time for other shallow bound exciton centers is observed indicates that the capture process of the free excitons to these centers is saturated very fast. In the case of the  $I_9$ , two reasons might enable the observation of the rise time. First, the initial capture of the free excitons might be slower for the deeper  $D^0$  donor corresponding to the  $I_9$  line compared to the shallower ones. Second, an additional channel exists for the creation of neutral donors  $D^0$  and donor bound excitons  $D^0X$  via the capturing of free electrons by the ionized  $D^+$  donors [241] which might contribute to the observed raise time. This charge transfer process from ionized to neutral bound exciton centers related to the same impurity is also demonstrated by excitation resonances in PLE measurements [79, 106].

The measured lifetimes of the various bound exciton transitions are plotted as function of the localization energy in Fig. 6.14b. Apparently, the time constants of the shallow bound excitons  $I_4$  to  $I_9$  are proportional to  $E_{loc}^{3/2}$  in agreement with earlier studies by Heitz et al. [244]. The observed relation for the shallow bound excitons can be explained by the model of Rashba and Gurgenishvili [240]. It is

well known that the radiative lifetime is inversely proportional to the oscillator strength [245, 246] with

$$\tau = \frac{ne^2\omega^2}{2\pi\epsilon_0m_0c^3f}, \quad (6.2)$$

where  $f$  is the oscillator strength of the optical transition,  $\omega$  is its frequency,  $n$  is the refractive index, and the other symbols have their usual meaning. According to Rashba and Gurgenishvili [240, 247], the oscillator strength of bound excitons is proportional to the volume of the region occupied by the electron-hole complex where coherent oscillations of the electron polarization occur. In the case of an exciton which is weakly bound to the neutral donor center as a whole quasi-particle, i.e. for  $E_{loc} \ll E_{ex}$ , the radius of this region is determined by the localization energy as  $a_{BE} \propto 1/\sqrt{E_{loc}}$ , where  $E_{ex}$  is the binding energy of the electron and hole in the exciton and  $a_{BE}$  is the Bohr radius of the bound excitons. Consequently, the radiative lifetime  $\tau$  is proportional to the localization energy

$$\tau \propto 1/f \propto 1/a_{BE}^3 \propto E_{loc}^{3/2}. \quad (6.3)$$

Despite the fact that this model is sufficient for a qualitative analysis, it should be noted that many contributions are neglected such as e.g. correlation effects as was pointed out by Sanders and Chang [248]. A corresponding effect is observed in confined potentials such as quantum wells and quantum dots. As the size of the nanostructure is reduced, the coherence volume of the exciton is reduced leading to a decreasing oscillator strength and an increasing radiative lifetime [249–251].

Returning to the time constants of the  $Y$  lines in Fig. 6.14b, it is apparent that these transitions strongly violate the discussed relation of the shallow bound excitons between localization energy and recombination dynamics. Despite the large localization energy of these excitons, lifetimes in the range or even shorter than for the shallow bound exciton  $I_4$  are observed. This discrepancy reminds of the unusually small activation energies and TES splittings of the  $Y$  lines with regard to their localization energy. Based on the lifetimes of the shallow bound excitons  $\tau_1$ , the observed lifetimes of the  $Y$  lines would correlate to a binding energy of 12.0-12.7 meV. This value is in good agreement with the previously determined activation energy  $E_a$  for these lines by temperature dependent PL measurements. The short lifetimes of the deeply bound excitons are not surprising since the condition  $E_{loc} \ll E_{ex}$  is not satisfied anymore and, as was discussed before, the exciton is not bound as a whole quasi-particle at these centers. In this model, the lowest activation energy  $E_a$  corresponds to the detachment of one of the particles forming the exciton. The coherence volume of the exciton is then determined by the largest orbit and hence by  $E_a$  instead of  $E_{loc}$ .

## 6.8 Uniaxial pressure coefficients

The application of uniaxial pressure leads to a deformation of the hexagonal lattice which enables the controlled variation of the  $c/a$  lattice ratio. In a wurtzite semiconductor with the space group  $C_{6v}^4$ , a reduction of symmetry is given for any uniaxial pressure direction not parallel to the  $c$ -axis. The lifting of degeneracy caused by this symmetry reduction leads to a splitting of the optical transition lines. For pressure parallel to the  $c$ -axis ( $\mathbf{P} \parallel \mathbf{c}$ ), only a shift of the exciton energy levels occurs as the symmetry is unchanged. In this section, uniaxial pressure parallel to the  $c$ -axis is applied in order to clarify if the previously observed differences between shallow bound excitons and the  $Y$  lines manifest themselves in the pressure coefficients of these deeply bound excitons, too.

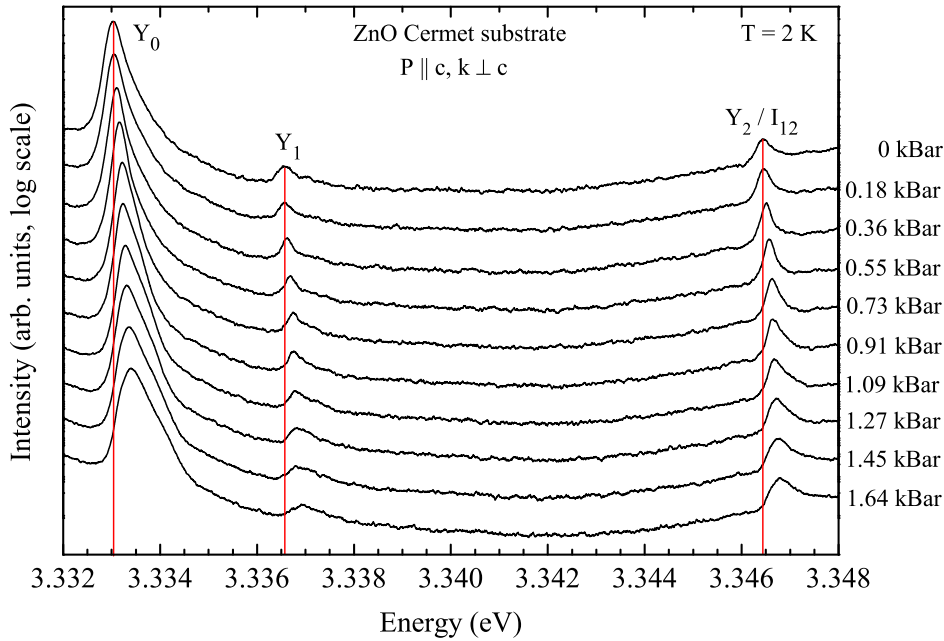


Figure 6.15: PL spectra of the Cermet substrate as function of external uniaxial pressure  $\mathbf{P} \parallel \mathbf{c}$  between 0 kBar and 1.64 kBar in the range of the deeply bound exciton lines at  $T = 2$  K. Vertical red lines mark the peak energies without external pressure.

Fig. 6.15 displays the PL spectra of the Cermet substrate in the range of the TES and  $Y$  transitions as function of uniaxial pressure at  $T = 2$  K. In the depicted spectral range, the lines  $I_{12}/Y_2$  (3.3465 eV),  $Y_1$  (3.3363 eV), and  $Y_0$  (3.3328 eV) are visible. With increasing pressure  $\mathbf{P} \parallel \mathbf{c}$ , all lines exhibit a shift towards higher energies. This shift is caused by the compressive strain along the  $c$ -axis due to the external pressure. The energetic position of each line is carefully determined and plotted as function of the pressure onto the sample in Fig. 6.16b. From the linear fits

Table 6.4: Uniaxial pressure coefficients of free, shallow, and deeply bound excitons for pressure  $\mathbf{P}\parallel\mathbf{c}$  at 2 K.  $E_{loc}$  denotes the localization energy of the exciton,  $E_a$  the activation energy,  $\partial E/\partial P$  the uniaxial pressure coefficient in absolute energies, and  $\partial E_{loc}/\partial P$  the pressure coefficient in localization energies.

exciton	energy $E$ (eV)	$E_{loc}$ (meV)	$E_a$ (meV)	$\partial E/\partial P$ (meV/GPa)	$\partial E_{loc}/\partial P$ (meV/GPa)
$A_T$	3.3759	-	-	4.71	-
$I_4$	3.3628	13.1	13	2.79	1.92
$I_6$	3.3608	15.1	15	2.84	1.87
$I_8$	3.3598	16.1	16	2.99	1.72
$I_9$	3.3567	19.2	19	3.37	1.34
$Y_2/I_{12}$	3.3465	29.4		1.95	2.76
$Y_1$	3.3363	39.6	12	2.15	2.56
$Y_0$	3.3328	43.1	12	2.09	2.62

of these values, the uniaxial pressure coefficients of the observed bound exciton transitions are determined (Fig. 6.16a) and listed in Table 6.4. For the shallow bound excitons, pressure coefficients between 2.79 meV/GPa ( $I_4$ ) and 3.37 meV/GPa ( $I_9$ ) are derived. By contrast, the  $Y_0$ ,  $Y_1$ , and  $Y_2/I_{12}$  bound excitons show a significantly smaller pressure dependence upon uniaxial compression with values around 2.1 meV/GPa. Based on the comparable pressure coefficients of  $Y_2/I_{12}$  with  $Y_0$  and  $Y_1$ , these three lines are attributed to the same group of deeply bound exciton transitions. If the  $I_{12}$  belongs to the 'shallow' bound excitons ( $I$ -lines), a significantly higher uniaxial pressure coefficient would be expected which scales with the localization energy  $E_{loc}$  or rather the associated donor binding energy  $E_D$ . However, this is obviously not the case. In order to express this difference also in the name of the exciton recombination line, it is suggested to label to the 3.3465 eV transition in ZnO  $Y_2$  instead of  $I_{12}$ . It should be noted that the  $Y_2$  was not visible in the ZnO substrate prior to the uniaxial pressure measurements (see also Fig. 6.2). Therefore, it is likely that the  $Y_2/I_{12}$  emission line originates from newly created structural defects due to the application of uniaxial pressure.

As can be seen from Fig. 6.16a, all bound exciton lines display a smaller energy shift as function of uniaxial pressure than the free exciton line  $A_T$ . Since the localization energy is given by the distance between the free exciton  $A_T$  and the respective bound excitons, this indicates the increasing of the localization energy upon uniaxial compression for all bound exciton lines. For the shallow bound excitons ( $I_i$ ), the influence of the pressure on the localization energy is larger in the case of shallow centers and smaller for deeper centers. In other words, the absolute pressure coefficients of the bound excitons are increasing with increasing localization energy.

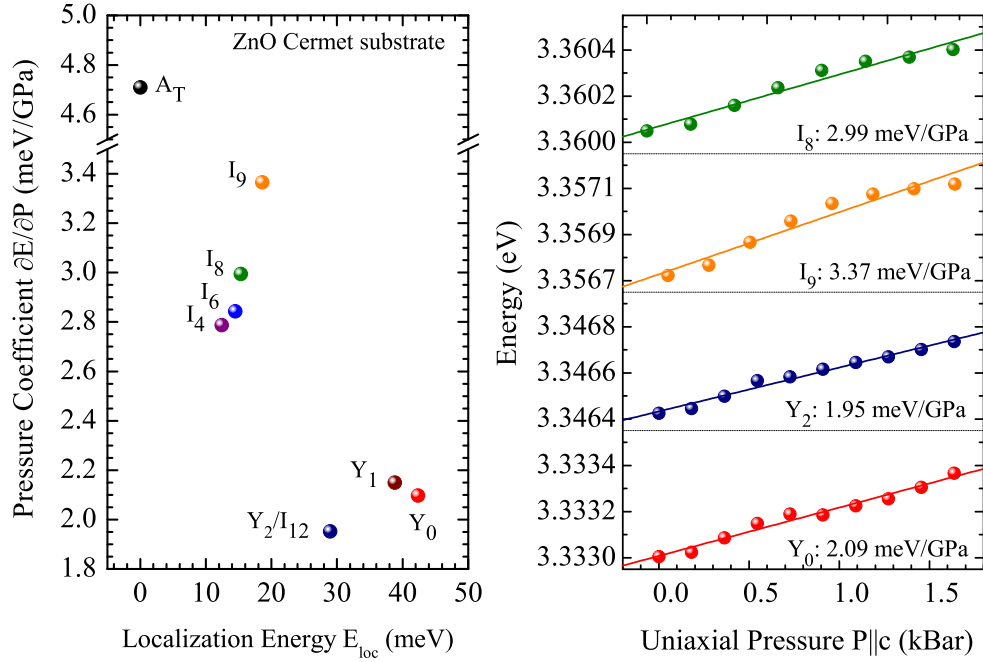


Figure 6.16: (a) Pressure coefficients for shallow and deeply bound excitons, (b) shifting behavior of the  $I_8$ ,  $I_9$ ,  $Y_2/I_{12}$ , and  $Y_0$  lines as function of applied uniaxial pressure.

However, the largest effect of the uniaxial compression in relation to the pressure dependence of the free exciton (smallest absolute pressure coefficient) is found for the  $Y_0$ ,  $Y_1$ , and  $Y_2/I_{12}$  lines (Table 6.4) which indicates a distinctly different structure of the  $Y$  defect cores in comparison to the shallow bound excitons. The observed pressure dependence is similar to the previously discussed decay dynamics, where the lifetimes (absolute pressure coefficients) increase as function of the localization energy for the shallow bound excitons whereas the lifetimes (absolute pressure coefficients) of the deeply bound excitons do not scale with the localization energy and are considerable smaller. Possible mechanisms of the additional stress effect on the deeply bound exciton complexes are discussed in section 6.11.

## 6.9 Spatial distribution of defect centers

In order to study the structure and distribution of the defects related to the emission of the different bound exciton lines, monochromatic cathodoluminescence images were recorded at low temperature. Fig. 6.17 shows CL images at two different sample positions at the energy of the  $Y_0$  emission line in comparison to the adjacent two electron satellite (TES) emission of the  $I_4$  bound exciton. Apparently, the two

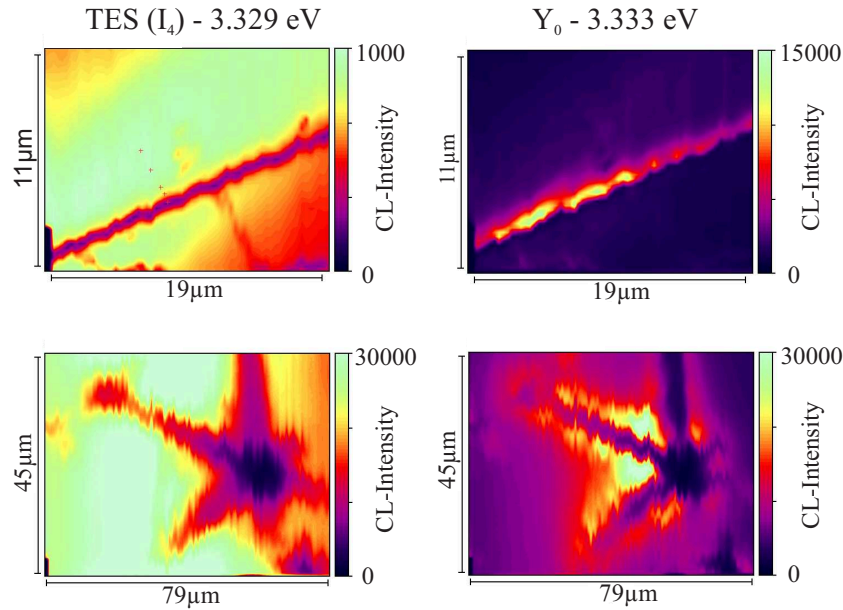


Figure 6.17: Monochromatic CL images in the vicinity of structural defects in ZnO at the spectral positions of the TES( $I_4$ ) (left) and  $Y_0$  (right) emission lines. Top: linear crack, bottom: hexagonal star-like defect.

emission peaks originate from distinctly different spatial area. For the TES luminescence, a mostly uniform distribution in the undistorted areas of the surface is observed. By contrast, the  $Y$  lines show the strongest intensity in the direct vicinity of linear cracks and from within the branches of hexagonal star-like defects. The intense  $Y_0$  luminescence originating from areas with strong local distortions in the crystal lattice confirms that these lines are related to extended structural defects. Confocal micro-PL scans further indicate a weaker intensity dependence of the  $Y$  lines on the focus position compared to the  $I$  lines. In the case of surface localized states, the opposite behavior would be expected. Another argument against surface related defects is given by the absence of these lines in nanostructures with dimension below 100 nm as they exhibit an increased surface to volume ratio [192,194,196,252]. Thus, it is concluded that the  $Y$  lines originate from defect centers such as dislocations which are not surface related. This is similar to the basal plane stacking faults giving rise to the 3.31 eV transition as discussed by Schirra et al. [189]. A possible explanation for the smaller focal dependency could be given by the larger excitation volume of these lines due to reabsorption of light from bound exciton emissions. The efficient capture of charge carrier to these centers as well as the significantly smaller absorption coefficient at the energy of deeper bound exciton emission lines in comparison to the above band edge laser excitation might lead to an excitation of defect centers well beyond the penetration depth of the 266 nm and

325 nm lasers. Therefore, a reduced dependence of the focal position in the samples should be expected.

## 6.10 Defect bound excitons in other compound semiconductors

Dean et al. first reported similar luminescence peaks in ZnSe labeled *Y* and *Z* which were attributed to localized recombinations within extended defects, involving a non-central force electronic system [237, 253]. In particular, a strong intensity of these lines was observed in the vicinity of heteroepitaxial interfaces in CVD grown samples as well as cut bulk samples. Similar observations of excitonic recombinations at structural defects have also been reported in many other II-VI and III-V semiconductors such as e.g. ZnTe, CdTe, ZnS, CdS, GaN and GaP [207, 209, 254–256]. Naumov et al. [254] discovered the intensity of *Y* line emissions in ZnTe epilayers to be a function of the lattice mismatch between layer and substrate and concluded that the observed luminescence is related to recombinations of excitons bound to extended structural defects, which should be represented by misfit dislocations. Comparable transition lines were also found in CdTe which were attributed to excitons bound to structural defects such as twins, dislocations or stacking faults [255]. In addition, Hoffmann and Gutowski [209, 256] performed cathodoluminescence wavelength imaging and magneto-optical Zeeman studies on CdS specimen. Several luminescence lines were attributed to defect bound excitons associated with screw dislocations. The Zeeman splitting of these lines was found to be rather isotropic in contradiction to the usual anisotropy for recombinations at point defects under the influence of the localized crystal field. It was concluded that the observed emission lines are related to deep excitons bound to dislocations, from which two lines exhibited an ionized-donor-complex like behavior. The presence of emission lines related to defect bound excitons in such a variety of different compound semiconductors impressively demonstrates the relevance of extended structural defects and strongly suggests the presence of extended defect bound exciton complexes with similar properties in ZnO.

## 6.11 Discussion of possible defect models

So far, distinctly different properties for the *Y* lines compared to the *I* lines were presented by a variety of different experimental techniques. Within this section, these results are compared and possible defect models for the *Y* lines are discussed. Thereto, the main results are briefly summarized as basis for the following discussion.

- (1) The *Y* lines are related to excitonic recombinations from a complex consisting

of two electrons and one hole with  $\Gamma_7$  symmetry (section 6.2). This configuration is similar to excitons bound to neutral shallow donors ( $I$  lines). The complex centers act as additional donors in ZnO.

(2) The lowest activation potential  $E_a$  (12 meV) for the  $Y$  centers is significantly smaller than the localization energy  $E_{loc}$  (about 40 meV) and the exciton binding energy  $E_{ex}$  (60 meV). The activation energy  $E_a$  does not correspond to the detachment of the exciton as a whole quasiparticle indicating that one of the particles (electron) forming the exciton is bound more deeply to the defect core while the second particle (hole) is weakly bound. The localization energy of the exciton in such a complex is given by

$$E_{loc} = E_{2e} - E_e + E_a - E_{ex}. \quad (6.4)$$

Here,  $E_e$  is the binding energy of one ground state electron at the defect core,  $E_{2e}$  is the binding energy of two electrons at the defect core, and  $E_a$  is the binding energy of the hole at the complex. This behavior is different from excitons bound to neutral shallow donors where the binding energy of the whole exciton at an impurity center is given by  $E_{loc} = E_a$ .

(3) One possible defect model explaining these results could consist of a doubly charged donor core  $D^{2+}$ . Such a center may possess one electron in the ground state and bind a second electron and a hole to form a bound exciton complex. However, in this case the binding energy of the ground state electron  $E_e$  would be larger than the binding energy of a single charged effective mass donor  $E_B$  by at least a factor of four. Thus, a greatly increased energy spacing between the exciton and its two electron satellite (TES) would be expected which is in contradiction to the energy of the observed TES transitions (see Fig. 6.10 in section 6.4). Consequently, the potential of the defect core should be strong enough to tightly bind the second electron while the binding energy of the first electron is not large. This is only possible if the electron-electron repulsion in the complex is reduced which occurs in the case of an extended defect core. Such an extended defect core might be composed of two or more donor ions, created by several short-range potentials, or be similar to the dislocation loops described by Dean [237]. It can be characterized by a structural parameter  $R$  or alternatively by the strain field induced by the dislocation. A theoretical description for dislocation bound excitons in II-VI semiconductors was developed by Rebane, Schreter and Steeds [257–260] which assumes that the exciton forming carriers are bound to a dislocation by its strain field.

(4) The model of the extended defect core may also account for the very small Huang-Rhys parameter  $S$  observed for these lines. Comparable values for the Huang-Rhys factor of defect bound excitons were reported in other compound semiconductors such as ZnSe and ZnTe, too. In ZnSe, the Huang-Rhys factor of similar

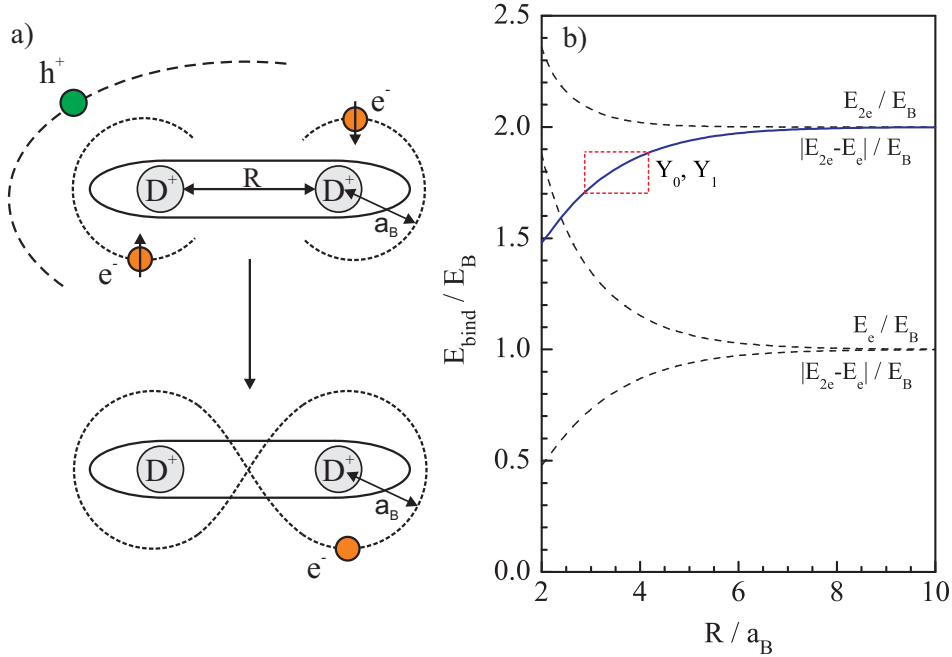


Figure 6.18: (a) Schematic picture of a deeply bound exciton complex. The defect core consists of two singly charged  $D^+$  ions separated by a distance  $R > 2a_B$ , where  $a_B$  is the Bohr radius of the effective mass donor. The ground state of the complex is represented by one electron bound to the defect core. In the excited state, two electrons with antiparallel spins are deeply bound to the defect core while the hole is weakly bound to the complex. (b) Dependency of the binding energy of the ground state electron  $E_e$ , of two electrons in the excited state  $E_{2e}$ , and of the second electron  $|E_{2e} - E_e|$  on the distance  $R$  between ions. The energy is measured in the effective mass Bohr energy  $E_B$ . The solid line shows the dependence of the second electron binding energy on  $R$  taking an short range potential correction of the order of  $E_B$  into account. The red box marks the characteristic region of increasing binding energy for the  $Y$  centers.

structural defect bound exciton lines  $Y$  and  $Z$  varies between  $S = 0.2$  and  $0.02$ , respectively [237, 261]. In ZnTe, Naumov et al. [254] reported Huang-Rhys values for the defect bound excitons  $Y_1$  and  $Y_2$  of  $S < 0.01$  and  $S = 0.2$ , respectively. These values are about one order of magnitude smaller than predicted for point defects with the same localization energy in ZnTe [237]. In agreement with these materials, the derived  $S$  values for the  $Y$  lines in ZnO are about one order of magnitude smaller than those of the shallow impurity bound excitons.

(5) As an example of the extended defect model, a double donor complex consisting of one neutral and one singly ionized donor is considered. An exciton bound to this complex can contribute one electron to the ionized donor resulting in two tightly bound electrons at two singly positively charged donors and one weakly bound hole.

The spins of the electrons will be oriented anti-parallel to each other. This model is in agreement with the observed linear splitting in a magnetic field since only one unpaired charge carrier is present equal to a simple neutral donor bound exciton. Due to the weak binding energy of the unpaired particle, the hole can be easily detached from the complex which could explain the small thermal activation energy  $E_a < E_{loc}$ . A schematic drawing of such a complex is shown in Fig. 6.18a. The distance  $R$  between the  $D^+$  ions in the defect core characterizes the spatial extension of the structural defect and should be greater than twice the Bohr radius  $a_B$  of the effective mass donor. In this case, the asymptotic expressions can be obtained for the binding energy of one electron  $E_e$  and two electrons  $E_{2e}$  bound to the  $D^+ - D^+$  defect core [262].

The binding energies of one electron  $E_e$ , two electrons  $E_{2e}$ , and the second electron  $E_{2e} - E_e$  as function of the distance  $R$  are shown by dashed lines in Fig. 6.18b. For large distances  $R$ , the ions are independent of the electron configuration and the one electron and two electron energies converge to the Bohr effective mass energy  $E_B$  of about 50 meV [40]:  $E_e \rightarrow E_B$  and  $E_{2e} \rightarrow 2E_B$  (see Fig. 6.18b). With decreasing  $R$ , the attraction of the second ion leads to an increase of  $E_e$  and  $E_{2e}$ . However, the electron-electron repulsion reduces the two electron binding energy  $E_{2e}$  and, hence, the binding energy of the second electron. The resulting binding energy of the second electron  $E_{2e} - E_e$ , which is calculated in the effective mass approximation with the Coulomb potential of the ions, is too small to result in a localization energy of the complex larger than the activation energy  $E_a$ . In fact, the short-range potential corrections for both  $D^+$  ions should be taken into account. Assuming the short-range potential correction energy  $E_{sh}$  to be the same for both ions, one has to add  $E_{sh}$  to  $E_e$  in order to obtain the binding energy of the first electron, and  $2E_{sh}$  to  $E_{2e}$  to obtain the energy of two electrons. As the result, the binding energy of the second electron is given by  $E_{2e} - E_e + E_{sh}$ . For the case that the energy of the short-range potential correction equals the Bohr effective mass energy  $E_{sh} = E_B$ , the dependence of the binding energy of the second electron on the ion distance  $R$  is shown in Fig. 6.18b by the solid line. Assuming a free exciton binding energy of  $E_{ex} = 60$  meV, the calculated values of  $E_{2e} - E_e$  are about 90 meV for the  $Y_0$  line and 86 meV for the  $Y_1$  line. These values are obtained with an activation energy of  $E_a = 12$  meV and localization energies of  $E_{loc} = 43.1$  and 39.6 meV, respectively. With  $E_B \approx 50$  meV [40] and  $E_{sh} = E_B$ , the  $Y$  lines should be related to an extended complex with a distance between the  $D^+$  ions of about 3.5 to 4.0  $a_B$ .

(6) A comparison of the recombination dynamics between  $I$  lines and  $Y$  lines reveals short and monoexponential lifetimes in the case of the defect center related excitons and longer biexponential time constants for the  $I$  lines (see Fig. 6.14 and Table 6.3 in section 6.7). While the lifetimes of the shallow bound excitons increase

as function of the localization energy as described by the model of Rashba and Gurgenishvili [240], the lifetimes of the defect bound excitons do not scale with the large localization energies  $E_{loc}$  of these centers, but rather with the small activation energies  $E_a$ . This is well explained by the presented model since the activation energy  $E_a$  corresponds to the detachment of the weakly bound hole. The radius of its orbit  $a_h \propto 1/\sqrt{E_a}$  determines the coherence region occupied by the exciton and thus the radiative lifetime. In addition, nonradiative decay channels for these deep centers related to the activation and recapture of the shallow bound hole might contribute to the observed short lifetimes. A rise time is not observed for the  $Y$  lines within the experimental time resolution of about 20 ps which might indicate a very fast formation of these complexes. This could be supported by the presence of an additional capture process of charge carriers. According to the presented model, these bound exciton complexes can be created not only by the capture of free excitons at the ionized  $D^+ - D^0$  defect, but also by the capture of holes to the neutral  $D^0 - D^0$  defect. The measured decay dynamics of the  $Y$  lines in ZnO are in agreement with the short and monoexponential decay of defect bound excitons in ZnSe reported by Dean [237].

(7) The uniaxial compression along the  $c$ -axis results in increasing localization energies of the shallow impurity bound excitons ( $I$  lines) and defect center bound excitons ( $Y$  lines) as discussed in section 6.8 (see Fig. 6.16). The effect of the uniaxial stress on the localization energies was observed to be larger for the  $Y$  lines than for the  $I$  lines. Within the presented defect model, this difference should be caused by an additional effect of the strain on the internal structural parameter  $R$  of the defect core. Assuming the defect core is extended in the plain perpendicular to the  $c$  axis, the uniaxial compression parallel to the  $c$  axis would lead to an increase of the structural parameter  $R$  of the defect core (or of the dislocation strain field) which is caused by the biaxial expansion of the lattice in the plain perpendicular to the  $c$  axis. The larger distance  $R$ , in turn, results in a reduced effect of the electron-electron repulsion and hence in an increase of the localization energy  $E_{loc}$  with increasing temperature. This relation is visualized by the dashed red rectangle in Fig. 6.18b which marks a characteristic region of increasing binding energy of the second electron  $E_{2e} - E_e$  as a function of  $R$  for the  $Y$  centers in the considered defect model. Taking Eq. 6.4 into account, it is apparent that the increase of  $E_{2e} - E_e$  is equivalent to an increase of  $E_{loc}$ . While the tendency is correct, the increase rate of the binding energy  $E_{2e} - E_e$  as function of  $R$ , which is predicted by the calculations shown in Fig. 6.18b, is too small in comparison to the experimentally observed pressure coefficients for the localization energy. A larger rate can be obtained if one assumes the presence of several short-range potential wells between the ionized ions in the defect core.

## 6.12 Summary

In conclusion, a comprehensive study of the origin and properties of deeply bound exciton lines was conducted and the results were compared to shallow donor bound excitons. Based on a variety of experimental results, it was shown that the  $Y_0$ ,  $Y_1$ , and  $Y_2$  originate from the radiative recombination of excitons bound to extended structural defects. These defect complexes introduce additional donors in the neutral charge state. All three lines cannot be described within the effective mass like model for shallow donor states. Rather, a model of deeply bound excitons with one weakly bound charge carrier was developed and discussed. A small activation energy of about 12 meV is derived from temperature dependent PL spectra despite the more than three times larger localization energy of these excitons. An additional doublet structure around 3.270 eV is exclusively observed in samples which exhibit the 3.333 eV emission line and is identified as its two electron satellite (TES) transitions. The energy spacing of these TES lines as well as the Huang-Rhys parameter  $S$  of the  $Y_0$  line were found to be exceptionally small. The recombination dynamics of the different exciton transitions exhibit striking differences between the shallow and deeply bound excitons. While the lifetime of the shallow bound excitons increases as function of the localization energy between 570 ps and 1.35 ns, significantly shorter lifetimes of about 200 ps are determined for the deeply bound excitons. A comparable tendency is observed for the uniaxial pressure coefficients ( $P||c$ ) of the different bound excitons with values of around 2 meV/GPa for the deeply bound excitons between 3.33 eV and 3.35 eV and 2.8 to 3.2 meV/GPa for the shallow donor bound exciton  $I_4$  to  $I_9$ . In addition, monochromatic CL images show that the luminescence lines originate from microscopically localized structures such as line defects and the areas in between the branches of hexagonal star like defects. The different experimental results can be explained within the developed model of excitons bound to extended structural defects. Several properties of these exciton complexes such as their short monoexponential decay dynamics and weak exciton-phonon coupling are furthermore in excellent agreement with reports of defect and dislocation bound excitons in other III-V and II-VI compound semiconductors.

## 7 Raman scattering under uniaxial and hydrostatic pressure

While the discussion in the previous chapters mainly focused on the properties of free and bound excitons, this chapter is dedicated to the study of ZnO lattice dynamics by Raman spectroscopy as function of external pressure. In the first part of this chapter, the elastic properties of wurtzite semiconductors (section 7.1) and the influence of pressure on these materials (section 7.2) are summarized. The basics of the Raman effect are very briefly explained (section 7.3) followed by a discussion about the lattice dynamics and phonon dispersion of ZnO in section 7.4. Subsequently, Raman spectra of ZnO substrates from different suppliers with *c*-plane and *a*-plane orientation are analyzed at ambient pressure (section 7.5). In the following sections, the influence of hydrostatic pressure on the phonon modes is studied (section 7.6). A variety of parameters is derived including high precision values of the hydrostatic pressure coefficients and Grüneisen parameters of all Raman active modes as well as Born's transverse effective charge for which an incorrect pressure dependence in a highly cited work by Decremps et al. [263] is discovered and revised. In addition, the Fano-asymmetry of the  $E_2^{high}$  is investigated as function of hydrostatic pressure. In the last part of this chapter (section 7.7), Raman measurements of ZnO single crystals under uniaxial pressure are reported for the first time. In combination with the hydrostatic pressure measurements on the same samples, the first experimental determination of the phonon deformation potentials of all Raman active modes is achieved. These values are derived in a straight-forward manner which does not rely on the error-prone determination of the deformation potentials from biaxially strained heteroepitaxial thin films.

### 7.1 Elastic properties of wurtzite materials

In general, strain and stress are expressed by the symmetric second-rank tensors  $\hat{\epsilon}$  and  $\hat{\sigma}$ , respectively. The strain tensor  $\hat{\epsilon}$  describes the deformation induced in the crystal by atomic displacements, whereas the stress tensor  $\hat{\sigma}$  defines the force per unit area applied to an elementary cube within the solid. In linear elasticity theory, the strain induced in a medium is proportional to the applied stress. The constants of proportionality can be expressed by the forth-rank compliance tensor

$\hat{S}$  and stiffness tensor  $\hat{C}$ . The relation between strain and stress is given by:

$$\epsilon_{ij} = \sum_{k,l} S_{ijkl} \sigma_{kl} \quad (7.1)$$

$$\sigma_{ij} = \sum_{k,l} C_{ijkl} \epsilon_{kl} \quad (7.2)$$

Since the strain and stress tensors are symmetric tensors, each can be described by six matrix elements rather than nine. In the contracted Voigt notation for symmetric tensors, the forth-rank compliance and stiffness tensors can be denoted by 6x6 matrices [264]. For wurtzite structures with  $C_{6v}$  symmetry,  $\hat{S}$  and  $\hat{C}$  possess five independent components. The matrix of the elastic stiffness coefficients is expressed by:

$$\begin{pmatrix} \sigma_{xx} \\ \sigma_{yy} \\ \sigma_{zz} \\ \sigma_{yz} \\ \sigma_{xz} \\ \sigma_{xy} \end{pmatrix} = \begin{pmatrix} C_{11} & C_{12} & C_{13} & 0 & 0 & 0 \\ C_{12} & C_{11} & C_{13} & 0 & 0 & 0 \\ C_{13} & C_{13} & C_{33} & 0 & 0 & 0 \\ 0 & 0 & 0 & C_{44} & 0 & 0 \\ 0 & 0 & 0 & 0 & C_{44} & 0 \\ 0 & 0 & 0 & 0 & 0 & (C_{11} - C_{12})/2 \end{pmatrix} \cdot \begin{pmatrix} \epsilon_{xx} \\ \epsilon_{yy} \\ \epsilon_{zz} \\ \epsilon_{yz} \\ \epsilon_{xz} \\ \epsilon_{xy} \end{pmatrix} \quad (7.3)$$

where the six elements of the strain tensor  $\hat{\epsilon}$  are defined in the Voigt notation by

$$(e_1, e_2, e_3, e_4, e_5, e_6) = (\epsilon_{xx}, \epsilon_{yy}, \epsilon_{zz}, 2\epsilon_{yz}, 2\epsilon_{xz}, 2\epsilon_{xy}). \quad (7.4)$$

Similarly, the relation using the compliance matrix can be written as:

$$\begin{pmatrix} \epsilon_{xx} \\ \epsilon_{yy} \\ \epsilon_{zz} \\ \epsilon_{yz} \\ \epsilon_{xz} \\ \epsilon_{xy} \end{pmatrix} = \begin{pmatrix} S_{11} & S_{12} & S_{13} & 0 & 0 & 0 \\ S_{12} & S_{11} & S_{13} & 0 & 0 & 0 \\ S_{13} & S_{13} & S_{33} & 0 & 0 & 0 \\ 0 & 0 & 0 & S_{44} & 0 & 0 \\ 0 & 0 & 0 & 0 & S_{44} & 0 \\ 0 & 0 & 0 & 0 & 0 & 2(S_{11} - S_{12}) \end{pmatrix} \cdot \begin{pmatrix} \sigma_{xx} \\ \sigma_{yy} \\ \sigma_{zz} \\ \sigma_{yz} \\ \sigma_{xz} \\ \sigma_{xy} \end{pmatrix} \quad (7.5)$$

The relation between the compliance and elastic stiffness constants follows by matrix inversion to:

$$S_{11} = \frac{C_{11}C_{33} - C_{13}^2}{(C_{11} - C_{12})(C_{11}C_{33} - 2C_{13}^2 + C_{12}C_{33})}, \quad (7.6)$$

$$S_{12} = -\frac{C_{12}C_{33} - C_{13}^2}{(C_{11} - C_{12})(C_{11}C_{33} - 2C_{13}^2 + C_{12}C_{33})}, \quad (7.7)$$

$$S_{13} = -\frac{C_{13}}{C_{11}C_{33} - 2C_{13}^2 + C_{12}C_{33}}, \quad (7.8)$$

$$S_{33} = \frac{C_{11} + C_{12}}{C_{11}C_{33} - 2C_{13}^2 + C_{12}C_{33}}, \quad (7.9)$$

$$S_{44} = \frac{1}{C_{44}}. \quad (7.10)$$

The elastic stiffness constants  $C_{11}$  and  $C_{33}$  correspond to longitudinal modes along the [1000] and [0001] directions, whereas the constants  $C_{44}$  and  $C_{66} = (C_{11} - C_{12})/2$  determine transverse modes propagating along the [0001] and [1000] directions, respectively.  $C_{13}$  in combination with the other four moduli describes the velocity of modes in less symmetrical directions such as [0011]. The values of the elastic constants can be determined using ultrasonic measurements [265–268] and Brillouin scattering [269, 270] or be theoretically derived by first-principles calculations [271–273].

Comparable to the elastic stiffness and compliance tensors, the symmetric fourth-rank tensors of the deformation potentials  $\hat{K}$  is defined by

$$d_{ij} = \sum_{k,l} K_{ijkl} \epsilon_{kl}, \quad (7.11)$$

where  $d_{ij}$  are the elements of the second rank tensor of the spring constants  $\hat{d}$ . Since the spring constants are related to the phonon frequencies, the phonon deformation potentials describe the influence of strain on the vibrational frequencies. Analogue to  $\hat{C}$  and  $\hat{S}$ , the tensor of the deformation potentials  $\hat{K}$  can be expressed by a 6x6 matrix with five independent components for wurtzite crystals belonging to the point group  $C_{6v}$ . For practical usage, the phonon deformation potentials  $a$  and  $b$  are defined by a combination of the  $K_{ijkl}$  which describe the specific cases of bisotropic and uniaxial strain, respectively.

## 7.2 Hydrostatic pressure

The application of hydrostatic pressure leads to a simultaneous decrease of the lattice constants  $a$  and  $c$ , and thus the volume  $V$ . Since no symmetry of the unstrained crystal is reduced, the symmetry of wurtzite ZnO under pressure is still described by the point group  $C_{6v}$ . The hydrostatic pressure  $P$  is described by the diagonal stress tensor

$$\hat{\sigma} = \begin{pmatrix} \sigma_{xx} & 0 & 0 \\ 0 & \sigma_{yy} & 0 \\ 0 & 0 & \sigma_{zz} \end{pmatrix}, \quad (7.12)$$

whereby the components of the stress tensor are equal with  $\sigma_{xx} = \sigma_{yy} = \sigma_{zz} = -P$ . Tensile stress is positive while compressive stress is negative by sign convention. With Eq. 7.3, the strain along the  $c$ -axis is given by  $\epsilon_{zz} = R^H \epsilon_{xx}$ , where

$$R^H = \frac{C_{11} + C_{12} - 2C_{13}}{C_{33} - C_{13}} \quad (7.13)$$

is the hydrostatic relaxation coefficient expressed in terms of the elastic stiffness constants  $C_{ij}$ .

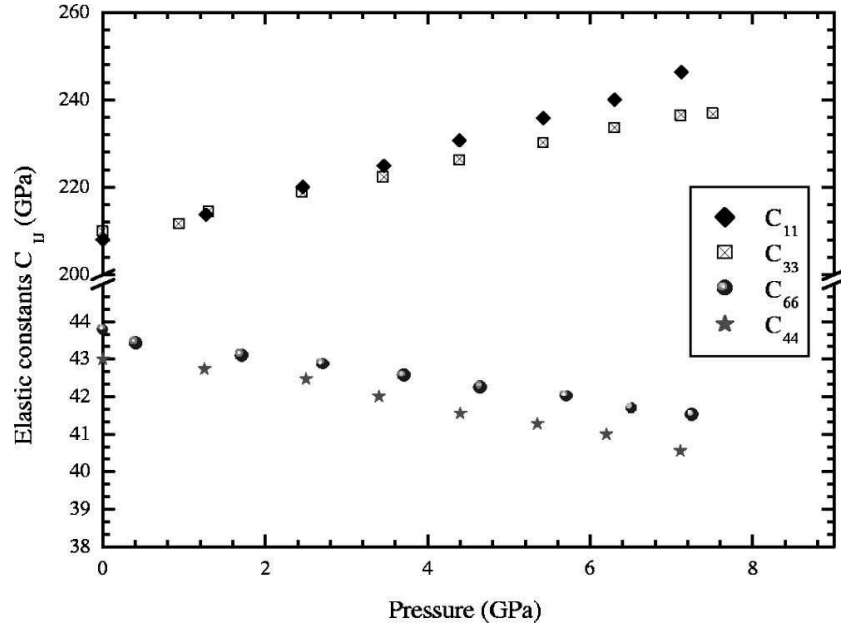


Figure 7.1: Elastic stiffness constants of ZnO as a function of hydrostatic pressure at ambient temperature. Taken from [268].

Similar to other II-VI semiconductors, ZnO undergoes a phase transition from the fourfold wurtzite (B4) structure to the sixfold correlated rocksalt (B1) structure upon the application of hydrostatic pressure. It is explained by the pressure induced reduction of the lattice dimensions, which causes the inter-ionic Coulomb interaction to favor the ionicity over the covalent nature. This correlates with the instability of the wurtzite structure against shearing deformations [268, 272]. Energy-dispersive X-ray diffraction delivers a critical pressure of 8.7 to 9.1 GPa for the phase transition at room temperature [274, 275]. The transition to the rocksalt structure is accompanied by a large decrease of the unit cell volume of about 17% [274, 276]. Upon decompression a strong phase hysteresis is present which leads to a reversion to the wurtzite phase at pressures of 1.9 to 2.0 GPa [274, 275]. For nanostructures the phase transition occurs at higher pressures between 12 GPa and 15 GPa [277, 278].

Fig. 7.1 displays the elastic stiffness constants as function of hydrostatic pressure. The elastic moduli were determined by ultrasonic measurements of the travel times of the sonic waves which correspond to the acoustic modes of ZnO using the ultrasonic phase comparison method [268]. With increasing pressure, a linear dependence of all elastic moduli up to  $P = 7.5$  GPa is observed. For higher hydrostatic pressures, the B4 to B1 phase transition begins to occur. As seen in Fig. 7.1, the slope of the longitudinal modes  $C_{11}$  and  $C_{33}$  as function of the hydrostatic pressure is positive with pressure derivatives of ( $dC_{11}/dP = 5.32$  and  $dC_{33}/dP = 3.78$ ). By contrast,

the elastic shear moduli  $C_{44}$  and  $C_{66}$  reveal a negative pressure dependence with values of  $dC_{44}/dP = -0.35$  and  $dC_{66}/dP = -0.30$  [268]. Thus, ZnO becomes softer against shear-type acoustic distortions under pressure. The elastic shear softening observed at room temperature is enhanced at elevated temperatures and leads to an onset of the B4 to B1 transition at about 6 GPa at 600°C [268].

Independent of the phonon deformation potentials, the influence of the atomic displacement – which is expressed by the variation of lattice constants and volume as function of hydrostatic pressure – on the electronic band structure is determined by the electronic deformation potentials. They describe the shifts of the electronic band energies as function of the strain. The variation of an energy level  $\delta E_{n,k}$  in the contracted Voigt notation (Eq. 7.4) is given by

$$\delta E_{n,k} = \sum_{j=1}^6 \Xi_j \epsilon_j, \quad (7.14)$$

where  $\Xi_j$  are the deformation potentials and  $\epsilon_j$  are the components of the strain tensor in the contracted notation. For a hydrostatic or uniaxial deformation of the crystal, the (volume) deformation potentials are

$$\Xi_V = V(\delta E/\delta V), \quad (7.15)$$

$$\Xi_a = a(\delta E/\delta a), \quad (7.16)$$

where  $\delta V$  and  $\delta a$  are deformation induced variations of the volume  $V$  and the lattice constant  $a$ , respectively. A uniform dilatation or compression by  $\delta V$  around the equilibrium volume  $V_0$  shifts the energies of the conduction band minimum  $E_{cb}$  and valence band maximum  $E_{vb}$  by amounts of  $\Delta E_{cb}$  and  $\Delta E_{vb}$ , respectively. In the regime of linear elasticity, these shifts of individual band edges as function of the volume change  $\delta V/V_0$  are determined by the absolute deformation potentials for the valence band  $\Xi_{vb} = V(\delta E_{vb}/\delta V)$  and for the conduction band  $\Xi_{cb} = V(\delta E_{cb}/\delta V)$ . The change in the band-gap energy  $E_g = E_{cb} - E_{vb}$  can therefore be expressed by the band-gap deformation potential  $\Xi_g = \Xi_{cb} - \Xi_{vb}$ . Reported values for the band-gap deformation potentials  $\Xi_g$  and hydrostatic pressure coefficients  $\alpha$  vary between  $\Xi_g = -3.47$  to  $-3.92$  eV and  $\alpha = 23.6$  to  $29.2$  meV/GPa, respectively [277, 279–281]. While shifts of bands relative to each other can be extracted from optical experiments, the absolute deformation potentials are difficult to obtain due to the lack of a precise reference for the potential energy in a homogeneously deformed crystal, but can be derived from theoretical calculations using an ab initio approach [58]. In terms of the relative band gap deformation potential  $\Xi_g$ , the band-gap energy shift can be approximated by

$$\Delta E = \Xi_g(V - V_0)/V. \quad (7.17)$$

The relative volume change as function of hydrostatic pressure is expressed by the Murnaghan equation of state [282]

$$P = (B/B')[(V_0/V)^{B'} - 1], \quad (7.18)$$

where  $B$  is the bulk modulus of wurtzite ZnO and  $B'$  the pressure derivative (dB/dP).

### 7.3 Raman effect

A brief introduction to Raman scattering is given in this chapter resulting in the selection rules for the first order Raman modes in wurtzite crystals such as ZnO. For a more comprehensive overview of light scattering phenomena, the gentle reader is referred to the books and reviews in Refs. [27, 283–285].

The electric field  $\mathbf{E}$  of a monochromatic electromagnetic wave in a crystals induces a polarization  $\mathbf{P}$

$$\mathbf{P}(\mathbf{k}_s, \omega_s) = \epsilon_0 \tilde{\chi}(\mathbf{k}_s, \omega_i, \omega_s) \mathbf{E}(\mathbf{k}_i, \omega_i) \quad (7.19)$$

where the indices  $i$  and  $s$  denote the incident and scattered light. Inelastic light scattering occurs if the susceptibility  $\tilde{\chi}$  is not constant as function of time or spatial coordinates. Otherwise, the incident light is scattered elastically. Consequently, the selection rules for first order Raman scattering can be expressed by

$$\mathbf{e}_s \cdot \frac{\partial \tilde{\chi}}{\partial u_j} \cdot \mathbf{e}_i \neq 0. \quad (7.20)$$

In Eq. 7.20  $\mathbf{e}_s$  and  $\mathbf{e}_i$  denote the direction of the unit vectors of the linear polarizations of the scattered and incident light and  $\partial \tilde{\chi} / \partial u_j$  the derivative of the second rank susceptibility tensors with respect to the displacement coordinate  $u_j$  which is usually substituted by the third rank Raman tensor  $\tilde{R}$  [27]. The intensity of the scattered light  $I_s$  is then proportional to

$$I_s \propto |\mathbf{e}_s \cdot \tilde{R} \cdot \mathbf{e}_i|^2. \quad (7.21)$$

The symmetry of the Raman tensor and hence the symmetry of the corresponding Raman-active modes can be deduced from the measurement of the dependence of the scattered intensity on the incident and scattered polarization. Using group theoretical concepts, the Raman selection rules can be determined by the Kronecker product of the irreducible representations  $\Gamma_s^*$  and  $\Gamma_i$  of the polarization vectors  $\mathbf{e}_s$  and  $\mathbf{e}_i$  for a given point group [285]:

$$\text{Raman active phonon} \iff \Gamma_p \in \Gamma_s^* \otimes \Gamma_i. \quad (7.22)$$

Hence, a phonon with symmetry  $\Gamma_p$  is Raman active if its irreducible representation is contained in the Kronecker product of the  $\Gamma_s^*$  and  $\Gamma_i$ .

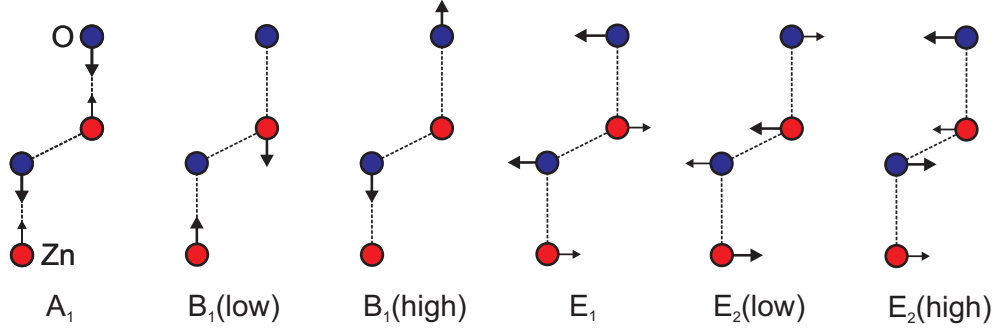


Figure 7.2: Schematic illustration of the ion displacements of optical phonon modes in ZnO. The larger arrows represent the dominating displacement vectors.  $A_1$ ,  $E_1$ ,  $B_1^{high}$  and  $E_2^{high}$  are oxygen-lattice dominated,  $B_1^{low}$  and  $E_2^{high}$  are dominated by zinc displacements.  $A_1$  and  $E_1$  are polar modes,  $B_1$  and  $E_2$  are non-polar.

## 7.4 Lattice dynamics and phonon dispersion of ZnO

The wurtzite modification of ZnO with the space group  $C_{6v}^4$  has  $n = 4$  atoms in the primitive unit cell which lead to  $3n = 12$  vibrational eigenmodes (3 acoustical and 9 optical modes). These modes are classified according to the following irreducible representations [283]

$$\Gamma = 2A_1(1) + 2B_1(1) + 2E_1(2) + 2E_2(2) \quad (7.23)$$

whereby the  $A_1$  and  $B_1$  modes are onefold and the E modes twofold degenerated as indicated by the number in brackets. The three acoustical phonon modes consist of one  $A_1$  mode and one  $E_1$  mode pair, the other nine modes are optical modes:

$$\Gamma_{opt} = A_1(1) + B_1^{low}(1) + B_1^{high}(1) + E_1(2) + E_2^{low}(2) + E_2^{high}(2) \quad (7.24)$$

The symmetry of these modes at the  $\Gamma$  point is given in the Koster notation by:

$$A_1 = \Gamma_1, B_1 = \Gamma_3, E_1 = \Gamma_5, E_2 = \Gamma_6, \quad (7.25)$$

Fig. 7.2 schematically visualizes the displacement of the six different optical vibration modes in Eq. 7.24. The  $A_1$  and  $B_1$  oscillate in the direction of the  $c$ -axis, while the  $E_1$  and  $E_2$  modes represent displacements perpendicular to the  $c$ -axis. The later modes oscillate linearly independent in the  $x$ - and  $y$ -direction with the same energy which leads to the twofold degeneracy of the  $E_1$  and  $E_2$  modes. The  $A_1$  and  $E_1$  mode patterns consist of an oscillation of the Zn- versus the O- sublattices which creates an oscillating polarization. The polarity induced macroscopic electric fields split these polar modes into longitudinal optical (LO) modes with an ion displacement vector parallel to the phonon propagation direction  $\mathbf{q}$  and transversal optical

(TO) modes with perpendicular displacement vectors. This splitting is not predicted by group theory as the description is limited to purely vibrational non-propagating eigenmodes at the  $\Gamma$  point with  $\mathbf{q} = 0$ . The frequency of the LO modes exceeds those of the TO modes since the macroscopic electric field acts as an additional restoring force for the ion oscillation [286]. This is expressed by the Lyddane-Sachs-Teller relation [287]

$$\left(\frac{\omega_{LO}}{\omega_{TO}}\right)^2 = \frac{\varepsilon_0}{\varepsilon_\infty} \quad (7.26)$$

The size of the LO-TO splitting is expressed by the transverse effective charge with [27]

$$(e_T^*)^2 = \varepsilon_0 \varepsilon_\infty V \mu (\omega_{LO}^2 - \omega_{TO}^2), \quad (7.27)$$

where  $\varepsilon_0$  is the vacuum permittivity,  $\varepsilon_\infty$  is the high frequency dielectric constant,  $\mu$  is the reduced mass of the anion-cation pair,  $V$  is the volume per pair, and  $\omega_{LO}$ ,  $\omega_{TO}$  are the phonon frequencies. The term 'transverse' originates from the  $e_T^*$  induced coupling between the transverse optical phonon mode and the infrared light wave resulting in phonon-polariton states. The transverse effective charge  $e_T^*$ , also referred to as Born's effective charge, determines the local polarization which is induced by a relative displacement of the sublattices.

In contrast to the  $A_1$  and  $E_1$  Raman modes, the  $B_1$  and  $E_2$  modes do not exhibit a LO-TO splitting as they are non-polar. No polarization is induced for the silent  $B$  modes, since one sublattice is essentially at rest while the neighboring atoms in the other sublattice move opposite to each other (Fig. 7.2). In the case of the  $E_2$  modes, the non-polarity is caused by the mutual compensation of the displacement vectors in each sublattice. The prominent displacement for the  $B_1^{low}$  and  $E_2^{low}$  modes occurs in the heavier Zn-sublattice whereas the stronger displacement in the lighter O-sublattice gives rise to the  $B_1^{high}$  and  $E_2^{high}$  modes (Fig. 7.2).

The elements of the Raman tensors determine if the modes are allowed or forbidden for a particular scattering geometry. Typically, a coordinate system  $x$ ,  $y$ ,  $z$  is chosen such that the  $z$ -direction represents the principal  $c$ -axis of the wurtzite crystal and  $x$  and  $y$  are perpendicular to  $z$  and to each other. The Raman tensors of the ZnO phonons for the deformation potential interaction are given by:

$$A_1(z) = \begin{pmatrix} a & 0 & 0 \\ 0 & a & 0 \\ 0 & 0 & b \end{pmatrix}, \quad E_1(x) = \begin{pmatrix} 0 & 0 & c \\ 0 & 0 & 0 \\ c & 0 & 0 \end{pmatrix}, \quad E_1(y) = \begin{pmatrix} 0 & 0 & 0 \\ 0 & 0 & c \\ 0 & c & 0 \end{pmatrix}$$

$$E_2^{(1)} = \begin{pmatrix} d & 0 & 0 \\ 0 & -d & 0 \\ 0 & 0 & 0 \end{pmatrix}, \quad E_2^{(2)} = \begin{pmatrix} 0 & d & 0 \\ d & 0 & 0 \\ 0 & 0 & 0 \end{pmatrix}. \quad (7.28)$$

Table 7.1: Raman (A) and IR activity of zone center phonons in hexagonal ZnO in different configuration. Polarization and light directions are denoted in the Porto notation.

Mode		$z(xx)\bar{z}$	$z(xy)\bar{z}$	$x(yy)\bar{x}$	$x(zz)\bar{x}$	$x(yz)\bar{x}$	$x(zy)y$	IR
		$z(yy)\bar{z}$		$y(xx)\bar{y}$	$y(zz)\bar{y}$			
$A_1$	TO	-	-	A	A	-	-	$\parallel c$
$A_1$	LO	A	-	-	-	-	-	-
$B_1^{low}$		-	-	-	-	-	-	-
$B_1^{high}$		-	-	-	-	-	-	-
$E_1$	TO	-	-	-	-	A	A	$\perp c$
$E_1$	LO	-	-	-	-	-	A	-
$E_2^{low}$		A	A	A	-	-	-	-
$E_2^{high}$		A	A	A	-	-	-	-

Table 7.1 lists the Raman activity of all optical phonons in ZnO for the different scattering geometries and polarizations. These are usually expressed in the Porto notation [173]  $\mathbf{k}_i(\mathbf{e}_i\mathbf{e}_s)\mathbf{k}_s$  where  $\mathbf{k}_i$  and  $\mathbf{k}_s$  indicate the direction of the incident and scattered light while  $\mathbf{e}_i$  and  $\mathbf{e}_s$  are the same as in Eq. 7.20. In addition, infrared active TO modes are indicated in the last column of Table 7.1.

The phonon dispersion relations for high symmetry directions in the Brillouin zone as derived from first principle calculations and recently published inelastic neutron scattering (INS) measurements are displayed in Fig. 7.3. Apparently, an excellent agreement between INS data and theoretical calculations could be achieved for the phonon dispersion relations throughout the whole Brillouin zone [288]. The green data points represent the phonon frequencies determined by first-order Raman scattering. A multitude of information can be derived from the phonon dispersion in Fig. 7.3. On the one hand, the acoustical branches allow a direct access to the elastic moduli which linear slopes near the  $\Gamma$  point represent the sound velocities  $v_s$ . In particular, the upper acoustical branch determines the sound velocity  $v_s$  of the longitudinal waves whereas shear waves are represented by the lower acoustical branch. On the other hand, the optical modes give access to the bond force constants and their anisotropy as well as to the effective charge which will be discussed in section 7.6.2. The zone center optical mode frequencies are found in the range between  $100 \text{ cm}^{-1}$  and  $600 \text{ cm}^{-1}$  which translates to energies between 12.5 meV and 75 meV.

## 7.5 Raman scattering without external pressure

The first comprehensive investigation of the Raman spectrum in ZnO was published in 1966 by Damen et al. [173]. Using polarized right-angle Raman scattering, sev-

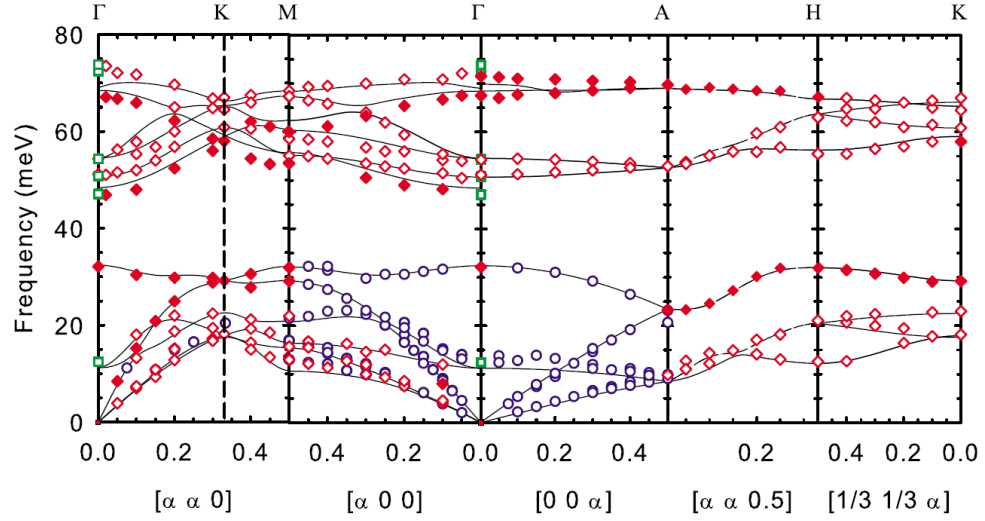


Figure 7.3: Phonon-dispersion relations of ZnO along the main symmetry directions. Red and blue data points represent inelastic neutron scattering (INS) measurements according to Ref. [288] and Refs. [289,290], respectively. Green squares are first-order zone center Raman data at 7 K in [291]. The solid curves display ab initio calculations reported in Ref. [292]. The  $x$ -axes are given in reciprocal lattice units. Taken from [288].

eral Raman modes of wurtzite ZnO could be identified and their zone-center phonon frequencies were determined. A complete assignment of all Raman active phonon modes was enabled from the results of different scattering geometries [293]. Already prior to the first experimental Raman data, a systematic theoretical study of the lattice dynamics of zinc-blende- and wurtzite-type crystals was published [294]. In 1977, a detailed study of the resonance behavior of the  $E_2^{high}$ ,  $A_1(TO)$ , and  $E_1(TO, LO)$  modes as well as several second order features was presented by Calleja and Cardona [295] (see also chapter 8). Data on the temperature dependence of ZnO phonons also dates back to the late 1970s. Recently, these works were complemented by a comprehensive study of the temperature dependence of first and second order Raman modes by Cusco et al. [296] who identified more than twenty different phonon frequencies related to first and second order modes in the Raman spectra of ZnO.

Fig. 7.4 shows unpolarized Raman spectra of two ZnO  $c$ -plane substrates (Tokyo Denpa and Cermet) and one  $a$ -plane substrate (CrysTec). The spectra are recorded without external pressure in backscattering geometry with the incident and scattered light perpendicular to the surface of the crystal. Due to the different surface orientations of  $c$ - and  $a$ -plane samples, different Raman modes are allowed or forbidden. In case of the  $c$ -plane samples, the incident and scattered light is parallel

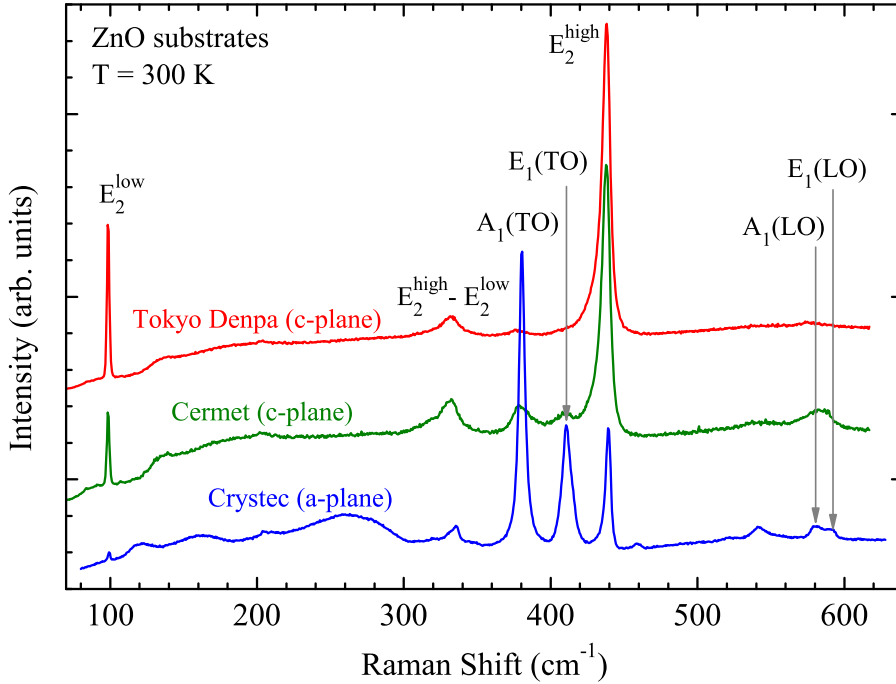


Figure 7.4: Raman spectra of  $a$ -plane and  $c$ -plane ZnO substrates from different manufacturers at  $T = 300$  K. Spectra are measured unpolarized in backscattering geometry perpendicular to the surface of the crystal.

to the  $c$ -axis ( $c||z$ ). According to the Raman selection rules in Table 7.1, the modes  $A_1(LO)$ ,  $E_2^{low}$ , and  $E_2^{high}$  are allowed in the  $z(\cdot)\bar{z}$  configuration. Indeed, the  $c$ -plane Raman spectra are dominated by the  $E_2^{high}$  and the  $E_2^{low}$  in both samples. However, the  $A_1(LO)$  has nearly vanishing intensity which is particularly apparent in the ZnO sample from Tokyo Denpa, although the mode is symmetry allowed. This is mainly caused by two different effects. First, the depicted Raman spectra are unpolarized, consequently, the  $E_2$  modes are much stronger since they are allowed for parallel and perpendicular polarizations, whereas the  $A_1(LO)$  only appears in parallel polarization. Second, even using a proper polarization of incident and scattered light, the  $A_1(LO)$  is usually very weak in ZnO [295, 296]. The reason is the virtual compensation of the two scattering terms given by the deformation potential and the electro-optic coupling coefficient which results for the LO phonons from its macroscopic electric field [297].

A comparison between the two different  $c$ -plane samples further reveals the presence of the forbidden  $A_1(TO)$ ,  $E_1(TO)$ , and  $E_1(LO)$  Raman modes in the Cermet samples. A possible explanation is the larger amount of crystal imperfections such as extended structural defects in the Cermet sample compared to the one from Tokyo Denpa. These defects may cause multiple reflections and local deviations of the

*c*-axis direction, thus giving rise to Raman modes which are usually forbidden in the  $z(\cdot)\bar{z}$  configuration. In fact, the appearance of forbidden Raman modes in the Cermet sample correlates nicely with an increased half width of the (002) reflection peak in XRD measurements and the observation of structural defect related luminescence lines which appear exclusively in the Cermet samples (see chapters 3.1 and 6).

In addition to the spectra of the two *c*-plane samples, Fig. 7.4 displays the Raman spectra of a ZnO *a*-plane substrate from CrysTec. According to the selection rules in Table 7.1, all but the LO modes should be visible in the unpolarized backscattering geometry  $x(\cdot)\bar{x}$ . In addition, the spectrum in Fig. 7.5 also shows weak  $A_1(LO)$  and  $E_1(LO)$  Raman modes. This partial lifting of the selection rules is commonly observed in ZnO and other materials and usually attributed to crystal imperfections, multi-reflections or deviations from strict normal incidence geometry. In the present case, this represents an advantage since it allows the observation of the shift of all Raman active modes in one geometry as function of hydrostatic pressure.

## 7.6 Raman scattering under hydrostatic pressure

Following the overview of the Raman spectra of different substrates in the previous section, the discussion now turns towards the influence of external hydrostatic pressure on the Raman modes of ZnO. Based on the evaluation of the optical Raman modes as function of hydrostatic pressure, the pressure coefficients and Grüneisen parameters are determined (section 7.6.1), the pressure dependence of the LO-TO splitting and Born's transverse effective charge is analyzed (section 7.6.2) and the asymmetric broadening of the  $E_2^{high}$  mode is investigated (section 7.6.3).

### 7.6.1 Grüneisen parameters

Fig. 7.5 displays three representative Raman spectra of the *a*-plane ZnO substrate at different hydrostatic pressures of 0.1, 2.5, and 4.8 GPa. Apparently, all first-order Raman active modes can be observed in the spectra. In addition, some second order modes such as the  $E_2^{high} - E_2^{low}$  at  $333\text{ cm}^{-1}$  are visible. The peak positions of the  $A_1$ ,  $E_1$ , and  $E_2^{low}$  phonons is determined by fitting every spectrum using Lorentzian line shapes. For the  $E_2^{high}$  mode a Fano profile is used since the line shape of this mode is strongly influenced by anharmonic effects in the lower pressure regime. This asymmetry is caused by the decay of this mode into a sum of transverse and longitudinal acoustic phonons (TA+LA) and will be discussed in section 7.6.3.

Fig. 7.6 displays the phonon frequencies of the first-order Raman modes between 0 and 5.5 GPa as function of hydrostatic pressure. The solid lines in Fig. 7.6 represent the results of least-squares fits to the data points using a linear relation. From these

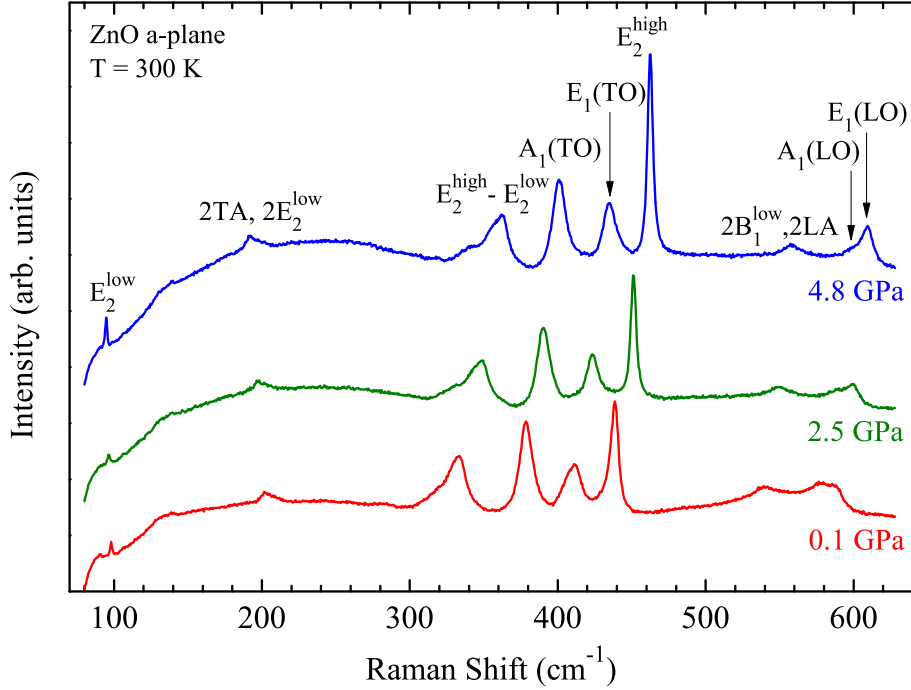


Figure 7.5: Representative Raman spectra of an a-plane wurtzite ZnO crystal at three different pressures of 0.1, 2.5, and 4.8 GPa. The spectra were vertically shifted for clarity.

fits, the zero pressure frequency  $\omega_0$  and the hydrostatic pressure coefficient  $\partial\omega/\partial P$  are derived. These values are listed in Table 7.2 together with previously published results by Decremps et al. [263]. The Grüneisen parameter can be computed for each single mode from the obtained data with

$$\gamma_i = d[\ln(\omega_i)]/d[\ln V] \approx (B_0/\omega_i) \times \partial\omega_i/\partial P \quad (7.29)$$

where  $\omega_i$  is the mode frequency,  $B_0$  is the bulk modulus, and  $P$  is the pressure. Evidently, the magnitude of the derived Grüneisen parameter depends on the bulk modulus for which different values were reported [274, 275, 298, 299]. In this work, a value of  $B_0 = 142.6(2)$  GPa reported by Desgreniers et al. [274] is used as it represents the result of the most reliable experimental study in the literature. The bulk modulus is related to the elastic stiffness constants by

$$B_0 = \frac{(C_{11} + C_{12})C_{33} - 2C_{13}^2}{C_{11} + C_{12} + 2C_{33} - 4C_{13}}. \quad (7.30)$$

The values of the Grüneisen parameters are found to be positive for all Raman modes except for the  $E_2^{low}$  mode. The negative pressure coefficient of the  $E_2^{low}$  mode expresses the softening of this mode under pressure. This mode is related to the transverse acoustic (TA) phonon branch of the cubic modification since it can be

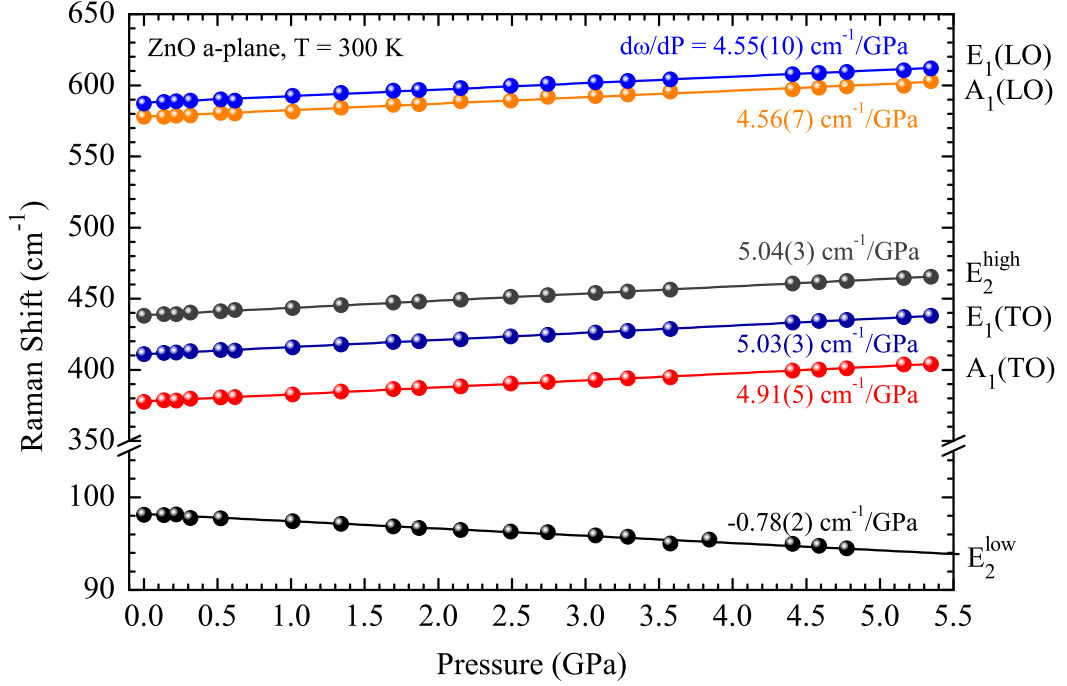


Figure 7.6: Pressure dependence of the first-order Raman modes. Solid lines are results of least-squares fits to the experimental data points using linear relations.

regarded as result of the back folding of the zinc blende (ZB) phonon branches in [111] direction ( $\Gamma - L$ ) into the zone center when turning from the zinc blende to the wurtzite structure [300] (see Fig. 7.7). This back folding in reciprocal space results from the doubling of the atomic periodicity length in real space along the wurtzite  $c$ -axis with respect to the periodicity length in the corresponding ZB [111] direction. Equivalent to the  $E_2^{low}$ , the back folding gives rise to the  $B_1^{low}$  from the longitudinal acoustical (LA) ZB phonon branch, whereas the wurtzite zone center modes related to the back folded optical modes are the  $B_1^{high}$  and  $E_2^{high}$  as depicted in Fig. 7.7. Since the zone-edge TA phonons of cubic III-V and II-VI semiconductors are known to exhibit negative Grüneisen parameters [229, 230], the negative slope of the  $E_2^{low}$  in wurtzite ZnO can nicely be explained by this argumentation.

The discrepancy between the determined Grüneisen parameters with those in Ref. [263] (see Table 7.2) is attributed to two different effects: first, a different bulk modulus  $B_0$  is chosen in this work and second, a larger inaccuracy in the determination of the phonon pressure coefficients occurred in Ref. [263] as reflected by the smaller amount and higher spread of the data points. The indetermination in the pressure coefficients is substantially reduced in the here presented measurements due to the clear observation of every peak in the Raman spectra of the  $a$ -plane substrates and the careful fitting procedure used to determine the peak positions. Consequently,

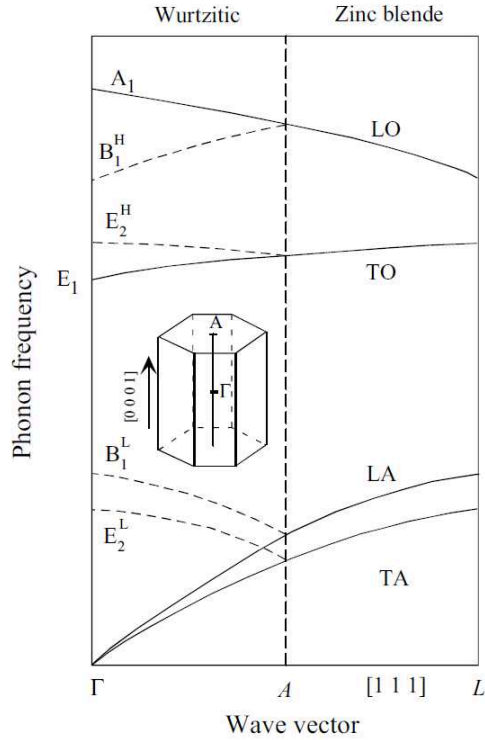


Figure 7.7: Schematic illustration of the phonon dispersion curves for zinc blende (ZB) and wurtzite structures. Phonon branches along the  $[111]$  direction in the zinc blende structure are folded back to branches of the wurtzite structure along the  $[0001]$  direction. Taken from [26].

the presented pressure coefficients and Grüneisen parameters can be considered as state-of-the-art values. It should be mentioned that hydrostatic pressure series were also conducted for the c-plane ZnO samples in Fig. 7.4 in order to clarify if reported variation of the lattice constants in different ZnO samples may also cause slight variations of the pressure coefficients. Since not all Raman active modes in the c-plane samples can be observed in one scattering direction, the best comparison can be achieved for the  $E_2^{high}$  modes which have a small half width and large intensity in both sample cut geometries. In addition, the  $E_2^{high}$  is a non-polar mode and as such not influenced by different carrier concentrations due to longitudinal-optical phonon-plasmon (LPP) coupling. Together with the values listed in Table 7.2, the following results for the hydrostatic pressure coefficients of the  $E_2^{high}$  are determined:  $438.65 + 5.00(2) \text{ cm}^{-1}/\text{GPa}$  for the c-plane Cermet,  $438.06 + 4.97(3) \text{ cm}^{-1}/\text{GPa}$  for the c-plane Tokyo Denpa and  $438.21 + 4.99(2) \text{ cm}^{-1}/\text{GPa}$  for the a-plane CrysTec. Evidently, the pressure coefficients are equal within the experimental error. The slight difference in the zero-field frequency of the  $E_2^{high}$  possibly indicates different residual strain levels in the samples due to impurities and/or defects.

### 7.6.2 Born's transverse effective charge

Following the determination of pressure coefficients and Grüneisen parameters, the discussion in this section focuses on the LO-TO splitting of the  $A_1$  and  $E_1$  modes due

Table 7.2: Coefficients from the linear fits to the data points of Fig. 7.6 using  $\omega_s = \omega_0 + (\partial\omega/\partial P)\cdot P$  and corresponding Grüneisen parameters. The values from Ref. [263] are listed for comparison. Numbers in parenthesis are error bars.

Mode	$\omega_0$ ( $\text{cm}^{-1}$ )	$\partial\omega/\partial P$ ( $\text{cm}^{-1}/\text{GPa}$ )	$\gamma_0$	$\partial\omega/\partial P$ [263] ( $\text{cm}^{-1}/\text{GPa}$ )	$\gamma_0$ [263]
$E_2^{low}$	98.2(1)	-0.78(2)	-1.13(4)	-0.93	-1.6
$E_2^{high}$	438.4(1)	5.04(3)	1.63(1)	5.16	2
$A_1(TO)$	377.8(1)	4.91(5)	1.85(2)	4.72	2.1
$E_1(TO)$	410.9(1)	5.03(3)	1.74(1)	4.38	1.8
$A_1(LO)$	578.0(3)	4.56(7)	1.12(2)	–	–
$E_1(LO)$	587.8(2)	4.55(10)	1.11(3)	4.78	1.4

to the interaction with the macroscopic electric field. The Born's transverse effective charge – which is computed from the value of the LO-TO splitting – was already studied for a wide variety of different materials including SiC, AlN, GaN, and ZnO. In the case of ZnO, the LO-TO splitting and the transverse effective charge were reported to increase with increasing pressure for the  $E_1$  mode [263]. This result is in clear contrast with the hydrostatic pressure dependence of these parameters in other II-VI compounds such as ZnSe and ZnTe [301], where the LO-TO splitting decreases with pressure. In addition, the increase of the transverse effective charge with pressure is also difficult to match with previous observations in GaN [302], AlN [302], GaAs [303], and GaP [304], where  $e_T^*$  was shown to decrease or at most to remain constant. This apparent inconsistency with the results published for ZnO provide a strong motivation to reinvestigate the pressure dependence of  $e_T^*$  in ZnO crystals.

Fig. 7.8 displays the pressure dependence of the LO-TO splitting for the  $A_1$  and  $E_1$  Raman modes. In both cases a similar behavior is observed with pressure coefficients of  $-0.36(10) \text{ cm}^{-1}/\text{GPa}$  for the  $A_1$  and  $-0.47(7) \text{ cm}^{-1}/\text{GPa}$  for the  $E_1$  mode. Within the experimental errors, these coefficients can be considered as equal. In spite of the scattering of the experimental data points, it is clear that the LO-TO splitting of both modes is reduced as function of the hydrostatic pressure. This result is in contrast to the published LO-TO splitting of the  $E_1$  by Decremps et al. [263]. In the latter work, the problem lies most probably in the determination of the pressure coefficient of the  $E_1(TO)$  mode. In their work, the  $E_1(TO)$  phonon is extremely weak which results in a significant contribution of the large asymmetric Fano-like profile of the  $E_2^{high}$  to the frequency position of the neighboring  $E_1(TO)$  mode. By contrast, the here presented results do not suffer from this effect, since the  $E_1(TO)$  is strongly present in the a-plane substrates and the influence of the asymmetric

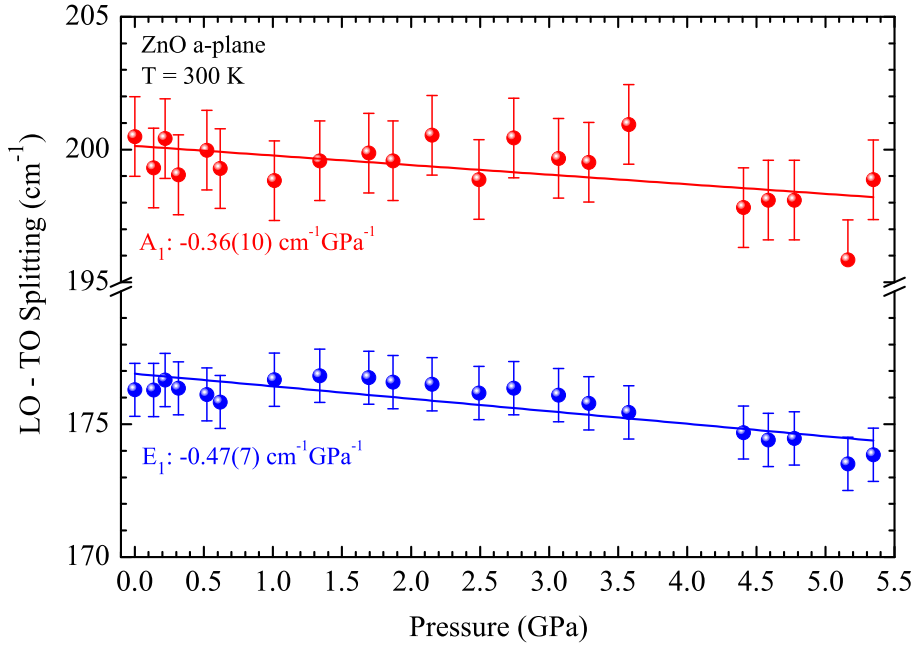


Figure 7.8: Pressure dependence of the LO-TO splitting for the polar  $A_1$  and  $E_1$  phonons. Solid lines are results of least-squares fits to the data points using linear relations.

$E_2^{high}$  is carefully considered by combined line shape fits of the two modes.

Based on the determined size of the LO-TO splitting, the Born's transverse effective charge can be calculated. According to Eq. 7.27, the effective charge depends on the LO-TO splitting, the unit-cell volume and the dielectric constant. The pressure dependence of the effective charge is consequently a combination of the pressure dependence of these three values. For the LO-TO splitting, the frequency shift as function of hydrostatic pressure was just determined in this section (Fig. 7.8). In the case of the unit cell volume  $V$ , the Murnaghan equation of state in Eq. 7.18 with the bulk modulus from Ref. [274] can be used to express the compression of the unit cell volume as function of hydrostatic pressure. Usually, Eq. 7.18 is expanded to the second order to describe the pressure dependence of the phonon frequencies. However, the shifting behavior of the optical Raman modes as function of the applied hydrostatic pressure in Fig. 7.6 can be well described by the first order term of the expanded Murnaghan equation since the second order term is negligible small. As to the high frequency dielectric constant  $\epsilon_\infty$ , there are no data for the pressure dependence available. Instead, the pressure dependence of the refractive index at optical frequencies  $n_0$  measured in the range up to 0.7 GPa [305] is used to obtain a coefficient of  $\partial\epsilon_\infty/\partial P = -0.014 \text{ GPa}^{-1}$ . Apparently, negative pressure coefficients are derived for all three parameters contributing to  $e_T^*$  in Eq. 7.27. Consequently, the effective charge in ZnO must decrease as well. The transverse effective

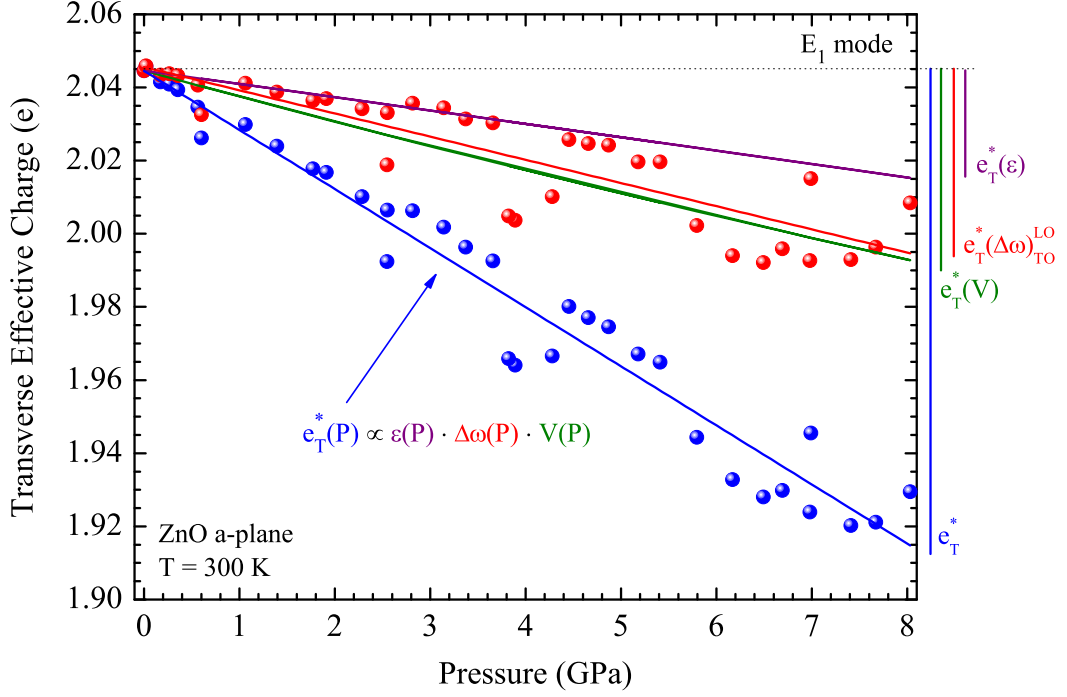


Figure 7.9: Hydrostatic pressure dependence of the transverse effective charge  $e_T^*(P)$  (blue). The pressure dependence of the contributing parameters, namely the LO-TO splitting  $\Delta\omega(P)$  (red), the unit cell volume  $V(P)$  (green), and the dielectric constant  $\epsilon(P)$  (purple), are visualized as derived from experimental measurements and theoretical considerations.

charge  $e_T^*$  exhibits a strong reduction with increasing pressure, yielding values of  $e_T^*(P)(A_1) = 2.17 - 14.6 \times 10^{-3}P/\text{GPa}$  and  $e_T^*(P)(E_1) = 2.04 - 13.7 \times 10^{-3}P/\text{GPa}$  (in units of the elementary charge) for the  $A_1$  and  $E_1$  phonons, respectively. These values are in good agreement with first principle calculations by Dal Corso et al. [306] who reported an effective charge of 2.05 (in units of the elementary charge) in ZnO.

For an intuitive visualization, the transverse effective charge of the  $E_1$  is displayed in Fig. 7.9 together with its separate parameters as function of hydrostatic pressure. Apparently, almost similar contributions to the pressure dependence of  $e_T^*$  are given by the volume compression and the LO-TO splitting, but a smaller pressure dependence is found for the dielectric constant. The relative contribution of each of these parameters are estimated to be about 40%, 38%, and 22% for the volume, mode splitting, and dielectric constant, respectively.

The question arises how the pressure dependence of the transverse effective charge in ZnO compares to other IV-IV and III-V semiconductors. In order to address this issue, the transverse effective charge of ZnO is normalized to its zero-pressure value and plotted in Fig. 7.10 as a function of pressure together with the data for SiC, AlN,

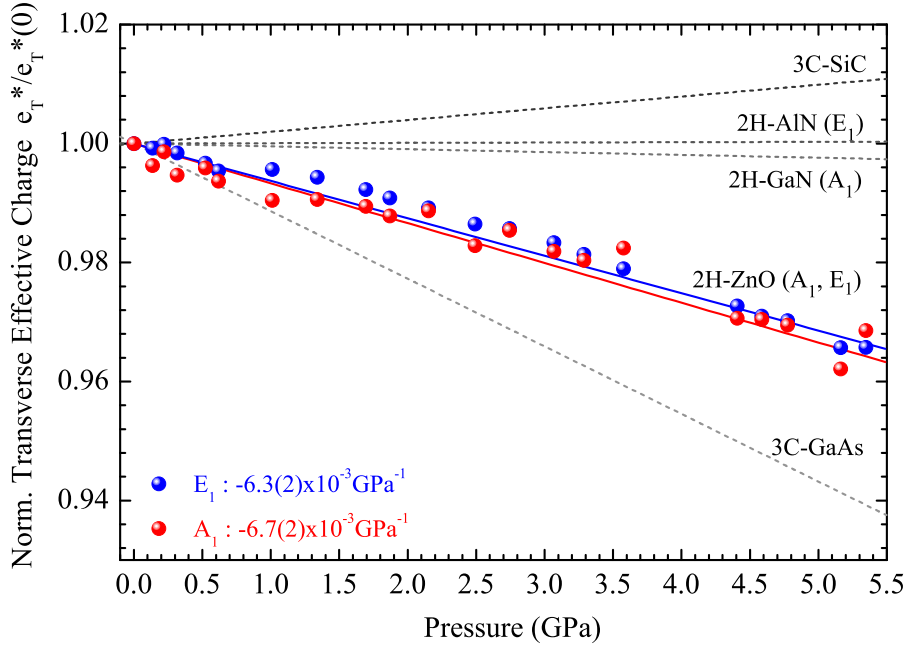


Figure 7.10: Pressure dependence of the transverse effective charge  $e_T^*$  normalized to its ambient pressure value. The gray lines correspond to the experimental results obtained for SiC, AlN, GaN, and GaAs extracted from Ref. [302, 303, 307].

GaN and GaAs which are extracted from Refs. [302, 303, 307]. While SiC is the only compound to exhibit an increase of the effective charge with increasing pressure, all other compound semiconductors show a decreasing or in the case of AlN constant value of  $e_T^*$ . A clear systematic in the magnitude and sign of the pressure coefficient of the transverse effective charge is found if correlated to the bond polarity. Within the four materials SiC, AlN, GaN, and ZnO, the bond polarity  $\alpha_p$  as defined by Harrison [308] increases with  $\alpha_p = 0.26, 0.58, 0.60,$  and  $0.78,$  respectively. For the heteropolar semiconductor compounds of the form  $A^N B^{8-N}$  with anion species belonging to the first row of the periodic table, this may indicate the following correlation of the bond polarity to the transverse effective charge: for bond polarities lower than 0.6, the effective charge increases with pressure in inverse proportion to the bond polarity whereas for bond polarities greater than 0.6,  $e_T^*$  becomes larger with increasing polarity. The here presented pressure dependence of the Born's transverse effective charge in ZnO therefore correlates with the bond polarity of ZnO in excellent agreement with various other compound semiconductors.

### 7.6.3 Line-shape asymmetry of the $E_2(\text{high})$

In addition to the mode Grüneisen parameters and pressure dependence of the transverse effective charge, the asymmetry of the  $E_2^{\text{high}}$  as function of hydrostatic pressure

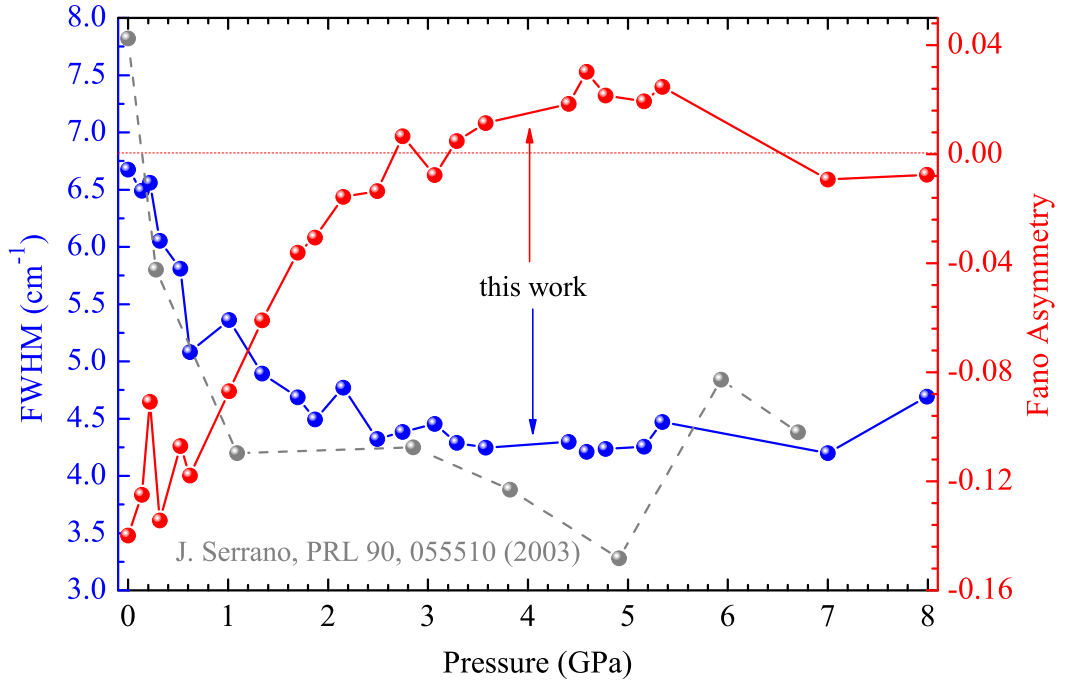


Figure 7.11: Phonon line widths (blue) and asymmetry (red) of the  $E_2^{high}$  as function of hydrostatic pressure up to 8 GPa at  $T = 300$  K. The dotted red line marks the zero asymmetry. Gray data points are plotted according to Ref. [309]. Lines are guides to the eye.

is investigated. As previously mentioned, the  $E_2^{high}$  mode exhibits a asymmetric broadening in the zero-pressure Raman spectrum which is best described by a Fano-like line shape. Fig. 7.11 shows the full width at half maximum (blue) and the asymmetry (red) of this mode as function of hydrostatic pressure between 0 and 8 GPa. Without external pressure, a line width of  $6.5 \text{ cm}^{-1}$  is determined. This value decreases to  $4.2 \text{ cm}^{-1}$  at a pressure of 3 GPa and remains constant for higher hydrostatic pressures. The derived pressure dependence of the line width is compared to the results of a recent study by Serrano et al. [309] which are shown in gray in Fig. 7.11. Based on the larger number of data points and smaller variations of absolute values compare to Ref. [309], the here presented results do not only allow the observation of a reduced line width of the  $E_2^{high}$  mode under hydrostatic pressure but also establish its constant value for  $P \geq 3$  GPa. In addition, it can be seen that the asymmetry of this mode decreases in accordance with the decrease of the line widths resulting in a symmetric Lorentzian line shape of the  $E_2^{high}$  for hydrostatic pressure of 3 GPa and above.

The observed pressure dependence can be explained considering the possible decay channels of the  $E_2^{high}$  mode into acoustical phonons. Ab initio calculation showed

that the frequency of the  $E_2^{high}$  mode is close to a singularity of the two-phonon density of states (DOS) which corresponds to a combination of transversal and longitudinal acoustical phonons (TA+LA) in the vicinity of the K point of the Brillouin zone [291,309]. The zero-field position of the  $E_2^{high}$  is found in the high energy flank of a sharp ridge of the two phonon DOS which leads to an anharmonic decay mechanism resulting in an asymmetric broadening of the line shape of this mode on its low energy side. The application of hydrostatic pressure shifts the  $E_2^{high}$  phonon frequency to higher wave numbers with a pressure coefficients of  $5.04 \text{ cm}^{-1}/\text{GPa}$  (Table 7.2), whereas the TA+LA density of states is expected to shift to smaller values [291]. This opposite pressure dependence leads to a significantly reduced two phonon density of states at the energy of the  $E_2^{high}$  mode at elevated hydrostatic pressures, thus suppressing the decay channel into TA+LA modes. In the Raman spectra, this correlates to the reduction of the asymmetry of the  $E_2^{high}$  and the narrowing of the line width of this mode.

## 7.7 Phonon deformation potentials

So far, the influence of hydrostatic pressure on the vibrational properties of wurtzite ZnO was discussed. This discussion is now extended by an analysis of the uniaxial pressure dependence of the first order Raman modes. This work represents the first study of the frequency shift of ZnO phonons as function of uniaxial pressure. In combination with hydrostatic pressure studies, this is of great use since it enables direct access to the phonon deformation potentials (PDP) of ZnO. The measurements of hydrostatic and uniaxial pressure coefficients at the same samples further guarantees the same phonon frequencies at zero pressure, thus facilitating the precise determination of the PDPs. For ZnO, no experimental values for the phonon deformation potentials are available in the literature. This is quite surprising for such an intensively investigated compound semiconductor, especially since the phonon deformation potentials are important material parameters which establish a direct relation between the frequency of the Raman modes and e.g. the biaxial strain in heteroepitaxial epilayers (Eq. 7.11).

In the case of e.g. GaN a rather error-prone approach for the determination of the phonon deformation potentials was chosen by Demangeot et al. [310] and Davydov et al. [311]. In these works, the Raman shifts of strained GaN thin films grown on  $\text{Al}_2\text{O}_3$  and 6H-SiC, respectively, were compared with hydrostatic pressure coefficients derived from bulk GaN crystals [312] in order to determine the PDPs. This comparison is problematic due to several reasons: (i) For thin films below the critical thickness, the heteroepitaxial layers are strained due to the lattice mismatch of substrates and epilayers. (ii) For thicker epilayers were the relaxation of

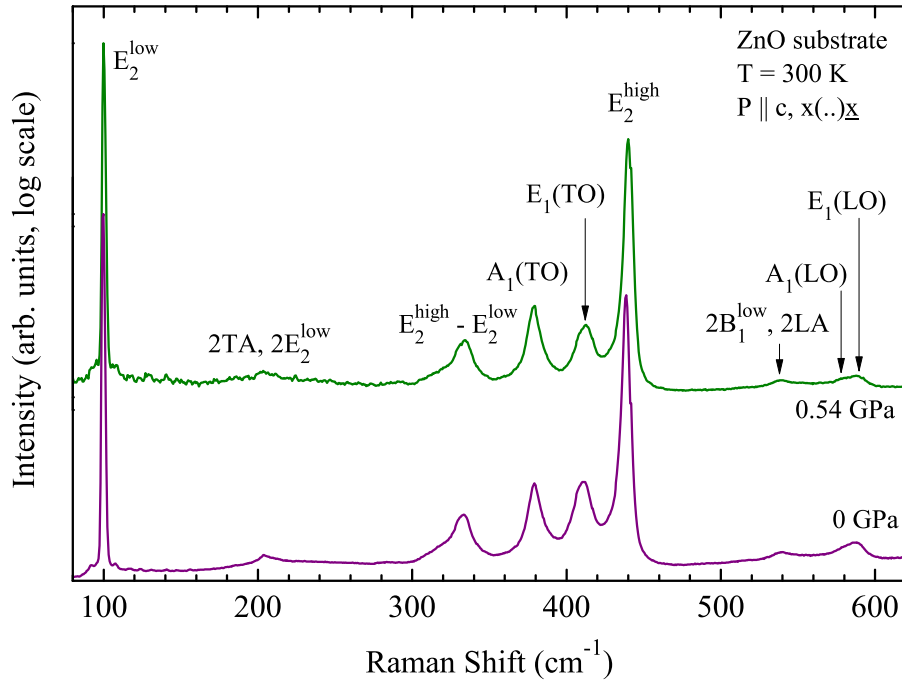


Figure 7.12: ZnO Raman spectra in the backscattering geometry for a uniaxial pressure parallel to the  $c$ -axis of 0 GPa and 0.54 GPa at  $T = 300$  K.

misfit strain is complete, an inhomogeneous strain distribution may occur due to the lattice deformation by the mismatch of the coefficients of thermal expansion of substrates and epilayers [204]. (iii) Rather large variations in the reported values of the bulk modulus can introduce an additional error in the determination of the PDPs [311]. (iv) Finally, the comparison of biaxial strain in heteroepitaxial layers [310,311] with hydrostatic pressure coefficients derived from a completely different bulk sample [312] seems problematic due to the neglected influence of the structural quality and defect concentrations on the strain. The significance of these aspects is demonstrated by the large deviation of reported phonon deformation potentials in GaN [310,311,313]. Consequently, the combination of Raman studies as function of hydrostatic and uniaxial pressure on the same samples enables a more reliable direct determination of the PDPs without inaccuracies due to the discussed issues. Since no direct determination of the phonon deformation potentials exists for GaN, too, Raman measurements as function of uniaxial and hydrostatic pressure are also performed for this material system and discussed in detail in Ref. [314].

Fig. 7.12 displays two representative Raman spectra at 0 GPa and at an uniaxial pressure of 0.54 GPa. This pressure corresponds approximately to the maximum uniaxial pressure which can be applied without compromising the reproducibility of the Raman shifts, i.e. the limit below which an elastic description of the compres-

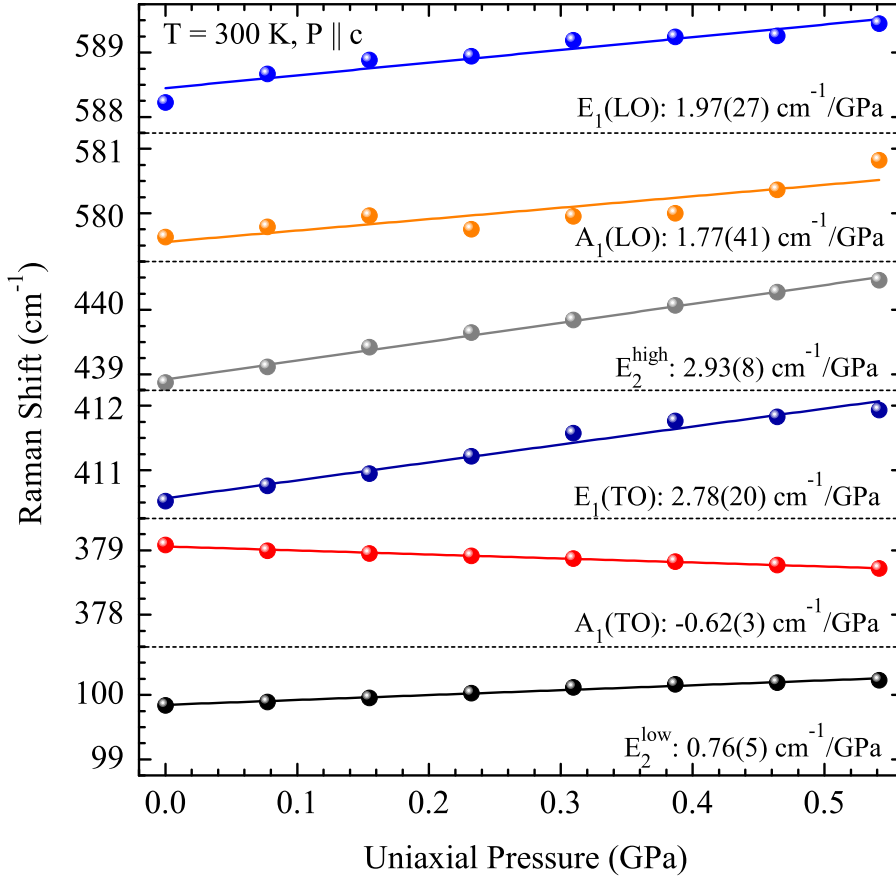


Figure 7.13: Frequency shift of the first-order Raman modes in ZnO as function of uniaxial pressure parallel to the  $c$ -axis ( $\mathbf{P} \parallel \mathbf{c}$ ) at  $T = 300$  K. Solid lines represent linear least squares fits to the experimental data points.

sion is applicable. The spectra are shown for the  $x(\dots)\bar{x}$  configuration with a uniaxial pressure parallel to the crystal  $c$ -axis  $\mathbf{P} \parallel \mathbf{c}$ . According to the Raman selection rules in Table 7.1, the  $E_2^{low}$ ,  $E_2^{high}$ ,  $A_1(TO)$  and  $E_1(TO)$  are allowed in this configuration. In addition, the  $A_1(LO)$  and  $E_1(LO)$  are weakly observed as previously discussed. Using appropriate Lorentzian and Fano-like line shape fits, the phonon frequencies are determined from the Raman spectra at different uniaxial pressures. These values are plotted for each mode as function of uniaxial pressure in Fig. 7.13. The solid lines represent linear least squares fits to the experimental data, thus delivering the uniaxial pressure coefficients  $-\tilde{b}_i = \partial(\omega_i)/\partial(\sigma_{zz})$ . These values are listed in Table 7.3 together with the hydrostatic pressure coefficients  $-(2\tilde{a}_i + \tilde{b}_i)$  which were determined in section 7.6.1. The minus sign is caused by sign convention for compressive pressure. The knowledge of these two parameters naturally determines the biaxial pressure coefficient  $-\tilde{a}$  which is also listed in Table 7.3.

The frequency shift  $\Delta\omega_i$  for each phonon mode (indicated by the index  $i$ ) as

Table 7.3: Experimental values for the uniaxial  $-\tilde{b}$  and hydrostatic  $-(2\tilde{a} + \tilde{b})$  pressure coefficients and derived phonon deformation potentials  $a$  and  $b$ . Numbers in parenthesis are error bars.

Mode	$-\tilde{a}$ (cm <sup>-1</sup> /GPa)	$-\tilde{b}$ (cm <sup>-1</sup> /GPa)	$-(2\tilde{a} + \tilde{b})$ (cm <sup>-1</sup> /GPa)	$-a$ GPa	$-b$ GPa
$E_2^{low}$	-0.77(4)	0.76(5)	-0.78(2)	-169	-4
$E_2^{high}$	1.06(6)	2.93(8)	5.04(3)	653	838
$A_1(TO)$	2.77(4)	-0.62(3)	4.91(5)	832	457
$E_1(TO)$	1.13(12)	2.78(20)	5.03(3)	660	821
$A_1(LO)$	1.40(24)	1.77(41)	4.56(7)	641	667
$E_1(LO)$	1.74(19)	1.97(27)	5.44(10)	628	686

function of strain and stress is given within the range of linear elasticity by

$$\Delta\omega_i(P) = 2a_i\epsilon_{xx} + b_i\epsilon_{zz} = 2\tilde{a}_i\sigma_{xx} + \tilde{b}_i\sigma_{zz}. \quad (7.31)$$

In order to determine the phonon deformation potentials  $a$  and  $b$ , the stress components  $\sigma_{xx}$  and  $\sigma_{zz}$  must be expressed by the strain components  $\epsilon_{xx}$  and  $\epsilon_{zz}$ . The correlation between these values is given by the matrix of elastic stiffness constants in Eq. 7.3 with

$$\sigma_{xx} = (C_{11} + C_{12})\epsilon_{xx} + C_{13}\epsilon_{zz}, \quad (7.32)$$

$$\sigma_{zz} = 2C_{13}\epsilon_{xx} + C_{33}\epsilon_{zz}. \quad (7.33)$$

Thus, the phonon deformation potentials  $a$  and  $b$  are given by:

$$a = \tilde{a}(C_{11} + C_{12}) + \tilde{b}C_{13}, \quad (7.34)$$

$$b = 2\tilde{a}C_{13} + \tilde{b}C_{33}. \quad (7.35)$$

Depending on the choice of the elastic stiffness constants  $C_{ij}$ , slight variations of the phonon deformation potentials may occur. It was argued that the most precise method to determine the elastic stiffness constants is given by ultrasonic measurements [265]. Here, the elastic constants published by Kobiakov [266] are used which were derived from ultrasonic measurements using the resonance-antiresonance technique [315]. This method allows the determination of elastic constants with an accuracy of  $\pm 0.001\%$  [266]. The measurements were performed on a variety of high quality ZnO single crystals establishing the general validity of the measured values. The reported values in GPa are:

$$C_{11} = 207.0, C_{12} = 117.7, C_{13} = 106.1, C_{33} = 209.5, C_{44} = 44.8, C_{66} = 44.6.$$

Substituting these values into Eq. 7.30, a bulk modulus of  $B_0 = 142.5$  GPa is calculated in excellent agreement with the reported value of Desgreniers [274] which was used to derive the Grüneisen parameters in section 7.6.1. With these elastic stiffness constants  $C_{ij}$ , the phonon deformation potentials  $a$  and  $b$  are now computed and listed in Table 7.3.

As can be seen from Fig. 7.13 and the values in Table 7.3, all modes except for the  $A_1(TO)$  shift to higher frequencies with increasing uniaxial pressure. The negative pressure coefficient of the  $A_1(TO)$  mode in ZnO is in accordance with results obtained for the  $A_1(TO)$  in CdS [316] and the singlet modes in cubic ZnS [317], but in contradiction to the uniaxial pressure dependence of the equivalent modes in cubic GaAs, Si, and diamond [318] as well as wurtzite GaN [314]. The differences between these materials can be understood taking Kleinman's internal strain parameter  $\zeta$  into account. It is given by

$$\zeta = \frac{\alpha - \beta}{\alpha + \beta}, \quad (7.36)$$

where  $\alpha$  and  $\beta$  are Keating's valence force field parameters for bond stretching and bond bending, respectively. Martin [319] has calculated the internal strain parameters  $\zeta$  for a variety of semiconductors. The smallest value of  $\zeta = 0.208$  was found for covalent bonded diamond and the largest of  $\zeta = 0.793$  and  $0.785$  for the strongly ionic materials CdTe and CuCl, respectively. By a comparison of the internal strain parameter with the frequency shift of the phonon modes under uniaxial pressure, a clear tendency is observed. The covalent bonded materials silicon and diamond exhibit large positive slopes of their singlet and doublet modes as function of uniaxial stress parallel to the e.g. [100]-axis [318]. With increasing ionicity, the slope of the Raman modes under uniaxial pressure is reduced but remains positive for e.g. GaAs [318] and GaN [314] with internal strain parameters  $\zeta$  between 0.5 and 0.6 [319,320]. For the more ionic bonded II-VI materials like cubic ZnS ( $\zeta = 0.74$ ) [319] and wurtzite CdS, a negative slope of the singlet modes in ZnS [317] and the  $A_1(TO)$  mode in CdS [316] was observed. This result is in agreement with the here observed negative pressure coefficient of the  $A_1(TO)$  mode in ZnO [314]. Thus, the negative pressure coefficient of the  $A_1(TO)$  in ZnO is related to a large internal strain parameter which expresses the large rigidity of the ionic bonds in ZnO. In other words, the bonds in ZnO are more vulnerable to bond bending than to bond stretching.

## 7.8 Summary

In conclusion, the lattice dynamics of ZnO was studied under the influence of hydrostatic and uniaxial pressure. High precision values for the pressure coefficients and Grüneisen parameters of all Raman active modes were derived. The LO-TO splitting and the Born's transverse effective charge of the polar modes  $E_1$  and  $A_1$

were found to decrease with increasing pressure. This dependence is correlated to the bond polarity and compared to the pressure dependence of the effective charge in other semiconductors such as SiC, AlN, and GaN. Furthermore, the line narrowing of the asymmetric  $E_2^{high}$  mode in ZnO is investigated as function of increasing hydrostatic pressure. It can be explained by a different pressure dependence of the  $E_2^{high}$  and the two phonon density of states in that frequency range which results in a suppression of the decay channel of the  $E_2^{high}$  into acoustical phonons at elevated pressures. Finally, the hydrostatic pressure measurements are complemented by Raman studies as function of uniaxial pressure which enabled the first experimental determination of the phonon deformation potentials in ZnO. The negative pressure coefficient of the  $A_1(TO)$  mode under uniaxial pressure was compared to other materials and a correlation to the bond ionicity was discussed.

## 8 Exciton and phonon dynamics under resonant excitation

This chapter investigates the effects of resonant and non-resonant excitation of excitons on the intensity and decay dynamics of phonon sidebands and longitudinal optical (LO) Raman modes. Section 8.1 covers the impact of varying excitation energies on the intensity of the Raman modes and luminescence replica. A strong enhancement of the Raman cross section of the LO modes is observed for excitation energies in resonance with excitonic states. Different enhancements of the first and second order LO modes are discussed considering the wave vector dependence of the Fröhlich interaction. The dynamical characteristics of Raman modes and luminescence bands under resonant excitation are studied on the picosecond time scale in section 8.2. Thereto, the excitation energy is tuned over the bound exciton resonance while the decay dynamics of the phonon assisted luminescence and Raman modes are measured (section 8.2.1). In addition, resonant time resolved measurements of Raman and luminescence lines are conducted as function of the temperature (section 8.2.2). The influence of the dissociation of the bound excitons at elevated temperatures on the lifetimes and resonance enhancement of the LO modes by exciton-phonon coupling is investigated.

### 8.1 Resonant Raman scattering at excitonic states

Resonant Raman scattering (RRS) in ZnO single crystals was first reported by Scott in 1970 [321], followed by more extensive studies by Oka et al. [322] and Calleja and Cardona [295]. Recently, the renewed interest in ZnO encouraged additional studies on RRS in ZnO thin films and nanostructures [296, 323–326]. However, most of the reported experiments were conducted using either the visible laser lines of an  $\text{Ar}^+ - \text{Kr}^+$  ion laser with excitation energies well below the band gap of ZnO [295] or the 325.0 nm line of a HeCd laser [321, 325, 326] which energy is considerably above the excitonic states. Therefore, no resonance with free or bound exciton states was achieved in these works. In an alternative approach, the 351.1 nm (3.531 eV) and 363.8 nm (3.408 eV) UV lines of the  $\text{Ar}^+ - \text{Kr}^+$  ion laser were used for excitation while the resonance condition with near band edge electronic states was achieved using the temperature shift of the band gap by variation of the temperature [323, 324].

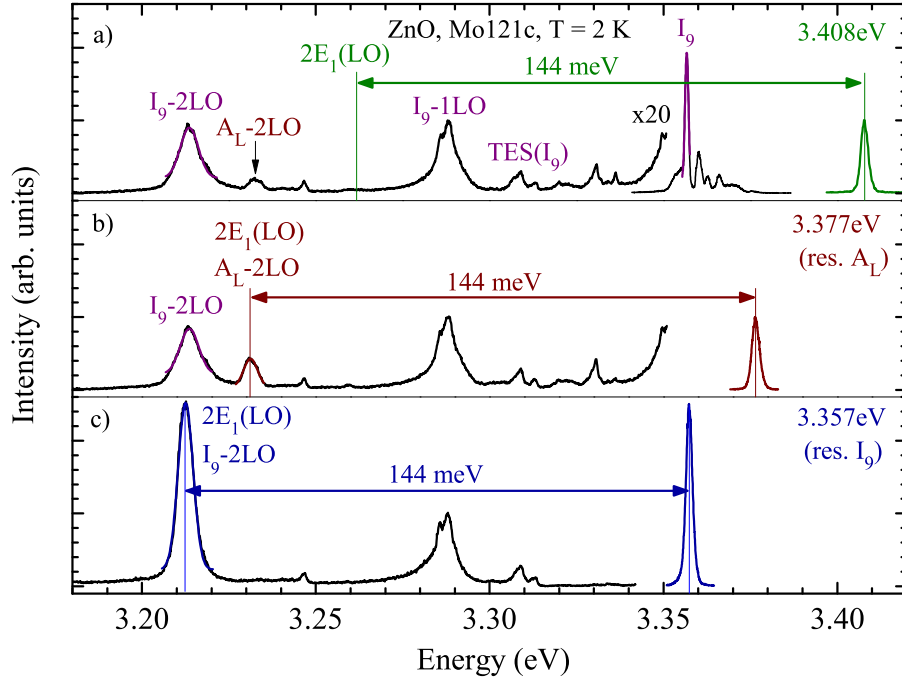


Figure 8.1: PL and Raman spectra of a ZnO single crystal for different excitation energies at  $T = 2$  K. (a) 3.408 eV (above the A and B free excitons), (b) 3.377 eV (in resonance with the  $A_L$  exciton), (c) 3.357 eV in resonance with the dominant donor bound exciton  $I_9$ . Arrows indicate the energy spacing between the laser and the  $2E_1(LO)$  Raman mode. Spectra are normalized to the  $I_9$ -1LO peak.

This method brings about certain difficulties such as the dissociation of bound excitons and the incomparability of intensities due to temperature dependence, which complicate or even preclude a comprehensive study of the exciton-phonon interaction in resonance with excitonic states. In order to avoid these issues and to excite resonantly at the precise energies of the free and bound excitons, a frequency-doubled titan-sapphire laser is used in this work which enables a continuous tuning of the wavelength between 353 nm (3.512 eV) and 400 nm (3.100 eV) (for details about the experimental setup see chapter 2).

Fig. 8.1 shows the photoluminescence spectra of a ZnO single crystal for three different excitation energies close to the band edge of ZnO at  $T = 2$  K. The spectra were acquired in backscattering geometry with the incident light oriented perpendicular to the crystal  $c$ -axis. The narrow line at the high energy side of each spectrum originates from the excitation laser. The highest excitation energy of 3.408 eV is above the energy of the A and B free exciton transitions. This spectrum is dominated by the narrow bound exciton lines among which the  $I_9$  at 3.357 eV has the highest intensity. Several additional peaks are observed between 3.18 eV and 3.35 eV.

The strongest emission lines at 3.285 eV and 3.213 eV are related to the first and second phonon replica of the  $I_9$  with an energy spacing of 72 meV and 144 meV, respectively. The intensity of these two peaks is approximately equal. The peak at 3.232 eV has an energy spacing of two LO phonon energies to the free exciton and is thus attributed to the  $A_L$ -2LO sideband. Furthermore, several smaller lines are observed which are discussed in greater detail in other sections of this work, e.g. the  $Y_0$  at 3.333 eV (chapter 6) and the two electron satellite doublet of the  $I_9$  at about 3.310 eV (sections 3.4 and 6.4). The second spectrum (Fig. 8.1b) is recorded with the excitation laser in resonance with the free  $A_L$  exciton at 3.377 eV. The spectrum in the range of the phonon sidebands is mainly identical to the first spectrum except for the intensity increase of the 3.232 eV line. This effect is caused by the resonant excitation with the free  $A_L$  exciton and is even more pronounced in the case of the bound excitons as shown in Fig. 8.1c. Here, the laser energy is in resonance with the strongest bound exciton line  $I_9$  at 3.357 eV. The phonon replica of the free exciton at 3.232 eV is not observed anymore as expected for an excitation energy below the energy of  $A_L$ . Furthermore, it can be seen that the intensity of the 3.213 eV transition increases by more than a factor of 2.5 compared to the higher excitation energies which are not in resonance with this specific bound exciton state. This is caused by the overlapping of two contributions: the 2LO phonon sideband of the  $I_9$  and the second order Raman process  $2E_1(\text{LO})$ . While the luminescence process exhibits similar intensities for the phonon replica under resonant and non-resonant excitation, the cross section of the inelastic Raman scattering is greatly increased in resonance with electronic states [327]. This resonance enhancement is particularly pronounced for the LO phonons which couple to electrons and holes by the Fröhlich interaction. Calleja and Cardona have shown that the Fröhlich interaction results in a resonant enhancement of the LO scattering in ZnO which starts already at photon energies of 1 eV below the fundamental band gap [295], i.e. resonant excitation occurs for all excitation energies close to the band gap. However, within this study the terms 'resonant' and 'non-resonant' are used to express the explicit resonance with a particular excitonic state. The importance of excitons as resonant intermediate states was already pointed out by Birman et al. in the late 1960s [328, 329]. It was shown that the small damping constants of free and bound excitons at low temperatures enhance the Raman cross section by several orders of magnitude. Coming back to the spectra in Fig. 8.1, the intensity increase of the 3.213 eV line can be explained by the resonance enhancement of the  $2E_1(\text{LO})$  Raman process. The observed intensity increase by a factor of 2.5 is not in contradiction to the much higher reported enhancements of the Raman cross section since this factor only describes the intensity ratio of the resonantly enhanced  $2E_1(\text{LO})$  Raman mode to the luminescence replica of the  $I_9$ .

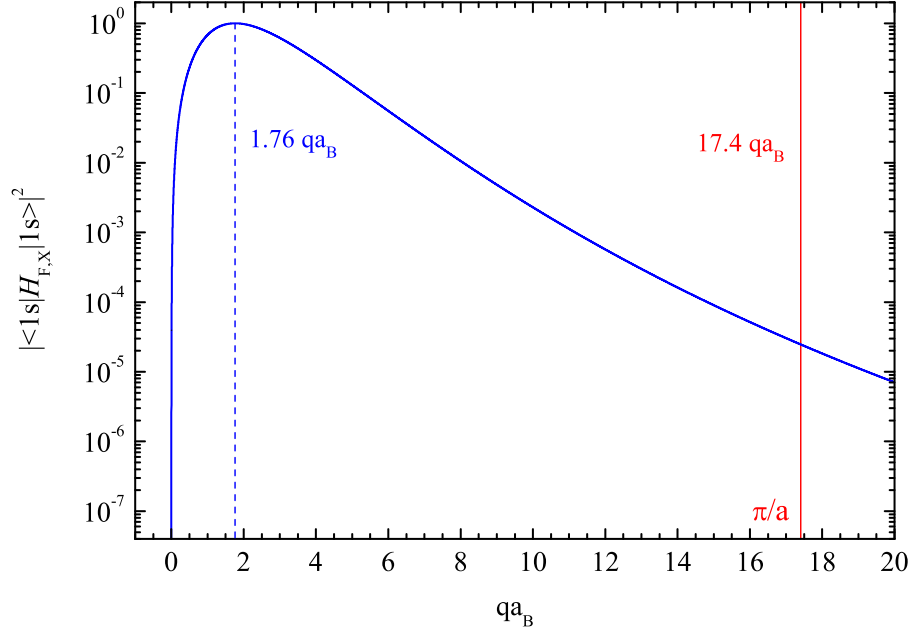


Figure 8.2: Normalized squared Fröhlich interaction matrix element for ZnO as function of the wave vector  $q$  times the exciton Bohr radius  $a_B$ . The wave vector dependence is calculated using effective electron and hole masses of  $m_e^* = 0.24$  [330] and  $m_h^* = 0.59$  [74]. The exciton-LO phonon interaction is largest for  $qa_B = 1.76$ . The vertical red line indicates the edge of the first Brillouin zone at  $\pi/a = 17.4 qa_B$  with  $a_B = 18 \text{ \AA}$  and  $a = 3.249 \text{ \AA}$ .

It is interesting to note that the resonance enhancement of the  $2E_1(LO)$  Raman mode is not reflected in the intensity of the first order  $E_1(LO)$  under resonant excitation of the  $I_9$ . This effect can be explained by the wave vector dependence of the Fröhlich interaction between excitons and LO-phonons [27]. Fig. 8.2 displays the normalized squared Fröhlich interaction matrix element as function of the wave vector  $q$  times the exciton Bohr radius  $a_B$ . This matrix element is given by:

$$|\langle 1s | H_{F,X} | 1s \rangle| = \frac{C_F}{q} \left( \frac{1}{[1 + (p_h a_B q / 2)^2]^2} - \frac{1}{[1 + (p_e a_B q / 2)^2]^2} \right) \quad (8.1)$$

where  $H_{F,X}$  is the Fröhlich interaction Hamiltonian for an exciton in the  $1s$  ground state [331],  $C_F$  is the Fröhlich coefficient which is dispensable here due to the normalization, and  $p_e$  and  $p_h$  are defined as

$$p_e = \frac{m_e^*}{m_e^* + m_h^*} \quad \text{and} \quad p_h = \frac{m_h^*}{m_e^* + m_h^*}. \quad (8.2)$$

The calculation of the wave vector dependence of the Fröhlich interaction is performed using values for the effective electron and hole masses  $m_e^* = 0.24$  [330] and  $m_h^* = 0.59$  [74], respectively. Apparently, the matrix element in Fig. 8.2 vanishes for

$q = 0$  where the macroscopic electric field of the LO phonons is uniform in space. Since the exciton as a whole quasiparticle is neutral, its energy cannot be changed by a uniform field. For the given electron and hole masses in ZnO, the strength of the Fröhlich interaction reaches a maximum at  $qa_B = 1.76$ . Hence, the strongest interaction occurs when the wavelength of the electric field is of the order of the exciton Bohr radius  $a_B$ . For large values of  $q$ , the matrix element decreases although significantly slower than it increases for small  $q$ . The vertical red line in Fig. 8.2 indicates the edge of the first Brillouin zone  $q = \pi/a$  with  $a = 3.249 \text{ \AA}$  in units of  $qa_B$ . Due to the small exciton Bohr radius  $a_B = 18 \text{ \AA}$  of ZnO, the zone edge is already reached at  $17.4 qa_B$  where the squared matrix element has still non-zero values. These findings can now be used to explain the difference in the resonance enhancement of the 1LO and 2LO Raman modes by the exciton-LO phonon interaction. In the case of first order Raman scattering, the maximum phonon wave vector  $q$  is determined by twice the photon wave vector  $k$  with  $q = 2k = 4\pi/\lambda \approx 3 \cdot 10^{-3} \text{ \AA}^{-1}$  for resonant excitation with  $\lambda = 375 \text{ nm}$  which corresponds to approximately  $1/20 qa_B$  in Fig. 8.2. For these  $q$  values, the Fröhlich interaction matrix element in Eq. 8.1 is very small. By contrast, the wave vector conservation for second order Raman scattering is satisfied when  $\mathbf{q}_1 \pm \mathbf{q}_2 \approx 0$ . Hence, no restrictions on the magnitude of the individual wave vectors exist. Although the two phonon density of states is particularly high at the zone edge where the matrix element is smaller, the total contribution of all two phonon  $q$  values results in a significantly larger matrix element of the exciton-LO phonon interaction which explains the stronger resonance enhancement of the  $2E_1(LO)$  compared to the  $E_1(LO)$  under resonant excitation in Fig. 8.1.

In a next step, the excitation energy dependence of the luminescence replicas and Raman modes is studied at an elevated temperature. The photoluminescence spectra at  $T = 77 \text{ K}$  are depicted in Fig. 8.3 for different excitation energies between  $3.357 \text{ eV}$  and  $3.256 \text{ eV}$ . The narrow emission lines at the high energy side of each spectrum represent the specific laser excitation. At a temperature of  $77 \text{ K}$ , most of the shallow bound excitons are dissociated since the thermal energy is comparable to the localization energy  $E_{loc}$  of the bound excitons. For high excitation energies, a dominant luminescence band at  $3.31 \text{ eV}$  with two phonon replicas can be observed. This peak was attributed to a band-acceptor transition ( $e, A$ ) related to basal plane stacking faults by Schirra et al. [189]. The luminescence band is superimposed by the first phonon replica of the free exciton  $A_L$ -1LO for large excitation energies. Furthermore, a peak at  $3.212 \text{ eV}$  appears for the highest excitation energy which has an energy spacing of  $144.5 \text{ meV}$  ( $1166 \text{ cm}^{-1}$ ) to the laser line and is indicated in the spectra by a red dot. This distance remains constant if the laser wavelength is shifted to lower energies (Fig. 8.3b). The energy spacing equals twice the energy of the  $E_1(LO)$  Raman mode ( $583 \text{ cm}^{-1}$ ) [295], evidently identifying this line as a second

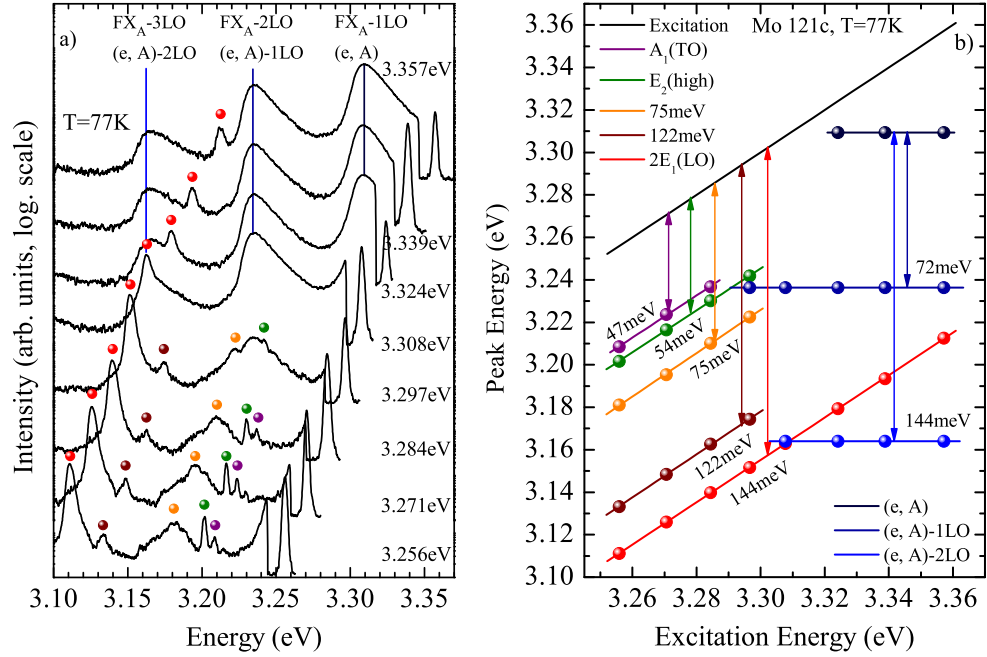


Figure 8.3: (a) PL and Raman spectra of a ZnO single crystal for different excitation energies between 3.357 eV and 3.256 eV at  $T = 77$  K. Vertical lines indicate the energy position of luminescence replica, colored dots mark lines which are related to first and second order Raman modes in ZnO. (b) Energy position of the luminescence and Raman peaks as function of the excitation energy. Luminescence bands are represented by horizontal lines which remain constant in energy, diagonal lines mark the energy position of the Raman modes which are shifted by the phonon energy compared to the excitation energy.

order  $2E_1(LO)$  Raman mode [322]. For an excitation energy of 3.308 eV, the energy of the  $2E_1(LO)$  Raman line matches that of the phonon replica at 3.165 eV leading to a superposition of the luminescence and Raman signals in the spectra. As the laser is tuned to lower energies, additional Raman modes appear which are not visible at higher excitation energies due to the strong luminescence background. However, for lower excitation energies, the 3.31 eV luminescence cannot be excited, thus leading to the disappearance of the phonon replicas. The lines at a distance of 47.2 meV ( $381\text{ cm}^{-1}$ ) and 54.2 meV ( $437\text{ cm}^{-1}$ ) from the laser line are identified as the transverse optical  $A_1(TO)$  mode and the non-polar optical  $E_2^{high}$  mode, respectively. As expected, the  $E_1(LO)$  mode is not visible in backscattering geometry. Instead, a rather broad peak with the maximum at a distance of 75 meV ( $605\text{ cm}^{-1}$ ) is observed which possibly originates from higher order scattering involving TA phonons. Furthermore, a Raman line at 122 meV ( $984\text{ cm}^{-1}$ ) can be observed. That mode has first been described by Damen et al. [173] as a multiphonon process. A recent

publication attributes this line to an  $A_1(2TO)$  process which involves phonon wave vectors considerably displaced from the zone center [296].

The energies of the observed Raman as well as luminescence peaks as a function of the excitation energy are illustrated in Fig. 8.3b. The horizontal lines represent the luminescence peaks at a constant energy, which appear for excitation energies higher than or equal to the energy of the 3.31 eV band while the inclined lines show the shifting of the Raman modes with constant distance to the laser excitation. Except for the strong  $2E_1(LO)$ , these lines are only visible for excitation energies lower than that of the defect band at 3.310 eV. The by far strongest intensity of all observed Raman modes is found for the  $2E_1(LO)$  mode. It is the only Raman mode visible for high excitation energies above 3.31 eV and remains dominant for excitation energies well below the depicted 3.256 eV spectrum. Similar to the previously discussed bound exciton resonance at low temperatures, the strong intensity of this mode can be explained by the relaxation of wave vector selection rules for second order Raman scattering, thus enabling a strong enhancement of the higher order LO phonons due to the Fröhlich interaction.

## 8.2 Time resolved exciton and phonon dynamics

Following the previous discussion, the question arises if the contributions of the coherent Raman process and the incoherent luminescence process under resonant excitation can be identified and distinguished. This is investigated in the following sections by time-resolved luminescence and Raman studies as function of excitation energy and temperature.

### 8.2.1 Dynamics as function of the excitation energy

Fig. 8.4 shows the luminescence intensity of a ZnO substrate from Tokyo Denpa between 3.19 eV and 3.30 eV as function of the excitation energy in a 3-dimensional surface plot at  $T = 2$  K. This plot is generated from a large number of single PL spectra with equal detection parameters and varying excitation energies between 3.378 eV and 3.340 eV. The region of the excitation energy covers the full range of excitonic states from the  $A_L$  free exciton-polariton to an energy well below the  $I_{10}$  bound exciton, thus enabling a detailed analysis of the effects of resonant excitation at excitonic states. At the highest excitation energy, the plot shows two luminescence peaks at about 3.290 eV and 3.218 eV which can be attributed to the 1LO and 2LO phonon sidebands of the dominant donor bound exciton  $I_6 (D^0X)$ . Furthermore, a small peak at 3.251 eV appears which originates from the first phonon replica of the two electron satellite of the  $I_6$  at 3.3225 eV (see also Table 6.1 in chapter 6.4). As the excitation energy is decreased, an increase of the emission intensity of all

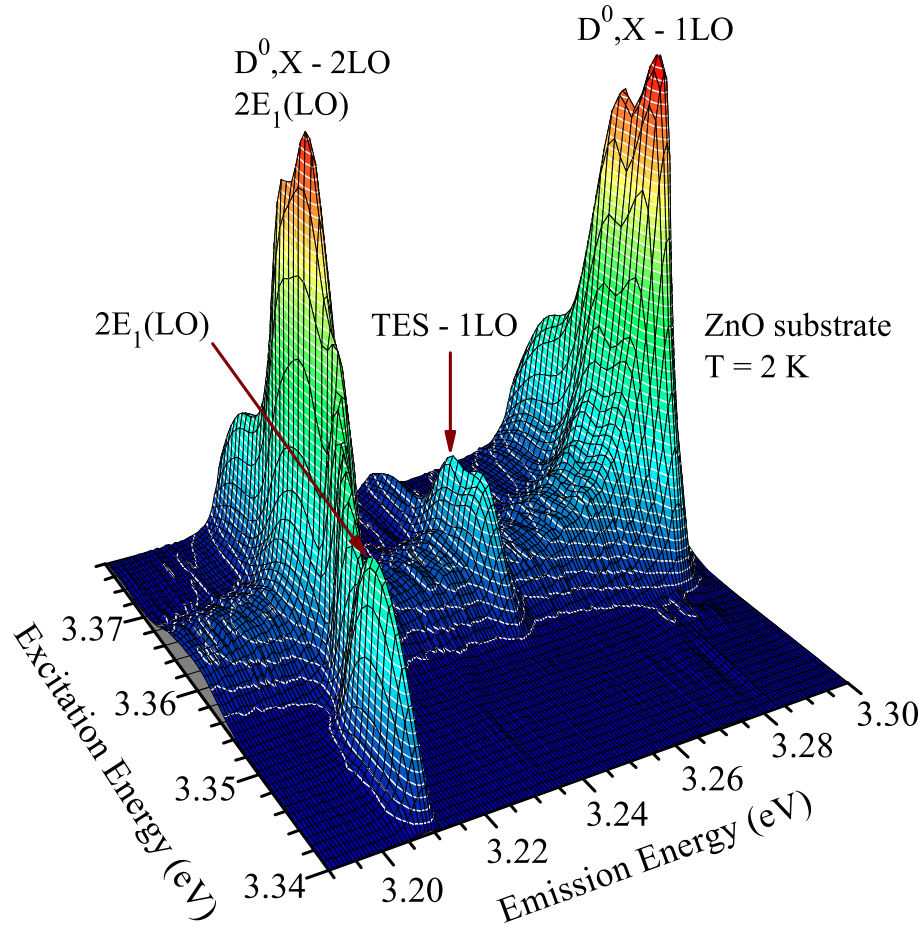


Figure 8.4: 3D surface plot of the emission of a ZnO substrate from Tokyo Denpa as function of the excitation energy at  $T = 2$  K. The strongest emission is observed for resonant excitation with the dominant bound exciton  $I_6$ . At lower energies, only the  $2E_1(LO)$  Raman process is observed whereas the phonon replicas of the bound exciton ( $D^0X - nLO$ ) and its two electron satellite (TES-1LO) disappear.

transitions is observed which culminates in a maximum intensity for an excitation energy of 3.361 eV. At this energy, the excitation is in incoming resonance with the dominant bound exciton line  $I_6$ . Apparently, the intensity of the two phonon replicas  $I_6$ -1LO and  $I_6$ -2LO is comparable in Fig. 8.4. This is in contrast to the stronger enhancement of the second order peak for resonant excitation at the bound exciton  $I_9$  which was discussed in the previous section. The difference can be explained by the pronounced dominance of the  $I_6$  in this sample which results in a large intensity of the 1LO and 2LO luminescence replicas exceeding those of the resonant Raman process. Thus, the different enhancements of the first and second order Raman modes are overshadowed by the luminescence replicas and cannot be observed. For smaller excitation energies, all peaks in the displayed spectral range decrease rapidly.

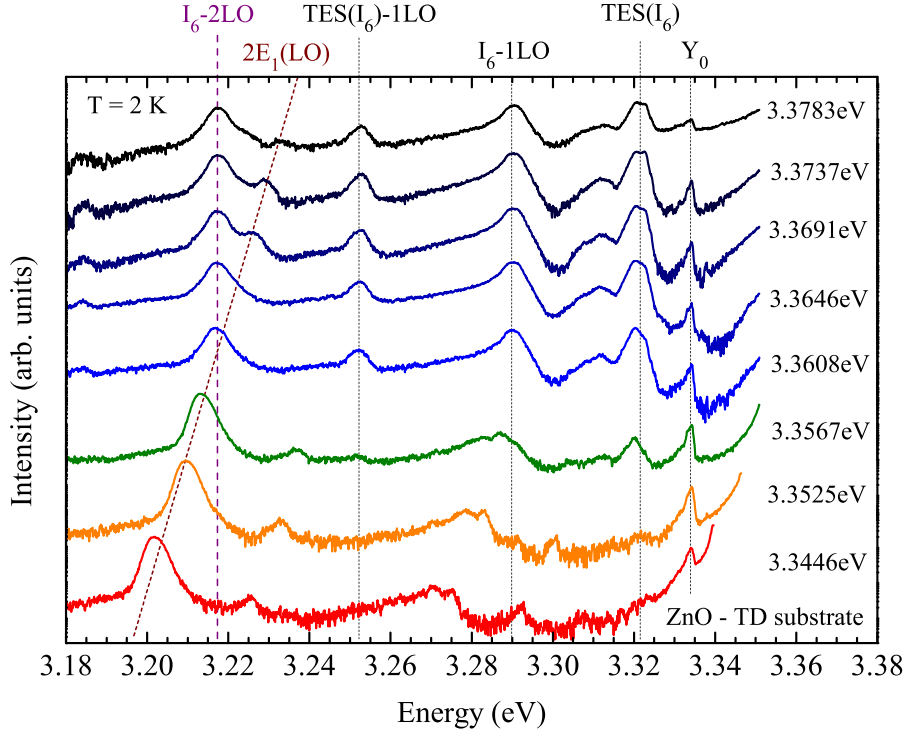


Figure 8.5: PL and Raman spectra of a ZnO substrate from Tokyo Denpa at selected excitation energies between 3.3783 eV and 3.3446 eV. Vertical thin lines mark luminescence peaks and their phonon sidebands. The purple line marks the position of the  $I_6$ -2LO, the dashed brown line visualizes the energy shift of the  $2E_1(LO)$  Raman mode as function of the excitation energy.

At an excitation energy of 3.354 eV (below the  $I_9$  bound exciton), the  $(D^0X)$ -1LO as well as the TES-1LO luminescence bands have disappeared since the laser energy is insufficient to excite the respective bound excitons. However, this is obviously not the case for the low energy peak in Fig. 8.4 which is present below an excitation energy of 3.35 eV, too. Based on the constant energy spacing of this peak to the excitation laser of 144.5 meV, it is identified as the  $2E_1(LO)$  Raman mode. The 3D plot vividly demonstrates the enhancement of the second order LO Raman modes by resonant Raman scattering since no additional first or second order Raman modes are visible on the linear intensity scale.

The energy shift of the  $2E_1(LO)$  Raman mode as function of the excitation energy can best be monitored for a selection of single spectra from Fig. 8.4 as indicated by the dotted brown line in Fig. 8.5. Under resonant excitation with the  $I_6$ , this Raman mode overlaps with the stationary 2LO phonon replica of the  $I_6$  which is marked by the dashed purple line. The lifetimes of these two different processes are now studied as function of the excitation energy.

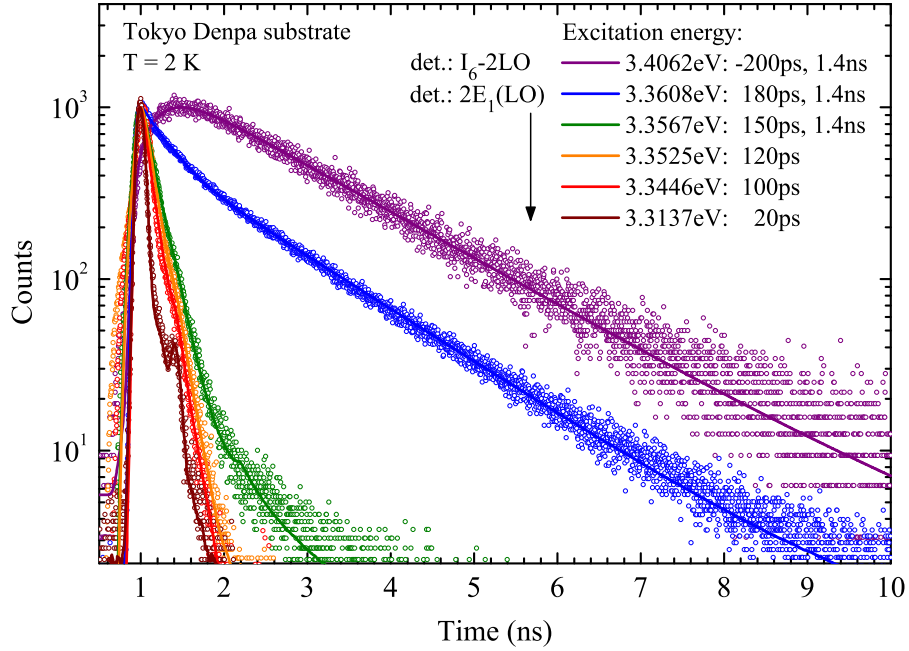


Figure 8.6: Transients of a ZnO substrate from Tokyo Denpa at the energy of the  $I_6$ -2LO phonon replica and  $2E_1(LO)$  Raman mode as function of the excitation energy at  $T = 2$  K. The transient with the highest excitation energy is measured at the energy of the  $I_6$ -2LO line. For lower excitation energy, the detection energy is shifted with the position of the  $2E_1(LO)$  Raman mode. Lifetimes are denoted next to the corresponding excitation energy. Colors of the transients match the spectra with equal excitation energies in Fig. 8.5.

Fig. 8.6 shows the transients of the  $I_6$ -2LO and  $2E_1(LO)$  for different excitation energies between 3.4062 eV and 3.3137 eV. The data was acquired using the single photon counting technique as described in chapter 2. For an excitation energy above the energy of the free A and B excitons (3.4062 eV), the dynamics of the  $I_6$ -2LO transition at 3.216 eV can be described by a mono-exponential rise and decay process with time constants of 200 ps and 1.4 ns respectively. Thereby, the rise time reflects the sum of relaxation, exciton capturing, and phonon scattering processes which occur prior to the radiative recombination of the  $I_6$ -2LO, whereas the measured decay time of 1.4 ns consists of contributions from the radiative and non-radiative lifetime of this energy level. The rise time of 200 ps is comparable to the decay time of the free exciton in this sample, thus indicating that the main contribution to the rise time is given by the capture of the free exciton at localized impurities. This interpretation seems reasonable as the relaxation of the charge carriers to the band extrema usually happens on a sub-ps timescale [332, 333]. The recombination dynamics change considerably if the energy of the excitation laser is reduced. This

is illustrated by the blue transient in Fig. 8.6 which is again recorded at an energy of 3.216 eV but with an excitation energy in resonance with the  $I_6$  bound exciton transition at 3.3608 eV. Apparently, no rise time can be detected but a second decay process with a time constant of about 180 ps appears. The absence of a rise time of the  $I_6$ -2LO confirms the previous explanation since no capture process of free excitons occurs in the case of resonant excitation. In addition, it shows that the excitation of the  $I_6$ -2LO phonon sideband by the emission of two LO phonons occurs on a short timescale below the time resolution of the setup. As for the decay dynamics, the long time constant of 1.4 ns is found to be unchanged. This time constant is related to the non-coherent luminescence process which is independent of the excitation energy. The newly observed shorter time constant must be of different origin. Based on the excitation energy dependent PL spectra it could be seen that the  $2E_1(LO)$  Raman mode and the 2LO phonon sideband overlap for resonant excitation. Consequently, it is conceivable that the second lifetime is related to the Raman process. However, it should be noted that typical phonon lifetimes in other II-VI and III-V semiconductors are between 1 ps and 10 ps [334–336]. In order to analyze a possible correlation, the excitation energy is further reduced – thus detuning the incoming resonance – while the detection energy is shifted with the excitation energy. This is indicated by the arrow in Fig. 8.6.

The spectrum with the next lower excitation energy of 3.3567 eV in Fig. 8.5 shows that the strongest peak in the spectrum is now shifted to lower energies as it originates from the  $2E_1(LO)$  Raman process whereas the intensity of the 2LO luminescence sideband is greatly decreased (Fig. 8.4). The transient at this energy (3.212 eV) still contains two different decay processes with time constants of 150 ps and 1.4 ns, although with reversed amplitudes. While the luminescence related long time constant dominates for higher excitation energies, the decreased intensity in the PL spectra of the phonon replica is now also expressed by a much smaller amplitude of the long decay constant. By contrast, the short process clearly dominates for lower excitation energies as can be seen from the green transient in Fig. 8.6. Apparently, not only the intensity ratio is changed for smaller excitation energies, but also the values of the shorter time constant are reduced. For an excitation energy of 3.3525 eV (orange spectrum and transient in Figs. 8.5 and 8.6), a strictly mono-exponential decay is determined for the  $2E_1(LO)$  with a lifetime of 120 ps. At this energy, neither the  $I_6$  nor deeper bound excitons such as the  $I_9$  can be excited and therefore no luminescence related long decay time of the respective phonon replica is observed. Even more interesting is the decrease of the shorter time constant which is further reduced down to the resolution limit of the setup of 20 ps at an excitation energy of 3.314 eV. This upper limit for the lifetime of the  $2E_1(LO)$  Raman process is in good agreement with reported phonon lifetimes in the single-digit picosecond range [334–

336]. Consequently, the short time constant at the energy of the  $2E_1(LO)$  mode represents the upper limit of the phonon lifetime under non-resonant excitation. For a resonant excitation at the bound exciton  $I_6$ , this lifetime increases to values of up to 180 ps. It is important to point out that no short lifetime around 20 ps is observed under resonant excitation. It is therefore concluded that the increased lifetime of up to 180 ps reflects the phonon lifetime of the resonantly enhanced  $2E_1(LO)$  mode by the Fröhlich interaction. Since the intermediate Raman scattering state for resonant excitation is given by the exciton, the measured lifetime is governed by the lifetime of the real excitonic state which exhibits comparable time constants. It is thereby shown that not only the cross section of the  $2E_1(LO)$  is greatly enhanced by the Fröhlich interaction but also that the LO phonon lifetime depends on the excitation energy and can reach values of up to 180 ps in resonance with bound excitons in ZnO.

### 8.2.2 Dynamics as function of the temperature

Apart from the adjustment of the excitation energy, the resonance of the excitation with bound exciton states can be tuned or detuned by a variation of the temperature, too. This resonance tuning is based on two effects. First, the increase of the sample temperature leads to a shift of the band gap and exciton energies and second, the thermal energy leads to a dissociation of shallow bound excitons which is expressed by the disappearance of bound exciton recombination lines above approximately 60 K in the case of the  $I_6$ . The first effect can be neglected for the discussion in this section as the exciton shift of less than 4 meV [222] in this temperature range is not sufficient to detune the resonance with other bound excitons such as the  $I_4$ . However, it can be seen that the delocalization of bound excitons at elevated temperatures has a pronounced influence not only on the resonance spectra, but also on the decay dynamics.

Fig. 8.7 displays temperature dependent spectra between 15 K and 80 K for excitation above the free  $A$  and  $B$  excitons (3.4158 eV) (a) and resonant excitation at the  $I_6$  bound exciton (3.3608 eV) (b) in the energy range between 3.18 eV and 3.35 eV. The spectra for both excitation energies exhibit many similarities at the same temperature. With increasing temperature, the intensity of the  $I_6$ -1LO and two electron satellite of  $I_6$  decreases whereas the phonon replicas of the free exciton increases. This is explained by the delocalization of shallow bound excitons due to the increase of the thermal energy which results in an increasing intensity of the free exciton emission. The main difference between the two excitation energies is observed at the 2LO energy. In the case of the high energy excitation at 3.4158 eV in Fig. 8.7a, the  $I_6$ -1LO and  $I_6$ -2LO exhibit a common intensity decrease as the temperature is increased. These two lines are not observed at temperature of 60 K and above in

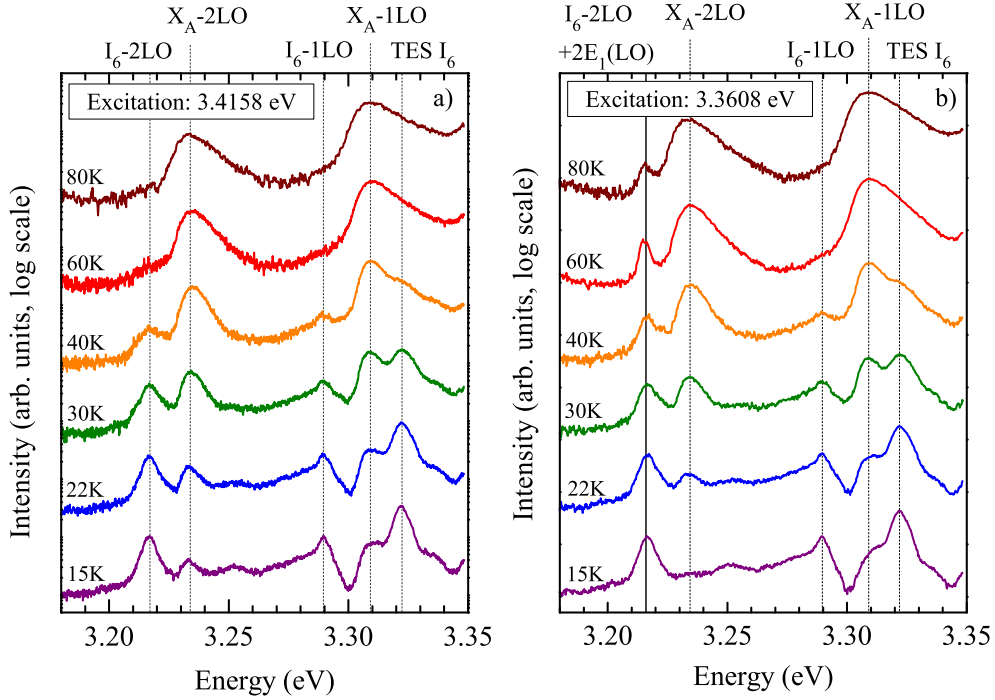


Figure 8.7: PL and Raman spectra of a ZnO substrate from Tokyo Denpa for two different excitation energies as function of the temperature between 15 K and 80 K. (a) excitation energy: 3.4158 eV (above the  $A$  and  $B$  free excitons), (b) excitation energy: 3.3608 eV (in resonance with the donor bound exciton  $I_6$ ). The dotted vertical lines mark the main luminescence features, the solid line in (b) indicates the peak for which time resolved measurements as function of the temperature were performed.

accordance with the localization energy of the corresponding bound exciton. By contrast, a different temperature dependence is observed under resonant excitation at 3.3608 eV (Fig. 8.7b). The 3.216 eV peak remains visible at temperatures above 60 K while the  $I_6$ -1LO shows the same temperature dependence as is the case of non-resonant excitation. In accordance with the previous discussion, the 3.216 eV line consists of contributions from the non-coherent luminescence process and the coherent Raman process. At elevated temperatures, the free exciton cannot bind to the shallow Al donor responsible for the  $I_6$  exciton line as the thermal energy is similar to the localization energy of the exciton. However, the electronic state is still present and can therefore promote the resonance enhancement of the 2LO Raman scattering.

It was already argued that a distinction between the 2LO luminescence replica and the  $2E_1(LO)$  Raman process under resonant excitation is not possible based on the energy of the transitions. However, time resolved measurements have proven

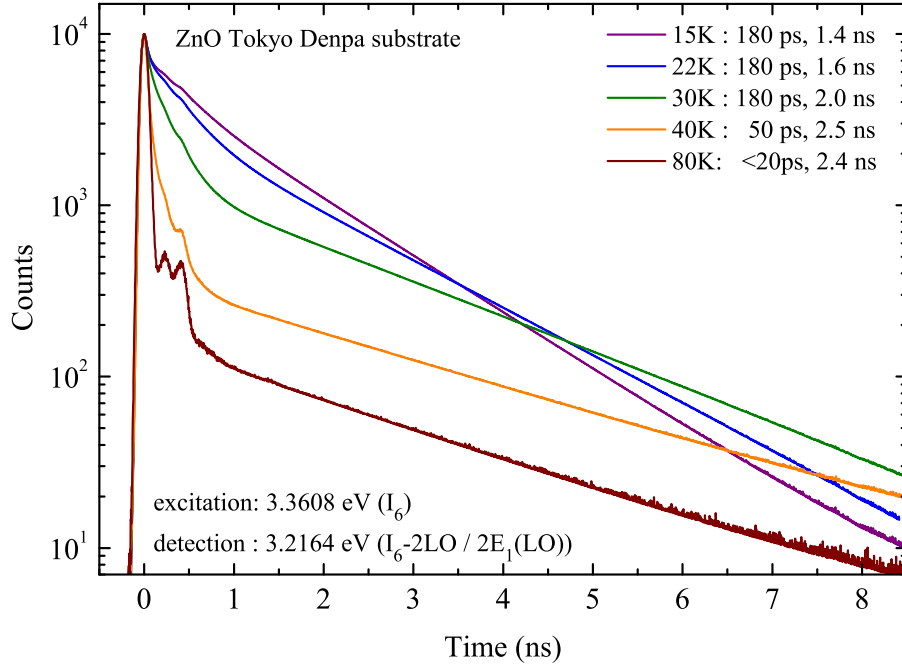


Figure 8.8: Transients of a ZnO substrate from Tokyo Denpa at the energy of the  $I_6$ -2LO phonon replica and  $2E_1(LO)$  Raman mode for different temperature between 15 K and 80 K. Excitation is in resonance with the donor bound exciton  $I_6$  at 3.3608 eV. Lifetimes are denoted next to the corresponding temperature. Colors of the transients match the spectra with equal temperatures in Fig. 8.7.

beneficial to distinguish the decay dynamics of the two processes as function of the excitation energy (section 8.2.1). In order to investigate the influence of the dissociation of bound excitons on the resonance enhancement, the decay dynamics of the overlapping  $I_6$ -2LO and  $2E_1(LO)$  lines are studied as function of the temperature. Fig. 8.8 shows the transients for the different temperatures (some colors as the spectra in Fig. 8.7) at an energy of 3.216 eV. For the lowest temperature of 15 K, the transient reflects the previously discussed dynamics in section 8.2 under resonant excitation. It can be fitted using a bi-exponential decay function which yields decay constants of 180 ps and 1.4 ns in agreement with the lifetimes in Fig. 8.6. With increasing temperature, the long time constant rises to about 2.5 ns at 60 to 80 K. The increase of this luminescence related decay time can be explained by the contributions of radiative and non-radiative decay channels. With increasing temperature, the non-radiative lifetime decreases while the radiative lifetime increases roughly proportional to  $T^{3/2}$  which is characteristic for particles in three dimensional space [337,338]. Since the measured lifetime  $1/\tau_{PL}$  is given by  $1/\tau_{PL} = 1/\tau_r + 1/\tau_{nr}$ , an increase of the lifetime with temperature is expected which is smaller than the increase of the radiative lifetime due to the substantial influence of non-radiative

recombinations at higher temperatures [78].

By contrast, the short decay constant remains constant up to approximately 30 K and decreases rapidly for higher temperatures (Fig. 8.8). At  $T = 80$  K, the measured lifetime of 20 ps is already limited by the time resolution of the setup. The strong decrease of the short lifetime at elevated temperatures suggests a correlation to the dissociation of the bound excitons. In other words, a typical phonon lifetime smaller than 20 ps is measured for temperatures at which the resonance with the bound excitons is destroyed due to thermal dissociation, whereas the measured lifetimes of the resonantly enhanced  $2E_1(LO)$  mode at low temperatures is governed by the lifetime of the bound exciton itself. This behavior demonstrates the importance of the bound exciton state for the enhancement of the LO phonon lifetime under resonant excitation.

### 8.3 Summary

In conclusion, the influence of resonant and non-resonant excitation on the luminescence and Raman scattering was investigated by energy dispersive and time resolved spectroscopy. A pronounced resonance enhancement of the  $2E_1(LO)$  Raman mode was observed for excitation energies in resonance with the dominating bound exciton states. This enhancement is caused by the Fröhlich interaction which leads to a strong coupling of excitons with longitudinal optical phonons. The enhancement of the  $2E_1(LO)$  was found to be stronger than those of the  $E_1(LO)$  Raman mode which is related to the fact that the Fröhlich interaction in ZnO favors phonons with wave vectors larger than those observable from first order Raman scattering. Calculations of the wave vector dependence of the Fröhlich interaction matrix element have determined a maximum coupling strength for  $qa_B = 1.76$  in ZnO. Time resolved measurements of the overlapping phonon replica and Raman modes under resonant excitation could distinguish two different time constants which are related to a slow non-coherent luminescence process and a fast coherent Raman process. For non-resonant excitation below the bound exciton energy, the decay dynamic of the  $2E_1(LO)$  Raman mode is strictly mono-exponential with a decay time  $\leq 20$  ps. Under resonant excitation, the decay constant of the  $2E_1(LO)$  process increases up to 180 ps which is comparable to the lifetime of the shallow bound excitons. It was shown that the decay dynamics of the  $2E_1(LO)$  Raman process depends on the excitation energy and that the corresponding decay constant is mainly governed by the lifetime of the real excitonic state under resonant excitation. This was further confirmed by time resolved measurements as function of the temperature which showed that the dissociation of bound excitons at elevated temperatures correlates with a decrease of the resonantly enhanced lifetime of the  $2E_1(LO)$  Raman mode.

## 9 Influence of substrate polarity on homoepitaxial ZnO epilayers

The influence of the polarity of *c*-plane ZnO substrates on the structural and optical properties of homoepitaxially grown ZnO films is investigated in this chapter. High resolution transmission electron microscopy (HRTEM) enables the determination of the polarity of the epilayers grown on the two different faces of the substrates in real space (section 9.2). The local strain distribution in the epilayers and substrates is mapped by depth resolved micro-Raman scattering in cross-section (section 9.3). In addition, the in-plane strain in the two polar layers is estimated from the shift of the free and bound exciton transitions. The PL spectra of the Zn- and O-polar epilayers are compared and distinct differences in the bound exciton luminescence are observed (section 9.4). These variations can be related to different impurity concentrations as determined by secondary ion mass spectroscopy.

### 9.1 The polar faces of wurtzite ZnO

Homoepitaxial growth of ZnO has the great potential to provide high quality epilayers without strain or dislocations induced by the mismatch of lattice or thermal expansion coefficients. A lower dislocation density and the absence of a defective substrate-layer interface are promising prospects. Due to the wurtzite structure of ZnO, different polar and non-polar faces exist. The bond polarity in ZnO is caused by the very strong electro negativity of oxygen (3.5) and the low electronegativity of zinc (0.91) which results in an ionicity of 0.616 on the Phillips scale [339]. Because of this high ionicity, the *c*-axis [0001] has a pronounced polar character. In the case of *c*-plane substrates, the sequence of positively charged Zn<sup>2+</sup> and negatively charged O<sup>2-</sup> ions in planes perpendicular to the *c*-axis (bilayer) implies two faces of opposite polarity. The surface polarity is defined by the type of atom in the top half of this bilayer with respect to the growth direction. In the Zn-terminated (0001) face, zinc atoms lie in the top layer, whereas in the O-terminated (000 $\bar{1}$ ) face, oxygen is in the top layer. By contrast, a non-polar character occurs for faces with equal numbers of oxygen and zinc ions. This is for example the case for the *a*-plane (11 $\bar{2}$ 0) and *m*-plane (10 $\bar{1}$ 0). Since electron affinities, chemical properties and defect characteristics strongly depend on the polarity of a material, the surface polarity is an important

parameter for the epitaxial growth.

It could be shown that the two polar faces of *c*-plane ZnO have different compositions and surface configurations leading to variations in the chemical and physical properties [340–343]. Other wurtzite semiconductors like GaN show similar dependencies on the surface polarity, which influences the diffusion process of impurities, defect incorporation, and dislocation formation. Consequently, the incorporation of shallow acceptors for p-type conductivity substantially depends on the polarity of the surface [344, 345]. This is best proven by the successful fabrication of p-conductive GaN:Mg on Ga-polar substrates, while N-polar GaN shows hexagonal hillocks, high resistivity, and no p-type conduction [346, 347]. Since ZnO has the same crystal structure and similar material parameters as GaN, Zn-polar faces are likely to possess more favorable properties towards p-conductive ZnO. This is supported by the first reports of successful p-type doping on Zn-polar ZnO [185, 348]. Nevertheless, only few publications report on the impact of surface polarity on structural and optical properties using homoepitaxy [340, 342, 343, 349]. The fact that many ZnO layers show rather large variation of the *c/a* lattice constant ratio, ranging between 1.6018 and 1.6035, could also be correlated to the impurity concentration and polarity of the substrate [30, 274, 275].

In order to investigate the influence of the substrate polarity on the structural and optical properties of ZnO films, nominally undoped ZnO layers of approximately 1.2  $\mu\text{m}$  in thickness were grown by chemical vapor deposition on Zn- and O-polar ZnO substrates [93]. The epilayers were grown simultaneously in the same reactor to ensure direct comparability between the samples. Before growth the substrates were annealed at 1150°C in a flowing oxygen atmosphere. This procedure removes polishing damages and produces terrace like structures which are necessary for two-dimensional growth.

## 9.2 Analysis of the polar faces by HRTEM

In the beginning of this chapter, it is investigated if the polarity of the substrate is preserved in the epilayer or if e.g. an inversion due to stacking faults at the interface may occur. Using high resolution transmission electron microscopy (HRTEM) imaging, the polarity can be determined in real space by imaging and identification of separately resolved Zn- and O-columns. These measurements were conducted by T. P. Bartel at the Lawrence Berkeley National Laboratory. In order to distinguish between the two columns, a direction must be chosen for which the projection of the Zn-O dumbbell is maximized. This is given for the  $[11\bar{2}0]$  zone axis where it is 1.18 Å wide. Resolving the dumbbell is complicated by the large atomic number difference of zinc ( $Z=30$ ) and oxygen ( $Z=8$ ). The large and heavy Zn-columns strongly

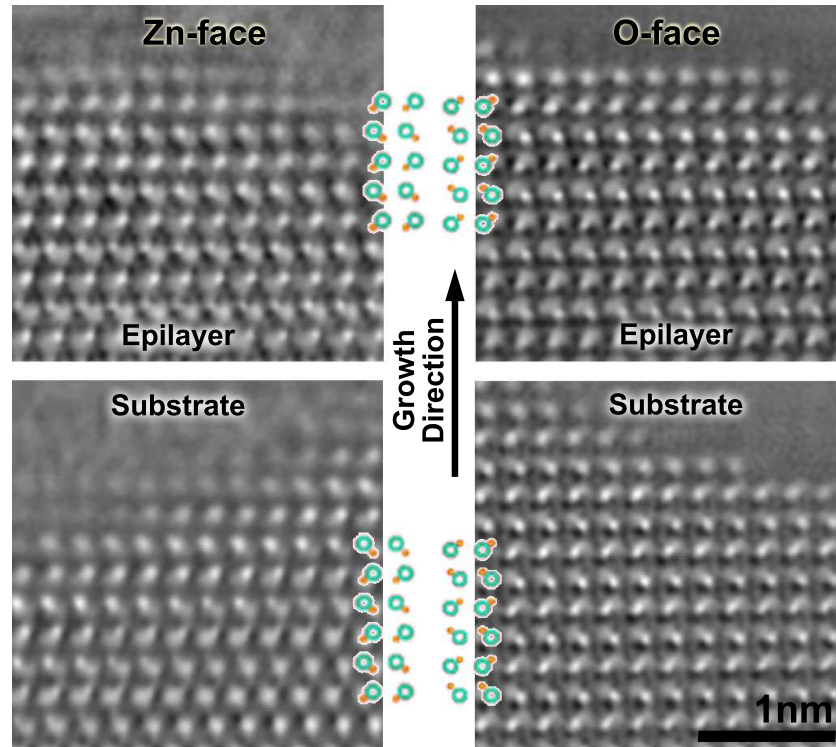


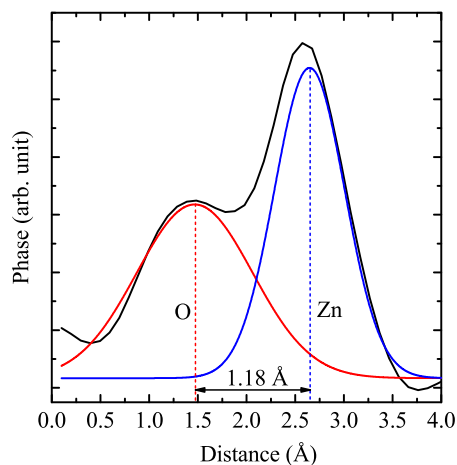
Figure 9.1: Phase of the exit waves of substrate and epilayer of the O-face (left) and Zn-face (right) samples. The overlay sketches the atoms in  $[11\bar{2}0]$  zone axis. Rings represent Zn-columns, dots O-columns.

localize the electron wave and induce a large phase shift that makes Zn-columns appear bright but small in phase images. The O-columns next to them appear large but smeared out and can be difficult to resolve. Only if the dumbbell is successfully resolved, Zn- and O-columns can be identified and allow a direct determination of the material's polarity.

Fig. 9.1 shows the phases of the reconstructed exit waves in the substrates and epilayers of the O-face and Zn-face samples in  $[11\bar{2}0]$  orientation. An atomic overlay sketches the Zn- and O-columns in this orientation (rings for Zn-columns, small dots for O-columns). It is seen that the polarity of the substrate is preserved in the epilayer. Exit wave reconstructions are undertaken in various locations of the epilayers and always show the same polarity [350]. Inversion domains as they are sometimes observed in GaN [351] were detected neither by HRTEM nor by dark field TEM imaging. It is thus concluded that in the studied samples the polarity of the homoepitaxially grown epilayers is solely controlled by the polarity of the substrates.

For a quantitative analysis, the phase is extracted from Fig. 9.1 by line scans over the Zn-O dumbbell. The maxima are fitted by Gaussian peaks for every column as

Figure 9.2: Line profile over the Zn-O dumbbell in  $[11\bar{2}0]$  direction. Zn- and O-columns are separately resolved and fitted by Gaussian peaks. The phase shift is determined by the height of the Gaussian fits.



shown in Fig. 9.2. Apparently, Zn- and O-columns are easily discernible and the polarity of the material can thus be determined on a microscopic level by HRTEM. The height of the Gaussian fit is used to quantify the phase shift. The same procedure is applied for simulated phase images (for details see Ref. [350]). The resulting phase shifts in the respective atomic columns are shown in Fig. 9.3 as a function of thickness whereby straight lines originate from the simulations and data points are from the experiment. The quantitative agreement of the simulations and the experiment is reasonable in both epilayers, confirming the correct identification of the Zn- and O-columns.

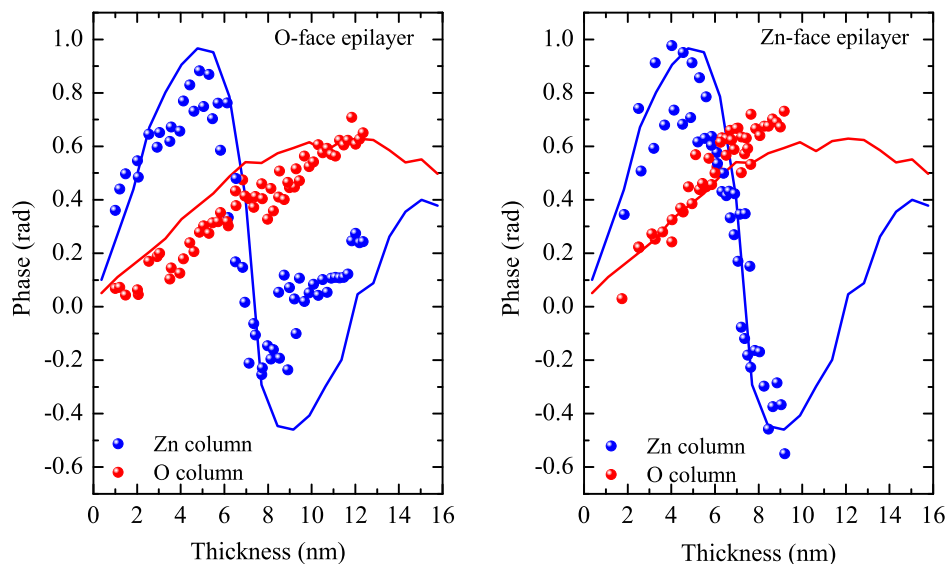


Figure 9.3: Phase of Zn- and O-columns in the epilayer of the Zn-face (upper graph) and O-face (lower graph) sample. Thin lines with data points represent experimental data, straight lines result from simulations.

For the O-columns in the O-polar epilayer, a reduced phase shift is observed, while in the Zn-polar sample the shift is increased. Under the presumption that the reconstruction and the thickness determination are accurate, it could be concluded that oxygen vacancies are present in the O-face material and heavy atoms such as Zn or dopants are present in the Zn-face material on oxygen sites. However, it has to be considered that an inaccurate determination of the thickness or slight tilting of the sample would complicate the interpretation of phase effects and possibly distort the previous interpretation. Despite these obstacles, the presented images provide a useful polarity determination at a microscopic level confirming the same polarity in epilayers and substrates.

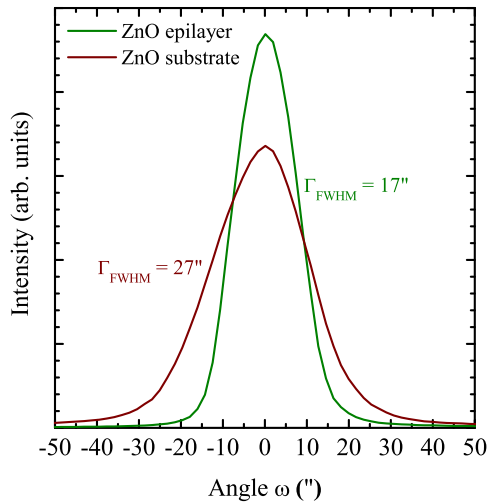


Figure 9.4: X-ray diffraction rocking curve of the (0004) peaks in ZnO epilayers and substrates. Equal spectra are measured for Zn-face and O-face with a FWHM of 17 arcsec for the epilayers and 27 arcsec for the substrates.

In addition, the crystal quality of the samples is studied by XRD measurements. Fig 9.4 displays the rocking curve ( $\omega$ -scan) of the (0004) diffraction peak of substrates and epilayers. Only one XRD spectrum is shown for the epilayers since no difference between the two different polarities could be observed. The full width at half maximum of the (0004) peak is determined to 17.0" in the Zn-face layer and 17.5" in the O-face layer compared to 27.0" in the substrate. These results demonstrate the superior structural quality of both epilayers in comparison to the substrate and a negligible impact of the substrate polarity on the XRD data.

### 9.3 Depth resolved strain distribution

Next, the distribution of local strain is investigated as a function of depth for both surface polarities. For this purpose, cross-sectional (in-plane) micro-Raman measurements in the  $x(yy)\bar{x}$  configuration are performed. The  $x(yy)\bar{x}$  geometry in the case of in-plane and the  $z(..)\bar{z}$  geometry in the case of on-plane measurements are selected to probe the strain properties. Thereto, the position of the  $E_2^{high}$  mode

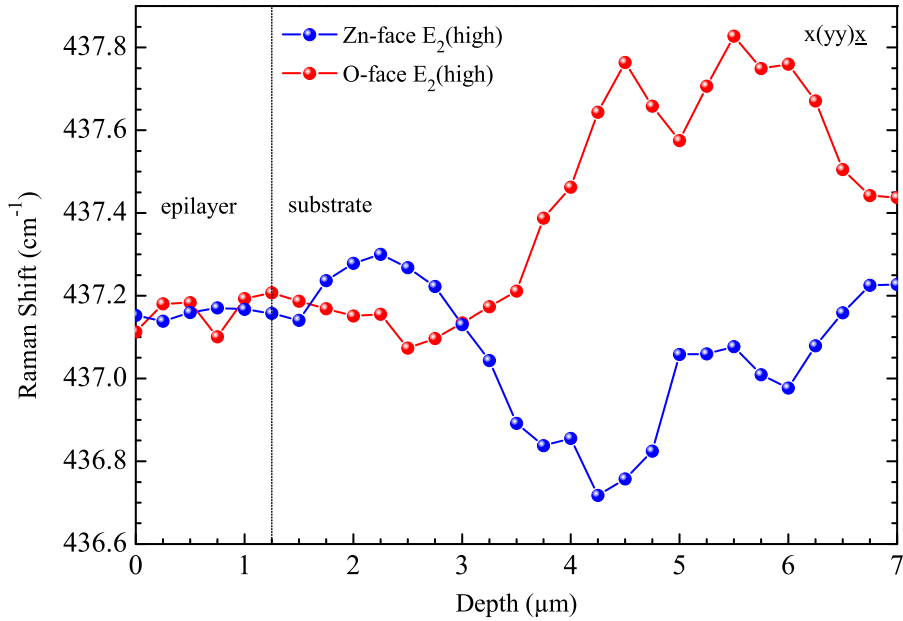


Figure 9.5: Depth dependent shift of the  $E_2^{high}$  mode in cross-sectional micro-Raman measurements. Circles and squares indicate the peak position in O-face and Zn-face terminated samples at room temperature.

is analyzed since it is, other than the TO and LO modes, non-polar and thus not affected by free carriers or internal electric fields but only by strain. Raman selection rules show that the  $A_1(TO)$ ,  $E_2^{low}$ , and  $E_2^{high}$  phonons are allowed for wurtzite ZnO in the  $x(yy)\bar{x}$  scattering geometry (see chapter 7.4). The depth dependent shift of the  $E_2^{high}$  optical phonon mode at room temperature is displayed in Fig. 9.5. The data points are determined from the position of this mode in cross-sectional Raman spectra with a spatial distance of 250 nm. This distance is about a factor of two below the resolution limit of the setup, thus no additional information would be expected using smaller steps. In order to account for the asymmetric broadening of the  $E_2^{high}$  mode (chapter 7.6.3), the precise Raman shift is determined from Fano-type line shape fits. Apparently, the frequency of the  $E_2^{high}$  is steady in the epilayer with small fluctuations of  $0.1 \text{ cm}^{-1}$  in the O-face sample. In contrast to the almost constant value in the epilayers, changes of up to  $0.8 \text{ cm}^{-1}$  in the top  $6 \mu\text{m}$  of the substrate are observed. These results demonstrate the uniform strain distribution in the homoepitaxial ZnO layers despite the presence of considerable strain variations in the substrates. This observation is also in agreement with the reduced half-width in the XRD spectra of the epilayers. Still, the variations in the O-polar epilayer suggest that larger localized strain fields may be present. A possible reason for the variation of local strain might be given by a higher (inhomogeneous) distribution of impurities and or defects as can be demonstrated by secondary ion

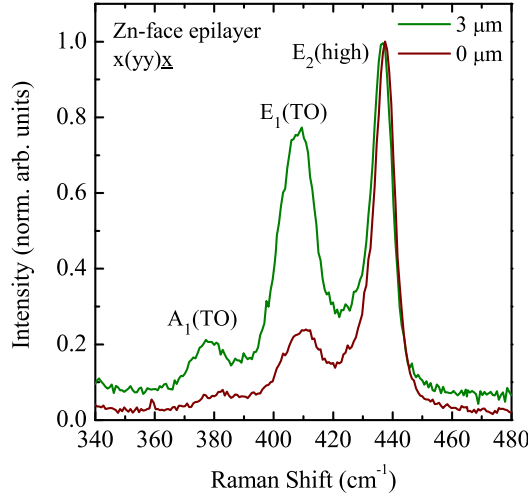


Figure 9.6: Raman spectra of the Zn-face epilayer on the Zn-polar ZnO substrate in the  $x(yy)\bar{x}$  configuration. Spectra are recorded in cross-section geometry at the surface of the epilayer and at a depth of  $3\ \mu\text{m}$ . Spectra are normalized to the  $E_2^{high}$ .

mass spectroscopy below.

Micro Raman measurements additionally provide information about crystal imperfections in the substrates and epilayers. Thereto, the depth dependence of the intensity ratio of the  $E_1(TO)$  to  $E_2^{high}$  Raman modes is analyzed in the  $x(yy)\bar{x}$  configuration. In this geometry the  $E_2^{low}$ ,  $E_2^{high}$  and  $A_1(TO)$  Raman modes are allowed. In contrast, the  $E_1(TO)$  mode is only allowed in crossed polarization  $x(yz)\bar{x}$  whereas the  $E_2^{high}$  is forbidden. Fig. 9.6 shows the in-plane Raman spectra of a Zn-face epilayer on a Zn-polar ZnO substrate at the surface of the epilayer and at a depth of  $3\ \mu\text{m}$ . The spectra are normalized to the maximum intensity of the  $E_2^{high}$ . At the surface, the Raman spectrum is clearly dominated by the  $E_2^{high}$  as predicted by selection rules. However, the spectrum at a depth of  $3\ \mu\text{m}$  shows a greatly increased intensity of the  $E_1(TO)$  mode which should be forbidden in this configuration. Similar spectra are recorded for both epilayers with a spatial distance of  $250\ \text{nm}$ . The intensities of the  $E_2^{high}$  and  $E_1(TO)$  are determined in all spectra. From these values, the intensity ratio of the two modes is plotted in Fig. 9.7 as function of depth between  $0$  and  $7\ \mu\text{m}$ . In the epilayer, the intensity ratio in both samples is small and of constant value as expected by the Raman selection rules with slightly higher variations in the O-face sample. On the contrary, the substrate shows regions with non-perfect crystal symmetry or orientation where the forbidden  $E_1(TO)$  appears with an intensity of up to  $80\%$  compared to the allowed  $E_2^{high}$  mode. Possible explanations for the appearance of a forbidden Raman mode are weakened selection rules due to crystal perturbations, multi-reflections, or a tilting of the  $c$ -axis. Such a tilting would lead to a changed geometry, consequently resulting in different selection rules. Hence, previously forbidden Raman modes could appear. These variations in the orientation of the  $c$ -axis can be measured by XRD in different reflections [352]. However, no evidence for a tilting of the  $c$ -axis is provided by the

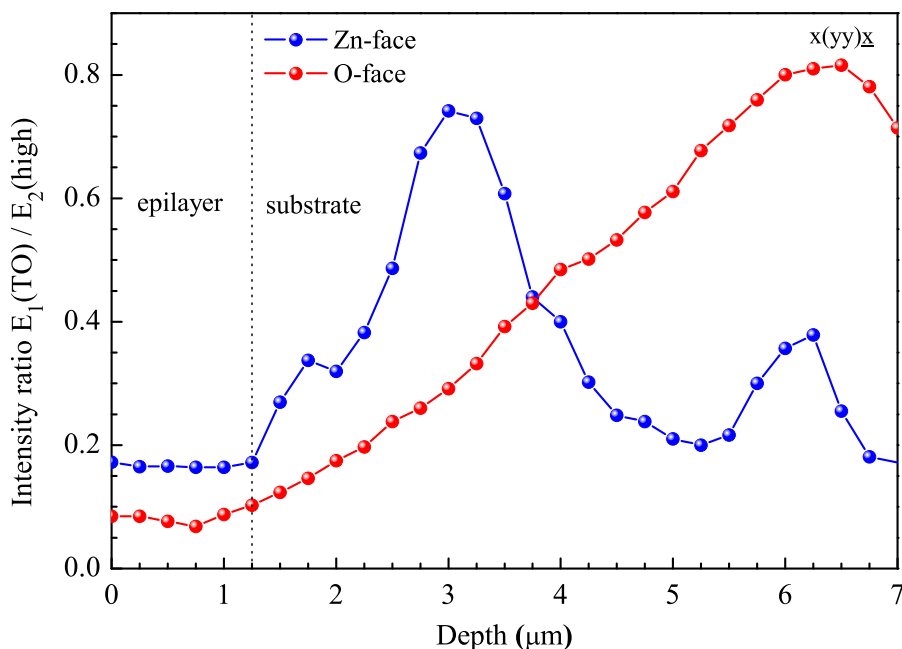


Figure 9.7: Depth resolved intensity ratio of the  $E_1(TO)$  to  $E_2(high)$  Raman modes for Zn-face and O-face ZnO between 0 to 7  $\mu\text{m}$ .

XRD data. Crystal perturbations such as defect clusters or inhomogeneous doping profiles due to impurity diffusion may also lead to a local relaxation of selection rules in Raman scattering. Although it is not possible to draw a final conclusion on the effects involved in the lowering or changing of the symmetry, the intensity ratio and strain evaluation of the Raman modes and the XRD data show the superior quality of the grown epilayers even on non-perfect crystal structures [164, 184].

## 9.4 Optical properties of the homoepitaxial layers

In order to determine the in-plane strain in the epilayers from low temperature photoluminescence spectroscopy, the shift of the free and bound exciton lines can be compared to their relaxed energies. This method is often applied in the literature, however, one should be aware that the accuracy of this approach (in particular in the case of small strain values as found in homoepitaxial layers) greatly depends on the choice and precision of reference values for transition energies in unstrained material. A relative estimate of the strain can be given if the transition energies of substrate and epilayers are compared.

Fig. 9.8 displays the low temperature photoluminescence spectra of two epilayers grown on Zn-face and O-face terminated substrates in the range of the free and bound exciton transitions. In the Zn-face sample, three transitions in the range of

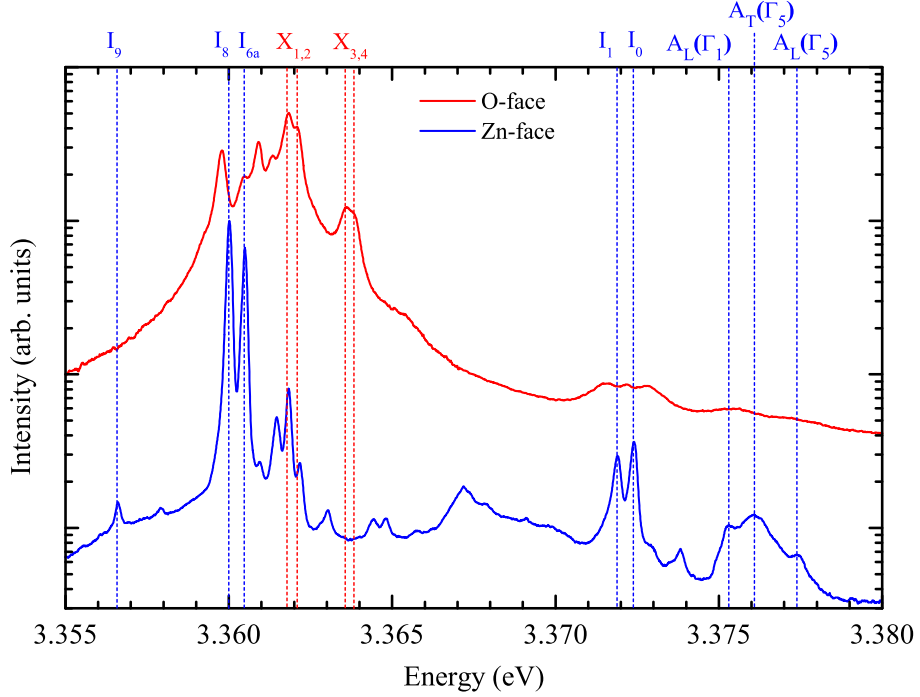


Figure 9.8: PL spectra of homoepitaxial grown ZnO layers on Zn- and O-face substrate surface, respectively ( $T=1.6$  K).

the free A exciton are present. The longitudinal and transversal A exciton-polaritons are observed at  $E(A_L(\Gamma_5)) = 3.37736$  eV and  $E(A_T(\Gamma_5)) = 3.37606$  eV, whereas the 3.37529 eV transition originates from the  $A(\Gamma_1)$  exciton. These values correspond to a blue shift of  $160 \mu\text{eV}$  compared to the transition energies of 3.3759 eV for the  $A_L$  and 3.3772 eV for the  $A_T$  in the substrate. The energy shift of the free excitons to higher energies can be related to the presence of uniaxial tensile strain along the  $c$ -axis  $\epsilon_{cc}$ , i.e. biaxial compressive strain in the  $a$ -plane [153]. The size of the excitonic shift is approximated by evaluating the strain Hamiltonian including first and second order terms [353]. It is given by:

$$E(X_A) = E_A^0 + (D_1 - D_2/\mu)\epsilon_{cc} + a_+(D_3 - D_4/\mu)\epsilon_{cc} - a_+a_-[(D_3 - D_4/\mu)\epsilon_{cc}]^2(E_C^0 - E_A^0)^{-1}, \quad (9.1)$$

where  $2a_{\pm} = 1 \pm [\Delta_1 - \Delta_2][(\Delta_1 - \Delta_2)^2 + 8\Delta_2^2]^{-1/2}$ , with the electronic deformation potentials  $D_i$ , the crystal-field and spin-orbit splitting parameters  $\Delta_1$  and  $\Delta_2$ , the Poisson ratio  $\mu = C_{13}/C_{33}$ , and the elastic moduli  $C_{ij}$ .  $E_A^0 = 3.3759$  eV and  $E_C^0 = 3.4199$  eV are used as energies of the free A and C exciton, respectively. Using values for the electronic deformation potentials and splitting parameters  $D_1 = -3.90$  eV,  $D_2 = -4.13$  eV,  $D_3 = -1.15$  eV,  $D_4 = 1.22$  eV,  $\Delta_1 = 38.3$ ,  $\Delta_2 = 2.1$  published by Wrzesinski et al. [82] and elastic constants  $C_{13} = 106.1$  and  $C_{33} = 209.5$

according to the work of Kobiakov [266] (section 7.7), a strain for the Zn-face sample of  $\epsilon_{cc} = 2.2 \cdot 10^{-4}$  along the c-axis and  $\epsilon_{aa} = -5.6 \cdot 10^{-5}$  in the a-plane is calculated. A similar calculation for the O-face sample is complicated by the much weaker and broadened free exciton luminescence. However, the position of the bound exciton transitions with their well known localization energies [40] suggests a somewhat larger blue-shift of approximately 250  $\mu\text{eV}$ . This corresponds to strain values of  $\epsilon_{cc} = 3.5 \cdot 10^{-4}$  and  $\epsilon_{aa} = -8.8 \cdot 10^{-5}$  in the O-polar sample.

In the range of the bound excitons, different excitonic recombinations can be observed which depend on the surface polarity of the ZnO substrate. This is reproducible for various Zn-face and O-face samples. The luminescence spectrum of the Zn-face grown sample exhibits a variety of well known donor bound exciton lines with a full width at half maximum (FWHM) as small as 80  $\mu\text{eV}$ . The spectrum of this sample is dominated by the  $I_{6a}$  (Al) and  $I_8$  (Ga) bound exciton lines. These lines are accompanied by the ionized donors  $I_0$  and  $I_1$  which form correlated pairs with the  $I_{6a}$  and  $I_8$ , respectively (chapter 3.4.1). In addition, several weaker emission lines are observed which can be attributed to the  $I_9$  at 3.3567 eV (In),  $I_5$  at 3.3615 eV, and  $I_4$  (H) at 3.3628 eV as well as excited states of the donor bound excitons (chapter 3.4.2).

By contrast, the spectra of the O-face samples show distinctively different emission lines in the bound exciton range. The spectrum in Fig. 9.8 is dominated by the  $I_8$ ,  $I_{6a}$ ,  $I_6$ , and  $I_5$  lines between 3.3598 eV and 3.3614 eV whereas no  $I_9$  is present. Additionally, two luminescence structures  $X_{1,2}$  and  $X_{3,4}$  are observed which consist each of two transition lines at 3.36185 eV ( $X_1$ ), 3.36214 eV ( $X_2$ ), 3.36365 eV ( $X_3$ ), and 3.36395 eV ( $X_4$ ). The energetic distance of 0.3 meV between  $X_1$  to  $X_2$  is the same as those of  $X_3$  to  $X_4$ . The line splitting of  $X_1$  to  $X_3$  and  $X_2$  to  $X_4$  is 1.8 meV. Temperature dependent measurements show a thermalization behavior which can be explained by a defect complex with energy splittings of 0.3 meV in the ground state and 1.8 meV in the excited state, respectively [93]. Consequently, these four transitions might be attributed to the same defect complex. This explanation is further supported by the fact that four individual bound excitons would also require the presence of four different additional impurity centers which were not reported before – a most unlikely assumption. Instead, a defect complex with split ground and excited state would only require one impurity type. A possible candidate for such a defect is a Zn interstitial-acceptor pair which should behave as a shallow donor complex [93, 354]. The donor-like character of the binding center for the  $X$ -transitions can indeed be proven by the magneto-optical PL results. This is shown by a temperature dependent study of the thermalization of these lines in a magnetic field in chapter 4.4.2. Furthermore, the neutral charge state of the donor complex could be established by the linear splitting of emission lines in magneto-PL

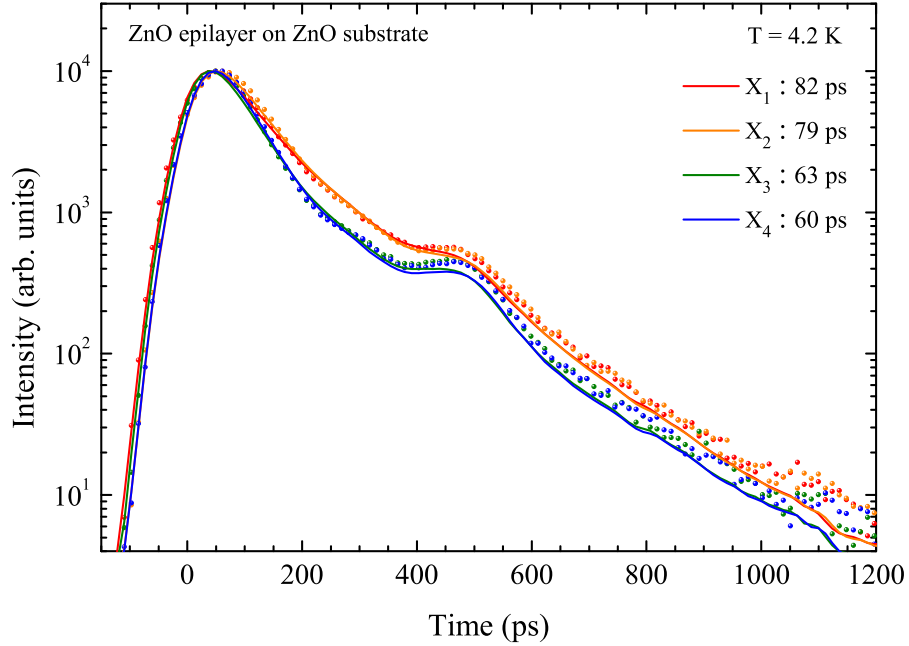


Figure 9.9: TRPL transients of the emission lines  $X_1$  to  $X_4$ . Dots represent data points, lines are monoexponential decay fits including a deconvolution with the system response.

measurements in the Voigt geometry as discussed in detail in chapter 4.4.1.

Additional support for the defect-complex model comes from the analysis of the recombination dynamics of the  $X$ -lines in the O-face samples by time resolved photoluminescence spectroscopy. The transients at the energy of the emission maxima are displayed in Fig. 9.9. The solid lines in the figure are monoexponential fits to the experimental data points. The deviation from a straight line originates from the deconvolution with the system response function taking into account e.g. the time walk of the detector and the half width of the laser (266 nm, 50 ps pulswidth). Apparently, all four transitions exhibit a strictly monoexponential decay as demonstrated by the excellent agreement between experimental data points and fits. The decay times of the different transitions are rather short for bound excitons in ZnO (between 60 ps and 82 ps) compared to typical lifetimes between 200 ps and about 1 ns (see also section 6.7). Thereby, shorter exciton lifetimes usually indicate a reduced crystal quality due to fast non-radiative transitions contributing to the measured lifetimes (chapter 6.7). Within the experimental time resolution, equal lifetimes for the line pairs  $X_1 / X_2$  ( $\approx 60$  ps) and  $X_3 / X_4$  ( $\approx 80$  ps) are observed. Such a behavior would be expected for a complex with a split excited state where the faster transitions  $X_{3,4}$  originate from the higher energy level whereas the  $X_{1,2}$  lines are caused by recombinations starting from a longer-living lower excited state.

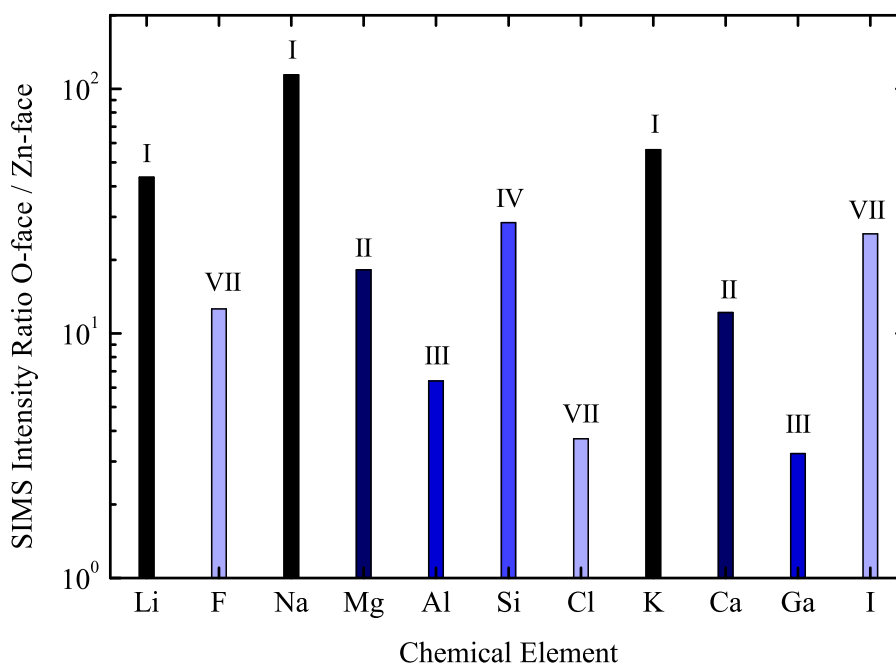


Figure 9.10: Intensity ratio of the normalized secondary ion intensities of the O-polar epitaxial film to the Zn-polar film.

It should be noted that the transition lines of this defect complex could not be observed in any sample grown on Zn-polar substrate. Although the Zn-face samples exhibit narrow peaks at similar energies compared to the  $X_{1,2}$  lines, these transitions do not originate from the same defect complex. This conclusion is supported by the strong correlation between the  $X_{1,2}$  and  $X_{3,4}$  lines concerning intensity ratio, energetic distance, thermalization, and decay constants, which is not given in the Zn-face samples. Particularly, the Zn-face sample shows neither any peaks at the energy of  $X_3$  and  $X_4$  nor a constant intensity ratio of excitonic transitions near  $X_1$  and  $X_2$  as observed in the O-face samples.

The question arises if the different exciton emission lines in the Zn-polar and O-polar epilayers are also reflected by the impurity concentration in the samples. In order to address this issue, secondary ion mass spectroscopy (SIMS) was performed in the group of B. K. Meyer at the Universität Giessen. Fig. 9.10 shows the impurity concentration of the O-polar layer normalized to those of the Zn-polar layer. For all displayed impurity atoms, the concentration is significantly higher in the O-face samples compared to the Zn-face samples. This is most pronounced for the alkali metals (Li, Na, and K) with up to two orders of magnitude higher concentrations in the O-face samples compared to the Zn-face samples. In addition, the concentrations of the group II elements Mg and Ca, the group VII halogens F and I, as well as silicon are higher by more than a factor of ten in the O-face layers. Since O-face and Zn-

face samples were always grown simultaneously in the same reactor chamber, the incorporation of different amounts of impurities due to different growth conditions can be excluded. Thus, it is concluded that the oxygen terminated face favors the incorporation of impurity atoms during growth. These impurities can originate either from the hot quartz reactor tubes of the growth chamber indicating a more efficient impurity incorporation in the O-face layer due to different surface kinetics of the polar faces or from the substrates suggesting a more efficient diffusion process of impurities from the substrate into the epilayers. The higher impurity concentration in the O-face samples is in agreement with the diverse bound exciton structure with additional transition lines and larger half width of the O-face samples. The weaker free exciton emission in the O-face samples can also be explained by a higher impurity concentration which leads to an efficient localization of free excitons at impurities and the formation of bound excitons. This interpretation is further supported by the higher in-plane strain and local strain variations in the O-face samples since impurities with their different ionic radii are expected to increase local strain fields. Consequently, it can be concluded that Zn-terminated ZnO substrates have favorable surface properties which allow the growth of epitaxial layers with smaller in-plane strain and lower impurity concentrations in comparison to O-face substrates.

## 9.5 Summary

In conclusion, the structural and optical properties of homoepitaxial ZnO layers grown on the two polar faces of *c*-plane ZnO substrates were studied. HRTEM could prove that the polarity of the epilayers is controlled by the polarity of the substrate. The identification of the atomic columns in the HRTEM images was confirmed by a good agreement of the phases of the reconstructed exit waves with theoretical simulations. XRD measurements showed that the quality of the epilayers is improved for both polarities compared to the substrate, but no significant differences between the two polar faces occurred. The reduction of strain in the epilayers compared to the substrates was demonstrated by micro-Raman measurements which further revealed slightly higher variations of the Raman shift of the  $E_2^{high}$  mode in the O-face samples. The residual strain along the *c*-axis was estimated by the shift of the free and bound excitons with a higher value in the O-polar epilayer.

The impact of different surface polarities is most pronounced in the excitonic luminescence spectra. A reduced full width at half maximum of exciton lines, a smaller shift of the free exciton, and less intense impurity related recombination lines in the Zn-face epilayers indicate a better quality compared to the O-face specimens. The oxygen polar epilayers were found to exhibit additional recombination lines which are attributed to a defect-impurity complex acting as neutral shallow donor.

The lifetime of these transitions is exceptionally small with values between 60 to 80 ps, indicating dominant non-radiative decay channels. The observed differences between the Zn- and O-polar epilayers are explained by a significantly increased impurity concentration as demonstrated by secondary ion mass spectroscopy. The different impurity levels in the polar epilayers – despite their simultaneous growth in the same reactor chamber – suggests a more efficient incorporation of impurities for oxygen polar surfaces compared to zinc polar ones.

## 10 Summary

Central topic of this work was the detailed investigation of optical and electronic properties of exciton complexes and the lattice dynamics of ZnO. The comparative analysis of ZnO crystals from different manufacturers revealed large variations in the near band edge luminescence of free and bound excitons. The exciton-polaritons with holes from all three valence bands in the ground state and partly also in the  $n = 2$  excited state could be detected by high sensitivity photoluminescence measurements. These data revealed considerable differences between the LT- and band splittings of the free excitons in different ZnO samples. Even larger variations were observed in the emission spectra of the bound excitons. Up to 20 different lines were resolved which differ in intensity and spectral position depending on the growth techniques, impurity and defect concentrations, and strain levels. Several correlated pairs of neutral and ionized bound excitons were identified based on their intensity ratios and localization energies.

The identification of the charge state of the bound exciton complexes was achieved by photoluminescence measurements in external magnetic fields. A non-linear zero-field splitting in the Voigt configuration was observed for the excitons with small localization energies below 10 meV. This splitting was explained by the exchange interaction between exciton states with different symmetry. Using group theoretical concepts, the selection rules for the splitting and mixing of these states in magnetic fields were analyzed. Thereby, it could be shown that the occurrence and intensity increase of forbidden transitions of ionized bound excitons in magnetic fields correlates with the admixture of oscillator strength from zero-field allowed transitions due to the  $B$  field. These results provided the first indisputable proof that not only the  $I_{2,3}$  emission lines but also the  $I_0$  and  $I_1$  lines originate from excitons bound to ionized impurities. Taken the correlation of these lines to their corresponding neutral bound excitons  $I_6$  and  $I_8$  into account, the  $I_0$  and  $I_1$  transitions could be attributed to exciton recombinations bound to ionized Al and Ga donors, respectively. For all stronger localized bound excitons starting with the shallow hydrogen donor  $I_4$ , the neutral charge state of the respective impurities was confirmed by a linear Zeeman splitting of the emission lines in a magnetic field. From the size of the line splittings in different orientations of the magnetic field, the electron- and anisotropic hole g-factors of all bound excitons as well as the zero-field exchange energy for the

ionized bound excitons were quantitatively determined. Based on a thermalization study of the Zeeman components of the bound excitons by temperature dependent magneto-PL measurements, all observed excitons could be attributed to donor-like impurities. The excited states of the donor bound excitons were identified by temperature dependent luminescence and luminescence excitation (PLE) spectroscopy. They were classified into vibrational-rotational excited states and electronic excited states of the bound excitons as well as excitons which involve holes from the  $B$  instead of the  $A$  valence band. PLE measurements further revealed charge transfer processes from ionized to neutral bound excitons, supporting the suggested correlation between excitons bound to the same chemical impurity in different charge states.

In addition to the shallow bound excitons, deeply bound exciton emission lines were observed in selected epitaxial and single crystal ZnO samples. These transitions are of particular interest since their energy region coincides with predicted localization energies of acceptor bound excitons in ZnO. The origin and properties of these deeply bound excitons were investigated by a variety of different experimental techniques. It could be shown that the  $Y_0$ ,  $Y_1$ , and  $Y_2$  lines stem from the radiative recombination of excitons bound to extended structural defects which introduce additional donors in the neutral charge state. Strong evidence was found that these binding centers cannot be described within an effective mass approach. This is expressed by unusually small values of the thermal activation energies, two electron satellite splittings, and Huang-Rhys parameters in contrast to the large localization energy of about 40 meV. Time resolved measurements revealed lifetimes in the range of 200 ps for the deeply bound excitons, whereas those of shallow bound excitons were found to increase as function of the localization energy between 570 ps and 1.35 ns. A similar tendency was observed for the uniaxial pressure coefficients ( $P||c$ ) which are significantly smaller in the case of the deeply bound excitons if compared to the shallow bound excitons. Based on these observations a defect model of an extended structural defect was developed. This model describes an exciton bound to an extended defect related double donor complex resulting in two tightly bound electrons at two singly positively charged donors and one weakly bound hole. The microscopic origin of these centers was studied by monochromatic cathodoluminescence imaging. It was shown that the luminescence lines originate from microscopically localized structures such as line defects and the areas in between the branches of hexagonal star like defects. Several properties of these exciton complexes such as their short monoexponential decay dynamics and weak exciton-phonon coupling are furthermore in excellent agreement with reports of defect and dislocation bound excitons in other III-V and II-VI compound semiconductors.

Another important core issue concerns the ordering of the valence bands in ZnO. This subject was intensively discussed in the literature since the first contradicting attributions in the 1960s. Despite the long lasting debate about the symmetry of the topmost valence band, no scientific consensus was achieved up to now. Within this work, high resolution magneto-photoluminescence measurements on narrow bound exciton lines in ZnO were able to resolve this controversy by the first observation of a hole state related fine splitting in the Voigt configuration. Theoretical considerations clearly demonstrated that the splitting can only occur if the hole originates from a valence band with  $\Gamma_7$  instead of  $\Gamma_9$  symmetry. Additional evidence for this assignment was given by angular and polarization dependent measurements. The parallel and perpendicular hole g-values were obtained in good agreement with published values derived from ab initio calculations. The influence of uniaxial and biaxial strain, misalignments of the  $c$ -axis, and the involvement of  $B$  valence band holes on the observed fine splitting was extensively analyzed. Based on this discussion, all possible counterarguments could be invalidated, thus proving beyond doubt the reversed valence band ordering compared to other wurtzite II-VI and III-V semiconductors of  $A(\Gamma_7)$ ,  $B(\Gamma_9)$ ,  $C(\Gamma_7)$ .

Apart from the excitonic properties and the valence band ordering, the lattice dynamics of ZnO was studied by Raman spectroscopy. Raman measurements as function of hydrostatic pressure were conducted on  $a$ -plane ZnO substrates in order to obtain the pressure coefficients and Grüneisen parameters of all Raman active modes with high precision. From these data, the pressure dependence of the longitudinal-transversal splitting of the optical modes was determined. The Born's transverse effective charge of the polar modes  $E_1$  and  $A_1$  was found to decrease with increasing hydrostatic pressure in contradiction to earlier published results for ZnO. In order to resolve this discrepancy, the derived pressure coefficient of the effective charge was compared to other compound semiconductors such as SiC, AlN, and GaN. These materials show a correlation between the pressure dependence of the effective charge and the bond polarity. While the previously published values for ZnO violated this relation, the newly derived pressure dependence is in good agreement with the large bond polarity of ZnO. Furthermore, the decrease of the line width and asymmetry of the  $E_2^{high}$  mode in ZnO as function of hydrostatic pressure was investigated. It could be explained by inverse slopes of the pressure coefficient of the  $E_2^{high}$  and the two phonon density of states in that frequency range which results in a suppression of the decay channel of the  $E_2^{high}$  into acoustical phonons at elevated pressures. The hydrostatic pressure measurements were complemented by a Raman study of ZnO as function of uniaxial pressure. The combination of these techniques enabled the first experimental determination of the phonon deformation potentials for all first order Raman active modes. The negative pressure dependence of the

$A_1(TO)$  mode was compared to uniaxial pressure studies of other materials and correlated to the large value of Kleinman's internal strain parameter for ZnO. The influence of resonant and non-resonant excitation on the luminescence and Raman scattering was investigated by energy dispersive and time resolved spectroscopy. For excitation energies in resonance with bound exciton states, a strong enhancement of the second order LO Raman modes was observed. This enhancement could be explained by the wave vector dependence of the Fröhlich interaction which leads to a strong coupling of excitons with LO phonons under resonant excitation. Time resolved measurements were applied to study the influence of the resonance on the lifetimes of phonon replicas and Raman modes. It was shown that the overlapping peaks from phonon replicas of exciton lines and LO Raman modes can be distinguished by the decay dynamics of the respective contributions. A bi-exponential decay was observed which could be attributed to a slow non-coherent luminescence process and a fast coherent Raman process. For non-resonant excitation, the decay dynamic of the second order LO Raman modes was strictly mono-exponential with a decay time  $\leq 20$  ps. This lifetime increased up to 180 ps under resonant excitation at bound excitons which is comparable to the lifetime of the shallow bound excitons. It was suggested that the measured lifetime of the LO Raman mode is governed by the lifetime of the exciton which serves as real intermediate state for the scattering process. This was further confirmed by time resolved measurements as function of the temperature which showed that the dissociation of bound excitons at elevated temperatures correlates with a decrease of the resonantly enhanced phonon lifetime down to typical values of a few picoseconds under non-resonant excitation.

Finally, the influence of the substrate polarity on the structural and optical properties of homoepitaxial ZnO layers was investigated. High resolution transmission electron microscopy could prove that the polarity of the epilayers is solely controlled by the polarity of the substrates without the presence of inversion domains. XRD measurements showed a comparable structural quality between the epilayers grown on the two polar faces which exceeded those of the substrates. This was correlated to a reduction of strain in the epilayers compared to the substrates by depth resolved micro-Raman measurements. The impact of different surface polarities was most pronounced in the excitonic luminescence spectra which indicated a superior quality of the Zn-face epilayers. Additional recombination lines in the O-face layers were attributed to a defect-impurity complex acting as a neutral shallow donor. The difference between the optical spectra of the Zn-polar and O-polar epilayers was explained by different impurity concentrations as demonstrated by secondary ion mass spectroscopy. Based on these results, homoepitaxial growth of ZnO is suggested to produce more advantageous results on the Zn-polar face of the substrates in agreement with similar observations for GaN.

# 11 Publications

## Books

**Zinc oxide: From fundamental properties towards novel applications**

C. F. Klingshirn, B. K. Meyer, A. Waag, A. Hoffmann, and J. Geurts

**- Chapter 8: Influence of External Fields**

M. R. Wagner and A. Hoffmann

Springer Series in Materials Science, Vol. 120

1st Edition, 2010, XIII, 300 p., 200 illus., 100 in color.

ISBN: 978-3-642-10576-0.

## Articles

(32) **Resonant phonon and exciton dynamics in ZnO**

M. R. Wagner, J. S. Reparaz, S. Werner, R. Kirste, G. Callsen, C. Thomsen, and A. Hoffmann

Phys. Rev. B, (*in preparation - based on chapter 8*).

(31) **Bound excitons in ZnO - structural defect complexes versus shallow impurity centers**

M. R. Wagner, G. Callsen, J.-H. Schulze, J. S. Reparaz, I. Ostapenko, C. Nenstiel, M. Kaiser, R. Kirste, M. Cobet, C. Thomsen, A. Hoffmann, A. V. Rodina, S. Lautenschläger, S. Eisermann, and B. K. Meyer

Phys. Rev. B, (*in preparation - based on chapter 6*).

(30) **Uniaxial pressure coefficients of neutral and ionized bound excitons in ZnO**

M. R. Wagner, G. Callsen, J. S. Reparaz, R. Kirste, A. Hoffmann, A. V. Rodina, and B. K. Meyer

Appl. Phys. Lett., (*in preparation*).

(29) **Zone center phonon deformation potentials of hexagonal ZnO and GaN determined by uniaxial pressure dependent Raman measurements**

G. Callsen, J. S. Reparaz, M. R. Wagner, R. Kirste, A. Hoffmann, C. Nenstiel, and M. R. Phillips

Appl. Phys. Lett., (*submitted*).

- (28) **Raman and photoluminescence spectroscopic detection of surface-bound  $\text{Li}^+\text{O}_2^-$  defect sites on Li-doped ZnO nanocrystals derived from molecular precursors**  
R. Kirste, Y. Aksu, M. R. Wagner, S. Khachadorian, S. Jana, M. Driess, C. Thomsen, and A. Hoffmann  
Chem. Phys. Chem., (*submitted*).
- (27) **Dielectric tensor of exciton-polaritons and exciton-phonon-complexes in ZnO and the dead layer effect in ellipsometry**  
M. Cobet, C. Cobet, B. K. Meyer, M. R. Wagner, N. Esser, C. Thomsen, and A. Hoffmann  
Phys. Rev. B, (*submitted*).
- (26) **Supramolecular assembly of carbon nanotubes and alkylated-fullerenes: nanocarbon-hybrid towards photovoltaic applications**  
Y. Shen, J. S. Reparaz, M. R. Wagner, A. Hoffmann, C. Thomsen, J.-O Lee, S. Heeg, B. Hatting, S. Reich, S. S. Babu, H. Möhwald, and T. Nakanishi  
J. Am. Chem. Soc. (JACS), (*submitted*).
- (25) **Anisotropic zinc oxide colloids showing shape dependent properties**  
C. Lizandara-Pueyo, S. Siroky, M. R. Wagner, A. Hoffmann, J. S. Reparaz, M. Lehmann, and S. Polarz  
Adv. Funct. Materials, DOI: 10.1002/adfm.201000997 (2010).
- (24) **Recombination dynamics in ZnO nanowires: surfaces states vs. mode quality factor**  
J. S. Reparaz, F. Güell, M. R. Wagner, G. Callsen, R. Kirste, S. Claramunt, J. R. Morante, and A. Hoffmann  
Appl. Phys. Lett. **97**, 133 116 (2010).
- (23) **Excited state properties of donor bound excitons in ZnO**  
B. K. Meyer, J. Sann, S. Eisermann, S. Lautenschläger, M. R. Wagner, M. Kaiser, G. Callsen, and A. Hoffmann  
Phys. Rev. B **82**, 115 207 (2010).
- (22) **Optical properties of InN grown on templates with controlled surface polarities**  
R. Kirste, A. Strittmatter, M. R. Wagner, J.-H. Schulze, R. Collazo, S. Sitar, M. Alevli, N. Dietz, and A. Hoffmann  
Phys. Stat. Sol. A **207**, 2351 (2010).

- 
- (21) **A molecular precursor route to a metastable form of zinc oxide**  
C. L. Pueyo, S. Siroky, S. Landsmann, M. W. E. van den Berg, M. R. Wagner,  
J. S. Reparaz, A. Hoffmann, and S. Polarz  
Chemistry of Materials **22**, 4263 (2010).
- (20) **Reduction of the transverse effective charge of optical phonons in ZnO under pressure**  
J. S. Reparaz, L. R. Muniz, M. R. Wagner, A. R. Goñi, M. I. Alonso, A.  
Hoffmann, and B. K. Meyer  
Appl. Phys. Lett. **96**, 231 906 (2010).
- (19) **Clebsch-Gordon coefficients for scattering tensors in ZnO and other wurtzite semiconductors**  
H. W. Kunert, M. R. Wagner, A. G. J. Machatine, P. Niyongabo, J. B. Mal-  
herbe, A. Hoffmann, J. Barnas, and W. Florek  
Phys. Stat. Sol. B **247**, 1802 (2010).
- (18) **Identification of a donor-related recombination channel in ZnO thin films**  
M. Brandt, H. v. Wenckstern, G. Benndorf, M. Lange, C. P. Dietrich, C.  
Kranert, C. Sturm, R. Schmidt-Grund, H. Hochmuth, M. Lorenz, M. Grund-  
mann, M. R. Wagner, M. Alic, C. Nenstiel, and A. Hoffmann  
Phys. Rev. B **81**, 073 306 (2010).
- (17) **Size-dependent recombination dynamics in ZnO nanowires**  
J. S. Reparaz, F. Güell, M. R. Wagner, A. Hoffmann, A. Cornet, and J. R.  
Morante  
Appl. Phys. Lett. **96**, 053 105 (2010).
- (16) **Lithium related deep and shallow acceptors in Li-doped ZnO nano-  
crystals**  
C. Rauch, W. Gehlhoff, M. R. Wagner, E. Malguth, G. Callsen, R. Kirste, B.  
Salameh, A. Hoffmann, S. Polarz, Y. Aksu, and M. Driess  
J. Appl. Phys. **107**, 024 311 (2010).
- (15) **Polariton effects in the dielectric function of ZnO excitons obtained  
by ellipsometry**  
M. Cobet, C. Cobet, M. R. Wagner, N. Esser, C. Thomsen, and A. Hoffmann  
Appl. Phys. Lett. **96**, 031 905 (2010).

- (14)  **$\Gamma_7$  valence band symmetry related hole fine splitting of bound excitons in ZnO observed in magneto-optical studies**  
M. R. Wagner, J.-H. Schulze, R. Kirste, M. Cobet, A. Hoffmann, C. Rauch, A. V. Rodina, B. K. Meyer, U. Röder, and K. Thonke  
Phys. Rev. B **80**, 205 203 (2009).
- (13) **A systematic study on zinc oxide materials containing group I metals (Li, Na, K) - Synthesis from organometallic precursors, characterization, and properties**  
S. Polarz, A. Orlov, A. Hoffmann, M. R. Wagner, C. Rauch, R. Kirste, W. Gehlhoff, Y. Aksu, M. Driess, M. W. E. van den Berg, and M. Lehmann  
Chem. Mater. **21**, 3889 (2009).
- (12) **Influence of substrate surface polarity on homoepitaxial growth of ZnO layers by chemical vapor deposition**  
M. R. Wagner, T. P. Bartel, R. Kirste, A. Hoffmann, J. Sann, S. Lautenschläger, B. K. Meyer, and C. Kisielowski  
Phys. Rev. B **79**, 035 307 (2009).
- (11) **Nitrogen incorporation in homoepitaxial ZnO CVD epilayers**  
S. Lautenschläger, S. Eisermann, B. K. Meyer, G. Callsen, M. R. Wagner, and A. Hoffmann  
Phys. Stat. Sol. RRL **3**, 16 (2009).
- (10) **Bound and free excitons in ZnO. Optical selection rules in the absence and presence of time reversal symmetry**  
M. R. Wagner, H. W. Kunert, A. G. J. Machatine, A. Hoffmann, P. Niyongabo, J. Malherbe, and J. Barnas  
Microelectron. J. **40**, 289 (2009).
- (09) **Elementary excitations in Si, Ge, and diamond time reversal affected**  
H. W. Kunert, A. G. J. Machatine, J. B. Malherbe, J. Barnas, A. Hoffmann, and M. R. Wagner  
Thin Solid Films **517**, 372 (2008).
- (08) **Infrared absorption, multiphonon processes and time reversal effect on Si and Ge band structure**  
H. W. Kunert, A. G. J. Machatine, J. B. Malherbe, J. Barnas, A. Hoffmann, and M. R. Wagner  
Thin Solid Films **517**, 134 (2008).

- 
- (07) **Asymmetry in the excitonic recombinations and impurity incorporation of the two polar faces of homoepitaxially grown ZnO films**  
S. Lautenschläger, J. Sann, N. Volvers, B. K. Meyer, A. Hoffmann, U. Haboeck, and M. R. Wagner  
Phys. Rev. B **77**, 144108 (2008).
- (06) **Optical and structural properties of homoepitaxial ZnO**  
T. P. Bartel, M. R. Wagner, U. Haboeck, A. Hoffmann, C. Neumann, S. Lautenschläger, J. Sann, and B. K. Meyer  
Proceedings of SPIE **6895**, 689502 (2008).
- (05) **Phonons and electronic states of ZnO, Al<sub>2</sub>O<sub>3</sub> and Ge in the presence of time reversal symmetry**  
A. G. J. Machatine, H. W. Kunert, A. Hoffmann, J. B. Malherbe, J. Barnas, R. Seguin, M. R. Wagner, P. Niyongabo, and N. Nephale  
J. Phys. Conf. Series **92**, 012071 (2007).
- (04) **Ionized and neutral donor-bound excitons in ZnO**  
B. K. Meyer, J. Sann, S. Lautenschläger, M. R. Wagner, and A. Hoffmann  
Phys. Rev. B **76**, 184120 (2007).
- (03) **Resonant Raman scattering at exciton intermediate states in ZnO**  
M. R. Wagner, P. Zimmer, A. Hoffmann, and C. Thomsen  
Phys. Stat. Sol. RRL **1**, 169 (2007).
- (02) **Photonic properties of ZnO epilayers**  
M. R. Wagner, U. Haboeck, P. Zimmer, A. Hoffmann, S. Lautenschläger, C. Neumann, J. Sann, and B. K. Meyer  
Proceedings of SPIE **6474**, 64740X (2007).
- (01) **Phonons in sapphire Al<sub>2</sub>O<sub>3</sub> substrate for ZnO and GaN**  
H. W. Kunert, A. G. J. Machatine, A. Hoffmann, G. Kaczmarczyk, U. Haboeck, J. Malherbe, J. Barnas, M. R. Wagner, and J. D. Brink  
Mater. Sci. Engineer. C **27**, 1222 (2007).

## 12 Conference contributions

(18) **Structural defect bound excitons in ZnO**

M. R. Wagner, G. Callsen, J.-H. Schulze, M. Kaiser, R. Kirste, A. Hoffmann, M. Noltemeyer, A. V. Rodina, S. Lautenschläger, S. Eisermann, and B. K. Meyer

74th DPG Spring Meeting 2010, Regensburg, Germany

(17) **Optical and vibrational properties of nonpolar a-plane versus polar c-plane ZnO**

M. R. Wagner, M. Cobet, G. Callsen, R. Kirste, M. Kaiser, A. Hoffmann, S. Eisermann, S. Lautenschläger, J. Sann, and B. K. Meyer

SPIE Photonics West 2010, San Francisco, CA, USA

(16) **Time resolved and magneto-optical studies of bound exciton complexes in homoepitaxial ZnO**

M. R. Wagner, A. Hoffmann, J.-H. Schulze, C. Rauch, G. Callsen, S. Lautenschläger, J. Sann, B. K. Meyer, and A. V. Rodina

14th International Conference on II-VI Compounds 2009, Sankt Petersburg, Russia

(15) **Optical and structural properties of ZnO substrates for homoepitaxial growth**

M. R. Wagner, G. Callsen, R. Kirste, J.-H. Schulze, S. Werner, A. Hoffmann, J. S. Reparaz, and A. R. Goñi

14th International Conference on II-VI Compounds 2009, Sankt Petersburg, Russia

(14) **Spectroscopy of transition metal ion doped GaN and ZnO**

M. R. Wagner, A. Hoffmann, O. Hitzemann, E. Malguth, W. Gehlhoff, M. Kaiser, M. H. Kane, and I. T. Ferguson

E-MRS Fall Meeting 2009, Warsaw, Poland

- 
- (13) **Towards high quality homoepitaxial ZnO epilayers: Substrate properties under the influence of internal and external strain fields**  
M. R. Wagner, G. Callsen, R. Kirste, J.-H. Schulze, S. Werner, A. Hoffmann, J. S. Reparaz, and A. R. Goñi  
E-MRS Spring Meeting 2009, Strasbourg, France
- (12) **The Li acceptor in ZnO nanocrystals fabricated using an organometallic precursor system**  
M. R. Wagner, R. Kirste, C. Rauch, W. Gehlhoff, A. Hoffmann, S. Polarz, Y. Aksu, M. Driess, and E. Malguth  
E-MRS Spring Meeting 2009, Strasbourg, France
- (11) **Electronic and optical properties of lithium doped ZnO nanocrystals**  
M. R. Wagner, R. Kirste, C. Rauch, G. Callsen, M. Cobet, W. Gehlhoff, E. Malguth, M. Lehmann, S. Polarz, Y. Aksu, and M. Driess  
73d DPG Spring Meeting 2009, Dresden, Germany
- (10) **Magneto-optic and recombination dynamic of complex bound excitons in homoepitaxially grown ZnO epilayers**  
M. R. Wagner, C. Rauch, J.-H. Schulze, A. Hoffmann, J. Sann, S. Lautenschläger, B. K. Meyer, and A. V. Rodina  
SPIE Photonics West 2009, San José, CA, USA
- (09) **Optical and vibrational properties of high quality ZnO substrates under uniaxial pressure**  
M. R. Wagner, A. Hoffmann, R. Kirste, G. Callsen, M. Kaier, E. Malguth, W. Gehlhoff, S. Lautenschläger, J. Sann, and B. K. Meyer  
SPIE Photonics West 2009, San José, CA, USA
- (08) **Electronic and structural characterization of Li doped ZnO nanocrystals**  
M. R. Wagner, R. Kirste, G. Callsen, E. Malguth, M. Kaiser, M. Rakel, Y. Aksu, M. Drieß, W. Gehlhoff, and A. Hoffmann  
UniCat Workshop - Organometallics and Materials Chemistry 2008, Berlin, Germany
- (07) **Structural and optical properties of high quality ZnO substrates for homoepitaxial growth**  
M. R. Wagner, R. Kirste, J.-H. Schulze, E. Malguth, A. Strittmatter, T. P. Bartel, S. Werner, G. Callsen, M. Kaiser, A. Hoffmann, S. Lautenschläger, J. Sann, and B. K. Meyer

5th International Workshop on ZnO and Related Materials 2008 - Ann Arbor, MI, USA

(06) **Coherent and non-coherent dynamics of phonons and excitons in homoepitaxial ZnO**

M. R. Wagner, R. Kirste, J.-H. Schulze, U. Haboeck, A. Hoffmann, J. Sann, S. Lautenschläger, and B. K. Meyer

29th ICPS 2008 - Int. Conference on the Physics of Semiconductors, Rio de Janeiro, Brazil

(05) **Optical and structural properties of homoepitaxial grown ZnO epilayers by chemical vapour deposition**

M. R. Wagner, R. Kirste, T. Bartel, J.-H. Schulze, U. Haboeck, A. Hoffmann, J. Sann, S. Lautenschläger, and B. K. Meyer

28th ISSLED 2008 - Int. Symp. on Semiconductor Light Emitting Devices, Phoenix, AZ, USA

(04) **Dynamics of charge carrier relaxation and recombination in high quality homoepitaxial-grown and single crystal ZnO**

M. R. Wagner, U. Haboeck, A. Hoffmann, S. Lautenschläger, J. Sann, and B. K. Meyer

72nd DPG Spring Meeting 2008, Berlin, Germany

(03) **Resonant Raman scattering and recombination dynamics in homoepitaxial-grown and single crystal ZnO**

M. R. Wagner, P. Zimmer, A. Hoffmann, S. Lautenschläger, J. Sann, and B. K. Meyer

71st DPG Spring Meeting 2007, Regensburg, Germany

(02) **Magneto-optical studies of bound exciton complexes in ZnO**

M. R. Wagner, U. Haboeck, R. McKenna, A. Hoffmann, A. Rodina, S. Lautenschläger, J. Sann, and B. K. Meyer

4th International Workshop on ZnO and Related Materials 2006, Gießen, Germany

(01) **Evidence for non-zero hole effective g-values by magneto-optical studies of bound exciton complexes in ZnO**

M. R. Wagner, R. McKenna, U. Haboeck, A. Hoffmann, S. Lautenschläger, J. Sann, and B. K. Meyer

E-MRS Spring Meeting 2006, Nice, France

## Bibliography

- [1] M. Zamfirescu, A. Kavokin, B. Gil, G. Malpuech, and M. Kaliteevski, “ZnO as a material mostly adapted for the realization of room-temperature polariton lasers”, *Phys. Rev. B* **65**, 161 205(R) (2002).
- [2] H. J. Bolink, E. Coronado, D. Repetto, and M. Sessolo, “Air stable hybrid organic-inorganic light emitting diodes using ZnO as the cathode”, *Appl. Phys. Lett.* **91**, 223 501 (2007).
- [3] C. Lao, Y. Li, C. P. Wong, and Z. L. Wang, “Enhancing the electrical and opto-electronic performance of nanobelt devices by molecular surface functionalization”, *Nanoletters* **7**, 1323 (2007).
- [4] D. C. Reynolds, D. C. Look, and B. Jogai, “Optically pumped ultraviolet lasing from ZnO”, *Solid State Commun.* **99**, 873 (1996).
- [5] D. M. Bagnall, Y. F. Chen, Z. Zhu, T. Yao, S. Koyama, M. Y. Shen, and T. Goto, “Optically pumped lasing of ZnO at room temperature”, *Appl. Phys. Lett.* **70**, 2230 (1997).
- [6] Z. K. Tang, G. K. L. Wong, P. Yu, M. Kawasaki, A. Ohtomo, H. Koinuma, and Y. Segawa, “Room-temperature ultraviolet laser emission from self-assembled ZnO microcrystallite thin films”, *Appl. Phys. Lett.* **72**, 3270 (1998).
- [7] M. Wraback, H. Shen, S. Liang, C. R. Gorla, and Y. Lu, “High contrast, ultrafast optically addressed ultraviolet light modulator based upon optical anisotropy in ZnO films grown on r-plane sapphire”, *Appl. Phys. Lett.* **74**, 507 (1999).
- [8] K. Nomura, H. Ohta, K. Ueda, T. Kamiya, M. Hirano, and H. Hosono, “Thin-film transistor fabricated in single-crystalline transparent oxide semiconductor”, *Science* **300**, 1269 (2003).
- [9] P. F. Carcia, R. S. McLean, M. H. Reilly, and J. G. Nunes, “Transparent ZnO thin-film transistor fabricated by rf magnetron sputtering”, *Appl. Phys. Lett.* **82**, 1117 (2003).
- [10] H. Frenzel, A. Lajn, M. Brandt, H. von Wenckstern, G. Biehne, H. Hochmuth, M. Lorenz, and M. Grundmann, “ZnO metal-semiconductor field-effect transistors with Ag-Schottky gates”, *Appl. Phys. Lett.* **92**, 192 108 (2008).
- [11] D. C. Look, D. C. Reynolds, J. W. Hemsky, R. L. Jones, and J. R. Sizelove, “Single crystalline ZnO films grown on lattice-matched 4ScAlMgO<sub>4</sub>(0001) substrates”, *Appl. Phys. Lett.* **75**, 2635 (1999).
- [12] D. C. Look, J. W. Hemsky, and J. R. Sizelove, “Residual native shallow donor in ZnO”, *Phys. Rev. Lett.* **82**, 2552 (1999).

- [13] F. D. Auret, S. A. Goodman, M. Hayes, M. J. Legodi, H. A. van Laarhoven, and D. C. Look, "Electrical characterization of 1.8 MeV proton-bombarded ZnO", *Appl. Phys. Lett.* **79**, 3074 (2001).
- [14] T. Minami, H. Sato, H. Nanto, and S. Takata, "Group III impurity doped zinc oxide thin films prepared by RF magnetron sputtering", *Jpn. J. Appl. Phys.* **24**, 781 (1985).
- [15] H. Kato, M. Sano, K. Miyamoto, and T. Yao, "Growth and characterization of Ga-doped ZnO layers on a-plane sapphire substrates grown by molecular beam epitaxy", *J. Cryst. Growth* **237**, 538 (2002).
- [16] T. Makino, Y. Segawa, S. Yoshida, A. Tsukazaki, A. Ohtomo, and M. Kawasaki, "Gallium concentration dependence of room-temperature near-band-edge luminescence in n-type ZnO:Ga", *Appl. Phys. Lett.* **85**, 759 (2004).
- [17] J. Meyer, P. Görrn, S. Hamwi, H.-H. Johannes, T. Riedl, and W. Kowalsky, "Indium-free transparent organic light emitting diodes with Al doped ZnO electrodes grown by atomic layer and pulsed laser deposition", *Appl. Phys. Lett.* **93**, 073 308 (2008).
- [18] C. F. Klingshirn, B. K. Meyer, A. Waag, A. Hoffmann, and J. Geurts, "Zinc oxide: From fundamental properties towards novel applications", *Springer Series in Materials Science* **120** (2010).
- [19] J. G. Lu, Y. Z. Zhang, Z. Z. Ye, Y. J. Zeng, H. P. He, L. P. Zhu, J. Y. Huang, L. Wang, J. Yuan, B. H. Zhao, and X. H. Li, "Control of p- and n-type conductivities in Li-doped ZnO thin films", *Appl. Phys. Lett.* **89**, 112 113 (2006).
- [20] Y. Kanai, "Admittance spectroscopy of Cu-doped ZnO crystals", *Jpn. J. Appl. Phys.* **30**, 703 (1991).
- [21] H. S. Kang, B. D. Ahn, J. H. Kim, G. H. Kim, S. H. Lim, H. W. Chang, and S. Y. Lee, "Structural, electrical, and optical properties of p-type ZnO thin films with Ag dopant", *Appl. Phys. Lett.* **88**, 202 108 (2006).
- [22] D. C. Look, "Two-layer Hall-effect model with arbitrary surface-donor profiles: application to ZnO", *J. Appl. Phys.* **104**, 063 718 (2008).
- [23] T. Ohgaki, N. Ohashi, S. Sugimura, H. Ryoken, I. Sakaguchi, Y. Adachi, and H. Haneda, "Positive Hall coefficients obtained from contact misplacement on evident n-type ZnO films and crystals", *J. Mater. Res. Rapid Commun.* **23**, 2293 (2008).
- [24] K. Nakahara, S. Akasaka, H. Yuji, K. Tamura, T. Fujii, Y. Nishimoto, D. Takamizu, A. Sasaki, T. Tanabe, H. Takasu, H. Amaike, T. Onuma, S. F. Chichibu, A. Tsukazaki, A. Ohtomo, and M. Kawasaki, "Nitrogen doped  $Mg_xZn_{1-x}O/ZnO$  single heterostructure ultraviolet light-emitting diodes on ZnO substrates", *Appl. Phys. Lett.* **97**, 013 501 (2010).
- [25] B. K. Meyer and S. Lautenschläger, private communications (2010).
- [26] H. Morkoc and U. Özgür, "Zinc oxide - fundamentals, materials and device technology", Wiley - VCH Verlag GmbH & Co. KGaA, Weinheim (2009).

- [27] P. Y. Yu and M. Cardona, “Fundamentals of semiconductors”, 4th edition, Springer, Berlin, Heidelberg, New York (2010).
- [28] C. F. Klingshirn, “Semiconductor optics”, Springer, 3rd edition, Berlin, Heidelberg, New York (2007).
- [29] C. Klingshirn, “ZnO: From basics towards applications”, *Phys. Stat. Sol. B* **244**, 3027 (2007).
- [30] U. Özgür, Y. I. Alivov, C. Liu, A. Teke, M. A. Reshchikov, S. Doğan, Avrutin, S.-J. Cho, and H. Morkoç, “A comprehensive review of ZnO materials and devices”, *J. Appl. Phys.* **98**, 041 301 (2005).
- [31] A. Jayaraman, “Diamond anvil cell and high-pressure physical investigations”, *Rev. Modern Phys.* **55**, 65 (1983).
- [32] A. Jayaraman, “Ultrahigh pressures”, *Rev. Sci. Instrum.* **57**, 1013 (1986).
- [33] H. K. Mao, J. Xu, and P. M. Bell, “Calibration of the ruby pressure gauge to 800 kbar under quasi-hydrostatic conditions”, *J. Geophys. Res.* **91**, 4673 (1986).
- [34] D. G. Thomas, “The exciton spectrum of zinc oxide”, *J. Phys. Chem. Solids* **15**, 86 (1960).
- [35] J. J. Hopfield, “Fine structure in the optical absorption edge of anisotropic crystals”, *J. Phys. Chem. Solids* **15**, 97 (1960).
- [36] J. J. Hopfield and D. G. Thomas, “Polariton absorption lines”, *Phys. Rev. Lett.* **15**, 22 (1965).
- [37] Y. S. Park, C. W. Litton, T. C. Collins, and D. C. Reynolds, “Exciton spectrum of ZnO”, *Phys. Rev.* **143**, 512 (1966).
- [38] B. Segall, “Intrinsic absorption ”edge” in II-VI semiconducting compounds with the wurtzite structure”, *Phys. Rev.* **163**, 769 (1967).
- [39] W. Y. Liang and A. D. Yoffe, “Transmission spectra of ZnO single crystals”, *Phys. Rev. Lett.* **20**, 59 (1968).
- [40] B. K. Meyer, H. Alves, D. M. Hofmann, W. Kriegseis, D. Forster, F. Bertram, J. Christen, A. Hoffmann, M. Straßburg, M. Dworzak, U. Haboecck, and A. V. Rodina, “Bound exciton and donor-acceptor pair recombinations in ZnO”, *Phys. Stat. Sol. B* **241**, 231 (2004).
- [41] J. Ewles, “Luminescent spectra of some solids at low temperatures”, *Proc. Roy. Soc. (London)* **A167**, 34 (1938).
- [42] R. Dingle, “Luminescent transitions associated with divalent copper impurities and the green emission from semiconducting zinc oxide”, *Phys. Rev. Lett.* **23**, 579 (1969).
- [43] P. Dahan, V. Fleurov, P. Thurian, R. Heitz, A. Hoffmann, and I. Broser, “Isotope shift in semiconductors with transition-metal impurities: Experiment and theory applied to ZnO:Cu”, *Phys. Rev. B* **57**, 9690 (1998).

- [44] P. Dahan, V. Fleurov, P. Thurian, R. Heitz, A. Hoffmann, and I. Broser, "Properties of the intermediately bound  $\alpha$ -,  $\beta$ - and  $\gamma$ -excitons in ZnO:Cu", *J. Phys. Condens. Matter* **57**, 2007 (1998).
- [45] I. J. Broser, R. K. F. Germer, H.-J. E. Schulz, and K. P. Wisznewski, "Fine structure and Zeemann effect of the excited state of the green emitting copper centre in zinc oxide", *Solid State Electronics* **21**, 1597 (1978).
- [46] P. J. Dean, D. J. Robbins, S. G. Bishop, J. A. Savage, and P. Porteous, "The optical properties of copper in zinc oxide", *J. Phys. C* **14**, 2847 (1981).
- [47] D. J. Robbins, D. C. Herbert, and P. J. Dean, "The origin of the  $\alpha$ ,  $\beta$ ,  $\gamma$  blue no-phonon transitions in ZnO:Cu - a deep-level problem", *J. Phys. C* **14**, 2859 (1981).
- [48] R. E. Dietz, H. Kamimura, M. D. Sturge, and A. Yariv, "Electronic structure of copper impurities in ZnO", *Phys. Rev.* **132**, 1559 (1963).
- [49] R. Kuhnert and R. Helbig, "Vibronic structure of the green photo-luminescence due to copper impurities in ZnO", *J. Luminescence* **26**, 203 (1981).
- [50] K. Vanheusden, C. H. Seager, W. L. Warren, D. R. Tallant, and J. A. Voigt, "Correlation between photoluminescence and oxygen vacancies in ZnO phosphors", *Appl. Phys. Lett.* **68**, 403 (1996).
- [51] S. A. Studenikin, N. Golego, and M. Cocivera, "Fabrication of green and orange photoluminescent, undoped ZnO films using spray pyrolysis", *J. Appl. Phys.* **84**, 2287 (1998).
- [52] S. B. Zhang, S. H. Wei, and A. Zunger, "Intrinsic n-type versus p-type doping asymmetry and the defect physics of ZnO", *Phys. Rev. B* **63**, 075 205 (2001).
- [53] F. H. Leiter, H. R. Alves, A. Hofstaetter, D. M. Hofmann, and B. K. Meyer, "The oxygen vacancy as the origin of a green emission in undoped ZnO", *Phys. Stat. Sol. B* **226**, R4 (2001).
- [54] F. Leiter, H. Alves, D. Pfisterer, N. G. Romanov, D. M. Hofmann, and B. K. Meyer, "Oxygen vacancies in ZnO", *Physica B* **340**, 201 (2003).
- [55] D. C. Reynolds, D. C. Look, B. Jogai, J. E. V. Nostrand, R. Jones, and J. Jenny, "Source of the yellow luminescence band in GaN grown by gas-source molecular beam epitaxy and the green luminescence band in single crystal ZnO", *Solid State Commun.* **108**, 701 (1998).
- [56] A. F. Kohan, G. Ceder, D. Morgan, and C. G. V. de Walle, "First-principles study of native point defects in ZnO", *Phys. Rev. B* **61**, 15 019 (2000).
- [57] B. Guo, Z. R. Qiu, and K. S. Wonga, "Intensity dependence and transient dynamics of donor-acceptor pair recombination in ZnO thin films grown on (001) silicon", *Appl. Phys. Lett.* **82**, 2290 (2003).
- [58] A. Janotti and C. G. V. de Walle, "Absolute deformation potentials and band alignment of wurtzite ZnO, MgO, and CdO", *Phys. Rev. B* **75**, 121 201(R) (2007).

- [59] A. Janotti and C. G. V. de Walle, “Fundamentals of zinc oxide as a semiconductor”, *Rep. Prog. Phys.* **72**, 126 501 (2009).
- [60] N. O. Korsunskaya, L. V. Borkovskaya, B. M. Bulakh, L. Y. Khomenkova, V. I. Kushnirenko, and I. V. Markevich, “The influence of defect drift in external electric field on green luminescence of ZnO single crystals”, *J. Luminescence* **102**, 733 (2003).
- [61] B. Lin, Z. Fu, and Y. Jia, “Green luminescent center in undoped zinc oxide films deposited on silicon substrates”, *Appl. Phys. Lett.* **79**, 943 (2001).
- [62] A. Janotti and C. G. V. de Walle, “Native point defects in ZnO”, *Phys. Rev. B* **76**, 165 202 (2007).
- [63] T. Sekiguchi, N. Ohashi, and Y. Terada, “Effect of Hydrogenation on ZnO Luminescence”, *Jpn. J. Appl. Phys.* **36**, L289 (1997).
- [64] C. G. V. de Walle, “Hydrogen as a cause of doping in zinc oxide”, *Phys. Rev. Lett.* **85**, 1012 (2000).
- [65] E. V. Lavrov, J. Weber, F. Börrnert, C. G. V. de Walle, and R. Helbig, “Hydrogen-related defects in ZnO studied by infrared absorption spectroscopy”, *Phys. Rev. B* **66**, 165 205 (2002).
- [66] A. Zeuner, H. Alves, D. M. Hofmann, B. K. Meyer, A. Hoffmann, U. Haboeck, M. Strassburg, and M. Dworzak, “Optical properties of the nitrogen acceptor in epitaxial ZnO”, *Phys. Stat. Sol. B* **234**, R7 (2002).
- [67] H. Alves, D. Pfisterer, A. Zeuner, T. Riemann, J. Christen, D. M. Hofmann, and B. K. Meyer, “Optical investigations on excitons bound to impurities and dislocations in ZnO”, *Opt. Materials* **23**, 33 (2003).
- [68] J. L. Merz, H. Kukimoto, K. Nassau, and J. W. Shiever, “Optical properties of substitutional donors in ZnSe”, *Phys. Rev. B* **6**, 545 (1972).
- [69] D. C. Reynolds, C. W. Litton, and T. C. Collins, “Zeeman effects in the edge emission and absorption of ZnO”, *Phys. Rev.* **140**, 1726 (1965).
- [70] B. K. Meyer, J. Sann, S. Lautenschläger, M. R. Wagner, and A. Hoffmann, “Ionized and neutral donor-bound excitons in ZnO”, *Phys. Rev. B* **76**, 184 120 (2007).
- [71] M. Cobet, “Ellipsometric study of ZnO from multimode formation of exciton-polaritons to the core-level regime”, PhD Thesis, TU Berlin, Germany (2010).
- [72] M. Rosenzweig, “Optische Eigenschaften exzitonischer Polaritonen in ZnO”, PhD Thesis, Technische Universität Berlin (1975).
- [73] K. Hümmer, “Exzitonische Polaritonen in einachsigen Kristallen”, Friedrich-Alexander-Universität, Erlangen-Nürnberg (1978).
- [74] K. Hümmer, R. Helbig, and M. Baumgärtner, “Manifestation of k-linear Term Effects on the Zeemann Splitting of the A1-Exciton Emission Lines in ZnO”, *Phys. Stat. Sol. B* **56**, 249 (1973).

- [75] S. F. Chichibu, T. Sota, G. Cantwell, D. B. Eason, and C. W. Litton, “Polarized photorefectance spectra of excitonic polaritons in a ZnO single crystal”, *J. Appl. Phys.* **93**, 756 (2003).
- [76] D. C. Reynolds, C. W. Litton, D. C. Look, J. E. Hoelscher, B. Claffin, T. C. Collins, J. Nause, and B. Nemeth, “High-quality, melt-grown ZnO single crystals”, *J. Appl. Phys.* **95**, 4802 (2004).
- [77] M. Cobet, C. Cobet, M. R. Wagner, N. Esser, C. Thomsen, and A. Hoffmann, “Polariton effects in the dielectric function of ZnO excitons obtained by ellipsometry”, *Appl. Phys. Lett.* **96**, 031 905 (2010).
- [78] S. F. Chichibu, T. Onuma, M. Kubato, A. Uedono, T. Sota, A. Tsukazaki, A. Ohtomo, and M. Kawasaki, “Improvements in quantum efficiency of excitonic emissions in ZnO epilayers by the elimination of point defects”, *J. Appl. Phys.* **99**, 093 505 (2006).
- [79] B. K. Meyer, J. Sann, S. Eisermann, S. Lautenschläger, M. R. Wagner, M. Kaiser, G. Callsen, J. S. Reparaz, and A. Hoffmann, “Excited state properties of donor bound excitons in ZnO”, *Phys. Rev. B* **82**, 115 207 (2010).
- [80] J. Lagois, “Depth-dependent eigenenergies and damping of excitonic polaritons near a semiconductor surface”, *Phys. Rev. B* **21**, 5511 (1981).
- [81] M. Fiebig, D. Fröhlich, and C. Pahlke-Lerch, “Multiphoton polariton spectroscopy on ZnO”, *Phys. Stat. Sol. B* **177**, 187 (1993).
- [82] J. Wrzesinski and D. Fröhlich, “Two-photon and three-photon spectroscopy of ZnO under uniaxial stress”, *Phys. Rev. B* **56**, 13 087 (1997).
- [83] M. Schilling, R. Helbig, and G. Pensl, “Bound exciton luminescence of Ar- and Al-implanted ZnO”, *J. Luminescence* **33**, 201 (1985).
- [84] K. Johnston, M. O. Henry, D. McCabe, E. McGlynn, M. Dietrich, E. Alves, and M. Xia, “Identification of donor-related impurities in ZnO using photoluminescence and radiotracer techniques”, *Phys. Rev. B* **73**, 165 212 (2006).
- [85] H. K. Ko, Y. F. Chen, S. K. Hong, H. Wenisch, T. Yao, and D. C. Look, “Gadoped ZnO films grown on GaN templates by plasma-assisted molecular-beam epitaxy”, *Appl. Phys. Lett.* **77**, 3761 (2000).
- [86] C. G. V. de Walle and J. Neugebauer, “Universal alignment of hydrogen levels in semiconductors, insulators and solutions”, *Nature* **423**, 626 (2003).
- [87] S. F. J. Cox, E. A. Davis, S. P. Cottrell, P. J. C. King, J. S. Lord, J. M. Gil, H. V. Alberto, R. C. Vilao, J. P. Duarte, N. A. de Campos, A. Weidinger, R. L. Lichti, and S. J. C. Irvine, “Experimental confirmation of the predicted shallow donor hydrogen state in zinc oxide”, *Phys. Rev. Lett.* **86**, 2601 (2001).
- [88] D. M. Hofmann, A. Hofstaetter, F. Leiter, H. Zhou, F. Henecker, B. K. Meyer, S. B. Orlinskii, J. Schmidt, and P. G. Baranov, “Hydrogen: A relevant shallow donor in zinc oxide”, *Phys. Rev. Lett.* **88**, 045 504 (2002).

- [89] D. C. Look, C. Coskun, B. Claffin, and G. C. Farlow, “Electrical and optical properties of defects and impurities in ZnO”, *Physica B* **340**, 32 (2003).
- [90] J. I. Pankove, “Hydrogen in semiconductors”, Academic Press, Boston (1991).
- [91] K. Minegishi, Y. Koiwai, Y. Kikuchi, K. Yano, M. Kasuga, and A. Shimizu, “Growth of p-type zinc oxide films by chemical vapor deposition”, *Jpn. J. Appl. Phys.* **36**, 1453 (1997).
- [92] K. Ip, M. E. Overberg, Y. W. Heo, D. P. Norton, S. J. Pearton, C. E. Stutz, B. Luo, F. Ren, D. C. Look, and J. M. Zavada, “Nitrogen incorporation and diffusivity in plasma-exposed bulk ZnO”, *Appl. Phys. Lett.* **82**, 385 (2003).
- [93] S. Lautenschläger, J. Sann, N. Volvers, B. K. Meyer, A. Hoffmann, U. Haboek, and M. R. Wagner, “Asymmetry in the excitonic recombinations and impurity incorporation of the two polar faces of homoepitaxially grown ZnO films”, *Phys. Rev. B* **77**, 144108 (2008).
- [94] P. H. Kasai, “Electron spin resonance studies of donors and acceptors in ZnO”, *Phys. Rev.* **130**, 989 (1963).
- [95] J. Sann, J. Stehr, A. Hofstaetter, D. M. Hofmann, A. Neumann, M. Lerch, U. Haboek, A. Hoffmann, and C. Thomsen, “Zn interstitial related donors in ammonia-treated ZnO powders”, *Phys. Rev. B* **76**, 195203 (2007).
- [96] J. Grabowska, A. Meaney, K. K. Nanda, J.-P. Mosnier, M. O. Henry, J.-R. Duclère, and E. McGlynn, “Surface excitonic emission and quenching effects in ZnO nanowire/nanowall systems: Limiting effects on device potential”, *Phys. Rev. B* **71**, 115439 (2005).
- [97] J. V. H. Smith and P. Petelenz, “Effective electron-hole interaction potentials and the binding energies of exciton-ionized-donor complexes”, *Phys. Rev. B* **17**, 3253 (1978).
- [98] J. J. Hopfield, *Proceedings of the Seventh International Conference on Physics of Semiconductors*, Paris p. 725 (1964).
- [99] D. C. Herbert, “Electron correlation and bound excitons in semiconductors”, *J. Phys. C* **10**, 3327 (1977).
- [100] W. R. L. Lambrecht, A. V. Rodina, S. Limpijumnong, B. Segall, and B. K. Meyer, “Valence-band ordering and magneto-optic exciton fine structure in ZnO”, *Phys. Rev. B* **65**, 075207 (2002).
- [101] J. Sann, “Photolumineszenz gebundener Exzitonen in Zinkoxid”, PhD Thesis, Giessen, Germany (2008).
- [102] J. Gutowski, N. Presser, and I. Broser, “Acceptor-exciton complexes in ZnO: A comprehensive analysis of their electronic states by high-resolution magneto-optics and excitation spectroscopy”, *Phys. Rev. B* **38**, 9746 (1988).
- [103] A. V. Rodina, M. Strassburg, M. Dworzak, U. Haboek, A. Hoffmann, A. Zeuner, H. R. Alves, D. M. Hofmann, and B. K. Meyer, “Magneto-optical properties of bound excitons in ZnO”, *Phys. Rev. B* **69**, 125206 (2004).

- [104] M. R. Wagner, J.-H. Schulze, R. Kirste, M. Cobet, A. Hoffmann, C. Rauch, A. V. Rodina, B. K. Meyer, U. Röder, and K. Thonke, “ $\Gamma_7$  valence band symmetry related hole fine splitting of bound excitons in ZnO observed in magneto-optical studies”, *Phys. Rev. B* **80**, 205 203 (2009).
- [105] J. Puls, F. Henneberger, and J. Voigt, “Excited states of bound excitons in wurtzite-type semiconductors”, *Phys. Stat. Sol. B* **119**, 291 (1983).
- [106] M. Brandt, H. von Wenckstern, G. Benndorf, M. Lange, C. P. Dietrich, C. Kranert, C. Sturm, R. Schmidt-Grund, H. Hochmuth, M. Lorenz, M. Grundmann, M. R. Wagner, M. Alic, C. Nenstiel, and A. Hoffmann, “Identification of a donor related recombination channel in ZnO thin films”, *Phys. Rev. B* **81**, 073 306 (2010).
- [107] G. Landwehr, “Application of high magnetic fields in semiconductor physics”, *Lecture Notes Phys.* **177** (1982).
- [108] G. Landwehr and W. Ossau, *Proc. Intern. Conf. on High Magnetic Fields in Semiconductors*, Vol. **1** and **2**, World Scientific, Singapore (1997).
- [109] G. Blattner, G. Kurtze, G. Schmieder, and C. Klingshirn, “Influence of magnetic fields up to 20 T on excitons and polaritons in CdS and ZnO”, *Phys. Rev. B* **25**, 7413 (1982).
- [110] D. Block, A. Herve, and R. T. Cox, “Optically detected magnetic resonance and optically detected ENDOR of shallow indium donors in ZnO”, *Phys. Rev. B* **25**, 6049 (1982).
- [111] D. G. Thomas and J. J. Hopfield, “Optical properties of bound exciton complexes in cadmium sulfide”, *Phys. Rev.* **128**, 2135 (1962).
- [112] G. F. Koster, J. O. Dimmock, R. G. Wheeler, and H. Statz, *Properties of the thirty-two point groups*, M.I.T. Press, Cambridge, Massachusetts (1963).
- [113] C. Rauch, “Magneto-optics of ZnO”, *Diploma Thesis*, Technische Universität Berlin (2008).
- [114] G. Blattner, “Der Einfluss externer Magnetfelder auf die freien und gebundenen Exzitonen in ZnO”, *PhD Thesis*, Universität Karlsruhe (1982).
- [115] L. Ding, C. Yang, H. He, F. Jiang, J. Wang, Z. Tang, B. A. Foreman, and W. Ge, “Unambiguous symmetry assignment for the top valence band of ZnO by magneto-optical studies of the free A-exciton state”, eprint arXiv:0706.3965v1 (2007).
- [116] M. R. Wagner, “Optical spectroscopy of defects and impurities in ZnO”, *Diploma Thesis*, Technische Universität Berlin (2005).
- [117] G. Blattner, C. Klingshirn, R. Helbig, and R. Meinl, “The influence of a magnetic field on the ground and excited states of bound exciton complexes in ZnO”, *Phys. Stat. Sol. B* **107**, 105 (1981).
- [118] P. Loose, M. Rosenzweig, and M. Wöhlecke, “Zeeman effect of bound exciton complexes in ZnO”, *Phys. Stat. Sol. B* **75**, 137 (1976).

- [119] R. Sauer and K. Thonke, “Donor related exciton luminescence in wide-bandgap semiconductors: Diamond, zinc oxide, and gallium nitride”, *Optics of Semiconductors and Their Nanostructures*, Springer, Berlin, pp. 73–106 (2004).
- [120] M. Straßburg, A. Rodina, M. Dworzak, U. Haboeck, I. L. Krestnikov, A. Hoffmann, O. Gelhausen, M. R. Phillips, H. R. Alves, A. Zeuner, D. M. Hofmann, and B. K. Meyer, “Identification of bound exciton complexes in ZnO”, *Phys. Stat. Sol. B* **241**, 607 (2004).
- [121] K. Thonke, T. Gruber, N. Teofilov, R. Schönfelder, A. Waag, and R. Sauer, “Donor-acceptor pair transitions in ZnO substrate material”, *Physica B* **308**, 945 (2001).
- [122] T. Skettrup, M. Suffczynski, and W. Gorzkowski, “Properties of excitons bound to ionized donors”, *Phys. Rev. B* **4**, 512 (1971).
- [123] D. G. Thomas and J. J. Hopfield, “Bound exciton complexes”, *Phys. Rev. Lett.* **7**, 316 (1961).
- [124] P. Schröer, P. Krüger, and J. Pollmann, “First-principles calculation of the electronic structure of the wurtzite semiconductors ZnO and ZnS”, *Phys. Rev. B* **47**, 6971 (1993).
- [125] Y.-N. Xu and W. Y. Ching, “Electronic, optical, and structural properties of some wurtzite crystals”, *Phys. Rev. B* **48**, 4335 (1993).
- [126] R. Laskowski and N. E. Christensen, “Ab initio calculation of excitons in ZnO”, *Phys. Rev. B* **73**, 045 201 (2006).
- [127] F. Fuchs, J. Furthmüller, F. Bechstedt, M. Shishkin, and G. Kresse, “Quasiparticle band structure based on a generalized Kohn-Sham scheme”, *Phys. Rev. B* **76**, 115 109 (2007).
- [128] A. Schleife, F. Fuchs, C. Rödl, J. Furthmüller, and F. Bechstedt, “Band-structure and optical-transition parameters of wurtzite MgO, ZnO, and CdO from quasiparticle calculations”, *Phys. Stat. Sol. B* **246**, 2150 (2009).
- [129] E. Christensen, “High pressure in semiconductor physics I”, *Semiconductors and semimetals*, edited by R. K. Willardson and E. R. Weber, Academic Press, New York **54**, 49 (1998).
- [130] V. I. Anisimov, J. Zaanen, and O. K. Andersen, “Band theory and Mott insulators: Hubbard U instead of Stoner I”, *Phys. Rev. B* **44**, 943 (1991).
- [131] G. Petukhov, I. I. Mazin, L. Chioncel, and A. I. Lichtenstein, “Correlated metals and the LDA+U method”, *Phys. Rev. B* **67**, 153 106 (2003).
- [132] A. Schleife, C. Rödl, F. Fuchs, J. Furthmüller, and F. Bechstedt, “Optical and energy-loss spectra of MgO, ZnO, and CdO from ab initio many-body calculations”, *Phys. Rev. B* **80**, 035 112 (2009).
- [133] S. L. Dudarev, G. A. Botton, S. Y. Savrasov, C. J. Humphreys, and A. P. Sutton, “Electron-energy-loss spectra and the structural stability of nickel oxide: An LSDA+U study”, *Phys. Rev. B* **57**, 1505 (1998).

- [134] L. Hedin, “New method for calculating the one-particle Green’s function with application to the electron-gas problem”, *Phys. Rev.* **139**, A796 (1965).
- [135] M. Kobayashi, G. S. Song, T. Kataoka, Y. Sakamoto, A. Fujimori, T. Ohkochi, Y. Takeda, T. Okane, Y. Saitoh, H. Yamagami, H. Yamahara, H. Saeki, T. Kawai, and H. Tabata, “Experimental observation of bulk band dispersions in the oxide semiconductor ZnO using soft x-ray angle-resolved photoemission spectroscopy”, *J. Appl. Phys.* **105**, 122403 (2009).
- [136] Q. Yan, P. Rinke, M. Winkelnkemper, A. Qteish, D. Bimberg, M. Scheffler, and C. G. V. de Walle, “Band parameters and strain effects in ZnO and group-III nitrides”, *Semicond. Sci. Technol.*, accepted for publication **26** (2011).
- [137] R. T. Girard, O. Tjernberg, G. Chiaia, S. Sönderholm, U. O. Karsson, C. Wigren, H. Nylen, and I. Lindau, “Electronic structure of ZnO(0001) studied by angle-resolved photoelectron spectroscopy”, *Surf. Sci.* **373**, 409 (1997).
- [138] K. Ozawa, K. Sawada, Y. Shirotori, and K. Edamoto, “Angle-resolved photoemission study of the valence band structure of ZnO(10-10)”, *J. Phys. Condens. Matter* **17**, 1271 (2005).
- [139] C. McGuinness, C. B. Stagescu, P. J. Ryan, J. E. Downes, D. Fu, K. E. Smith, and R. G. Egdell, “Influence of shallow core-level hybridization on the electronic structure of post-transition-metal oxides studied using soft x-ray emission and absorption”, *Phys. Rev. B* **68**, 165104 (2003).
- [140] C. L. Dong, C. Persson, L. Vayssieres, A. Augustsson, T. Schmitt, M. Mattesini, R. Ahuja, C. L. Chang, and J.-H. Guo, “Electronic structure of nanostructured ZnO from x-ray absorption and emission spectroscopy and the local density approximation”, *Phys. Rev. B* **70**, 195325 (2004).
- [141] J.-H. Guo, L. Vayssieres, C. Persson, R. Ahuja, B. Johansson, and J. Nordgren, “Polarization-dependent soft-x-ray absorption of a highly oriented ZnO microrod-array”, *J. Phys. Condens. Matter* **17**, 235 (2005).
- [142] A. R. H. Preston, B. J. Ruck, L. F. J. Piper, A. DeMasi, K. E. Smith, A. Schleife, F. Fuchs, F. Bechstedt, J. Chai, and S. M. Durbin, “Band structure of ZnO from resonant x-ray emission spectroscopy”, *Phys. Rev. B* **78**, 155114 (2008).
- [143] J. L. Birman, “Polarization of fluorescence in CdS and ZnS single crystals”, *Phys. Rev. Lett.* **2**, 157 (1959).
- [144] J. L. Birman, “Some selection rules for band-band transitions in wurtzite structure”, *Phys. Rev.* **114**, 1490 (1959).
- [145] G. Dresselhaus, “Spin-orbit coupling effects in zinc blende structures”, *Phys. Rev.* **100**, 580 (1955).
- [146] K. Hümmer, “Interband Magnetoreflexion of ZnO”, *Phys. Stat. Sol. B* **86**, 527 (1978).
- [147] D. C. Reynolds, D. C. Look, B. Jogai, C. W. Litton, G. Cantwell, and W. C. Harsch, “Valence-band ordering in ZnO”, *Phys. Rev. B* **60**, 2340 (1999).

- [148] J. Wrzesinski and D. Fröhlich, “Determination of electronic parameters of ZnO by nonlinear spectroscopy”, *Solid State Commun.* **105**, 301 (1998).
- [149] K. Thonke, N. Kerwien, A. Wyszomolek, M. Potemski, A. Waag, and R. Sauer, *Proceedings of the 26th ICPS*, ed.: A. R. Long and J. H. Davies p. 22 (2003).
- [150] M. Goano, F. Bertazzi, M. Penna, and E. Bellotti, “Electronic structure of wurtzite ZnO: Nonlocal pseudopotential and ab initio calculations”, *J. Appl. Phys.* **102**, 083 709 (2007).
- [151] L. Ding, B. K. Li, H. T. He, W. K. Ge, J. N. Wang, J. Q. Ning, X. M. Dai, C. C. Ling, and S. J. Xu, “Classification of bound exciton complexes in bulk ZnO by magnetophotoluminescence spectroscopy”, *J. Appl. Phys.* **105**, 053 511 (2009).
- [152] D. C. Reynolds and T. C. Collins, “Excited terminal states of a bound exciton-donor complex in ZnO”, *Phys. Rev.* **185**, 1099 (1969).
- [153] B. Gil, “Oscillator strengths of A, B, and C excitons in ZnO films”, *Phys. Rev. B* **64**, 201 310R (2001).
- [154] S. F. Chichibu, A. Uedono, A. Tsukazaki, T. Onuma, M. Zamfirescu, A. Ohtomo, A. Kavokin, G. Cantwell, C. W. Litton, T. Sota, and M. Kawasaki, “Exciton Polaron spectra and limiting factors for room temperature photoluminescence efficiency in ZnO”, *Semicond. Sci. Technol.* **20**, S67 (2005).
- [155] S. Adachi, K. Hazu, T. Sota, S. Chichibu, G. Cantwell, D. C. Reynolds, and C. W. Litton, “Biexcitons and their dephasing processes in ZnO”, *Phys. Stat. Sol. C* **2**, 890 (2005).
- [156] S. Adachi, “Polarization and wave-vector-dependent measurements by four-wave mixing in ZnO: valence-band ordering and biexcitons”, *J. Luminescence* **112**, 34 (2005).
- [157] P. Hohenberg and W. Kohn, “Inhomogeneous electron gas”, *Phys. Rev.* **136**, B864 (1964).
- [158] M. Cardona, “Optical properties of the silver and cuprous halides”, *Phys. Rev.* **129**, 69 (1963).
- [159] K. Shindo, A. Morita, and H. Kamimura, “Spin-orbit coupling in ionic crystals with zincblende and wurtzite structures”, *J. Phys. Soc. Jpn.* **20**, 2054 (1965).
- [160] W. Pacuski, D. Ferrand, J. Cibert, C. Deparis, J. A. Gaj, P. Kossacki, and C. Morhain, “Effect of the s, p-d exchange interaction on the excitons in  $Zn_{1-x}Co_xO$  epilayers”, *Phys. Rev. B* **73**, 035 214 (2006).
- [161] D. C. Reynolds, C. W. Litton, T. C. Collins, J. E. Hoelscher, and J. Nause, “Observation of donor-acceptor pair spectra in the photoluminescence of H- and Zn-implanted ZnO single crystals”, *Appl. Phys. Lett.* **88**, 141 919 (2006).
- [162] A. Ashrafi and C. Jagadish, “Review of zincblende ZnO: Stability of metastable ZnO phases”, *J. Appl. Phys.* **102**, 071 101 (2007).

- [163] W. M. Chen, I. A. Buyanova, A. Murayama, T. Furuta, Y. Oka, D. P. Norton, S. J. Pearton, A. Osinsky, and J. W. Dong, “Dominant factors limiting efficiency of optical spin detection in ZnO-based materials”, *Appl. Phys. Lett.* **92**, 092103 (2008).
- [164] M. R. Wagner, T. P. Bartel, R. Kirste, A. Hoffmann, J. Sann, S. Lautenschläger, B. K. Meyer, and C. Kisielowski, “Influence of substrate surface polarity on homoepitaxial growth of ZnO layers by chemical vapor deposition”, *Phys. Rev. B* **79**, 035307 (2009).
- [165] M. R. Wagner, H. W. Kunert, A. G. J. Machatine, A. Hoffmann, P. Niyongabo, J. Malherbe, and J. Barnas, “Bound and free excitons in ZnO. Optical selection rules in the absence and presence of time reversal symmetry”, *Microelectron. J.* **40**, 289 (2009).
- [166] R. Stepniewski, M. Potemski, A. Wyszomolek, K. Pakula, J. M. Baranowski, J. Lusakowski, I. Grzegory, S. Porowski, G. Martinez, and P. Wyder, “Symmetry of excitons in GaN”, *Phys. Rev. B* **60**, 4438 (1999).
- [167] D. C. Reynolds and C. W. Litton, “Edge emission and Zeeman effects in CdS”, *Phys. Rev.* **132**, 1023 (1963).
- [168] A. V. Rodina, M. Dietrich, A. Göldner, L. Eckey, A. Hoffmann, A. L. Efros, M. Rosen, and B. K. Meyer, “Free excitons in wurtzite GaN”, *Phys. Rev. B* **64**, 115204 (2001).
- [169] B. Gil, O. Briot, and R.-L. Aulombard, “Valence-band physics and the optical properties of GaN epilayers grown onto sapphire with wurtzite symmetry”, *Phys. Rev. B* **52**, R17028 (1995).
- [170] B. Gil, F. Hamdani, and H. Morkoc, “Oscillator strengths for optical band-to-band processes in GaN epilayers”, *Phys. Rev. B* **54**, 7678 (1996).
- [171] B. Gil, A. Lusson, V. Sallet, S.-A. Said-Hassani, R. Triboulet, and P. Bigenwald, “Strain-fields effects and reversal of the nature of the fundamental valence band of ZnO epilayers”, *Jpn. J. Appl. Phys.* **40**, L1089 (2001).
- [172] W. Shan, R. J. Hauenstein, A. J. Fischer, J. J. Song, W. G. Perry, M. D. Bremser, R. F. Davis, and B. Goldenberg, “Strain effects on excitonic transitions in GaN: Deformation potentials”, *Phys. Rev. B* **54**, 13460 (1996).
- [173] T. C. Damen, S. P. S. Porto, and B. Tell, “Raman effect in ZnO”, *Phys. Rev.* **142**, 570 (1966).
- [174] A. Schleife, C. Rödl, F. Fuchs, J. Furthmüller, and F. Bechstedt, “Strain influence on valence-band ordering and excitons in ZnO: An ab initio study”, *Appl. Phys. Lett.* **91**, 241915 (2007).
- [175] A. V. Malyshev, I. A. Merkulov, and A. V. Rodina, “Effective mass calculation of the shallow acceptor ground state g-factor for A(3)B(5) semiconductors”, *Phys. Stat. Sol. B* **210**, 865 (1998).
- [176] A. V. Malyshev, I. A. Merkulov, and A. V. Rodina, “Ground-state characteristics of an acceptor center in wide-gap semiconductors with a weak spin-orbit coupling”, *Sov. Phys. Solid State* **40**, 1002 (1998).

- [177] T. Koda and D. W. Langer, “Splitting of exciton lines in wurtzite-type II-VI crystals by uniaxial stress”, *Phys. Rev. Lett.* **20**, 50 (1968).
- [178] D. W. Langer, R. N. Euwema, K. Era, and T. Koda, “Spin exchange in excitons, the quasicubic model and deformation potentials in II-VI compounds”, *Phys. Rev. B* **2**, 4005 (1970).
- [179] D. C. Reynolds, D. C. Look, B. Jogai, and T. C. Collins, “Spin splitting of donor-bound excitons in ZnO due to combined stress and spin exchange”, *Phys. Rev. B* **56**, 13 (1997).
- [180] O. Akimoto and H. Hasegawa, “Strain-induced splitting and polarization of excitons due to exchange interaction”, *Phys. Rev. Lett.* **20**, 916 (1968).
- [181] E. Tomzig and R. Helbig, “Band-edge emission in ZnO”, *J. Luminescence* **14**, 403 (1976).
- [182] A. Schildknecht, R. Sauer, and K. Thonke, “Donor-related defect states in ZnO substrate material”, *Physica B* **340**, 205 (2003).
- [183] R. Sauer and K. Thonke, “Donor related exciton luminescence in wide-bandgap semiconductors: Diamond, zinc oxide, and gallium nitride”, *Optics of semiconductors and their nanostructures*, editors: H. Kalt and M. Hetterich, Springer, p. 73 (2004).
- [184] M. R. Wagner, P. Zimmer, A. Hoffmann, and C. Thomsen, “Resonant Raman scattering at exciton intermediate states in ZnO”, *Phys. Stat. Sol. RRL* **1**, 169 (2007).
- [185] D. C. Look, D. C. Reynolds, C. W. Litton, R. L. Jones, D. B. Eason, and G. Cantwell, “Characterization of homoepitaxial p-type ZnO grown by molecular beam epitaxy”, *Appl. Phys. Lett.* **81**, 1830 (2002).
- [186] M. R. Wagner, U. Haboek, P. Zimmer, A. Hoffmann, S. Lautenschläger, C. Neumann, J. Sann, and B. K. Meyer, “Photonic properties of ZnO epilayers”, *Proceedings of SPIE* **6474**, 64740X (2007).
- [187] H. Kato, M. Sano, K. Miyamoto, and T. Yao, “Effect of O/Zn flux ratio on crystalline quality of ZnO films grown by plasma-assisted molecular beam epitaxy”, *Jpn. J. Appl. Phys.* **42**, 2241 (2003).
- [188] H. Shibata, M. Watanabe, M. Sakai, K. Oka, P. Fons, K. Iwata, A. Yamada, K. Matsumura, K. Sakurai, H. Tambo, K. Nakahara, and S. Niki, “Characterization of ZnO crystals by photoluminescence spectroscopy”, *Phys. Stat. Sol. C* **1**, 872 (2004).
- [189] M. Schirra, R. Schneider, A. Reiser, G. M. Prinz, M. Feneberg, J. Biskupek, U. Kaiser, C. E. Krill, K. Thonke, and R. Sauer, “Stacking fault related 3.31-eV luminescence at 130-meV acceptors in zinc oxide”, *Phys. Rev. B* **77**, 125215 (2008).
- [190] I. C. Robin, P. Marotel, A. H. El-Shaer, V. Petukhov, A. Bakin, A. Waag, M. Lafossas, J. Garcia, M. Rosina, A. Ribeaud, S. Brochen, P. Ferret, and G. Feuillet, “Compared optical properties of ZnO heteroepitaxial, homoepitaxial 2D layers and nanowires”, *J. Cryst. Growth* **311**, 2172 (2009).

- [191] T. Hirai, Y. Harada, S. Hashimoto, N. Ohno, and T. Itoh, "Luminescence of bound excitons in ZnO:Zn phosphor powders", *J. Luminescence* **113**, 115 (2005).
- [192] J. Fallert, R. J. B. Dietz, M. Hauser, F. Stelzl, C. Klingshirn, and H. Kalt, "Random lasing in ZnO nanocrystals", *J. Luminescence* **129**, 1685 (2009).
- [193] C. Rauch, W. Gehlhoff, M. R. Wagner, E. Malguth, G. Callsen, R. Kirste, B. Salameh, A. Hoffmann, S. Polarz, Y. Aksu, and M. Driess, "Lithium related deep and shallow acceptors in Li-doped ZnO nanocrystals", *J. Appl. Phys.* **107**, 024311 (2010).
- [194] D. Stichtenoth, C. Ronning, T. Niermann, L. Wischmeier, T. Voss, C.-J. Chien, P.-C. Chang, and J. G. Lu, "Optical size effects in ultrathin ZnO nanowires", *Nanotechnology* **18**, 435701 (2007).
- [195] M. Lange, J. Zippel, G. Benndorf, C. Czekalla, H. Hochmuth, M. Lorenz, and M. Grundmann, "Temperature dependence of localization effects of excitons in ZnO/Cd<sub>x</sub>Zn<sub>1-x</sub>O/ZnO double heterostructures", *J. Vac. Sci. Technol. B* **27**, 1741 (2009).
- [196] M. Lorenz, J. Lenzner, E. M. Kaidashev, H. Hochmuth, and M. Grundmann, "Cathodoluminescence of selected single ZnO nanowires on sapphire", *Ann. Phys. (Leipzig)* **13**, 39 (2004).
- [197] J. S. Reparaz, F. Güell, M. R. Wagner, A. Hoffmann, A. Cornet, and J. R. Morante, "Size-dependent recombination dynamics in ZnO nanowires", *Appl. Phys. Lett.* **96**, 053105 (2010).
- [198] B. Wang, M. J. Callahan, L. O. Bouthillette, and M. J. S. C. Xu, "Hydrothermal growth and characterization of nitrogen-doped ZnO crystals", *J. Cryst. Growth* **287**, 381 (2006).
- [199] H. Tampo, H. Shibata, P. Fons, A. Yamada, K. Matsubara, K. Iwata, K. Tamura, H. Takasu, and S. Niki, "The effects of thermal treatments on the electrical properties of phosphorus doped ZnO layers grown by MBE", *J. Cryst. Growth* **278**, 268 (2005).
- [200] K. Iwata, H. Tampo, A. Yamada, P. Fons, K. Matsubara, K. Sakurai, S. Ishizuka, and S. Nici, "Growth of ZnO and device applications", *Appl. Surf. Sci.* **244**, 504 (2005).
- [201] T. Gruber, G. M. Kirchner, R. Kling, F. Reuss, W. Limmer, and A. Waag, "Influence of biaxial strains on the vibrational and exciton energies in ZnO", *J. Appl. Phys.* **96**, 289 (2004).
- [202] L. Wang and N. C. Giles, "Determination of the ionization energy of nitrogen acceptors in zinc oxide using photoluminescence spectroscopy", *Appl. Phys. Lett.* **84**, 3049 (2004).
- [203] S. Heitsch, C. Bundesmann, G. Wagner, G. Zimmermann, A. Rahm, H. Hochmuth, G. Benndorf, H. Schmidt, M. Schubert, M. Lorenz, and M. Grundmann, "Low temperature photoluminescence and infrared dielectric functions of pulsed laser deposited ZnO thin films on silicon", *Thin Solid Films* **496**, 234 (2006).

- [204] S. H. Park, T. Hanada, D. C. Oh, T. Minegishi, H. Goto, G. Fujimoto, J. S. Park, I. H. Im, J. H. Chang, M. W. Cho, T. Yao, and K. Inaba, “Lattice relaxation mechanism of ZnO thin films grown on  $c - \text{Al}_2\text{O}_3$  substrates by plasma-assisted molecular-beam epitaxy”, *Appl. Phys. Lett.* **91**, 231 904 (2007).
- [205] C. Bekeny, T. Voss, B. Hilker, J. Gutowski, R. Hauschild, H. Kalt, B. Postels, A. Bakin, and A. Waag, “Influence of ZnO seed crystals and annealing on the optical quality of low-temperature grown ZnO nanorods”, *J. Appl. Phys.* **102**, 044 908 (2007).
- [206] D. W. Hamby, D. A. Lucca, and M. J. Klopstein, “Photoluminescence of mechanically polished ZnO”, *J. Appl. Phys.* **96**, 043 504 (2005).
- [207] S. Fischer, G. Steude, D. M. Hofmann, F. Kurth, F. Anders, M. Topf, B. K. Meyer, F. Bertram, M. Schmidt, J. Christen, L. Eckey, J. Holst, A. Hoffmann, B. Mensching, and B. Rauschenbach, “On the nature of the 3.41 eV luminescence in hexagonal GaN”, *J. Cryst. Growth* **189**, 556 (1998).
- [208] Y. Ohno, H. Koizumi, T. Taishi, I. Yonenaga, K. Fujii, H. Goto, and T. Yao, “Optical properties of dislocations in wurtzite ZnO single crystals introduced at elevated temperatures”, *J. Appl. Phys.* **104**, 073 515 (2008).
- [209] J. Gutowski and A. Hoffmann, “Magneto-optics of excitons bound to dislocations in CdS”, *Materials Science Forum* **38**, 1391 (1989).
- [210] D. Galland and A. Herve, “ESR spectra of the zinc vacancy in ZnO”, *Phys. Lett.* **33A**, 1 (1970).
- [211] D. Galland and A. Herve, “Temperature dependence of the ESR spectrum of the zinc vacancy in ZnO”, *Solid State Commun.* **14**, 953 (1974).
- [212] L. S. Vlasenko and G. D. Watkins, “Optical detection of electron paramagnetic resonance for intrinsic defects produced in ZnO by 2.5-MeV electron irradiation in situ at 4.2 K”, *Phys. Rev. B* **72**, 035 203 (2005).
- [213] X. J. Wang, L. S. Vlasenko, S. J. Pearton, W. M. Chen, and I. A. Buyanova, “Oxygen and zinc vacancies in as-grown ZnO single crystals”, *J. Phys. D* **42**, 175 411 (2009).
- [214] F. Tuomisto, V. Ranki, K. Saarinen, and D. C. Look, “Evidence of the Zn vacancy acting as the dominant acceptor in n-type ZnO”, *Phys. Rev. Lett.* **91**, 205 502 (2003).
- [215] Y. P. Varshni, “Temperature dependence of the energy gap in semiconductors”, *Physica* **34**, 149 (1967).
- [216] A. Manoogian and J. C. Woolley, “Temperature dependence of the energy gap in semiconductors”, *Can. J. Phys.* **62**, 285 (1984).
- [217] K. P. O’Donnell and X. Chen, “Temperature dependence of semiconductor band gaps”, *Appl. Phys. Lett.* **58**, 2924 (1991).
- [218] R. Pässler, “Semi-empirical descriptions of temperature dependences of band gaps in semiconductors”, *Phys. Stat. Sol. B* **236**, 710 (2003).
- [219] A. R. Hutson, “Electronic properties of ZnO”, *J. Phys. Chem. Solids* **8**, 467 (1959).

- [220] L. Vina, S. Logothetidis, and M. Cardona, “Temperature dependence of the dielectric function of germanium”, *Phys. Rev. B* **30**, 1979 (1984).
- [221] J. Wang, G. Du, B. Zhao, X. Yang, Y. Zhang, Y. Ma, D. Liu, Y. Chang, H. Wang, H. Yang, and S. Yang, “Epitaxial growth of  $\text{NH}_3$ -doped ZnO thin films on sapphire substrates”, *J. Cryst. Growth* **255**, 293 (2003).
- [222] D. W. Hamby, D. A. Lucca, M. J. Klopstein, and G. Cantwell, “Temperature dependent exciton photoluminescence of bulk ZnO”, *J. Appl. Phys.* **93**, 3214 (2003).
- [223] H. P. He, Z. Z. Ye, S. S. Lin, H. P. Tang, Y. Z. Zhang, L. P. Zhu, J. Y. Huang, and B. H. Zhao, “Determination of the free exciton energy in ZnO nanorods from photoluminescence excitation spectroscopy”, *J. Appl. Phys.* **102**, 01351 (2007).
- [224] H. Ibach, “Thermal expansion of silicon and zinc oxide (ii)”, *Phys. Stat. Sol. B* **33**, 257 (1969).
- [225] R. R. Reeber, “Lattice parameters of ZnO from 4.2 to 296 K”, *J. Appl. Phys.* **41**, 5063 (1970).
- [226] B. Yates, R. F. Cooper, and M. M. Kreitman, “Low-temperature thermal expansion on zinc oxide: Vibrations in zinc oxide and sphalerite zinc sulfide”, *Phys. Rev. B* **4**, 1314 (1971).
- [227] S. Biernacki and M. Scheffler, “Negative thermal expansion of diamond and zinc-blende semiconductors”, *Phys. Rev. Lett.* **63**, 290 (1989).
- [228] T. H. K. Barron, J. G. Collins, and G. K. White, “Thermal expansion of solids at low temperatures”, *Advances in Physics* **29**, 609 (1980).
- [229] B. A. Weinstein and R. Zallen, “Light scattering in solids IV”, edited by M. Cardona and G. Güntherodt, Springer, Berlin, Heidelberg p. 463 (1984).
- [230] S. Klotz, J. M. Besson, M. Braden, K. Karch, P. Pavone, D. Strauch, and W. G. Marshall, “Pressure induced frequency shifts of transverse acoustic phonons in germanium to 9.7 GPa”, *Phys. Rev. Lett.* **79**, 1313 (1997).
- [231] K. Huang and A. Rhys, “Theory of light absorption and non-radiative transitions in f-centres”, *Proc. R. Soc. Lond. A* **204**, 406 (1950).
- [232] J. J. Hopfield, “A Theory of Edge-Emission Phenomena in CdS, ZnS and ZnO”, *J. Phys. Chem. Solids* **10**, 110 (1959).
- [233] O. Goede and E. Gutsche, “Edge emission in CdS as internal radiative transition in donor-acceptor associates”, *Phys. Stat. Sol. B* **17**, 911 (1966).
- [234] D. J. Mowbray, O. P. Kowalski, M. S. Skolnick, M. Hopkinson, and J. P. R. David, “Optical spectroscopy of AlGaInP based wide band gap quantum wells”, *Superlattice Microst.* **15**, 313 (1994).
- [235] K. J. Nash, M. S. Skolnick, P. A. Claxton, and J. S. Roberts, “Phonon sideband of photoluminescence as a probe of exciton states in a quantum well”, *Phys. Rev. B* **39**, R5558 (1989).

- [236] R. Pecharroman-Gallego, “Temperature and well number dependence of exciton localization in InGaN/GaN quantum wells”, *Semicond. Sci. Technol.* **22**, 1276 (2007).
- [237] P. J. Dean, “Comparison of MOCVD-grown with conventional II-VI materials parameters for EL thin films”, *Phys. Stat. Sol. A* **81**, 625 (1984).
- [238] T. Koida, S. F. Chichibu, A. Uedono, A. Tsukazaki, M. Kawasaki, T. Sota, Y. Segawa, and H. Koinuma, “Correlation between the photoluminescence lifetime and defect density in bulk and epitaxial ZnO”, *Appl. Phys. Lett.* **82**, 532 (2003).
- [239] Y. Zhong, A. B. Djuricic, Y. F. Hsu, K. S. Wong, G. Brauer, C. C. Ling, and W. K. Chan, “Exceptionally long exciton photoluminescence lifetime in ZnO tetrapods”, *J. Phys. Chem. C* **112**, 16 286 (2008).
- [240] E. I. Rashba and G. E. Gurgenishvili, “Edge absorption theory in semiconductors”, *Sov. Phys. Sol. State* **4**, 759 (1962).
- [241] F. Bertram, J. Christen, A. Dadgar, and A. Krost, “Complex excitonic recombination kinetics in ZnO: Capture, relaxation, and recombination from steady state”, *Appl. Phys. Lett.* **90**, 041 917 (2007).
- [242] O. Brandt, J. Ringling, K. H. Ploog, H.-J. Wünsche, and F. Henneberger, “Temperature dependence of the radiative lifetime in GaN”, *Phys. Rev. B* **58**, R15 977 (1998).
- [243] W. Shan, X. C. Xie, J. J. Song, and B. Goldenberg, “Time-resolved exciton luminescence in GaN grown by metalorganic chemical vapor deposition”, *Appl. Phys. Lett.* **67**, 2512 (1995).
- [244] R. Heitz, C. Fricke, A. Hoffmann, and I. Broser, “Picosecond energy transfer between excitons and defects in II-VI semiconductors”, *Mat. Sci. Forum* **83**, 1241 (1992).
- [245] D. L. Dexter, *Solid State Physics*, ed. F. Seitz and D. Turnbull, Academic New York **6**, 353 (1958).
- [246] G. W. 't Hooft, W. A. J. A. van der Poel, L. W. Molenkamp, and C. T. Foxon, “Giant oscillator strength of free excitons in GaAs”, *Phys. Rev. B* **35**, R8281 (1987).
- [247] E. I. Rashba, “Giant oscillator-strengths associated with exciton complexes (review)”, *Sov. Phys. Semiconductors-USSR* **8**, 807 (1975).
- [248] G. D. Sanders and Y.-C. Chang, “Radiative decay of the bound exciton in direct-gap semiconductors: The correlation effect”, *Phys. Rev. B* **28**, 5887 (1983).
- [249] J. Bellessa, V. Voliotis, R. Grousson, X. L. Wang, M. Ogura, and H. Matsuhata, “Quantum-size effects on radiative lifetimes and relaxation of excitons in semiconductor nanostructures”, *Phys. Rev. B* **58**, 9933 (1998).
- [250] V. A. Fonoberov and A. A. Balandin, “Excitonic properties of strained wurtzite and zinc-blende GaN/Al<sub>x</sub>Ga<sub>1-x</sub>N quantum dots”, *J. Appl. Phys.* **94**, 7178 (2003).
- [251] V. A. Fonoberov and A. A. Balandin, “Radiative lifetime of excitons in ZnO nanocrystals: The dead-layer effect”, *Phys. Rev. B* **70**, 195 410 (2004).

- [252] J. S. Reparaz, F. Güell, M. R. Wagner, G. Callsen, R. Kirste, S. Claramunt, J. R. Morante, and A. Hoffmann, “Recombination dynamics in ZnO nanowires: Surface states versus mode quality factor”, *Appl. Phys. Lett.* **97**, 133 116 (2010).
- [253] P. J. Dean, A. D. Pitt, M. S. Skolnick, P. J. Wright, and B. Cockayne, “Optical properties of undoped organometallic grown ZnSe and ZnS”, *J. Cryst. Growth* **59**, 301 (1982).
- [254] A. Naumov, K. Wolf, T. Reisinger, H. Stanzl, and W. Gebhardt, “Luminescence due to lattice-mismatch defects in ZnTe layers grown by metalorganic vapor phase epitaxy”, *J. Appl. Phys.* **73**, 2581 (1993).
- [255] S. Fujii, T. Terada, Y. Fujita, and T. Iuchi, “New deep-level photoluminescence bands of homoepitaxial CdTe films grown by metalorganic chemical vapor deposition”, *Jpn. J. Appl. Phys.* **28**, 1712 (1989).
- [256] A. Hoffmann, J. Christen, and J. Gutowski, “Cathodoluminescence wavelength imaging for spatial mapping of excitons bound to dislocations and structural defects in CdS”, *Advanced Materials for Optics and Electronics* **1**, 25 (1992).
- [257] Y. T. Rebane and Y. G. Shreter, “Polycrystalline semiconductors II”, *Springer Proceedings in Physics* 54, Editors: J. H. Werner and H. P. Strunk p. 28 (1991).
- [258] J. W. Steeds, J. L. Batstone, Y. T. Rebane, and Y. G. Shreter, “Polycrystalline semiconductors II”, *Springer Proceedings in Physics* 54, Editors: J. H. Werner and H. P. Strunk, p. 45 (1991).
- [259] Y. T. Rebane, “Gauge properties of  $\mathbf{k} \cdot \mathbf{p}$  Hamiltonians for crystals with linear topological defects”, *Phys. Rev. B* **52**, 1590 (1995).
- [260] Y. T. Rebane and J. W. Steeds, “Topological interaction of coulombic impurity centers with dislocations in semiconductors”, *Phys. Rev. Lett.* **75**, 3716 (1995).
- [261] M. Kutrowski, T. Wojtowicz, G. Cywinski, L. V. Titova, E. Martin, X. Liu, J. K. Furdyna, and M. Dobrowolska, “Observation of photoluminescence related to Lomer-Cottrell-like dislocations in ZnSe epilayers grown on in situ cleaved (110) GaAs surfaces”, *J. Appl. Phys.* **97**, 013 519 (2005).
- [262] L. D. Landau and E. M. Lifshitz, *Quantum Mechanics*, Pergamon Press, New York (1989).
- [263] F. Decremps, J. Pellicer-Porres, A. M. Saitta, J.-C. Chervin, and A. Polian, “High-pressure Raman spectroscopy study of wurtzite ZnO”, *Phys. Rev. B* **65**, 092 101 (2002).
- [264] J. F. Nye, *Physical properties of crystals*, Oxford Univ. Press, Oxford, p. 134 (1969).
- [265] T. B. Bateman, “Elastic moduli of single-crystal ZnO”, *J. Appl. Phys.* **33**, 3309 (1962).
- [266] I. B. Kobiakov, “Elastic, piezoelectric and dielectric properties of ZnO and CdS single crystals in a wide range of temperatures”, *Solid State Commun.* **35**, 305 (1980).
- [267] G. Carlotti, G. Socino, A. Petri, and E. Verona, “Acoustic investigation of the elastic properties of ZnO films”, *Appl. Phys. Lett.* **51**, 1889 (1987).

- [268] F. Decremps, J. Zhang, B. Li, and R. C. Liebermann, "Pressure-induced softening of shear modes in ZnO", *Phys. Rev. B* **63**, 224 105 (2001).
- [269] G. Carlotti, D. Fioretto, G. Socino, and E. Verona, "Brillouin scattering determination of the whole set of elastic constants of a single transparent film of hexagonal symmetry", *J. Phys. Condens. Matter* **7**, 9147 (1995).
- [270] T. Azuhata, M. Takesada, T. Yagi, S. F. Chichibu, K. Torii, A. Nakamura, T. Sota, G. Cantwell, D. B. Eason, and C. W. Litton, "Brillouin scattering study of ZnO", *J. Appl. Phys.* **94**, 968 (2003).
- [271] R. Ahuja, L. Fast, O. Eriksson, J. M. Wills, and B. Johansson, "Elastic and high pressure properties of ZnO", *J. Appl. Phys.* **83**, 8065 (1998).
- [272] A. Zaoui and W. Sekkal, "Pressure-induced softening of shear modes in wurtzite ZnO: A theoretical study", *Phys. Rev. B* **66**, 174 106 (2002).
- [273] M. Catti, Y. Noel, and R. Dovesi, "Full piezoelectric tensors of wurtzite and zinc blende ZnO and ZnS by first-principles calculations", *J. Phys. Chem. Solids* **64**, 2183 (2003).
- [274] S. Desgreniers, "High-density phases of ZnO: Structural and compressive parameters", *Phys. Rev. B* **58**, 14 102 (1998).
- [275] H. Karzel, W. Potzel, M. Köfferlein, W. Schiessl, M. Steiner, U. Hiller, G. M. Kalvius, D. W. Mitchell, T. P. Das, P. Blaha, K. Schwarz, and M. P. Pasternak, "Lattice dynamics and hyperfine interactions in ZnO and ZnSe at high external pressures", *Phys. Rev. B* **53**, 11 425 (1996).
- [276] C. H. Bates, W. B. White, and R. Roy, "New high-pressure polymorph of zinc oxide", *Science* **137**, 993 (1962).
- [277] W. Shan, W. Walukiewicz, J. W. A. III, K. M. Yu, Y. Zhang, S. S. Mao, R. Kling, C. Kirchner, and A. Waag, "Pressure-dependent photoluminescence study of ZnO nanowires", *Appl. Phys. Lett.* **86**, 153 117 (2005).
- [278] J. Z. Jiang, J. S. Olsen, L. Gerward, D. Frost, D. Rubie, and J. Peyronneau, "Structural stability in nanocrystalline ZnO", *Euro. Phys. Lett.* **50**, 48 (2000).
- [279] A. Mang, K. Reimann, and S. Rübenacke, "Band gaps, crystal-field splitting, spin-orbit coupling, and exciton binding energies in ZnO under hydrostatic pressure", *Solid State Commun.* **94**, 251 (1995).
- [280] A. Segura, J. A. Sans, F. J. Manjon, A. Munoz, and M. J. Herrera-Cabrera, "Optical properties and electronic structure of rock-salt ZnO under pressure", *Appl. Phys. Lett.* **83**, 278 (2003).
- [281] J. Huso, J. L. Morrison, H. Hoeck, X.-B. Chen, L. Bergman, S. J. Jokela, M. D. McCluskey, and T. Zheleva, "Pressure response of the ultraviolet photoluminescence of ZnO and MgZnO nanocrystallites", *Appl. Phys. Lett.* **89**, 171 909 (2006).
- [282] F. D. Murnaghan, "The compressibility of media under extreme pressures", *Proc. Nat. Acad. Sci.* **30**, 244 (1944).

- [283] R. Loudon, “The Raman effect in crystals”, *Advances in Physics* **13**, 423 (1964).
- [284] W. Hayes and R. Loudon, “Scattering of light by crystals”, John Wiley and Sons (1978).
- [285] M. Cardona, “Light scattering in solids II”, edited by M. Cardona and G. Güntherodt, Springer, Berlin, Heidelberg (1982).
- [286] P. Brüesch, “Phonons: Theory and Experiments I”, edited by M. Cardona, P. Fulde, H.J. Queisser, Springer series in solid-state sciences, Berlin **34**, 117 (1982).
- [287] R. H. Lyddane, R. G. Sachs, and E. Teller, “On the polar vibrations of alkali halides”, *Phys. Rev.* **59**, 673 (1941).
- [288] J. Serrano, F. J. Manjón, A. H. Romero, A. Ivanov, M. Cardona, R. Lauck, A. Bosak, and M. Krisch, “Phonon dispersion relations of zinc oxide: Inelastic neutron scattering and ab initio calculations”, *Phys. Rev. B* **81**, 174304 (2010).
- [289] A. W. Hewat, “Lattice dynamics of ZnO and BeO”, *Solid State Commun.* **8**, 187 (1970).
- [290] K. Thoma, B. Dorner, G. Duesing, and W. Wegener, “Lattice dynamics of ZnO”, *Solid State Commun.* **15**, 1111 (1974).
- [291] J. Serrano, F. Widulle, A. H. Romero, A. Rubio, R. Lauck, and M. Cardona, “Dependence of phonon widths on pressure and isotopic mass: ZnO”, *Phys. Stat. Sol. B* **235**, 260 (2003).
- [292] J. Serrano, A. H. Romero, F. J. Manjon, R. Lauck, M. Cardona, and A. Rubio, “Pressure dependence of the lattice dynamics of ZnO: An ab initio approach”, *Phys. Rev. B* **69**, 094306 (2004).
- [293] C. A. Arguello, D. L. Rousseau, and S. P. S. Porto, “First-order Raman effect in wurtzite-type crystals”, *Phys. Rev.* **181**, 1351 (1969).
- [294] M. Tsuboi, “Optically active lattice vibrations of zinc blende type and wurtzite type crystals”, *J. Chem. Phys.* **40**, 1326 (1964).
- [295] J. M. Calleja and M. Cardona, “Resonant Raman scattering in ZnO”, *Phys. Rev. B* **16**, 3753 (1977).
- [296] R. Cuscó, E. Alarcón-Lladó, J. Ibáñez, L. Artús, J. Jiménez, B. Wang, and M. J. Callahan, “Temperature dependence of Raman scattering in ZnO”, *Phys. Rev. B* **75**, 165202 (2007).
- [297] R. H. Callender, S. S. Sussman, M. Selders, and R. K. Chang, “Dispersion of Raman cross section in CdS and ZnO over a wide energy range”, *Phys. Rev. B* **7**, 3788 (1973).
- [298] J. E. Jaffe and A. C. Hess, “Hartree-Fock study of phase changes in ZnO at high pressure”, *Phys. Rev. B* **48**, 7903 (1993).
- [299] J. E. Jaffe, J. A. Snyder, Z. Lin, and A. C. Hess, “LDA and GGA calculations for high-pressure phase transitions in ZnO and MgO”, *Phys. Rev. B* **62**, 1660 (2000).

- [300] J. L. Birman, “Simplified LCAO method for zincblende, wurtzite, and mixed crystal structures”, *Phys. Rev.* **115**, 1493 (1959).
- [301] S. S. Mitra, O. Brafman, W. B. Daniels, and R. K. Crawford, “Pressure-induced phonon frequency shifts measured by Raman scattering”, *Phys. Rev.* **186**, 942 (1969).
- [302] A. R. Goni, H. Siegle, K. Syassen, C. Thomsen, and J.-M. Wagner, “Effect of pressure on optical phonon modes and transverse effective charges in GaN and AlN”, *Phys. Rev. B* **64**, 035 205 (2001).
- [303] R. Trommer, H. Müller, M. Cardona, and P. Vogl, “Dependence of the phonon spectrum of InP on hydrostatic pressure”, *Phys. Rev. B* **21**, 4869 (1980).
- [304] B. A. Weinstein and G. J. Piermarini, “Raman scattering and phonon dispersion in Si and GaP at very high pressure”, *Phys. Rev. B* **12**, 1172 (1975).
- [305] K. Vedam and T. A. Davis, “Pressure dependence of the refractive indices of the hexagonal crystals beryl,  $\alpha$ -CdS,  $\alpha$ -ZnS, and ZnO”, *Phys. Rev.* **181**, 1196 (1969).
- [306] A. D. Corso, M. Posternak, R. Resta, and A. Baldereschi, “Ab initio study of piezoelectricity and spontaneous polarization in ZnO”, *Phys. Rev. B* **50**, 10 715 (1994).
- [307] D. Olego, M. Cardona, and P. Vogl, “Pressure dependence of the optical phonons and transverse effective charge in 3C-SiC”, *Phys. Rev. B* **25**, 3878 (1982).
- [308] W. A. Harrison, *Electronic structure and the properties of solids*, Dover, New York, p. 175 (1989).
- [309] J. Serrano, F. J. Manjon, A. H. Romero, F. Widulle, R. Lauck, and M. Cardona, “Dispersive phonon linewidths: The E2 phonons of ZnO”, *Phys. Rev. Lett.* **90**, 055 510 (2003).
- [310] F. Demangeot, J. Frandon, M. A. Renucci, O. Briot, B. Gil, and R. L. Aulombard, “Raman determination of phonon deformation potentials in  $\alpha$ -GaN”, *Solid State Commun.* **100**, 207 (1996).
- [311] V. Y. Davydov, N. S. Averkiev, I. N. Goncharuk, D. K. Nelson, I. P. Nikitina, A. S. Polkovnikov, A. N. Smirnov, M. A. Jacobson, and O. K. Semchinova, “Raman and photoluminescence studies of biaxial strain in GaN epitaxial layers grown on 6H-SiC”, *J. Appl. Phys.* **82**, 5097 (1997).
- [312] P. Perlin, C. Jaubertie-Carillon, J. P. Itie, A. S. Miguel, I. Grzegory, and A. Polian, “Raman scattering and x-ray-absorption spectroscopy in gallium nitride under high pressure”, *Phys. Rev. B* **45**, 83 (1992).
- [313] J.-M. Wagner and F. Bechstedt, “Properties of strained wurtzite GaN and AlN: Ab initio studies”, *Phys. Rev. B* **66**, 115 202 (2002).
- [314] G. Callsen, J. S. Reparaz, M. R. Wagner, R. Kirste, A. Hoffmann, C. Nenstiel, and M. R. Phillips, “Zone center phonon deformation potentials of hexagonal ZnO and GaN determined by uniaxial pressure dependent Raman measurements”, *Appl. Phys. Lett.* (submitted).

- 
- [315] D. I. Bolef, “Physical acoustics. Principles and methods”, edited by W. P. Mason, Academic Press, New York **1** (1964).
- [316] R. J. Briggs and A. K. Ramdas, “Piezospectroscopic study of the Raman spectrum of cadmium sulfide”, *Phys. Rev. B* **13**, 5518 (1976).
- [317] M. Siakavellas, A. G. Kontos, and E. Anastassakisa, “Strain dependent optical phonon frequencies of cubic ZnS”, *J. Appl. Phys.* **84**, 517 (1998).
- [318] M. Cardona, “Semiconductors under uniaxial strain”, *Phys. Stat. Sol. B* **198**, 5 (1996).
- [319] R. M. Martin, “Elastic properties of ZnS structure semiconductors”, *Phys. Rev. B* **1**, 4005 (1970).
- [320] K. Kim, W. R. L. Lambrecht, and B. Segall, “Electronic structure of GaN with strain and phonon distortions”, *Phys. Rev. B* **50**, 1502 (1994).
- [321] J. F. Scott, “UV resonant Raman scattering in ZnO”, *Phys. Rev. B* **2**, 1209 (1970).
- [322] Y. Oka and T. Kushida, “Resonance Raman scattering in CdS and ZnO by tunable dye laser”, *J. Phys. Soc. Jap* **33**, 1372 (1972).
- [323] V. V. Ursaki, I. M. Tiginyanu, V. V. Zalamai, E. V. Rusu, G. A. Emelchenko, V. M. Masalov, and E. N. Samarov, “Multiphonon resonant Raman scattering in ZnO crystals and nanostructured layers”, *Phys. Rev. B* **70**, 155 204 (2004).
- [324] V. V. Zalamai, V. V. Ursaki, E. V. Rusu, P. Arabadji, I. M. Tiginyanu, and L. Sirbu, “Photoluminescence and resonant Raman scattering in highly conductive ZnO layers”, *Appl. Phys. Lett.* **84**, 5168 (2004).
- [325] L. Bergman, X.-B. Chen, J. Huso, J. L. Morrison, and H. Hoek, “Raman scattering of polar modes of ZnO crystallites”, *J. Appl. Phys.* **98**, 093 507 (2005).
- [326] B. Kumar, H. Gong, S. Y. Chow, S. Tripathy, and Y. Hua, “Photoluminescence and multiphonon resonant Raman scattering in low-temperature grown ZnO nanostructures”, *Appl. Phys. Lett.* **89**, 071 922 (2006).
- [327] R. C. C. Leite and S. P. S. Porto, “Enhancement of Raman cross section in CdS due to resonant absorption”, *Phys. Rev. Lett.* **17**, 10 (1966).
- [328] A. K. Ganguly and J. L. Birman, “Theory of lattice Raman scattering in insulators”, *Phys. Rev.* **162**, 806 (1967).
- [329] B. Bendow and J. L. Birman, “Theory of resonant Raman scattering in crystals: A generalized bare-exciton approach”, *Phys. Rev. B* **4**, 569 (1971).
- [330] W. S. Baer, “Faraday rotation in ZnO: Determination of the electron effective mass”, *Phys. Rev.* **154**, 785 (1967).
- [331] Y. Toyozawa, “On the dynamical behavior of an exciton”, *Prog. Theor. Phys. Suppl.* **12**, 111 (1959).
- [332] T. Yamamoto and H. Katayama-Yoshida, “Solution using a codoping method to unipolarity for the fabrication of p-type ZnO”, *Jpn. J. Appl. Phys.* **38**, 166 (1999).

- [333] J. Takeda, N. Arai, Y. Toshine, H.-J. Ko, and T. Yao, “Ultrafast dynamics of exciton-exciton and exciton-longitudinal optical-phonon scattering processes in ZnO epitaxial thin films”, *Jpn. J. Appl. Phys.* **45**, 6961 (2006).
- [334] F. Vallée, “Time-resolved investigation of coherent LO-phonon relaxation in III-V semiconductors”, *Phys. Rev. B* **49**, 2460 (1994).
- [335] H. Siegle, L. Filippidis, G. Kaczmarczyk, A. P. Litvinchuk, A. Hoffmann, and C. Thomsen, “Time-resolved Raman scattering in gallium nitride”, *Proceedings of the 23th ICPS*, ed.: M. Scheffler and R. Zimmermann, p. 533 (1996).
- [336] V. Kutzer, H. Siegle, C. Thomsen, A. Hoffmann, and I. Broser, “Intensity-dependent hot-phonon relaxation in ZnSe”, *Mater. Sci. Engineer. B* **43**, 46 (1997).
- [337] J. Feldmann, G. Peter, E. O. Göbel, P. Dawson, K. Moore, C. Foxon, and R. J. Elliott, “Linewidth dependence of radiative exciton lifetimes in quantum wells”, *Phys. Rev. Lett.* **59**, 2337 (1987).
- [338] H. Akiyama, S. Koshihara, T. Someya, K. Wada, H. Noge, Y. Nakamura, T. Inoshita, A. Shimizu, and H. Sakaki, “Thermalization effect on radiative decay of excitons in quantum wires”, *Phys. Rev. Lett.* **72**, 924 (1994).
- [339] J. C. Phillips, “Bonds and bands in semiconductors”, Academic Press, New York (1973).
- [340] R. E. Sherriff, D. C. Reynolds, D. C. Look, B. Jogai, J. E. Hoelscher, T. C. Collins, G. Cantwell, and W. C. Harsch, “Photoluminescence measurements from the two polar faces of ZnO”, *J. Appl. Phys.* **88**, 3454 (2000).
- [341] B. Meyer and D. Marx, “Density-functional study of the structure and stability of ZnO surfaces”, *Phys. Rev. B* **67**, 035 403 (2003).
- [342] H. Matsui, H. Saeki, T. Kawai, A. Sasaki, M. Yoshimoto, M. Tsubaki, and H. Tabata, “Characteristics of polarity-controlled ZnO films fabricated using the homoepitaxy technique”, *J. Vac. Sci. Technol. B* **22**, 2454 (2004).
- [343] H. Xu, K. Ohtani, M. Yamao, and H. Ohno, “Surface morphologies of homoepitaxial ZnO on Zn- and O-polar substrates by plasma assisted molecular beam epitaxy”, *Appl. Phys. Lett.* **89**, 071 918 (2006).
- [344] M. Sumiya, K. Yoshiura, K. Ohtsuka, and S. Fuke, “Dependence of impurity incorporation on the polar direction of GaN film growth”, *Appl. Phys. Lett.* **76**, 2098 (2000).
- [345] F. Tuomisto, K. Saarinen, B. Lucznik, I. Grzegory, H. Teisseyre, T. Suski, S. Porowski, P. R. Hageman, and J. Likonon, “Effect of growth polarity on vacancy defect and impurity incorporation in dislocation-free GaN”, *Appl. Phys. Lett.* **86**, 031 915 (2005).
- [346] L. K. Li, M. J. Jurkovic, W. I. Wang, J. M. V. Hove, and P. P. Chow, “Surface polarity dependence of Mg doping in GaN grown by molecular-beam epitaxy”, *Appl. Phys. Lett.* **76**, 1740 (2000).

- [347] A. J. Ptak, T. H. Myers, L. T. Romano, C. G. V. de Walle, and J. E. Northrup, “Magnesium incorporation in GaN grown by molecular-beam epitaxy”, *Appl. Phys. Lett.* **78**, 285 (2000).
- [348] X.-L. Guo, J.-H. Choi, H. Tabata, and T. Kawai, “Fabrication and optoelectronic properties of a transparent ZnO homostructural light-emitting-diode”, *Jpn. J. Appl. Phys.* **40**, L177 (2001).
- [349] S. A. Chevtchenko, J. C. Moore, U. Özgür, X. Gu, A. A. Baski, H. Morkoç, B. Nemeth, and J. E. Nause, “Comparative study of the (0001) and (000-1) surfaces of ZnO”, *Appl. Phys. Lett.* **89**, 182111 (2006).
- [350] T. P. Bartel, “Chemical inhomogeneity in  $\text{In}_x\text{Ga}_{1-x}\text{N}$  and ZnO: a HRTEM study on atomic scale clustering”, PhD thesis, Technische Universität Berlin (2008).
- [351] T. V. Shubina, A. A. Toropov, V. N. Jmerik, M. G. Tkachman, A. V. Lebedev, V. V. Ratnikov, A. A. Sitnikova, V. A. Vekshin, S. V. Ivanov, P. S. Kop’ev, P. Bigenwald, J. P. Bergman, P. O. Holtz, and B. Monemar, “Intrinsic electric fields in N-polarity GaN/ $\text{Al}_x\text{Ga}_{1-x}\text{N}$  quantum wells with inversion domains”, *Phys. Rev. B* **67**, 2003 (2003).
- [352] V. Ratnikov, R. Kyutt, T. Shubina, T. Paskova, E. Valcheva, and B. Monemar, “Bragg and Laue x-ray diffraction study of dislocations in thick hydride vapor phase epitaxy GaN films”, *J. Appl. Phys.* **88**, 6252 (2000).
- [353] J. E. Rowe, M. Cardona, and F. H. Pollak, “Valence band symmetry and deformation potentials of ZnO”, *Solid State Commun.* **6**, 239 (1968).
- [354] D. C. Look, G. C. Farlow, P. Reunchan, S. Limpijumnong, S. B. Zhang, and K. Nordlund, “Evidence for native-defect donors in n-type ZnO”, *Phys. Rev. Lett.* **95**, 225502 (2005).

# Acknowledgment

This work would not have been possible without the support of many people. In particular, I would like to express my gratitude to ...

- Prof. Dr. Axel Hoffmann for the opportunity to work in his group, for his continuing support and encouragement in all matters of physics and beyond and for his personal dedication to the wellbeing and development of his students and research assistances. His enthusiasm and comprehension for all kinds of physical problems were a great help and strong motivation during the past years. I am also grateful for the frequent possibilities to present research results on scientific conferences all over the world and for the opportunity to work as a guest researcher at the ICMAB in Barcelona and the University of Pretoria.
- Prof. Dr. Bruno K. Meyer for the productive cooperation resulting in several joint publications, the never ending supply of new ideas and samples and his willingness to be co-supervisor of this work.
- Prof. Dr. Christian Thomsen for reviewing this thesis, for his support in the UniCat cluster, and for the pleasant atmosphere in his working group.
- Prof. Dr. Michael Lehmann for being the chairman of my defense.
- Prof. Dr. Michael Driess and his coworkers for the collaboration in the UniCat cluster.
- Prof. Dr. Sebastian Polarz for the cooperation and supply of samples.
- Prof. Dr. Matthew Phillips for stimulating my enthusiasm for research and Australian wine during my time at the University of Technology Sydney and for the pleasant evenings during international conferences and his visits to Berlin.
- Prof. Dr. Herbert W. Kunert and Prof. Dr. Johan B. Malherbe for their hospitality and support at the University of Pretoria in South Africa.
- Dr. Anna V. Rodina for many valuable contributions and discussions about excitons and defects, for her immediate email answers at all hours, and for her active interest in my research.

- 
- Dr. Stefan Lautenschläger and Dr. Joachim Sann for the continuous physical discussion, exchange of ideas and supply of new samples.
  - Dr. Juan Sebastian Reparaz for sharing my office and my sometimes unusual working hours, for all the lunches at the 'Steinecke' with countless discussions and creative new ideas, for introducing me to the worlds of pressure, nanowires and Argentinean steaks and for the great time during the ICPS and PLMCN in Rio de Janeiro and Mexico.
  - Ronny Kirste for the realization of several joint research projects, for introducing me to Raman spectroscopy, for many physical discussions and for the annually time together at the Photonics West in-between talks, national parks and shopping centers.
  - my former diploma students Christian Rauch, Jan-Hindrik Schulze, Gordon Callsen, and Martin Kaiser for their competent work and contributions to this thesis:
  - Christian Rauch for his commitment to the magnetic field studies and for our continuing cooperation on positron annihilation research.
  - Jan-Hindrik Schulze for his commitment to the time resolved and magnetic field studies and for his active support in the planning and construction of a new picosecond lab.
  - Gordon Callsen for his exceptional competence in experimental issues, the continuous motivation and capability to improve existing setups, the strive for the highest possible precision in experimental measurements and the commitment to the uniaxial pressure studies.
  - Christian Nenstiel, Martin Kaiser, and Miran Alic for support with the photoluminescence excitation spectroscopy measurements.
  - Stefan Werner for our joint work on resonant Raman scattering and the regular food supply for upcoming night shifts.
  - Dr. Enno Malguth and Dr. Munise Cobet for plenty of interesting discussions and amusing anecdotes during our shared office time.
  - Dr. Til Bartel for the HRTEM measurements.
  - Irina Ostapenko for the CL measurements.
  - Dr. Harald Scheel for support with the magnetic field cryostat and many more technical challenges.

- Heiner Perls, Bernd Schöler, Michael Mayer, Werner Kaczmarek, Michaela Sofsky, Nobert Lindner, and Nobert Zielinski for the swift and extensive assistance with all technical problems.
- Ines Rudolph and Doreen Nitzsche for help with all administrative issues.
- Diane Feldmann, Juan Sebastian Reparaz, Ronny Kirste, Anna Rodina, and Gordon Callsen for proof reading.

I am grateful to all members of the working groups of Axel Hoffmann and Christian Thomsen for the productive, cheerful and pleasant atmosphere. Many of my coworkers and former diploma students have become good friends over the years and made my PhD time at the Technische Universität Berlin not only successful but also very enjoyable. Thank you!

Financial support is acknowledge from the Ernst-von-Siemens foundation, the cluster of excellence UniCat 'Unifying concepts in catalysis' and the Sonderforschungsbereich SFB 787.

My deepest gratitude goes to my family for their unconditional support and to

Diane Feldmann for her love, encouragement, and support, and for the best Thai green chicken curries.